

Assessment of the Adhesion Performance of Diamond-Like Carbon Coatings at Elevated Temperature

**vom Fachbereich Material- und Geowissenschaften
der Technischen Universität Darmstadt**

zur Erlangung des Grades
Doctor rerum naturalium
(Dr. rer. nat.)

Dissertation
von M.Sc. Richard Braak
aus Flörsheim

1. Gutachter: Prof. Dr.-Ing. Karsten Durst
2. Gutachter: Prof. Dr. Wolfgang Ensinger

Darmstadt 2020

Assessment of the Adhesion Performance of Diamond-Like Carbon Coatings at Elevated Temperature

Bewertung der Haftungsperformance von Beschichtungen aus diamantähnlichem Kohlenstoff bei erhöhter Temperatur

Genehmigte Dissertation von M.Sc. Richard Braak

Fachbereich Material- und Geowissenschaften, Technische Universität Darmstadt

1. Gutachter: Prof. Dr.-Ing. Karsten Durst

2. Gutachter: Prof. Dr. Wolfgang Ensinger

Tag der Einreichung: 14.09.2020

Tag der Prüfung: 10.11.2020

Braak, Richard: Assessment of the Adhesion Performance of Diamond-Like Carbon Coatings at Elevated Temperature

Darmstadt, Technische Universität Darmstadt,

Jahr der Veröffentlichung der Dissertation auf TUPrints: 2021

URN: urn:nbn:de:tuda-tuprints-145772

Tag der mündlichen Prüfung: 10.11.2020

Veröffentlicht unter CC BY-SA 4.0 International

<https://creativecommons.org/licenses/>

Erklärung zur Dissertation

Die Dissertation ist von mir mit einem Verzeichnis aller benutzten Quellen versehen. Ich erkläre, dass ich die Arbeit - abgesehen von den in ihr ausdrücklich genannten Hilfen - selbständig verfasst habe.

Abstract

Coatings of *diamond-like carbon* (DLC) are amorphous thin films with diamond-like properties and therefore excellently suited for the reduction of friction and wear in tribological systems. A reduced wear rate corresponds to a longer mean lifetime of the system. However, an adhesive failure of the DLC coating can lead to immediate failure of the application. Particularly, intrinsic compressive stresses within the DLC coatings are a driving force for delamination of these thin films.

In order to assess the risk for an adhesive failure, it is common sense that the *adhesion* of the coating is the essential property of the coating system. However, it will be shown, that for DLC coatings, the delamination initiation and its propagation rely on different characteristic stress conditions. This is especially relevant for coating systems with extended adhesion layer systems. For a reliable assessment of the risk for adhesive failure, this interplay between initiation and propagation of delamination must be considered. Therefore the term *adhesion performance* is introduced as a systemic measure dependent on the application conditions and comprising delamination initiation and progression. For establishing the model for the adhesion performance, the Evans-&-Hutchinson-model based on buckling of an Euler column is extended by considering the initiation of buckling, as well as the re-initiation of buckling after break-away of a coating segment, where a characteristic residual crack remains and crack growth can be driven by corrosive means. Finally, thermal aging is investigated, motivated by elevated application temperatures, which can activate diffusion processes, altering the adhesion performance.

A routine for assessing the adhesion performance is worked out based on the three aspects *delamination initiation*, *buckling* and *re-initiation of delamination*, complemented by the influence of thermal aging on the adhesion performance. This approach is performed on nine different adhesion layer designs as support for hydrogenated and H-free DLCs. The adhesion layer designs comprise metallic Cr- and Ti-adhesion layers with different kinds of carbide interlayers, such as Cr_xC_y , TiC and SiC, partly with alterations in the deposition process. The coating systems are extensively analyzed via transmission electron microscopy, in order to correlate structure and phase compositions with the adhesion

performance. A design concept for adequate adhesion performance with respect to automotive applications with steel substrates and elevated temperatures was furthermore derived based on the findings.

Contents

1	Introduction	5
2	Theoretical Background	7
2.1	Material Class of Diamond Like Carbon	7
2.1.1	Properties	8
2.1.2	DLC Coatings for Automotive Applications	10
2.2	Deposition Process of DLC Coating Systems	11
2.2.1	Substrate Pre-Treatment & Metal Base Layer	11
2.2.2	Subplantation of C-Ions	12
2.2.3	Plasma Assisted Chemical Vapor Deposition	13
2.2.4	Cathodic Arc Evaporation	15
2.3	Mechanical Characterization	16
2.3.1	Nanoindentation Testing	16
2.3.2	Wafer Curvature Test	17
2.4	Thermal Stability of DLC	18
2.5	Delamination Behavior of DLC	20
2.5.1	Intrinsic Strain Energy	21
2.5.2	Buckling Driven Delamination	21
2.5.3	Adhesion Testing	25
2.5.4	Chemical Stability of the Interface Region	30
2.5.5	Optimization Approaches for Stable Interface Regions	33
3	Coating System Design and Methods	35
3.1	Coating System Design	35

3.2	Specimen Preparation	37
3.3	Analytical Methodology	39
3.4	WP1: Coating System Assessment	39
3.4.1	Structural Characterization	39
3.4.2	Mechanical Properties	42
3.4.3	Adhesion Performance Assessment	45
3.4.4	Thermal Annealing	46
3.5	WP2: Buckling Driven Delamination	47
3.5.1	Stress Field Nano Scratch	47
3.5.2	Stress Field Quantification	48
3.5.3	In-Situ Rockwell Indentation	51
3.5.4	Ex-Situ Analysis	52
3.6	WP3: Adhesion Fatigue	52
3.6.1	Skewed Cylinder Test	52
3.7	WP4: Interfacial Corrosion	53
3.7.1	Sonotrode Test	53
3.7.2	Thermal Annealing Tests	53
3.7.3	Ex-Situ Investigations	54
3.8	WP5: Thermal Aging & SCC	55
3.8.1	Incubation Time Estimation	55
3.8.2	Stress Corrosion Tests	56
4	Characterization and Adhesion Assessment	59
4.1	Structural Analysis	59
4.1.1	ta-C with Ti Adhesion Layer	60
4.1.2	ta-C with Carbide Interlayers	64
4.1.3	a-C:H-based Systems	69
4.1.4	Mechanical Characterization	72
4.2	Adhesion Performance Assessment	73
4.3	Long Time Thermal Annealing	78
4.3.1	Change in Adhesion Performance	79

4.3.2	Change in Structure	83
5	In-Plane Stress Field Analysis	92
5.1	Adhesion Performance Evaluation	92
5.1.1	Definition of Terminology	93
5.1.2	As-Deposited State	93
5.1.3	Annealed State	96
5.2	Induced Anisotropic Stress Fields	98
5.2.1	Stress Field Evaluation	98
5.2.2	Damage Evolution	101
5.3	Stress Fields in the SFNS	105
5.4	Quantification of Strain Energy Release Rate	107
5.5	Conclusions of the Stress Field Analysis	110
5.6	Skewed Cylinder Test	111
6	Local Thermo-Chemical Aging	113
6.1	As-Deposited State	114
6.2	Long Time Thermal Annealing	115
6.2.1	a-C:H System with Gradient Interlayer	115
6.2.2	a-C:H System with Step-wise Interlayer	121
6.2.3	Comparison of both Systems	124
7	Thermal Aging and Corrosion assisted Delamination	127
7.1	Aging of the Interface Region	128
7.2	Retarded Delamination Progression	131
7.2.1	Buckling Driven Delamination	131
7.2.2	Medium Driven Progression	136
7.3	Post Mortem Oxidation of Titanium	143
7.4	Passivation of Pre-Damages	144
7.5	Conclusions on Thermo-Chemical Stability	150
7.5.1	Consequences for Analysis	152

8	Summary and Conclusions	153
8.1	New Concept: Adhesion Performance	154
8.2	Holistic Measurement of Adhesion Performance	159
8.3	Holistic Layout Design	165
8.3.1	Mechanical Strength	165
8.3.2	Stress Management	167
8.3.3	Thermal and Chemical Stability	167

Chapter 1

Introduction

Modern common rail systems for Diesel injection rely on the outstanding tribological properties of diamond like carbon coatings (DLC). With high hardness and low friction coefficient of DLC, supplemented with the in-service formation of graphene-like tribolayers, wear and friction of tribological contacts are significantly reduced. This saves energy and enhances the lifetime of the tribological system. Furthermore, mechanical and thermal load on the coated part can be increased and the geometric dimensions reduced. Even tribological contacts without lubrication are possible by the introduction of DLCs on one contact partner [1].

For protection of the substrate, in-service delamination of the coating needs to be prevented. Otherwise severe damage of the substrate is expected. Adhesion of tribological hard coatings is usually treated as a single property of the coating-substrate system, e.g. in common adhesion tests [2, 3]. In this work, it will be shown that this approach is premature when extended interface regions, such as adhesion layers prevail and thermal and chemical aspects play a role. Therefore the term adhesion performance is introduced as an application dependent systemic measure, which enables the prediction, whether adhesive failure will occur. Therefore, also the influence of external loads, temperature and environment is included in the complex model for the adhesion performance.

Subsequent to the introductory part (chapter 1) and an overview of corresponding literature (chapter 2), the experimental methodology and the concepts for adhesion layer design are presented in chapter 3. Nine different adhesion layer systems are used for the analysis, starting with a first assessment with common adhesion tests in the as-deposited

and in a thermally annealed state, supplemented with transmission electron microscopy (TEM) of the interface regions, all discussed in chapter 4.

The influence of indentation stress fields on the delamination behavior is dealt with in chapter 5. Furthermore, the *stress field nanoscratch* is presented for provoking controlled buckling, which is the generic mechanical delamination mechanism for DLCs [4].

Thermal and thermo-chemical aspects are investigated via thermal annealing experiments. Chapter 6 deals with growth defects, which gives the atmosphere access towards the interface region for chemical attacks. In chapter 7, thermal aging of metastable interface regions is discussed. Thermal aging was found to enable stress corrosion driven delamination as a critical step in the overall damage progression.

Based on the experimental findings, an adhesion performance model for compressively stressed hard coatings is presented in chapter 8, as well as a routine for an extended testing and deduced guidelines for adhesion layer design optimization.

Chapter 2

Theoretical Background

2.1 Material Class of Diamond Like Carbon

Due to its four valence electrons and a small atomic radius, carbon is the most flexible element with respect to the formation of molecular and crystalline structures. Carbon has three possible binding states: sp^1 with two localized σ -bonds as in ethyne (common precursor gas for hydrogen containing DLC), sp^2 with three planar σ -bonds as in graphene and in the sheets of a graphite crystal and sp^3 with four tetrahedral σ -bonds as in a diamond crystal. For sp^1 - and sp^2 -hybridized C, the remaining valence electrons can be found in delocalized π states and are responsible for the electronic properties of the species.

The thermodynamically stable graphite and the metastable diamond are natural, genuine crystals. Plasma deposition processes allow for the production of materials without long range order, first applied by Aisenberg and Chabot [5] using ion beam technique. The resulting amorphous carbon exhibits a mixture of sp^2 and sp^3 bonding and its hardness scales directly with the content of sp^3 bonds.

A large variety of amorphous carbon (a-C) coatings with different properties arises directly from a large diversity of process routes. *Physical vapor deposition* (PVD) of DLC relies on solid carbon targets as precursors, resulting in a large group of H-free coatings. Whereas, via *plasma enhanced chemical vapor deposition* the carbon material is provided by a gaseous precursor leading to hydrogen incorporation into the amorphous structure.

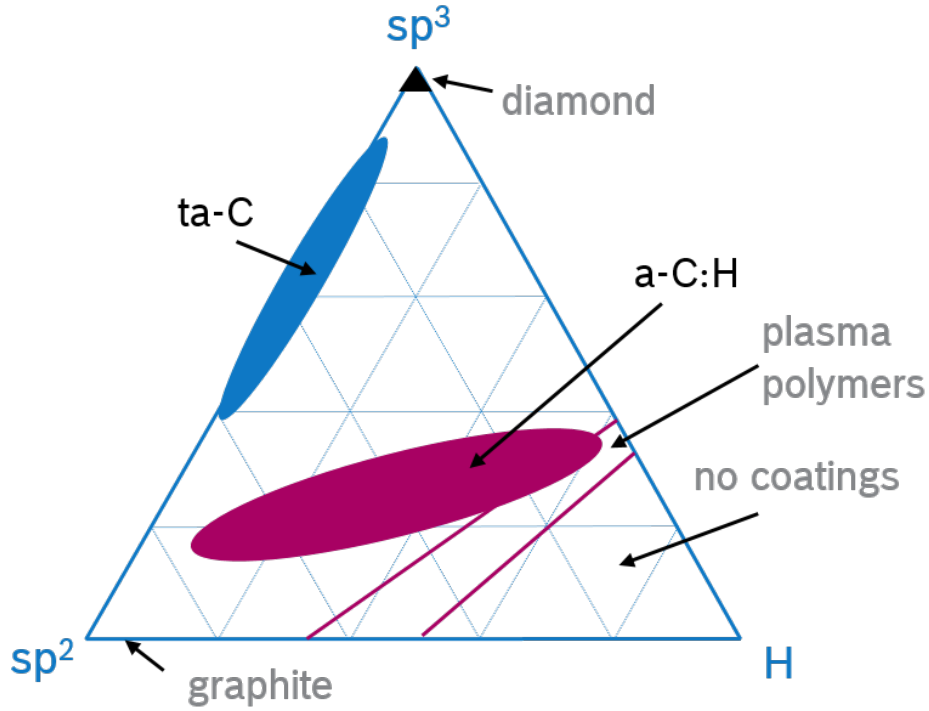


Figure 2.1: Ternary phase diagram for carbon based materials according to [6]: Amount of H, sp^2 - and sp^3 -hybridized carbon. Towards the sp^3 -corner, the materials get more diamond-like, whereas towards the sp^2 -corner more graphitic. With increasing amount of H, the polymeric character increases, until only gaseous species exist.

The materials with more diamond-like character is the group of the *diamond-like amorphous carbon*, which are best described by the ternary phase diagram (refer to fig. 2.1), introduced by Jacob and Möller [6] with sp^2 -bonds, sp^3 -bonds and H at its three corners. The diamond-like properties arise from the tetrahedral sp^3 -bonds, present in the carbon network. Accordingly, the diamond character is most pronounced for materials close to the sp^3 corner, which are the H-free (ta-C) [7] and H-containing (ta-C:H) *tetrahedral amorphous carbon*. For a-C and for *hydrogenated amorphous carbon* (a-C:H), the sp^2 content is significantly higher.

2.1.1 Properties

Diamond like carbon coatings possess outstanding tribological properties, such as high hardness, low friction coefficient (CoF), high wear protection of the coated substrate and a protecting mechanism for the corresponding counterpart.

Hardness H is often regarded as an empirical value related to the resistance against pen-

etration or scratching of a counter part. However on the atomic scale, it is related to the sum of all binding energies per unit volume, i.e. the enthalpy density [8]. The highest contribution arises from the strong, directed σ -bonds [9]: Occupied σ -states are formed in the valence band and empty σ -states in the conduction band with a wide gap between both states, resulting in a high binding energy [10]. On the contrary, for the π -bonds of sp^2 (and sp^1)-sites the energy gap is much smaller resulting in lower binding energy [11]. C-H σ -bonds are similar to the C-C bonds, exhibiting high binding energies, but are not contributing on the network formation and are therefore negatively influencing the hardness. Therefore, not only the sp^3 -, but also the H-content is important for the hardness of DLCs.

A high amount of sp^3 -hybridized C-C σ -bonds is generated by an ion bombardment during the deposition, which is increasing the diamond character. Mechanical properties of ta-C are hence much superior to those of a-C:H, caused by the high C-C coordination [12]. Besides hardness, most of the other properties of ta-C also correlate directly with the sp^3 content [13], such as density, optical band gap and Youngs modulus E . A linear correlation of $E/H = 10$ is typically observed. Reported hardness value ranges from 3 [14] to 88 GPa [15] and modulus from 100 [16] up to 1100 GPa [15], covering a wide range up to almost diamond properties.

Intrinsic compressive residual stress in the range of several GPa [13, 17, 18] are introduced into the growing thin film via ion-bombardment as well. So a correlation between hardness and residual stress is usually observed, but a causal relationship between intrinsic residual stress and sp^3 -share is not given. A high amount of intrinsic stress can lead to adhesive failure in terms of delamination of the coating [19].

With decreasing deposition temperature T_{dep} , the residual compressive stress increases [20]. By incorporation of Si, the residual compressive stress level can successively be reduced [21, 22, 23]. However, intrinsic compressive stress has definitely positive effects on the mechanical properties, as for example crack propagation can be decelerated [24] and crack formation within the coating, which is based on tensile stresses, is shifted to a higher external load, as the compressive stress first has to be overcome in order to reach the tensile region.

The low CoF of DLC is caused by a low surface roughness on sufficiently polished substrates and by its surface chemistry [25]. The substrate surface is reproduced with only slight cauliflower-like texture resulting from the plasma deposition process. Surface roughness can be decreased by reducing the surface diffusion and recrystallization during nucleation and growth of the coating [25].

A further contribution on the low friction coefficient is caused by self-lubrication: A small amount of graphene-like sheets forms, which lubricate the tribological system, accompanied with the deposition of a protective, graphitic transfer layer on the counter body. When applied on gear wheels, DLCs enable even dry lubrication [1, 26] which is otherwise inconceivable due to abrasive wear. CoFs of below 0.1 are reported [23, 27].

The environmental medium plays an important role as well: In dry atmosphere the CoF of DLC is highest (0.15 in dry nitrogen [28]), whereas smallest amounts of moisture decreases the friction (0.1 humid air [28]). The sensitivity is attributed to an intercalation of water molecules into graphitic basal planes. Thereby, dangling bonds are deactivated via chemisorption of those molecules [28]. Dangling bonds are to some extent also saturated by incorporation of hydrogen (a-C:H) [29].

2.1.2 DLC Coatings for Automotive Applications

In automotive industry, DLCs are widely used in several tribological contact applications. E.g. modern Diesel common rail injection systems with high fuel pressures of up to 2500 bar [30] and temperatures of up to 300 °C [31] (proximity to the combustion chamber), rely on the protective properties of DLC. Typical parts in a common rail injector, which are coated are nozzle needles or valve pieces. In a corresponding Diesel high pressure pump, additional tribological contacts are equipped with DLC coatings.

Parts serving as substrate usually consists of high strength or high speed steels. Adhesion of DLC deposited directly onto steel however is reported to be poor (e.g. [32, 33, 34]) and adhesion layers consisting of carbide forming metals [35, 36] (like Cr, W, Ti,...) are used to constitute the adhesion.

2.2 Deposition Process of DLC Coating Systems

H-containing DLCs are often deposited via plasma enhanced (or assisted) chemical vapor deposition (PECVD, PACVD), H-free DLCs via physical vapor deposition PVD-processes with high energy, such as cathodic arc evaporation. Both are used for the sample preparation in this work. PECVD processes are realized by a continuous power supply, whereas the high energy PVD processes are realized as pulsed processes, to avoid overheating of the cathodes. An overview over the most prominent process routes is given in table 2.1. Details for the relevant processes for this work are presented in the following, including pre-treatment of the substrate surface.

Table 2.1: Most common deposition methods, relevant for DLC divided into continuous and pulsed processes. PECVD and CAE are used in this work.

power	method	DLC species
continuous	magnetron sputtering (MS)	a-C
continuous	plasma enhanced chemical vapor deposition (PECVD)	a-C:H, ta-C:H
continuous	mass selected ion beam (MSIB)	ta-C
cont./pulsed	Cathodic Arc Evaporation (CAE)	ta-C
pulsed	pulsed laser deposition (PLD)	ta-C
pulsed	high power pulse MS (HPPMS)	ta-C
pulsed	deep oscillation MS (DOMS)	ta-C

2.2.1 Substrate Pre-Treatment & Metal Base Layer

Contaminations, such as dirt and grease for example reduce the number of atomic bonds at the later interface. So in order to achieve sufficient adhesion strength per unit area on a machined steel part, a cleaning step is mandatory. A second step, which can also be considered as mandatory is the plasma etching of the substrate which is done directly in the deposition chamber. More resistant dirt as well as passivation layers can be removed, and additionally the surface gets activated for the subsequent deposition process.

With too long etching durations, a re-deposition of contamination species can occur, as well as sequential sputtering, i.e. a preferential etching of different surface orientations or a slower etching at hard carbide phases in precipitation hardened steels. Additionally, the thermal energy introduced into the part is not negligible and temperatures of up to

300 °C can be reached during plasma etching [20].

Metal adhesion layers are often deposited via magnetron sputtering. A detailed analysis of the morphology of sputter deposited thin films is expressed by the famous structure zone diagram (SZD) [37]. During epitaxial growth sufficient thermal energy is available at the substrate surface for the following processes to simultaneously occur: Adsorption of the incoming species, surface diffusion, desorption, nucleation and island growth. Coalescence of islands during growth yields tensile stresses, which is the case for metallic adhesion layers MS-deposited at low temperatures, as done in this work.

2.2.2 Subplantation of C-Ions

In order to achieve an amorphous structure, the processes corresponding to epitaxial growth must be prevented. Surface diffusion can be disturbed via ion bombardment, higher surface energy and lower T_{dep} [25]. Active water cooling of the part holder leads to high sp^3 to sp^2 ratios and high hardness [20], but is rather uneconomical. The usual approach is to provide an intense ion bombardment and to hinder the part to store too much heat, which is achieved by rotation of the sample holder. Bombardment of a foreign ion species as Ar for instance produces an amorphous structure as well. For very high hardness of the film however, subplantation of incident C-ions underneath the surface of the growing film is necessary, which induces the sp^3 formation [38, 39, 40, 41, 42].

For the formation of sp^3 -bonds, an optimum ion energy is postulated, which corresponds to an optimum bias voltage in a PVD or PECVD process, applied by a self-bias or adjusted via additional external voltage support. The energy density of the penetrating particles can be measured by the proportional current density at the substrate.

Too low ion energies have several drawbacks: A high surface roughness, strict interface to the substrate, low density [43], a significant content of voids [44] and a strongly columnar film growth can arise [27]. Adsorption and rebound are dominant, which both lower the sp^3 -content [43]. The character of the thin films become successively more graphitic for a-C and more polymeric for a-C:H [45].

On the other hand, an excess of energy leads to resputtering and damaging of the coat-

ing in the sense of voids and plastic flow [46]. The film is again less dense with a lot of defects [43]. It leads also to relaxations in the "heat-affected zone" [43] and the coatings get successively more graphitic for both types, H-free and H-containing [14, 45]. Also delamination was observed [27].

Consequently, a sufficiently high ion flux with a narrow energy distribution, low pressure and a controlled bias voltage favor sp^3 formation and increase the coatings density and reduce the amount of disordered structure [27, 47]. A high ion density in the plasma is therefore required [25, 47].

The optimum energy is discussed controversially in literature. Several work groups postulate an optimum of 100 eV [18, 47, 48, 49] per C-atom, with a postulated maximum sp^3 -content of 85 % [18]. However further optima are stated elsewhere: -60 V bias voltage [27], 70 eV/ion [43] and 20 to 40 eV/ion [25].

From the bombardment and sputtering of ions, compressive residual stresses arise [18, 25]. The compressive residual stress increases with increasing ion impact energy and decreasing deposition temperature [20]. Molecular dynamic simulations (MD) suggest that the intrinsic stress is a consequence of decreased binding angles [43]. Furthermore four regions are identified within the growing film [43]: A substrate region, a transition region, a stable region and a surface region. The highest intrinsic compressive stresses thereby prevail in the transition region.

Besides intrinsic stress thermal stress arises simultaneously. Thermal stress is caused by the typically different expansion coefficient of the substrate and the thin film material. DLC has to be deposited at rather low temperatures with respect to the sp^3 -formation. For sufficiently low T_{dep} , the thermal part of the stress can be neglected [19].

2.2.3 Plasma Assisted Chemical Vapor Deposition

Plasma density n_0 and electron temperature T_e are the fundamental parameters of plasma deposition. With a high T_e the ionization gets maximized [47]. Ionized species can be accelerated via external power supply and the mean ion energy is proportional to the bias voltage [47]. A high ionization degree in the plasma therefore yields a good control of

the kinetic energy of the deposited particles. Process routes for DLC can be divided into processes with continuous and with pulsed power supply. Continuous processes are rather simple in process management. More sophisticated pulsed processes have their justification by the high plasma density and high energy introduction into the growing film with simultaneously suppressing the heat entry.

PECVD is the major technique for deriving hydrogenated amorphous carbon. The C, as well as the incorporated H, are provided by the gas phase, wherefore several different precursor materials are available. Important for the coating properties is the C to H ratio and the mass of the gas molecules. Increasing the hydrogen content in the sputtering gas mixture results in decreasing hardness (14 GPa to 3 GPa) and decreasing mass density [14].

The choice of precursor gas also influences the deposition rate, which increases roughly exponentially with decreasing ionization potential [50]. In this respect, ethyne is an appropriate candidate. The ionization potential of benzene is even lower, with the same C to H ratio as ethyne. However, benzene with its six C atoms requires a high bias voltage to reach the optimum energy per C atom for a high sp^3 content in the coating [47].

By using precursor gases with additional atomic species, doping of the DLC is possible. Metal doped DLCs (Me-DLCs) exhibit pronounced columnar structures [51] with nano-scale Me-carbide-inclusions in an sp^2 -rich matrix [52, 53]. Incorporation of Si reduces the H-content, which increases the thermal stability and homogeneous nano-layers can be produced with smooth surfaces [23]. Furthermore, the intrinsic stress gets reduced with increasing Si-content [21, 22].

A controlled Ar-plasma is widely utilized in order to ionize the hydrocarbons and furthermore giving additional Ar-ion impact on the growing film. Due to the low mass of electrons, they have a higher mobility compared to the quite heavy ions in the plasma, which results in a space-charge region at the electrodes, often called sheath, which leads to a net voltage, the so called self-biasing [47].

With magnetic constraining of the plasma, lower pressures are possible and thereby, the mean free path exceeds the sheath thickness which results in a more narrow energy distribution [47]. Generally high rates and low intrinsic stresses are achieved via PECVD. A

high plasma density leads to ta-C:H [47, 48].

By increasing the excitation frequency towards very high frequency (VHF) or using inductively coupled plasma (ICP), the ion density can be increased. Alternatively, electron cyclotron resonance (ECR) via microwaves can be used: Thereby, a large, static axial magnetic field is applied to force electrons to oscillate with cyclotron-resonance frequency (2.45 GHz). This can additionally be capacitively coupled with radio frequency (RF at 13.6 MHz) voltage. Electron cyclotron wave resonance (ECWR) [54] exploits a standing wave, leading to extremely high plasma densities of 10^{12} cm^{-3} [47].

2.2.4 Cathodic Arc Evaporation

Cathodic vacuum arc deposition or cathodic arc evaporation (CVAD/CAE) is a widely used technique which delivers high ion densities of up to 10^{13} cm^{-3} , provided via high current and low voltage [7, 47, 55, 56, 57]. Solid, graphitic carbon targets are used as cathode, on which an arc is ignited, evaporating the precursor material. Thereby, the current can be direct current (DC) in a typical range of 50 to 200 A, pulsed with several kA or a superposition of DC and pulsed current [57]. Using pulsed deposition methods, the heat entry can be reduced significantly [25].

Drawback of the CAE technique is the formation of droplets consisting of molten target material, which get also deposited and incorporated as macro-particles into the growing film [7, 47, 57, 58].

A measure to avoid those macro-particles and resulting growth defects are diverse filtering concepts (FCVA) [7, 13, 27, 57, 58]. Most common filters use magnetic fields, which forces the electrons from the plasma on spiral paths creating electrical fields, that the ions of the plasma follow. The result is an ambipolar transport. Neutrals do not follow and can be sorted out, e.g via blinds. The net plasma beam is neutral (positive plus negative) enabling deposition also on insulators.

At arc spots on metal targets, the electrical resistance increases and the arc moves to a next spot with less resistance. In contrast on graphitic targets, the resistance at the arc spot decreases and the arc stays at the same spot, requiring magnetic steering to move the

arc manually [7]. Laser triggering can be used to navigate the arc spot in a very precise manner [59].

With CAE, hard ta-C is attained [7, 13, 47, 57] with sp^3 -ratios of 70 to 90% [55, 56]. The coatings are usually brittle [60] and possess high residual stresses [27, 47, 57, 60], which limits the film thickness to several hundred nanometers or even less [60]. Combinations of DC discharge and high current arc pulses are also possible [20, 61].

2.3 Mechanical Characterization

2.3.1 Nanoindentation Testing

Nanoindentation according to ISO 14577 [62] is an instrumented indentation technique for the estimation of surface near mechanical properties, including indentation hardness H_{IT} , modulus E_{IT} and yield stress by applying the Oliver-Pharr method [63].

A tip area function is derived in a preceding calibration step specifically for each indenter tip, performed on a fused silica standard. The tip area function $A(h)$ connects the indentation depth h to the projected contact area A . During nanoindentation on a sample surface a load indentation curve is recorded. With $A(h)$ and the maximum applied load P_{max} , H_{IT} can be derived via equation 2.1:

$$H_{IT} = \frac{P_{max}}{A(h)} \quad (2.1)$$

During unloading, the elastic strain relaxes. With the initial slope $S = dP/dh$ of the unloading curve and via equation 2.2, the indentation modulus can be derived:

$$E_{IT} = \frac{\sqrt{\pi}}{2} \cdot \frac{S}{\sqrt{A(h)}} \quad (2.2)$$

Diamond tips with defined geometry like a Berkovich pyramid are typically used. As a practical rule of thumb for the measurement of thin films, the upper limit for indentation depth is 10% of the film thickness, as otherwise, the results are increasingly influenced by the substrate's mechanical properties. Furthermore, the surface roughness must be

taken into account, which influences the scattering predominantly. A sufficient depth compared to the surface roughness is needed, which might contradict the 10 %-rule in some cases. With a high number of measurements the influence of the surface roughness, can be statistically balanced, yielding a reasonable mean value with error bars of equal size in positive and negative direction.

The replacement of the plastified material via penetration of the indenter into the sample can cause a pile-up around the indentation, which usually fully build up during unloading, when the elastic part of the deformation relaxes. Dependent on the materials plastification behavior, also a sink-in is possible for some materials.

With the method of the continuous stiffness measurement (CSM) [64], a depth-profile of hardness and modulus can be derived. The working principle relies on a superimposed oscillation, which enables measurement of a small scale load-indentation-curve including the relaxation part and a successive derivation of the mechanical properties incrementally for each step.

A preceding sample preparation, e.g. a calotte grinding or a small angle cross section (SACS) [65] furthermore allows for the measurement of a depth profile through a whole coating system. The different phases or gradient phases are spread by the small angle preparation. Furthermore, the resulting surface is very smooth, enabling measurement with small indentation depths. With a succession of indentations along a line across the SACS, the depth profile is measured. For succeeding measurement spots within the same phase, the influence of the underlying phases decreases. Trends of mechanical properties can be derived by this means, if certain phases exhibit sufficiently high thicknesses.

2.3.2 Wafer Curvature Test

The intrinsic residual stress σ_0 can be estimated with the curvature test: A thin crystalline Si (111)-beam with very low roughness (below 1 nm) and very well defined dimensions and mechanical properties is co-deposited within the deposition chamber. The aspects of the beam are dimensioned in such a way, that the intrinsic stress of the DLC causes the beam to bent. The curvature of the stripe is optically measured in order to derive the

intrinsic stress using the Stoney equation [66]:

$$\sigma_0 = -\frac{1}{6} \cdot \frac{E_{sub}}{1 - \nu_{sub}} \cdot \frac{h_{sub}^2}{h_f} \cdot \frac{1}{r_{exp}} \quad (2.3)$$

with the radius of the curvature r_{exp} , the modulus E_{sub} and Poisson ratio ν_{sub} of the substrate and with the thickness of substrate h_{sub} and thin film h_f .

The equation is valid while the coating thickness is much smaller than the thickness of the beam [67]. A modification of the Stoney equation accounting for the initial curvature before deposition can enhance the precision [68]. For thicker coatings, an extension of the Stoney's equation is necessary, where a stress gradient is considered [69]. Furthermore, the film thickness is physically limited, given by a possible cleavage of the Si-beam. Instead, a Ti beam can be used [70].

2.4 Thermal Stability of DLC

In this work, applications are considered, where DLC is subjected to elevated temperatures. For those applications, the thermal stability of the whole coating system has to be ensured for the parts designed life-time. In this section, a literature overview on the thermal stability of amorphous carbon coatings on Si-wafers is given and summarized in a schematic representation in figure 2.2.

Thermal stability of DLC is limited by the conversion of the metastable sp^3 - into the stable sp^2 -state with an activation energy of 3.5 eV at 1300 K [47], accompanied with the loss of the sp^3 -related properties. Thereby, clusters of planar hexagonal rings consisting of sp^2 bonds form, while the size and number grow with temperature T [11]. They can be embedded in a diamond-like matrix [82, 83], whereby the clusters primarily grow at edges of the coating [83]. Annealing ta-C up to 500-600 °C allows furthermore an almost complete relaxation of the compressive stress [15, 18, 71, 84, 85] and also causes the optical gap to vanish, which leads to a strongly decreased electrical resistivity [18].

Raman spectroscopic analyses of several H-free amorphous carbons (a-C, ta-C) evidenced a decreasing thermal stability with decreasing fraction of sp^3 bonded carbon [72] (com-

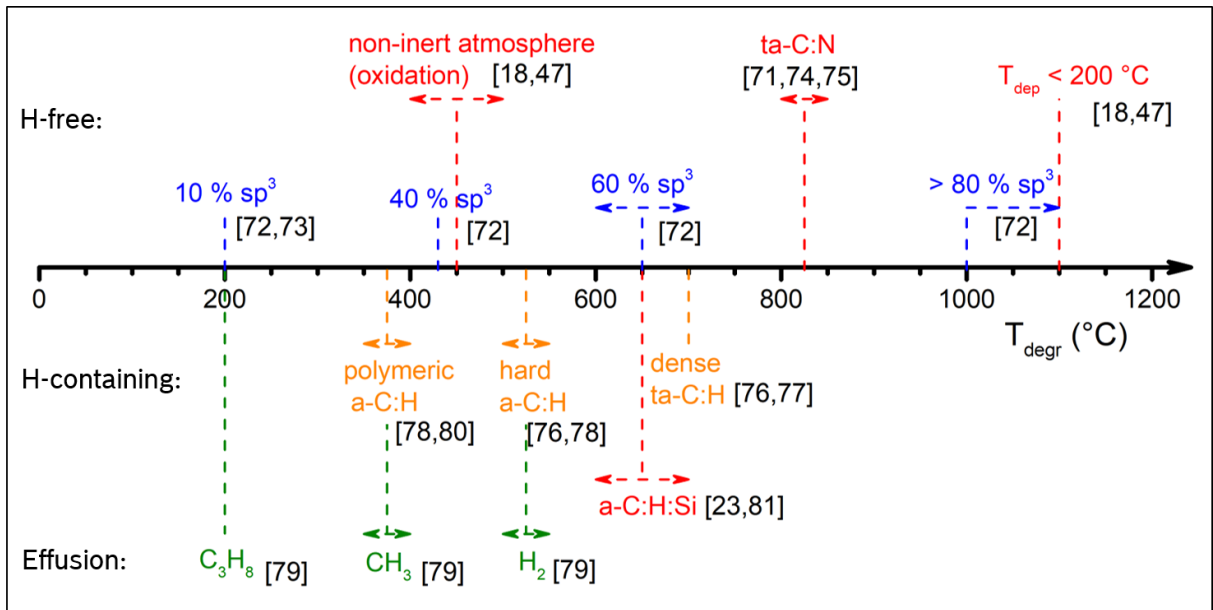


Figure 2.2: Degradation temperatures for different DLC coatings in vacuum: H-free (upper part) with different amount of sp^3 bonded carbon with a maximum for $T_{dep} \leq 200$ °C. Thermal stability is decreased with incorporation of N and even further in non-inert atmosphere (oxidation of carbon). For H-containing DLCs (lower part) the thermal stability is decreased, caused by effusion of hydrogen and hydrocarbons. Data from literature [18, 23, 47, 71, 72, 73, 74, 75, 76, 77, 78, 79, 80, 81].

pare to figure 2.2). Highest presented sp^3 -content is achieved with deposition temperatures below 200 °C with thermal stability up to 1100 °C [18, 47]. Due to the wide range of accessible sp^3 -content in H-free amorphous carbons, also the degradation temperature T_{degr} covers a wide range down to 200 °C [73].

An incorporation of N into the system is supposed to decrease the thermal stability [74, 75, 85]. In non-inert atmosphere the thermo-chemical stability is reduced significantly via oxidation of carbon [18, 47].

Hydrogen containing amorphous carbons (a-C:H, ta-C:H) are thermally less stable than their H-free counterparts: Mass spectroscopic thermal effusion measurements [78] showed that hydrogen can leave the amorphous structure in form of hydrocarbon molecules or molecular H_2 . The degradation temperature is connected to the effusion temperature [79] (compare to the lower part of figure 2.2). Hydrocarbon effusion is predominant in more polymeric [79] carbon coatings arising at lower temperatures: The lowest threshold reported was 200 °C, where mostly C_3H_8 [79] effuses. For denser coatings, but still with polymeric character the main effusion was CH_3 [79] with effusion temperatures in the range of 350 to 400 °C [78, 80].

With the hydrocarbon effusion, parts of the network are removed. Dense coatings with more diamond-like properties effuse almost exclusively H_2 [79], which is supposed to promote the degradation of the coating by an additional loss in sp^3 -bonding [80]. However, sp^3 -bonding between two carbon atoms and between C and H must not be mixed up, as the latter does not participate in the crosslinking. Other mechanisms have to be taken into account, e.g. the recombination of atomic H into molecular H_2 , accompanied with an energy gain which might lead to an atomic rearrangement in the carbon network [25]. Nevertheless, the effusion temperatures are higher compared to the hydrocarbon effusion: ta-C:H (>60 % sp^3) derived from methane behaves similar to hard a-C:H with effusion temperatures around 500 to 550 °C [76, 78]. For the even denser ta-C:H derived from ethyne, the highest effusion temperature was found with 700 °C [76, 77, 79].

Incorporation of Si is supposed to stabilize a-C:H by a replacement of the H [23, 81]. The silicon participates in the network formation with its four covalent bonds analogous to the carbon. The critical temperature of a-C:H:Si is increased up to 600 [23] or even 700 °C [21, 81] which is comparable to the dense ta-C:H.

Establishing sufficient adhesion of a DLC on a Si substrate represents no issue, due to well defined and clean substrate surfaces, as well as chemical similarity of carbon and silicon. For automotive applications, in addition to sufficient thermal stability of the coating itself, a thermally stable adhesion system for DLC on steel parts is required, which is addressed in the present work. The reviewed data of this chapter gave a well assessment of the coatings stability during the planned annealing experiments.

2.5 Delamination Behavior of DLC

In order to develop a model for the adhesion performance of a compressively stressed coating system, the coatings delamination behavior must be analyzed. In anticipation of the results of this work, the delamination behavior can be divided in three steps: Delamination initiation, progression and re-initiation of delamination. Each step is determined by buckling of the coating, driven by (intrinsic) residual compressive stresses. External mechanical and thermo-chemical loads are furthermore influencing the behavior. A liter-

ature overview on relevant aspects is given in the following.

2.5.1 Intrinsic Strain Energy

The intrinsic adhesion strength is defined as the bonding strength times the number of bonds [86] per unit area. For crack advance, not only the interface chemistry, but also the elastic-plastic behavior of the interface region has to be considered [70]. Analogous to the Griffith criterion from fracture mechanics, the adhesion energy can be defined as the work of fracture per unit area and corresponds to the critical strain energy release rate G_c for delamination.

The delamination behavior of DLC coatings is mainly determined by the in-plane compressive residual stress caused by the ion impact [39, 40, 42] during deposition. Compressive stress has its benefits in terms of hampering tensile crack formation. However, at the interface, high compressive in-plane stress acts as an additional driving force for delamination.

For a coating system with a planar interface between the substrate and an amorphous coating with homogeneously distributed intrinsic stress, an isotropic, biaxial stress state can be assumed with a corresponding elastically stored in-plane strain energy per unit area Ω_0 [87]:

$$\Omega_0 = \frac{(1 - \nu_f)}{E_f} \cdot h_f \cdot \sigma_0^2 \quad (2.4)$$

The stored energy scales quadratically with σ_0 and linearly with h_f , as long as σ_0 is independent of h_f . E_f and ν_f are the Young's modulus and the Poisson's ratio of the thin film.

2.5.2 Buckling Driven Delamination

In figure 2.3, a coating segment is schematically depicted as a compressed spring accounting for the in-plane strain energy. Removal of a coating segment is always accompanied with a release of the elastically stored energy Ω_0 . Delamination of a coating segment

is therefore always accompanied by an out-of-plane deflection which can be described mathematically by buckling of a Euler column [4]. Besides a partly relaxation of the compressive stress, tensile stresses at the fixed edges arise. The rotational symmetry of the isotropic biaxial stress state within the coating causes a buckle with circular contour, in contrast to a Euler column.

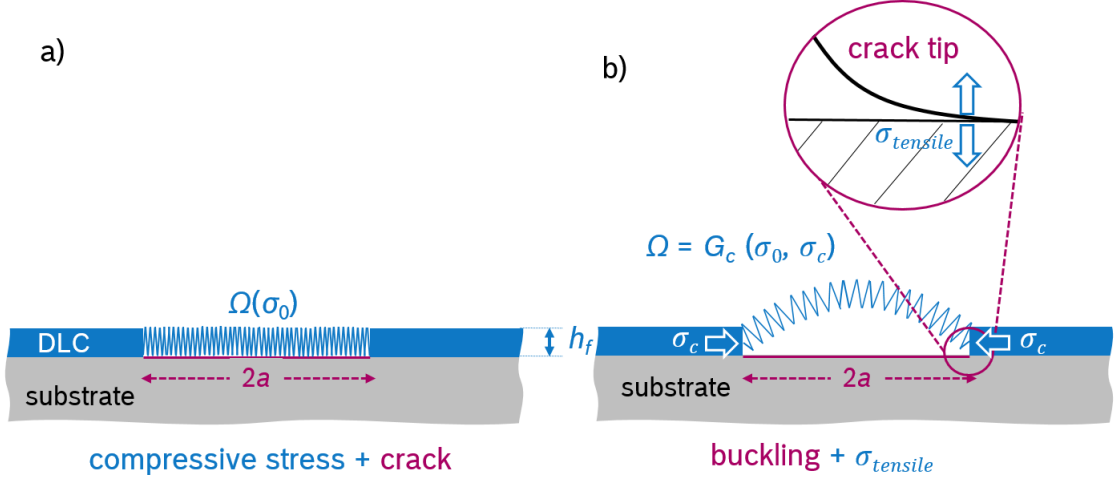


Figure 2.3: Delamination of a coating segment, schematically depicted as a compressed spring: a) Initial condition with crack of length $2a$. b) Buckling of a coating segment during delamination, caused by the stress relaxation, leads to tensile stresses $\sigma_{tensile}$ at the annular crack tip, which drive the crack propagation.

Evans and Hutchinson [4] modeled this buckle type as a clamped circular plate [88] with a fixed annular edge. The radius a of the plate corresponds to a preexisting, interfacial penny shaped crack. Equation 2.5 describes the critical stress σ_c which is necessary for buckle formation against the stiffness of the coating segment as a function of h_f , a and a geometry factor $k = 14.68$ accounting for the circular shape of the buckle in three dimensions [4]:

$$\sigma_c = \frac{kE_f}{12(1-\nu_f^2)} \cdot \left(\frac{h_f}{a}\right)^2 \quad (2.5)$$

σ_c relaxes during buckle formation. Forced by its geometry, the residual stress in the buckle is transferred to its edges, so directly towards the annular crack front (compare to figure 2.3 b)) with a mixture of mode I (tensile) and mode II (shear stress). The relaxation of the coating segment commences via failure of the interface, leading to buckle

growth with the strain energy release rate G , which scales with σ_0^2 ($\propto \Omega_0$) and gets reduced by the already relaxed part of Ω_0 , which scales with σ_c^2 , according to equation 2.6 [4]:

$$G = (1 - \nu_f)(1 - \alpha)h_f(\sigma_0^2 - \sigma_c^2)/E_f \quad (2.6)$$

with $\alpha = (1 + 1.207(1 + \nu_f))^{-1}$.

Figure 2.4 shows the two intrinsic mechanisms which are stabilizing the interfacial crack front at characteristic buckle radii and limiting buckle growth: Mode change and spallation. During growth of a circular buckle its aspect ratio (radius vs. height) increases and thereby the share of shear mode on the mode mixture increases successively (compare to fig. 2.4 a)). Once the strain of the atomic bonds at the crack front is subcritical, the crack front stabilizes.

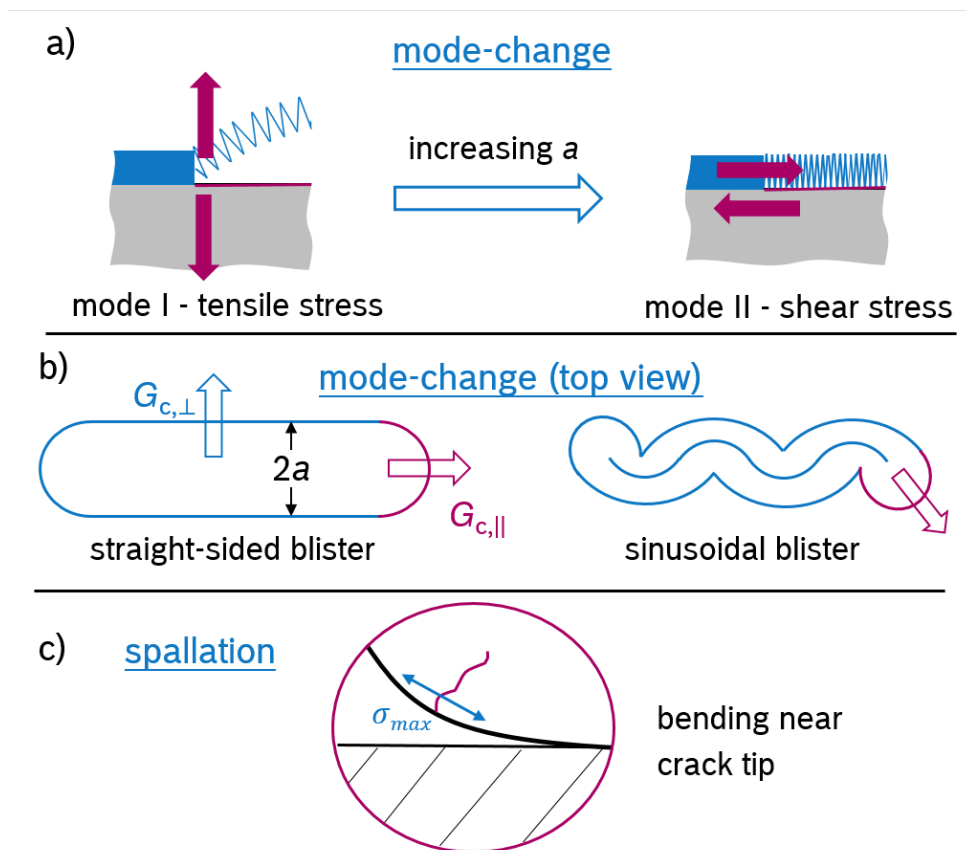


Figure 2.4: Intrinsic size-effects of the buckling driven delamination: a) Increasing aspect ratio changes stress mode from I into mode II and stabilizes the crack front. b) Types of buckling driven delamination with constant crack radii. c) Spallation with through thickness crack caused by bending of the coating. The remaining coating exhibits a residual interface crack.

However, the energy release rate is still high and new buckle nuclei are built along the crack front which can grow analogous until they reach the size, where the share of mode I is sufficiently reduced and the crack front stabilizes again. By superposition of these buckles, differently shaped types of buckling driven delamination arise (fig. 2.4 b)): The straight-sided blister growing along a straight line [89], the sinusoidal blister following a sinus shaped path [89, 90] or large area blistering with periodical patterns [91]. In both cases, the propagating, radial crack fronts are small enough to exhibit sufficient share of mode I.

The straight-sided blister can be described as an infinitely extended Euler column with the critical stress perpendicular to the direction of propagation $\sigma_{c,\perp}$ as [4]:

$$\sigma_{c,\perp} = \frac{\pi^2}{12} \cdot \frac{E_f}{(1 - \nu_f^2)} \cdot \left(\frac{h_f}{a}\right)^2 \quad (2.7)$$

The corresponding $G_{c,\perp}$ at the stable flanks is [92]:

$$G_{c,\perp} = \frac{(1 - \nu_f^2) \cdot h_f}{2E_f} \cdot (\sigma_0 - \sigma_{c,\perp}) \cdot (\sigma_0 + 3\sigma_{c,\perp}) \quad (2.8)$$

In propagation direction, the strain energy release rate is [92]:

$$G_{c,\parallel} = \frac{(1 - \nu_f^2) \cdot h_f}{2E_f} \cdot \sigma_0^2 \cdot \left(1 - \frac{\sigma_{c,\perp}}{\sigma_0}\right)^2 \quad (2.9)$$

Furthermore, buckling causes a bending of the coating, most pronounced close to the crack front with a strong tensile stress on the bottom side of the thin film (compare to figure 2.4 c). As a function of the buckle radius, the bending strain exhibits a sharp maximum [4]. Hence a critical radius b_{spall} exists, where a through thickness fracture accompanied with spallation of the buckled segment is most likely to occur (refer to equ. 2.10) [4]. The through thickness fracture occurs at the point of highest bending strain and leaves therefore an interfacial crack in the remaining coating.

$$b_{spall} = 1.92 \cdot h_f \cdot \sqrt{\frac{E_f}{\sigma_0}} \quad (2.10)$$

2.5.3 Adhesion Testing

There is a large number of adhesion tests for different coating types and also the number of adhesion tests for hard coatings is huge. Most of them are restricted by certain preconditions. E.g. the pull tester, relying on a punch glued to the coating surface, is limited to an adhesive strength of 90 to 100 MPa, which corresponds to the adhesive strength of the epoxy glue on DLC films [93, 94].

Furthermore, in context of the model for the adhesion performance of DLC coatings within this work, the methods have to be differentiated, whether they test a delamination initiation, a delamination progression or combinations of them.

Most frequently used tests to assess the adhesion of DLC are the standardized Rockwell C indentation test (HRC) according to VDI 3198 [2] and the scratch test according to DIN 4856. Both are used as reference tests in this work and are briefly described in the following. A review on further techniques can be found in the introduction in Drory et al. [87].

Rockwell C Indentation according to DIN 4856

The HRC test is based on an indentation with a diamond cone, analogous to the Rockwell C hardness measurement [95, 96]. For evaluation of the adhesion quality, the circumference of the residual imprint is examined for cracks and delaminations by microscopical means. In VDI 3198 [2], six quality classes are defined (compare to fig. 2.5) ranging from HF1, pristine adhesion, to HF6, weak adhesion. HF4 is denoted as still acceptable adhesion and HF5 as unacceptable. VDI 3198 was withdrawn and meanwhile replaced by ISO 26443:2008 [3], but the up-to-date standard (DIN 4856 [97]) is similar to the original with slight changes in the category definition and the possibility to adjust the indentation load.

Drory and Hutchinson [87] analyzed the stress state of the case with large area delamination around an HRC-imprint, corresponding to HF6. High in-plane shear stresses are introduced by the indentation in the radial direction close to the rotational symmetric indenter. These high shear stresses are supposed to force crack formation of the coatings

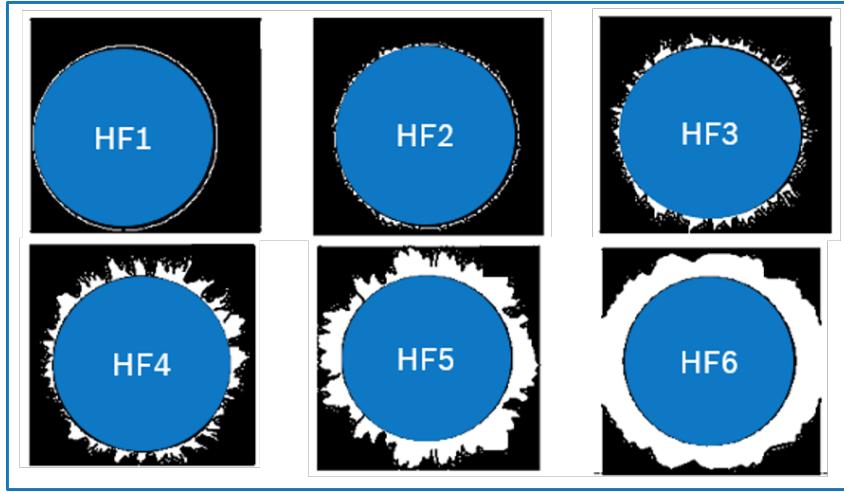


Figure 2.5: Schematic representation of the six categories for adhesion quality according to VDI 3198. HF1 - pristine adhesion with no delamination, HF2 to HF5 with increasing degree of connection between the single delaminations and HF6 with an annular connected delamination around the whole imprint.

interface to the substrate, which lead to delamination [87]. In polar coordinates, the total strain energy per unit area Ω of the resulting biaxial in-plane stress can be written as [87]:

$$\Omega = \frac{1}{2} \sigma_{ij} \epsilon_{ij} h_f = \frac{h_f}{2E_f} \cdot (\sigma_{rr}^2 + \sigma_{\theta\theta}^2 - 2\nu_f \sigma_{rr} \sigma_{\theta\theta}) \quad (2.11)$$

with the normal components of the stress tensor in polar coordinates (radial r and azimuthal direction θ) σ_{rr} and $\sigma_{\theta\theta}$ as well as the strain components $\epsilon_{rr} = \frac{\sigma_{rr} - \nu_f \sigma_{\theta\theta}}{E_f}$ and $\epsilon_{\theta\theta} = \frac{\sigma_{\theta\theta} - \nu_f \sigma_{rr}}{E_f}$. The isotropic state (equation 2.4) corresponds to $\sigma_{rr} = \sigma_{\theta\theta} = \sigma_0$.

When the HRC test result exhibits a concentric delamination with radius r in the range of 2 to 5 times the radius of the residual imprint, the crack front perpendicular to the direction of propagation can be simplified as a straight line. Parallel to the crack front, the strain energy is assumed to stay constant and $\sigma_{\theta\theta}$ does not contribute to the energy release. With this assumption G_c can be estimated (equ. 2.12) [87]:

$$G_c = \frac{(1 - \nu_f^2)}{2E_f} \cdot h_f \cdot \sigma_{rr}^2(r) \quad (2.12)$$

The σ_{rr} as a function of the radial distance r to the indentation center can be derived from simulation.

In the case, when concentric delamination (HF6) is not the case, the mechanisms around the indentation are more complex [70]. E.g. the tensile azimuthal component of the biax-

ial stress close to the indentation usually introduces radial cracks [98].

Instrumented Scratch Test according to EN ISO 20502:2016

Instrumented scratch test according to EN ISO 20502:2016 [99] is a further frequently used method for evaluating adhesion of hard coatings and relies on applying a lateral load in addition to the normal load. Thereby, in-plane shear stresses are introduced into the coating around the indenter, which can initialize interface cracking, which is beneficial for the adhesion evaluation of hard coatings [100]. For sufficiently large interface cracks, the compressive in-plane stress within the coating leads to buckling which occurs in front of the moving indenter or laterally [101, 100]. Behind the indenter, tensile stresses are introduced and patterns of succeeding cracks within the coating are usually observed [101]. For very small loads, the effects of the normal loads are dominant and circular cracks can form, enabled by tensile radial stresses [101].

In the default test routine, a normal force of 1 to 100 N is applied with an indenter with Rockwell C geometry [96]. Other geometries and forces can be used, if useful for a specific coating-substrate-system. The sample stage is moved with constant velocity underneath the indenter, to form a scratch on the surface.

Three different procedures are described in the EN ISO 20502:2016: Progressive force scratch test (PFST), constant force scratch test (CFST) and multi-pass scratch test (MPST), which are described in the following. The most frequently used scratch test is the PFST, where the normal load is getting linearly increased in order to investigate the response of the coating to the load increase. Events of failure can be detected microscopically, via scanning electron microscopy (SEM), as well as in-situ acoustic emission or in-situ friction force measurements.

Typical damage patterns within the coating are circular cracks and wear craters. The first occurrence of such events is denoted as the corresponding critical normal load (L_c). L_{c1} denotes crack formation, L_{c2} flaking and L_{c3} break through the coating, uncovering the substrate in the middle of the scratch track. They are schematically depicted in figure 2.6. A catalogue of divers coating specific shapes of the crack pattern, as well as delamination

pattern is attached to the EN ISO 20502:2016 for comparison.

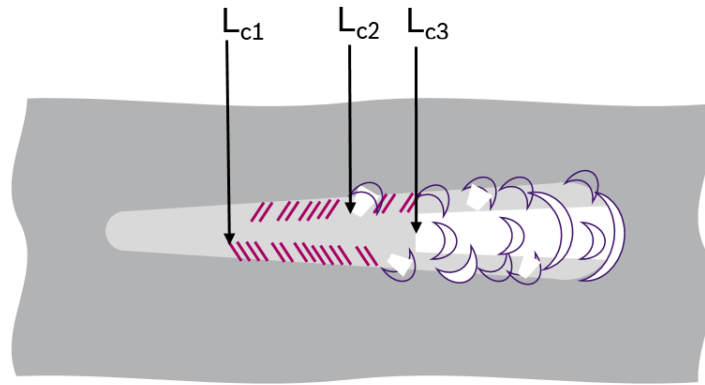


Figure 2.6: Schematic representation of a scratchtest with critical loads according to EN ISO 20502:2016 [99]: Crack formation at L_{c1} , flaking at L_{c2} and break through the coating at L_{c3} .

Critical normal loads are not only depending on adhesion strength of the coating, but also on other parameters such as rate of load increase, traverse velocity, wear of the diamond tip and roughness of coating and substrate [99]. For a direct comparison of coating performances, the following parameters must therefore be identical: Hardness and surface roughness of substrate and thin film, film thickness, coefficient of friction between coating and tip, as well as intrinsic stress of the coating [99].

In the CFST, scratch tests with different constant loads are performed while the load is increased incrementally from one scratch test to the next, e.g. around an L_c -value of a previous PFST. In the MPST, a single scratch test with sub-critical constant load is performed with several passes. The resulting failures then correspond to a fatigue damage, which is hence a better simulation of realistic application conditions [99].

If the focus lies on applications with small scale parts, a nanoscratch is more suitable. The geometry of the diamond tip is adjusted to introduce high stresses into the interface region between coating and substrate by applying small normal loads in the range of mN up to a few N.

Microcantilever bending

A sophisticated method for measuring the intrinsic adhesion of an interface is the microcantilever bending test [102]. Via focused ion beam (FIB) milling, a free standing beam is prepared out of the coating with one end still attached to the substrate. Via micro-mechanical loading of the free end of the beam, the interfacial fracture strength can be estimated, when fracture of the interface was successfully provoked [102]. With a notched beam, the corresponding interfacial fracture toughness can be derived [102].

Buckling Analysis

In order to estimate the critical strain energy release rate of a coating system, buckling can be analyzed with the Hutchinson model [4] and the above presented equations, if it occurs spontaneously in a homogeneous coating [89]. Furthermore, buckling can be provoked by increasing the biaxial in-plane compression via deposition of a top layer with compressive intrinsic stress, combined with nanoindentation for buckling initiation [89].

Skewed Cylinder Test

In a tribologic contact with reciprocating parts, besides a continuous abrasion, a cycling fatigue at the interface can occur [24, 103]. Djoufack et al. [104] investigated the occurrence of coating delamination for an H-free DLC-coated cylinder, sliding against an uncoated steel cylinder as counter body in the skewed cylinder test. Figure 2.7 shows a schematic set-up. In a conventional skewed cylinder test, the abrasive wear track is analyzed in terms of wear depth or volume as a function of load, temperature, inclination angle between the two cylinders and lubricant.

However, by plotting the occurrence of adhesive failure in a parameter room, the onset of this adhesive failure mode can be evaluated for the different parameters and their mutual influences can be detected. The result is depicted in figure 2.7 b) and c).

With increasing T or normal load F , the spontaneous failure becomes more likely to occur. The lubricant have an effect too: Using a low viscous and low lubricity fuel (Diesel

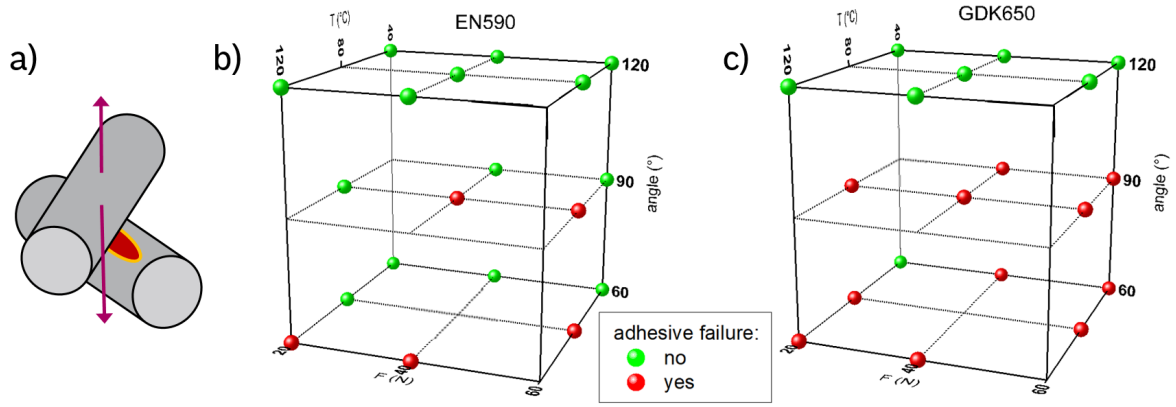


Figure 2.7: a) Schematic representation of the skewed cylinder test. b) and c) Three dimensional maps of the abrupt failure mode (red dots) versus continuous abrasive wear mode (green) in a skewed cylinder model test according to Djoufack et al. [104] for two different lubricants. Experimental results are influenced by temperature, mechanical load, tilt angle and Diesel type as lubricant.

fuel GDK with less additives, rated as borderline) instead of European standard Diesel (EN 590), the failure mode is reached with lower values for T or F . An angle between the two cylinders of 60° is rather harmless compared to 90 or 120° . This is attributed to a reduced contact time.

Since the cycling fatigue of the interface region is an important aspect of the adhesion performance, some fatigue tests are performed in this work as well (refer to chapter 5).

2.5.4 Chemical Stability of the Interface Region

In a corrosive environment, the high amount of compressive residual stress can lead to stress corrosion cracking (SCC) in the interface region [70, 105, 106].

SCC describes crack growth under sub-critical tensile loads caused by corrosive media. Corrosion can either occur in form of anodic metal dissolution or cathodic corrosion with H-formation causing an embrittlement of ductile materials. Both corrosion types are facilitated at the strained material at the crack front, causing crack advance.

During SCC, crack growth commences far below a critical strain energy release rate (i.e. $G \ll G_c$), whereas the crack propagation rate v depends on G [107]:

$$v = \frac{v_0}{B} \sinh \left(\frac{G - G_{TH}}{\eta} \right) \quad (2.13)$$

Thereby, η is the energy per bond area, B is the number of bonds at the crack tip, v_0 is a material dependent and geometry-independent velocity and G_{TH} is the threshold strain energy release rate, at which under-critical crack growth sets in. Via fitting of the $v - G$ curve, the macroscopic crack velocity parameters η , v_0/B and G_{TH} can be obtained, from which crack velocity parameters on atomic scale can be derived [70].

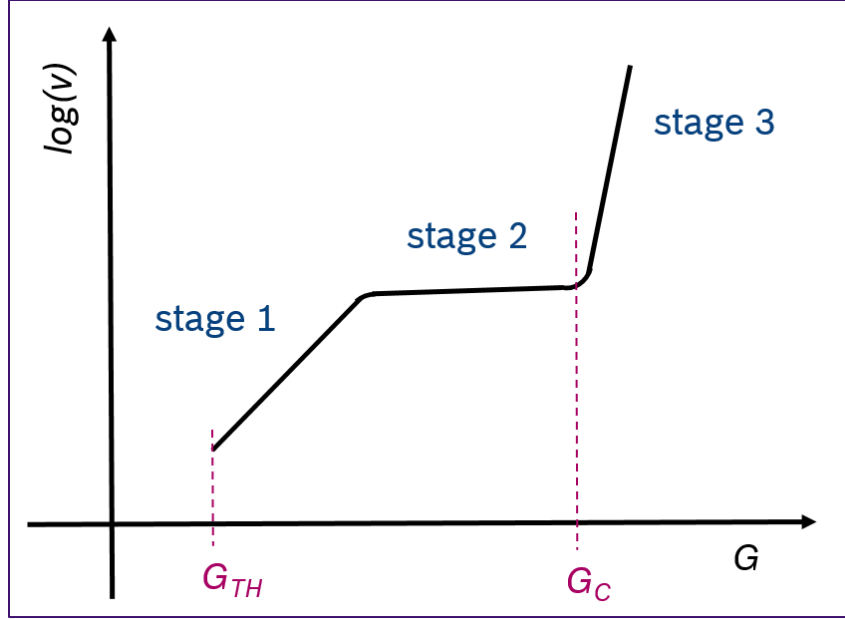


Figure 2.8: Sigmoidal curve for stress corrosion cracking with three stages. Stage I: reaction controlled, stage 2: steady state, stage 3: critical failure.

Figure 2.8 shows schematically a typical $v - G$ curve with sigmoidal shape, associated with three stages. In stage 1, starting at G_{TH} (e.g. $G_{TH} = 1 \text{ Jm}^{-2}$ for soda-lime-glass under tensile load [107]) a linear slope prevails which is determined by a reaction-controlled crack propagation which is described by the reaction rate model with Maxwell-Boltzmann statistics [108]:

$$v = cK^m \quad (2.14)$$

with the crack growth exponent m , the stress intensity factor K and a constant c , which depends on material and environment [109]. m is ranging from 2 to 10 for ductile materials and up to 40 for ceramics [109, 110]. Furthermore, m increases, when medium is more aggressive [109]. In stage 2 - the steady state crack propagation - the velocity is constant, whereas in stage 3, the crack propagates with critical failure.

Falub et al. monitored the delamination progression of an a-C:H on a CoCrMo-substrate after immersion in a phosphate-buffered saline (PBS) solution at 37°C. By analyzing the delamination speed around Rockwell C indentations with varying film thickness, the analogous sigmoidal curve of SCC for the crack velocity versus G was obtained. Thereby G is varied on the one hand over the radial distance to the indentation and on the other hand by the accumulated stress with the film thickness (compare to equation 2.12) [70].

During immersion in PBS, the average speed of delamination was increased by a factor of 4.5 [70] and delamination stopped almost completely in vacuum instead of air [70]. A similar increase in v is known for oxides and ceramics after immersion in water [109].

Formed cracks proceed in the middle of a roughly 5 nm thin carbide layer between the CoCrMo and DLC [105]. The no longer adhering coating can buckle and break so that circular pits remain [105].

Waters et al. [89] investigated buckling geometries in thin DLC films and derived the critical energy release rate for buckling. They reported a crucial influence of moisture on G_c for an a-C:H coating on top of a Ti-layer. There is some evidence that this observation can also be attributed to stress corrosion cracking, assuming that the measured critical energy release rate corresponded to the threshold energy release rate G_{TH} , which was reduced under exposure to moisture.

DLC coatings are very dense and in non-inert atmosphere, access to the interface region is a crucial aspect. Molecules of environmental species like oxygen or water can penetrate the coating through film defects, such as pinholes or small crevices and slowly corrode the interface [70, 105, 111]. In combination with residual stresses, this is expected to lead to ongoing delamination [112, 113], but the mechanisms including electrochemical aspects are not fully understood [113].

Cracks can be induced by indentation [70], while further stress concentrations arise at the surface of imperfections [114]. Pinholes, ranging from tens of nm to tens of microns in lateral size [105], can be caused by dust particles for instance. Bonds around a pinhole are supposed to break by corrosion and the no longer adhering thin film can buckle eventually [105]. After cleavage of a coating segment circular pits are left [105].

Woekel et al. [115] found local delaminations analogous to these pits starting at pinholes

originating from nodular growth defects, which vanish during thermal annealing.

In chapter 6, experimental results are presented, which confirm the formation of pinholes at locations of former growth defects. However the mechanism of a potential ongoing delamination is found to be a complex process and a strong influence of the adhesion layer design on the thermo-chemical stability of the interface region will be demonstrated.

2.5.5 Optimization Approaches for Stable Interface Regions

When it comes to adhesion, results are always controversial. As will be shown in the present work this is presumably caused by the fact that actually, the adhesion performance has been evaluated, which is a systemic measure and thereby depends strongly on the test conditions. Nevertheless, a literature overview is given in the following.

For automotive applications, DLC is often deposited on steel substrates, where the adhesion is reported to be very poor [32, 33, 116]. The adhesion is commonly increased by the introduction of adhesion layers, often single element layers such as Si, Ti, Cr [27, 60] or Al [32, 33] layers.

Be											B	C
Mg											Al	Si
Ca		Ti	V	Cr		Fe	Co	Ni	Cu	Zn	Ga	Ge
		Zr	Nb	Mo			Rh	Pd	Ag	Cd		
Ba		Hf	Ta	W				Pt	Au	Hg		Pb

Figure 2.9: Periodic table of stable (blue) and unstable (red) carbide formers according to Outka et al. [114]

Carbide forming metals are supposed to yield the most stable interface towards the DLC coating. Therefore, Outka et al. [114] presented the periodic table of stable and unstable carbide formers, which is shown in figure 2.9. Thereby, some elements form stable carbides with negative formation enthalpies [114], which are frequently reported to provide the best adhesion. A common concept is, that metallic layers such as Cr, Ti or Ta provide good adhesion to the substrate, followed by a carbide interlayer, such as WC or

SiC for a good matching towards the carbon phase [23].

Early transition metals form interstitial carbides and elements like Si covalent carbides. Some elements however, e.g. the late transition elements form unstable carbides with positive formation enthalpies or even no carbides at all. Through the diversity of deposition methods, properties of each phase can be altered, additionally to pure chemical aspects. With the use of HPPMS, good adhesion on steel without interlayer is reported [27] contradicting other reports [32, 33, 116].

Interlayers are also controversially discussed in literature, such as Ti interlayers, which has a negative formation enthalpy [114], but weak adhesion is reported by some groups [32, 33, 116]. Others [19] reported good adhesion for Ti adhesion layers, when the ion energy is adjusted correctly. Too high energies (around 1 keV) lead to in-situ modification of the Ti surface, whereas an ion energy of 100 eV is sufficient to form a very thin interface layer by ion bombardment, which allows the growth of ta-C films up to 6 μm in thickness [19]. Further improvement yield TiN and TiCN transition layers on top of the Ti layer [19].

Furthermore intermediate metal or compound layers (Ti, Zr, W, Nb, Si, Cr, or WC) have demonstrated their potential in improving DLC film adhesion according to Pauleau [19]. Coatings with a gradient in hardness show better adhesion, compared to hard coatings directly deposited on steel: Scratchtests showed delamination for the latter case only and also sliding test performance significantly increased with the gradient in ball on disc tests [117].

For stainless steel, CoCr and Ti-alloys as substrate material, a consistent optimum temperature at deposition start with respect to the adhesion was found [118]. The optimum T at approximately 75 °C is attributed to a high sp^3 -content of the functional layer [118]. This has to be considered for the plasma etching process preliminary to the deposition process.

Si-doped DLC as an interlayer is reported to increase the adhesion as well [119, 113] and leads additionally to a high threshold for stress corrosion cracking [70].

Chapter 3

Coating System Design and Methods

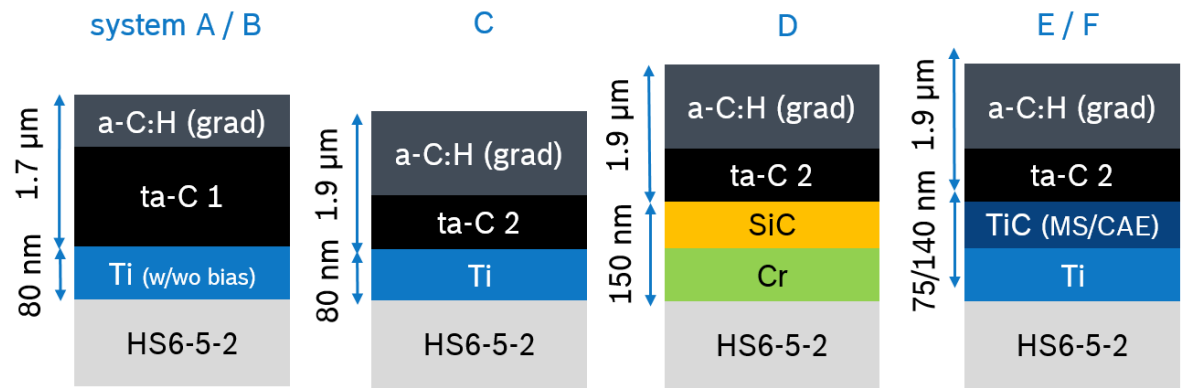
Aim of this work is to deduce an adequate adhesion layer system for DLC in applications at elevated temperatures in corrosive environments. Therefore, a model for the adhesion performance of DLC coatings is to be derived and furthermore, based on this model, a reliable test method for the adhesion performance. In the following, the coating system designs for this study are presented, followed by the methodology of this work, where different work packages (WP) to different aspects of the adhesion performance are defined. Subsequently, a description of the carrying out of the single experiments, sorted by the work packages is given.

3.1 Coating System Design

Figure 3.1 shows the coating system designs for this study. The influence of the functional layer on the adhesion performance is supposed to be great, dependent on the amount of intrinsic strain energy and prevailing binding properties at the interface towards the subjacent layers. Therefore, three different types of DLC functional layer are studied: An a-C:H functional layer and two ta-C based coatings with a-C:H top layers, all suited for automotive applications.

The focus of this study lies on the variation of the adhesion layer design with nine different systems. In this work the transition metals Ti and Cr are chosen as metallic base layers, justified by their formation of stable carbides, which is expected to be beneficial

ta-C-based



a-C:H-based

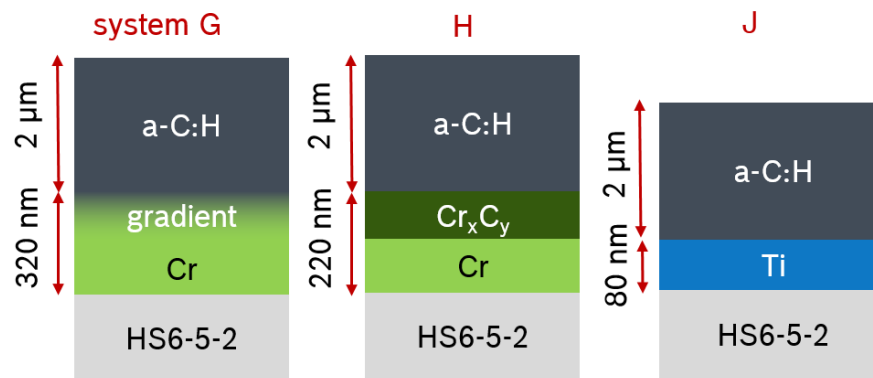


Figure 3.1: Schematic representations of the coating system designs with metal base layer consisting of Ti (A, B, C, E, F and J) and Cr (D, G and H) respectively. Systems A to F have a ta-C based functional layer and different transitions between metal and DLC: Thin intermixing zone via additional bias (A), abrupt transition (B and C), SiC-interlayer (D), TiC-interlayer via MS (E) and CAE (F). Coating systems G to J have an a-C:H functional layer with gradual transition (G), Cr_xC_y -interlayer (H) and abrupt transition (J).

for the thermal stability of the interface region [114].

For mechanical aspects, a smooth transition from the crystalline, metallic phase towards the covalently cross-linked amorphous phase is expected to result in best mechanical adhesion performance. This hypothesis is justified by the fact, that locations with high stress concentrations are possible sites for crack initiation and facilitate crack propagation.

A gradual material transition on the other hand is expected to avoid discontinuities in the intrinsic stress, as well as in the mechanical properties, which again would result in stress localization in the event of mechanical loading. For a possible falsification, also adhesion systems with abrupt transitions are tested.

The carbide phases are generated by intermixing of the metal base material via C-

implantation, as well as deposition of extended carbide phases. For a range of metals including the substrate material Fe, the smaller C-atoms are interstitially solved in a metallic lattice, which facilitates C diffusion through the metal. In contrast Si exclusively forms carbides with a covalent network, where diffusion is limited to vacancy diffusion. In system D it is tested, if this can be exploited by including a SiC interlayer. Furthermore, a strong network with mostly tetrahedral sp^3 bonds is expected to form also in the carbide layer. Cr is used again as base layer due to empirical evidence for a good adhesion on steel substrates. Substrate material and part geometry are kept constant in this work to avoid a further increase in complexity.

3.2 Specimen Preparation

The general process of specimen preparation for this work is schematically shown in figure 3.2, starting with the same substrates for all coating systems: Polished, plane-parallel flat plates of the high speed steel HS6-5-2 with surface roughness $R_z = 0.3 \mu m$, surface dimensions of 10 mm times 8.7 mm and a thickness of 3 mm. The microstructure of the HS6-5-2 is martensitic with carbides. Pre-annealing of the steel plates at $560^\circ C$ ensures the thermal stability during the later annealing experiments at temperatures of up to $500^\circ C$. By using HS6-5-2, realistic application conditions are ensured and comparable to series parts.

Prior to the coating process, a water based chemical cleaning was performed. Plasma deposition of the coating systems was carried out in an industrial coating machine (in-house construction) at *Robert Bosch GmbH* with three-fold rotation. The coating processes started with a plasma etching in the deposition chamber, as a further cleaning step as well as for activation of the substrate surface for the subsequent deposition of the metallic base adhesion layers.

The metal base layers were deposited via unbalanced magnetron sputtering (UBMS) with Cr and Ti cathodes respectively. For coatings of systems A, B, C and J, a single 80 nm thin Ti layer is used as adhesion support. Exclusively for system A, an additional bias voltage is applied during the first period of ta-C growth with the intention to increase the

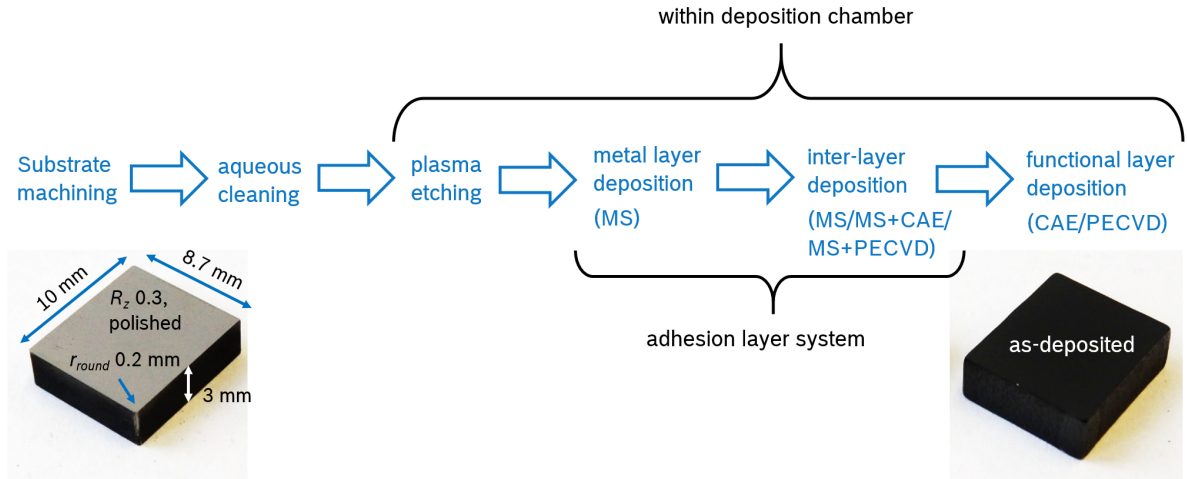


Figure 3.2: Flow-chart representing the sample preparation from substrate machining to the plasma deposition. Substrate dimensions are assigned (r_{round} is the radius of the corner rounding).

intermixing of Ti and C.

The carbide layers in coating systems D, E and H are deposited via MS with a single carbide target. In systems F and G the carbide phases are deposited via co-deposition. For system F, co-evaporation is achieved with MS of a Ti-target and CAE with a graphite target. For system G, a material gradient is generated by decreasing the MS power of a Cr-cathode during co-evaporation and simultaneously increasing the power of the PECVD-process with ethyne as precursor gas.

The two hydrogen-free DLC functional layers, mainly differing in thickness and hardness (refer to the characterization in chapter 4), were deposited via CAE with high plasma density, whereas the $2 \mu\text{m}$ thick hydrogen-containing a-C:H functional layers, were deposited via PECVD with an inlet of ethyne, combined with a high frequency electro-magnetic excitation to provide a sufficient ion density in the plasma. Thereby, intense ion bombardment is achieved, yielding good coating properties [120]. Parameters of a comparable coating system can be found in Schaufler et al. [121].

3.3 Analytical Methodology

In figure 3.3, a flow chart with the methodology of this work is presented. The study is divided into work packages, which yield certain submodels of the holistic picture of the adhesion performance. The corresponding submodels are indicated in the flow chart on the right hand side of each work package.

First of all, a structural characterization of the coating systems in the as-deposited as well as in the annealed state is performed via TEM-analysis. Furthermore, HRC and nanoscratch tests were performed in both states. Aim of this first assessment is to deduce structural mechanical weaknesses, as well as thermal instabilities.

In succeeding work packages, different failure mechanisms as contributors to the adhesion performance are dealt with. Mechanical failure mechanisms, which are analyzed, are buckling driven delamination via compressive stress relaxation and cycling fatigue of the interface region. Furthermore, thermal aging of the adhesion layer systems and electrochemical driven crack propagation are investigated.

3.4 WP1: Coating System Assessment

In the first work package, each coating system is examined with a view to mechanical weak points within the layered structures, as well as to thermal instabilities. Therefore TEM analysis and mechanical adhesion performance tests were performed in the as-deposited and in an annealed state (defined in subsection 3.4.4) in order to allow for a correlation of potential anomalies in performance with the structure of the adhesion systems. The procedures are explained in this section.

3.4.1 Structural Characterization

The structural characterization of the coating systems is made via TEM analysis performed at the *Fraunhofer-Institut für Werkstoff- und Strahltechnik* (IWS) in Dresden on electron transparent lamellas. The lamellas were prepared via the precision ion prepara-

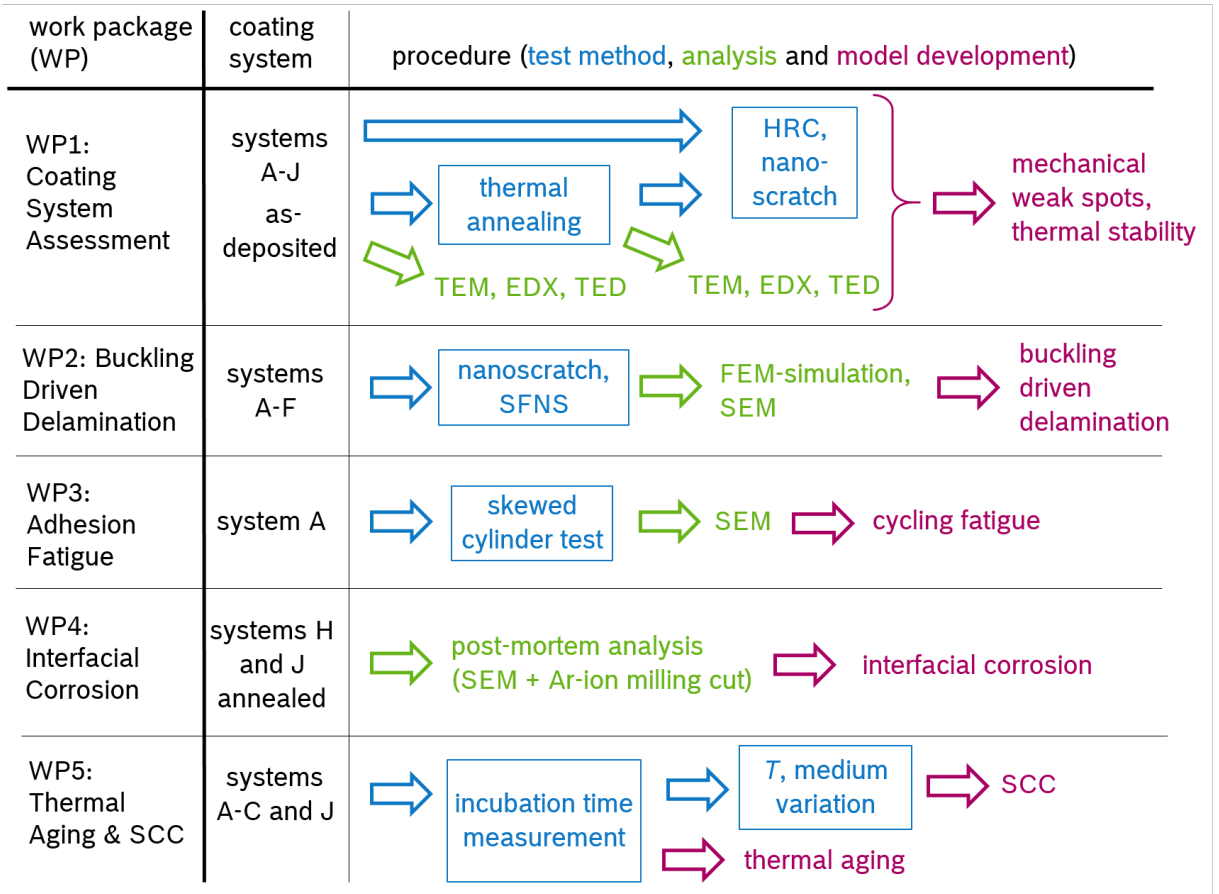


Figure 3.3: Methodology of the investigations: Coating system assessment and characterization, as well as adhesive failure mode analysis, including buckling driven delamination, fatigue, thermal aging and corrosion.

tion system (PIPS), which relies on a combination of mechanical preparation via cutting and grinding and adjusted ion thinning. Bright-field imaging of the interface regions was combined with energy dispersive X-ray analysis (EDX) via EDX-line scans for material composition analysis, as well as transmission electron diffraction (TED) for crystallographic structure estimation.

EDX measurements were also performed on additional spots, so that for each phase, which is observed via material contrast in the bright field TEM image, corresponding mass fractions w_i in wt. % are derived. These are recalculated into the atomic composition with the atomic fractions x_i via equation 3.1 with the molar masses M_i of the detected elements:

$$x_i = \frac{w_i}{M_i \cdot \sum_i \frac{w_i}{M_i}} \quad (3.1)$$

In this work, one major focus lies on the thermal stability of the coating systems. During the low temperature deposition, surface diffusion is limited, which might lead to

metastable phases. These have the potential to segregate during subsequent thermal annealing. Accordingly, the data from the TEM analysis is used to identify these metastable phases.

First, the bright field images were used to identify the several formed phases via their density contrast. The crystallographic information from the TED of single phases is used as a clear indicator for a certain phase formation. In addition with the elemental composition from the EDX, possible phases are searched for in the corresponding binary phase diagrams. These diagrams typically correspond to a cooling from a liquid solution. Therefore, the following four assumptions are made in order to allow for a transfer to a phase formation via deposition with limited surface diffusion:

1. It is assumed that thermodynamically stable phases form, if the composition of the deposited material fits. This is justified by a homogeneous material distribution over the whole part, which is given by the design of the coating machine.
2. If the composition is unfavorable, the film is expected to grow similar to an analogous metastable solid solution, which is rapidly cooled down. Accordingly, intrinsic stresses result after the deposition process due to the actual misfit of the crystal parameters.
3. Unstable phases, which correspond to a frozen liquid solution are expected not to form during film growth, as the surface diffusion is not completely suppressed at expected deposition temperatures of around 200 °C.
4. Residual contaminants are supposed to be solved in the formed matrix phases.

For the structural characterization after annealing, the as-deposited structure is taken into account and the potential precipitation phases identified in the corresponding phase diagrams. Besides the thermal stability aspect, also potential mechanical weak spots are looked for in terms of textures or phases with significantly lower density.

3.4.2 Mechanical Properties

Indentation hardness and modulus of the coating systems were derived via nano-indentation operated in CSM-mode [64] with a maximum indentation depth of 40 nm performed on a SACS [65], which allows for the measurement of a depth profile through the whole coating systems. For the functional layers, σ_0 is estimated via the curvature test.

Nanoindentation Testing

For preparation of the SACS, the flat samples are glued on an Al-punch via *UHU* superglue. After drying, the punch with the fixed sample is mounted in a grinding aid. With a water level and adjustable polytetrafluoroethylene (PTFE) feet of the grinding aid, a grinding angle of below 1° is adjusted.

Polishing is performed with diamond lap foils with grain size decreasing from 3 to 1 to $0.5 \mu\text{m}$. In between, establishing of the cross section is controlled with an optical microscope.

Subsequently a linear pattern of indentations along the cross section and thereby sequentially through the uncovered layer system was executed, starting at the substrate, heading towards the functional layer. This is schematically shown in figure 3.4 a).

For this purpose, the samples are glued on an aluminum sample holder with a *Crystalbond 509* from *PLANO GmbH*. Instrumented nano-indentation is performed on an *iNano* from *Nanomechanics Inc.* for the estimation of the indentation hardness H_{IT} and modulus E_{IT} by applying the CSM-mode [64] with following input parameters: Strain rate 0.1 %/s, maximum indentation depth 40 nm, harmonic displacement 2 nm, frequency 100 Hz, dwell time at maximum load 1 s, criteria for surface detection 200 N/m.

A diamond tip with pyramidal Berkovich-geometry (3 faced pyramid with opening angle of 65.27°) is used as indenter. In a preceding calibration step, performed on a fused silica standard, the tip area function was calibrated.

Figure 3.4 b) and c) presents exemplary results of nanoindentation profiles via SACS on coating system G with a-C:H functional layer in the as deposited state.

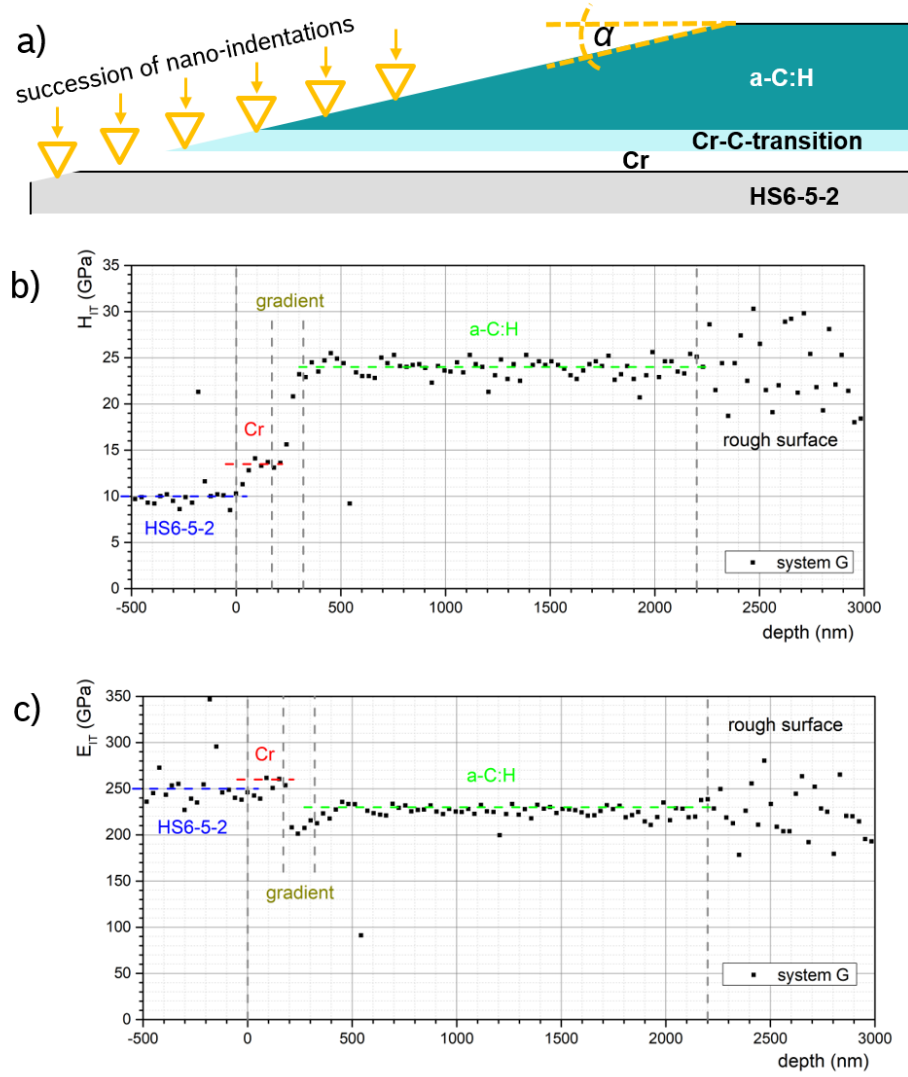


Figure 3.4: CSM nanoindentation measurement on a SACS, exemplary for system G: a) schematic representation of the procedure and resulting profiles for b) H_{IT} and c) E_{IT} .

Hardness and modulus are originally derived versus the distance on the SACS surface with an unspecified small angle α . The estimation of the corresponding depth with respect to the coating system is made by comparing the hardness and modulus profiles with the thickness measurements via TEM imaging. The x-scale of the indentation measurement is adjusted, by fitting some characteristic values to the thickness measurement. Those characteristic values are the points where a monotonous increase in hardness begins or ends, or where the scattering from the surface starts.

The HS6-5-2 substrate and the a-C:H functional layer can be well identified and yield constant values over a certain range, so that H_{IT} and E_{IT} can be attributed to them. For the Cr layer it is only just possible to derive corresponding data. The values for the transition region, indicated as gradient in figure 3.4, are gradually approaching the values

of the a-C:H layer, but with a low depth resolution. Characteristic values of intermediate phases with constant properties could not be estimated.

Figure 3.5 shows the corresponding results for system C with ta-C functional layer and a-C:H running-in layer. The ta-C layer and the substrate can be evaluated. The 80 nm thin Ti-layer however, could not be resolved.

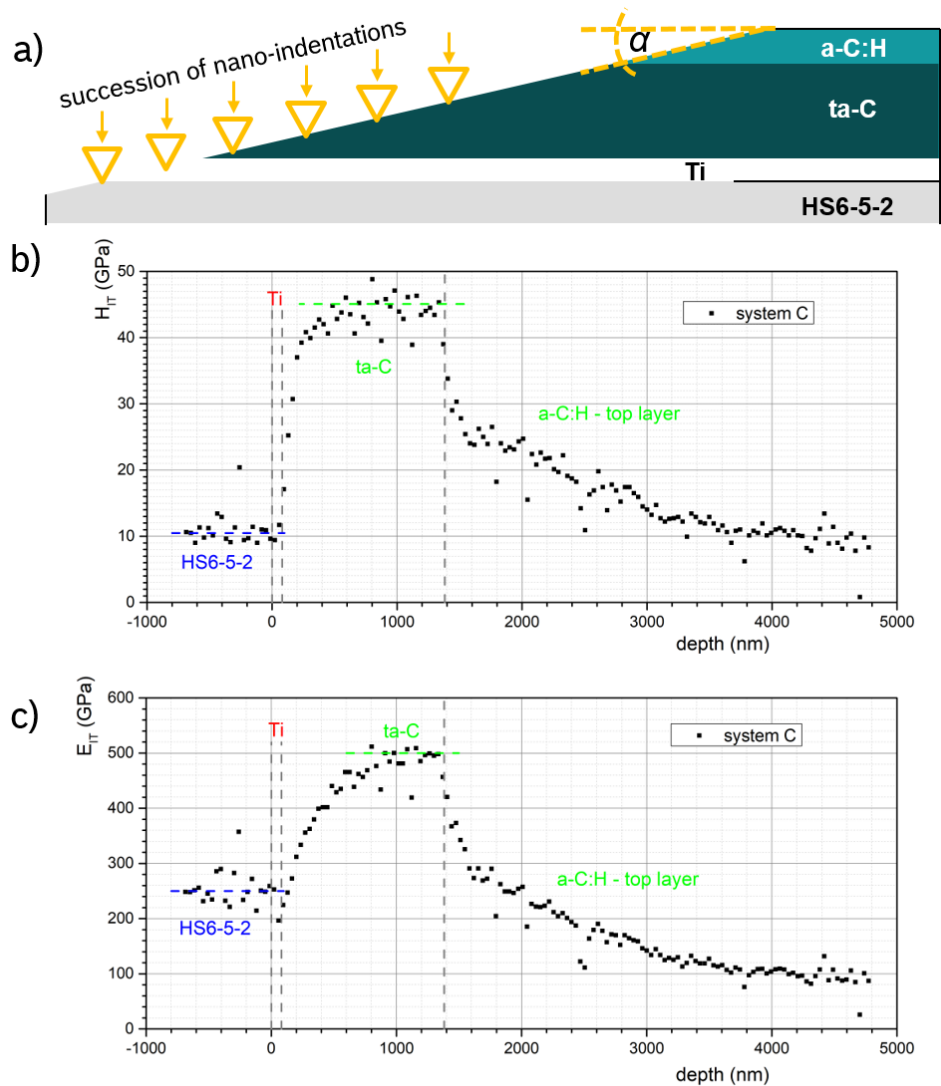


Figure 3.5: CSM nanoindentation measurement on a SACS, exemplary for system C: a) schematic representation of the procedure and resulting profiles for b) H_{IT} and c) E_{IT} .

The running-in layer shows a gradual decrease in hardness and modulus over its whole thickness. A single value cannot be attributed to this layer. For the coating systems with carbide interlayers, the properties of these interlayers were accordingly difficult to estimate, because they are also more or less gradually adapting the values of the functional

layers, similar as for coating system G. A phase with gradual transition in properties can thereby not be distinguished from a phase with constant properties and a gradually decreasing contribution from the subjacent layer to the measuring result. E_{IT} is even more sensitive to the underlying phases than H_{IT} (compare b) and c) in figure 3.5). Therefore the evaluation is reduced to the phases, where constant values over a sufficient depth are derived, which are the substrate, the functional layer (without running-in layer) and the Cr-layer.

Wafer Curvature Test

The intrinsic residual stress σ_0 was estimated with the curvature test: Thin crystalline Si (111)-beams with dimensions of 14 mm times 40 mm times 0.675 mm and a very low roughness (below 1 nm) were deposited with the same functional coatings used in this work within the same deposition chamber. The dimensions of the substrate beam are chosen in such a way, that the planar strain in the coatings causes a curvature, which is optically measured with a laser scanning microscope (LSM) of the type *VK-9700 Violet Laser COLOR 3D LSM* from *keyence*. The intrinsic stress was derived from the curvature via the Stoney equation 2.3 [66].

3.4.3 Adhesion Performance Assessment

For an initial assessment of the coating systems and as starting point for further analysis, the HRC and the nanoscratch test were used. The HRC-test according to VDI 3198 [2] (diamond cone, 120° opening angle, 200 μm tip radius, 1472 N total load) was performed with three tests per sample on a *Zwick/Roell* hardness testing machine of the type *ZHU250CL-A*. For the evaluation procedure according to VDI 3198 [2] refer to chapter 2.5.3. Additional overview images of the residual imprints are taken with a *ZEISS Sigma* SEM.

Single nanoscratch tests (diamond cone, 90° opening angle, 10 μm tip radius, 600 μm length, speed of 10 $\mu\text{m/s}$) with linearly increasing load from 0 to 2 N were performed on a universal nanomechanical tester *UNAT* from *ASMEC*. The device is depicted in figure 3.6,

five scratches each sample were produced. A signal for the lateral force in the direction of the moving indenter is permanently measured during scratching. From a discontinuity in the lateral force signal, the mean L_{c3} (refer to chapt. 2.5.3) was derived. Afterwards, the scratch tracks were microscopically recorded on the *UNAT*.

The delaminated areas A_D around the scratch tracks are estimated digitally. Therefore, a binarization of the microscopic image was done with a noncommercial program, internally used at *BOSCH*, which leaves the pixels of the delaminated area in the images in a specific color. These pixels are counted and divided by the pixel density, which gives A_D .

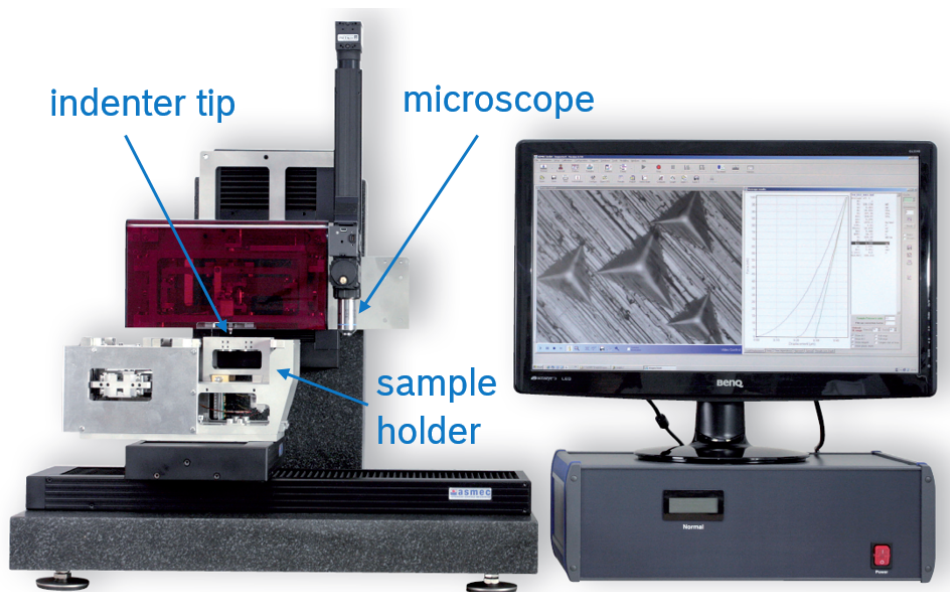


Figure 3.6: Universal Nano Tester (*UNAT*) used for instrumented scratch testing, including positioning and documentation via microscopy.

3.4.4 Thermal Annealing

In order to model application conditions, long time furnace annealing for five days in an N_2 -furnace (*Nabertherm*) at $350^\circ C$ was performed. Samples of each coating system were put into a wire mesh container into the furnace with a distance of at least a sample length between each two samples. The furnace was purged three times with N_2 with high mass flow and pumped subsequently. Afterwards, the furnace is continuously purged with N_2 with low mass flow during the whole annealing process. However, the furnace contained some undetermined amount of residual air.

This long time furnace annealing at 350 °C simultaneously performed for each coating system defines the term *annealed state* of the coating systems, which is used for convenience to describe the state after this treatment.

3.5 WP2: Buckling Driven Delamination

In the second work package, mechanical aspects of the adhesion performance are focused. For compressively stressed thin films these rely on buckling [4]. With the stress field nano-scratch a method for provoking buckling under controlled conditions is presented and the stress fields around indentation based experiments are analyzed and discussed.

3.5.1 Stress Field Nano Scratch

The procedure of the newly developed SFNS consists of two steps. First a high load indentation is performed, introducing plastic deformation into the substrate surface region and thereby providing a wide ranging residual, in-plane stress field in the thin DLC film. A pyramidal indentation (diamond Vickers pyramidal tip, i.e. four faced pyramid with opening angle of 68°) was used, since it avoids homogeneously distributed radial cracks by a stress concentration at the corners of the indenter. Along the edges of the pyramidal imprints no radial cracks are therefore expected, which could disturb buckling driven delamination, which shall be provoked by the SFNS.

Demands on the indentation loads are 1. to be sufficiently high in order to provide a stress field, which enables buckling driven delamination and 2. to be small enough for later application of the method on parts with small coated areas. A load of 981 N according to HV100 for Vickers hardness measurement was chosen and applied via a *Stiefelmayer* hardness measurement machine.

Secondly, a nanoscratch is produced in the vicinity of the imprint edges, causing locally high shear stress concentrations at the interface, provoking the initiation of interfacial cracks and thereby local delamination. With the *UNAT*, two nanoscratches are performed on each sample, with scratch direction towards the Vickers imprint with a constant load

(diamond cone, 90° opening angle, $10\ \mu\text{m}$ tip radius, $2\ \text{N}$, $600\ \mu\text{m}$ length, speed of $10\ \mu\text{m/s}$). The radial component of the residual stress field of the Vickers imprint provides a gradually increasing compressive stress field to the center of the imprint. A gradual increase of the normal load during scratching towards the imprint is therefore obsolete. The normal load of $2\ \text{N}$ was chosen to ensure a break through the coating along the whole scratch track.

The resulting delamination occurrences were optically recorded with a *Leica DFC 495* optical microscope from *Microsystems Ltd.*. On hand on the microscopic images, quantification of A_D was done analogous to the single nanoscratch tests, described in section 3.4.3. Additionally the maximum radial distance r_{max} , where secondary buckling (for the terminology refer to subsection 5.1.1 of chapter 5) occurs and the maximum annular path length of secondary buckling l_{max} are measured on hand on the microscopic images.

3.5.2 Stress Field Quantification

For the discussion in chapter 5 and for the quantification of the strain energy release rate, the residual stress fields within the DLC introduced by HRC and the Vickers indentation are needed. The quantification of the stress fields around an indentation event requires computational simulation.

Model according to Drory

As boundary conditions for the simulation, the following assumptions are made, following the model of Drory and Hutchinson [87]: 1. Since the thickness of the coating is much smaller compared to the indentation depth, the influence of the coating on the strain evolution can be neglected [87]. 2. Crack formation is neglected, as this would require data for the fracture strength of all phases and their interfaces, which is highly error prone. 3. The strain, which is introduced into the coating via bending, caused by the out of plane deflection (pile-up) of the substrate material is small compared to the strain introduced by the in-plane strain of the substrate and is therefore neglected too. By neglecting crack

formation and the bending strain, the corresponding errors are increasingly pronounced, the closer to the indentation center. However, the stress field remote to the indentation center are of highest interest, where no crack formation via the indentation is expected and out-of plane deflection of the substrate is negligible [87].

With these assumptions, the in-plane strains introduced into the thin film are the strains at the substrate surface [87]. This allows for a simulation of the indentation into the *uncoated substrate*. The in-plane stresses in radial direction σ_{rr} and azimuthal direction $\sigma_{\theta\theta}$ of the thin film are derived from the simulated strains ϵ_{rr} and $\epsilon_{\theta\theta}$ at the substrate surface with equation 3.2:

$$\sigma_{ii} = \frac{E_f}{1 - \nu_f^2} \cdot (\epsilon_{ii} + \nu_f \cdot \epsilon_{jj}) + \sigma_0 \quad (3.2)$$

With indices i and j as place holders for r and θ and vice versa. The quantification is done for system B with ta-C 1. It is assumed that the $1.3 \mu\text{m}$ thick ta-C coating with the higher hardness and intrinsic compressive stress determines the buckling behavior. The softer, $0.4 \mu\text{m}$ thick a-C:H top layer is neglected in the calculation.

FEM Simulation

Finite element method (FEM) was used to model Rockwell, as well as Vickers indentation into an uncoated steel substrate with the software *ABAQUS CAE volume 6.14* from *Dassault Systèmes*. A two dimensional axis symmetric solid state model was used with a deformable substrate and an analytical rigid indenter. The indenter was restricted to a displacement in y-direction, which is perpendicular to the substrate surface, which was aligned in x-direction. A friction coefficient of the interface between indenter and substrate surface was set to 0.005. After establishing contact via a small displacement of the rigid indenter of $0.005 \mu\text{m}$ in negative y-direction with respect to the substrate surface, the indentation was simulated load controlled, by applying the maximum load on the rigid indenter. After the maximum indentation depth is reached, the load is removed and the indenter is displaced to its original position and the substrate relaxation is allowed to fully establish.

The designed mesh of the substrate with quadratic elements of the type CAX4R is depicted in figure 3.7 a). Below the indentation center, where the highest stress evolves and along the surface of the steel part, the mesh was refined to a mesh-size of $1\ \mu\text{m}$ with the purpose to evaluate the surface strains with a high resolution over a long radial distance. With increasing distance from indentation center and from the substrate surface the mesh size is gradually increased. This was done iteratively, starting with large elements and decreasing the mesh size successively, until no significant steps in the output data along the substrate surface are observed anymore.

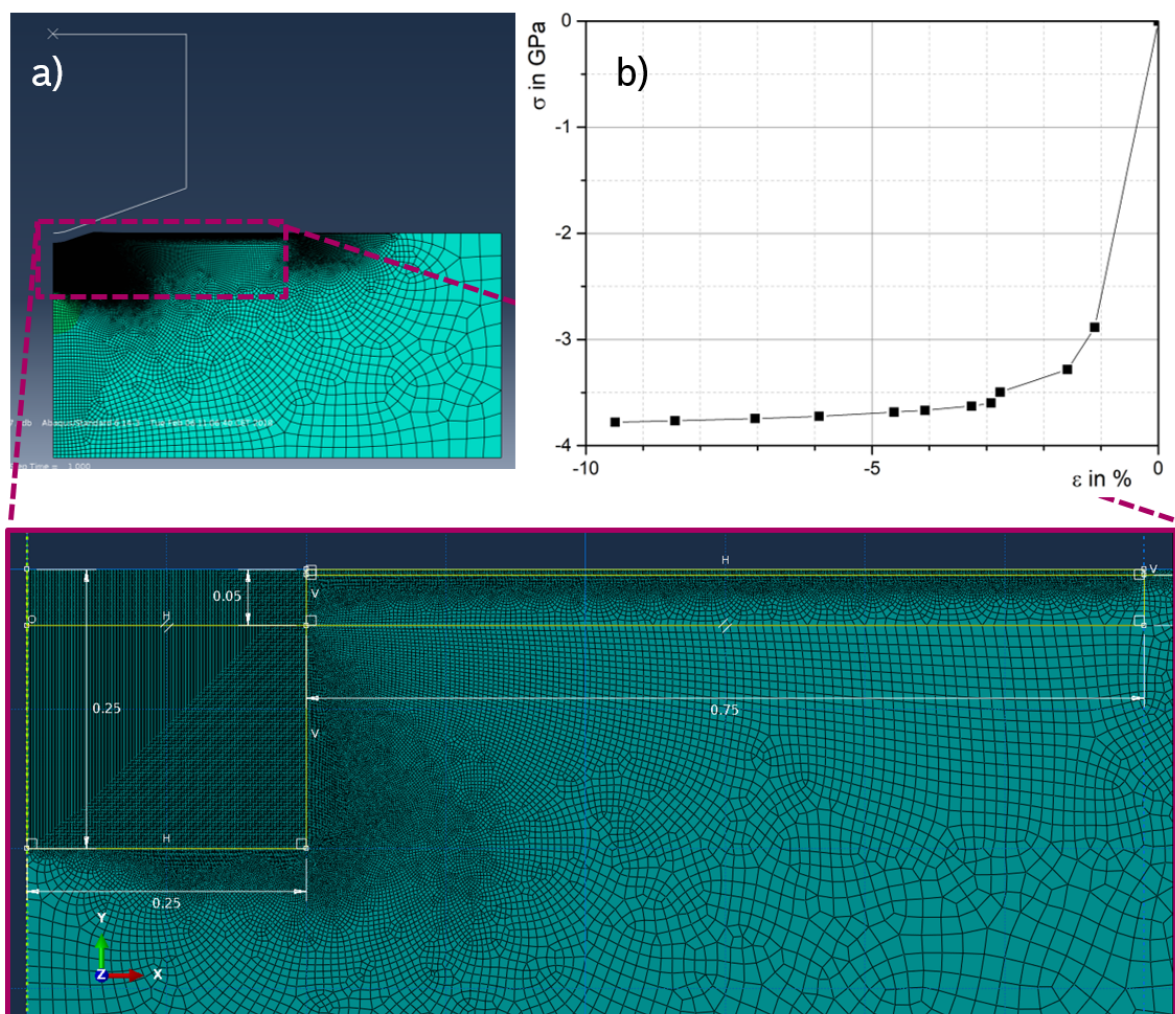


Figure 3.7: FEM-simulation of the indentation experiments: a) Mesh with focus on the surface region. Therefore the mesh was refined in the vicinity of the surface. b) Elastic-plastic data for compression for the HS6-5-2 substrate material.

Elastic modulus of the steel was set to 210 GPa, according to the nanoindentation measurement. An elastic-plastic behavior was assumed and data from a preceding work,

derived via load indentation experiments, were utilized. The data are plotted in figure 3.7 b). For the Rockwell C diamond cone, the dimensions stated above are used, for the Vickers pyramid an equivalent cone (140.6° opening angle [122], 200 μm tip radius), allowing for an analogous rotational symmetric simulation.

Data for the simulated ϵ_{rr} and $\epsilon_{\theta\theta}$ were exported along a path along the substrate surface with increments of 1 μm according to the mesh size along the surface. The data was exported in the state of maximum indentation depth, as well as in the end state, after elastic relaxation. The stress field is fully established only in the end state, so this data is used for the discussion in chapter 5.

3.5.3 In-Situ Rockwell Indentation

With a sample of coating system F, Rockwell indentation with in-situ SEM observation was performed. The sample was glued on a steel sample holder with a fast drying silver conducting paste of the type *ACHESON 1415* from *PLANO GmbH*. The experiment was done on a micro-tension/-pressure table *SEM Tester 2000* from *MTI Instruments* with a 9 kN load cell. The *SEM Tester 2000* was installed in a *Mira3*-SEM from *TESCAN* for the in-situ observation. The table was controlled via the software *MTEST Quattro* from *ADMET Inc.*.

Initially, a preload of 10 N was introduced with a speed of 0.05 mm/s. Further indentation was displacement controlled with a speed of 0.01 mm/s to several load steps, where the indentation is stopped for a detailed SEM observation. The load steps are: 100, 200, 300, 400, 500, 600, 800, 1000, 1200 and 1500 N. Before SEM-imaging, at each load step, a small fraction of the load is relieved via a 5 s displacement with a speed of 0.0005 mm/s. The angle between sample surface and electron beam of the SEM was 65°. Imaging with secondary electron (SE) contrast was performed with a 5 kV excitation voltage.

The measurement was performed within the master thesis of Tobias Schmiedl in a cooperation of *TU Darmstadt* and *Robert Bosch GmbH* [123].

3.5.4 Ex-Situ Analysis

In order to analyze the failure modes during damage progression, different samples have been analyzed further with a *Zeiss SIGMA* SEM. The SE-detector was used with a low acceleration voltage of 3 kV, in order to get surface sensitive images with high topography contrast. Relevant sections of the residual HRC imprints of systems E and F in the as-deposited state, as well as of system A in the annealed state are analyzed too with the same set up. Furthermore, primary and secondary buckling are analyzed for coating systems B and C.

The Vickers indentation of system A in the annealed state showed areal progressing buckling driven delamination, which was recorded on video with the following procedure. Directly after Vickers indentation, the *Stiefelmayer*-hardness measurement device changes from indenter to camera. This is an implemented function, which enables to measure the residual imprint size. However buckling driven delamination just started. This was completely reproducible and a video of the screen was recorded with a digital camera (*SONY Cyber-shot DSC-HX50*), showing the evolving concentric delamination around the residual imprint.

3.6 WP3: Adhesion Fatigue

The third work package covers buckling initiation via cyclic loading of the adhesion layer system under tribological test conditions.

3.6.1 Skewed Cylinder Test

The adhesive cycling fatigue behavior is tested with the skewed cylinder test for a ta-C based coating system, where the occurrence of buckling is expected. The skewed cylinder tests were performed analogous to the description in Djoufack et al. [103] (also refer to section 2.5.3) on an *SRV4* from *OPTIMOL INSTRUMENTS*. The test samples are cylinders made from a 100Cr6 steel, coated with the same coating system of Djoufack

et al. [104], which is very similar to system B of the present work. As counter bodies, uncoated 100Cr6 cylinders are used.

For four parameter combinations, three sample each were tested, if buckling driven delamination occurred or not. These points have been missing in the parameter room of Djoufack et al. [104], so the results can be included and furthermore both results (buckling and no buckling) are expected. The parameter combinations were: 1. 40 N normal load, 60° contact angle, 60 °C temperature and Diesel EN590 as lubricant; 2. 60 N, 120°, 120 °C, EN590; 3. 20 N, 90° , 40 °C, Diesel GDK650; 4. 60 N, 120° , 120 °C, GDK650.

3.7 WP4: Interfacial Corrosion

In work package four, the analysis of growth defects and their thermal aging is analyzed, which can be an important step in the aging process of a coating system via giving the surrounding medium access towards the interface.

3.7.1 Sonotrode Test

The HRC and the nanoscratch tests assess the adhesion of the coatings very locally. For an assessment of a more extended area, the sonotrode test was performed according to ASTM G32-92 [124] for assessing the coating systems G and H in the as-deposited state. Furthermore, a sample of system G is tested in the annealed state. The sonotrode test is based on a controlled, indirect acoustic cavitation with 0.5 mm distance between the flat sample and a Ti flat sonotrode from *KLN* in deionized water with corrosion inhibitor at 23 °C.

3.7.2 Thermal Annealing Tests

The above stated annealing at 350 °C long time furnace annealing was reproduced with samples of system G at 500 °C with otherwise same conditions and procedure in the same

N₂-furnace (*Nabertherm*) for five days.

Furthermore a sample of system G was thermally annealed on a *VWR Hotplate* heating plate at 310 °C for 7 h in order to generate an intermediate step of the thermal defects.

3.7.3 Ex-Situ Investigations

Ex-situ SEM-imaging with a *Zeiss SIGMA* SEM in the SE-mode at 3 kV and EDX-analysis (*Oxford instruments*) at 15 kV were performed on the eroded surface. The higher acceleration voltage for EDX is necessary for electron excitation from higher energy states, which are required for a reliable differentiation of some elements, e.g. O and Cr, which have very similar energy differences for the lowest excitation. The ex-situ SEM/EDX analysis was performed with the same set-up for all samples.

With focus on growth defects and resulting annealing defects system G is analyzed in the as-deposited and after all aforementioned thermal treatments. Furthermore, system H is analyzed in the annealed state, sizes of the volcano-like structures are estimated by drawing circles around them and measuring their radius.

The cavitation erosion is analyzed for systems G and H, as well as the cavitation erosion, which was performed on a sample of system G in the annealed state. The residual scratch track after nanoscratch testing on system G annealed is also analyzed via SEM.

Detailed analyses are done via SEM at ion milling cross sections. Therefore two samples were prepared: System G in the annealed state and subsequent cavitation erosion and system H in the annealed state.

To decrease preparation artefacts, a glass plate is glued with *petropoxy 154* onto the sample surface. The glue was hardened at 120 °C for 15 min. Afterwards, the samples were cut in half via water cooled cutting with a *Struers Secotom-50* machine. Thereby also the eroded area resulting from the sonotrode test was cut in half. After a polishing step with a *BUEHLER Peta GRINDER POLISHER*, the samples were fixed onto a steel sample holder with a silver conducting paste of the type *ACHESON 1415* from *PLANO GmbH*. The silver paste was dried on a heating plate at 100 °C for 15 min. Ion milling at the polished cuts was performed with an *IM 4000 Plus Ion Milling System* from *Hitachi* with

an Ar-flow of 0.10 sccm, a discharge voltage of 1.5 kV and an acceleration voltage of 6 kV. A discharge current of around $400 \mu\text{A}$ was established. The duration was 1 h.

3.8 WP5: Thermal Aging & SCC

In work package five, the kinetics of the thermal aging are analyzed, as well as the mechanisms during delamination progression. For system J, the samples in the annealed state were completely delaminated. Observation during thermal annealing in the furnace was not possible. Therefore, additional heating plate experiments were performed in lab atmosphere in order to monitor the corresponding failure development.

3.8.1 Incubation Time Estimation

For samples of system J, the heat treatment lead to a characteristic delamination pattern localized at certain sample edges. The *incubation time* for occurrence of these characteristic edge delaminations is estimated via annealing experiments on a *VWR Hotplate* heating plate in laboratory air with different temperatures ranging from 300 to 500 °C. The heating experiments were stopped, when edge delamination was achieved and the corresponding incubation time t_{crit} (up to 4 h) was determined. The samples were cooled down rather quickly by placing them on a significantly larger steel block at room temperature.

For a confirmation that the characteristic edge delamination can be attributed to the coating process, the deposition of coating system J is reproduces with exact conditions, except for a tilt by 45° for some samples and by 90° for some further samples. The samples were all mounted vertically on top of each other on a sample holder which height is similar to the height of the inner part of the deposition chamber. The sample holder rotates around its axis for a homogeneous deposition process. By the tilt of the samples, there rotation axis is tilted accordingly.

3.8.2 Stress Corrosion Tests

For monitoring the retarded delamination progression, samples in the incubated state (annealing until the incubation time was reached) are investigated. The delamination progression, starting from defects, is documented with a *Leica DFC 495* optical microscope from *Microsystems Ltd.* on a daily basis for several weeks. Same is done for an introduced defect (HRC test with aforementioned procedure). Via SEM/EDX-analysis the verification is done, that the delamination proceeds along the interface between DLC and Ti.

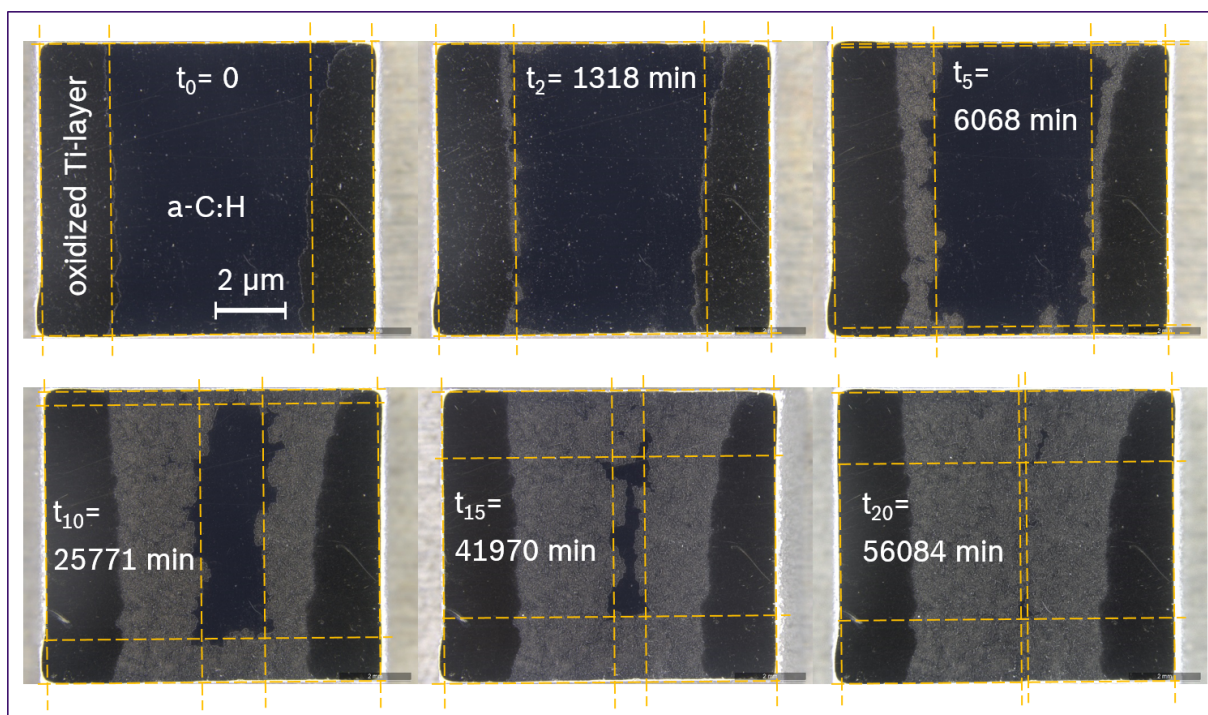


Figure 3.8: Estimation of the delamination velocity of a sample of system J, after annealing at 375 °C for 8 min 42s on a heating plate (exemplary times): The dotted lines indicate the measurement procedure, for which the distance from the sample edges was tracked. The four distances at t_0 were used as reference values, which were subtracted. The mean value of the four resulting distances for each time versus the time between the record of the current and the reference picture yield the velocity.

For a quantification of the delamination speed, the delaminated edges of the samples of system J in the incubated state served as initial point for the subsequent monitoring of the retarded delamination progression. At room temperature and laboratory air, the progression was monitored over several weeks and microscopic images were taken (*Leica DFC 495*). Figure 3.8 shows some representative images at different observation times for

a sample of system J in the incubated state. The characteristic edge delamination can be seen on the left and right hand side of the samples with dark color from the oxidation of the adhesion layer.

Lines parallel to the sample edge were drawn along the delamination edge for determination of the delamination progress. For a curvy shape of the delamination edge, the line is drawn in such a way, that the area of residual coating on the delaminated side and delaminated area on the coated side equal. The reference state is the image at t_0 . All distances are subtracted by the corresponding reference values. The mean value of the resulting delamination progression length in all four directions are derived and by this and the time difference between the corresponding documentation times, the velocity is estimated.

The progression velocity of the delamination was further investigated as a function of the preliminary annealing time (successively longer than t_{crit}) and under exposure to different liquid media. Therefore, aside from room temperature, the delamination progression was monitored at 100 and 200 °C, again on a *VWR Hotplate* heating plate in laboratory air for several minutes. For the medium exposure experiments the samples were put into a vessel filled with different media (tap water, deionized water and deionized water with 1% HCl).

The sonotrode test was performed on system A* in the as-deposited and in the annealed state analogous to the coating system stated above (refer to section 3.7.1).

For testing the passivation effect of the Ti layer of the ta-C based coating systems, residual imprints and scratch tracks from HRC and scratch tests with well established delaminations were reviewed months ago after the actual testing and microscopically imaged (*Leica DFC 495*). Afterwards they were exposed to water (analogous to section 3.8.2) and again microscopically imaged. Subsequently, an engraving was applied on the surface of the intact coating with a standard engraving tool with rotating metal head loaded with diamond particles, followed by a second water exposure and microscopic imaging.

Corrosion tests were also performed via high humidity experiments. Samples of coating system C* with small pre-damages were loaded with a drop of 1% HCl. After the drop has dried, the samples were exposed to an atmosphere with 97% relative humidity for 1

day at room temperature. Relative humidity was adjusted in an excicator via saturated potassium sulfate solution.

Resulting delamination progression were furthermore studied via SEM/EDX measurements in the aforementioned manner.

Chapter 4

Characterization and Adhesion

Assessment

In this chapter, the structure of the layered coating systems is analyzed via TEM bright-field imaging combined with transmission electron diffraction and EDX chemical analysis. Furthermore, a first assessment of the adhesion performance of the interlayer systems is made by the HRC and the nanoscratch test for the as-deposited state. In order to assess the thermal stability of the adhesion layer systems, structural analysis and adhesion performance testing are also performed for the annealed state (refer to chapter 3). Furthermore, the mechanical properties of the used coating systems are presented, which amongst others serve as input parameters for the FEM-simulation in the next chapter (chap. 5).

4.1 Structural Analysis

Figure 4.1 shows an exemplary TEM analysis of the structure of the functional ta-C coating with a-C:H running-in layer, as used for systems A to F. The ta-C appears darker in the bright-field image than the a-C:H, which is caused by the higher density of the H-free layer with higher amount of sp^3 -networking. Both phases are basically amorphous and monolithic, but exhibit a periodic nano-layering parallel to the substrate surface which is attributed to the substrate holder rotation within the batch coating machine. The contin-

uously changing angle of incidence of the impacting ions can lead to a periodic alternation in density of the growing structure, which is visible as contrast in the bright-field image.

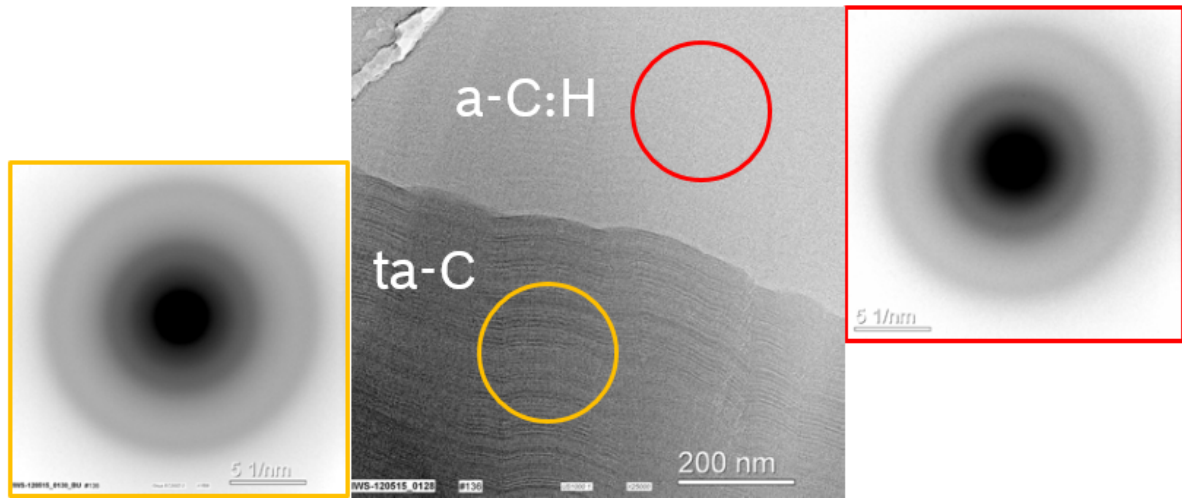


Figure 4.1: TEM bright-field image of the ta-C functional layer with a-C:H running-in layer of coating system A. The ta-C appears darker compared to the a-C:H, corresponding to its higher density. A nanolayering, parallel to the substrate surface is observed for both phases. The TED analysis shows an amorphous structure for both.

The ta-C phases of systems A to F exhibited no detectable structural difference via TEM analysis. Same is true for the a-C:H phases of coating systems A to J. In the following the focus of the structural analysis is set on the adhesion layer systems. The results are clustered into three groups of coating systems: 1. ta-C functional layer and Ti adhesion layer (systems A-C), 2. ta-C functional layer and carbide interlayers (systems D-F) and 3. a-C:H functional layer (systems G-J).

4.1.1 ta-C with Ti Adhesion Layer

In figure 4.2, the transition region of the three coating systems with a single Ti phase as adhesion support for the ta-C based coatings are presented: Systems A and B with ta-C 1 and system C with ta-C 2 functional layer.

A monolithic Ti phase is observed for all three samples with around 85 nm thickness. In the upper half towards the functional layer, a slightly columnar structure arises with fine C-channels between the grains in each of the three coating systems. The main structural difference found is the occurrence of a very thin transition region between Ti and C for

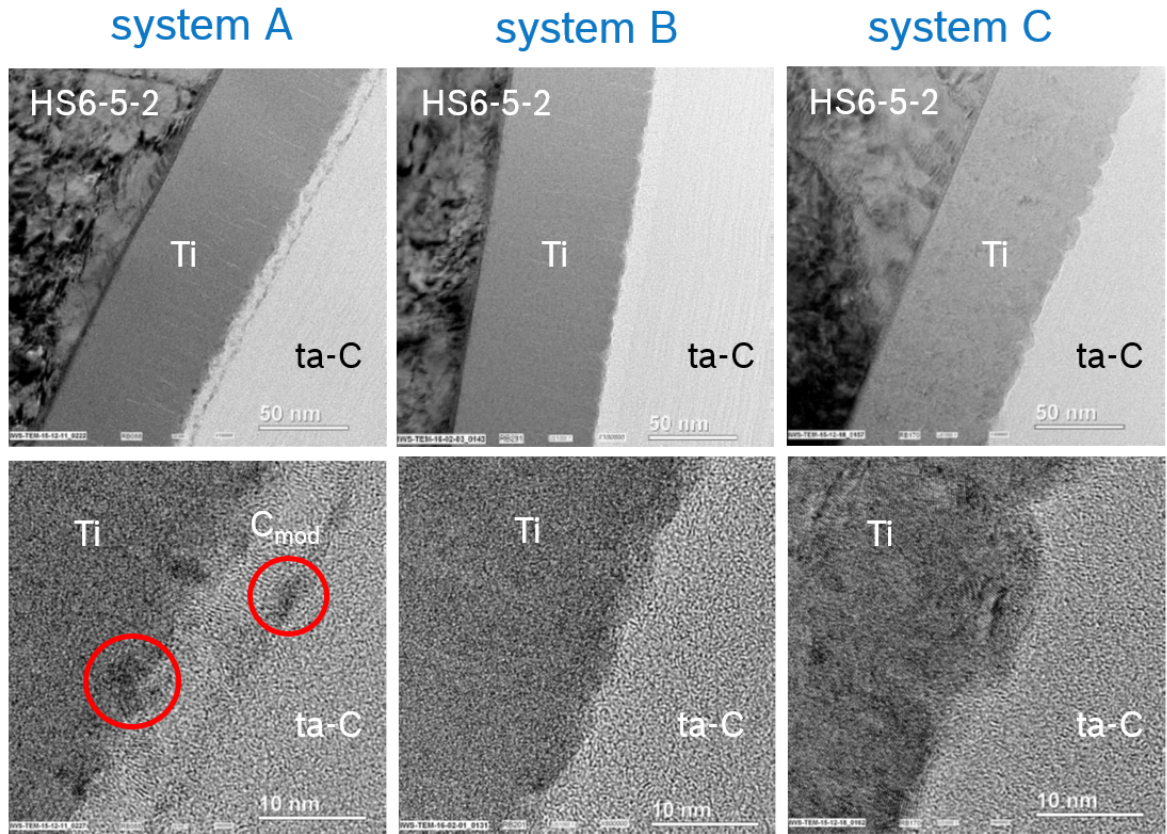


Figure 4.2: TEM-images of the interface regions of coating systems A, B and C. In each case, the adhesion layer consists of a single Ti-layer. The close-ups of the transition region below each survey image show that system A has a slightly more pronounced Ti-C intermixing and a subsequent modified C-phase, not found in systems B nor in C. Some nano-crystals are found in this intermixing zone, as indicated by red circles.

system A, where TiC nano-crystallites have formed. Furthermore, an additional texturing of the ta-C close to the transition region is visible. The modified phase has a graphitic or turbostratic character with orientation orthogonal to the interface and thickness of 10 to 15 nm. Both features can be attributed to the electrical biasing during the initial state of the carbon deposition. Some TiC nano-crystallites are found in the modified layer as well.

A common feature of all systems (this is true also for systems D-J) is an amorphous intermixing-zone, formed at the substrate surface with a thickness of 5 nm and consisting of Fe, Ar, C and the metal species from the base adhesion layers. This zones can be attributed to a mismatch between the lattice parameters of the Fe-substrate and the Cr and Ti metal layers.

Figure 4.3 shows the EDX line scans performed on the TEM-lamellas for system A to C, quantitative results are summarized in the table below the scans. A certain amount of Fe

and also some Cr are found in all Ti layers with different concentrations, which can be traced back to the steel clamping lugs of the Ti-targets. The lug material is co-evaporated during the sputter process, which is only partly suppressed by management of the sputter track by means of electromagnetic steering.

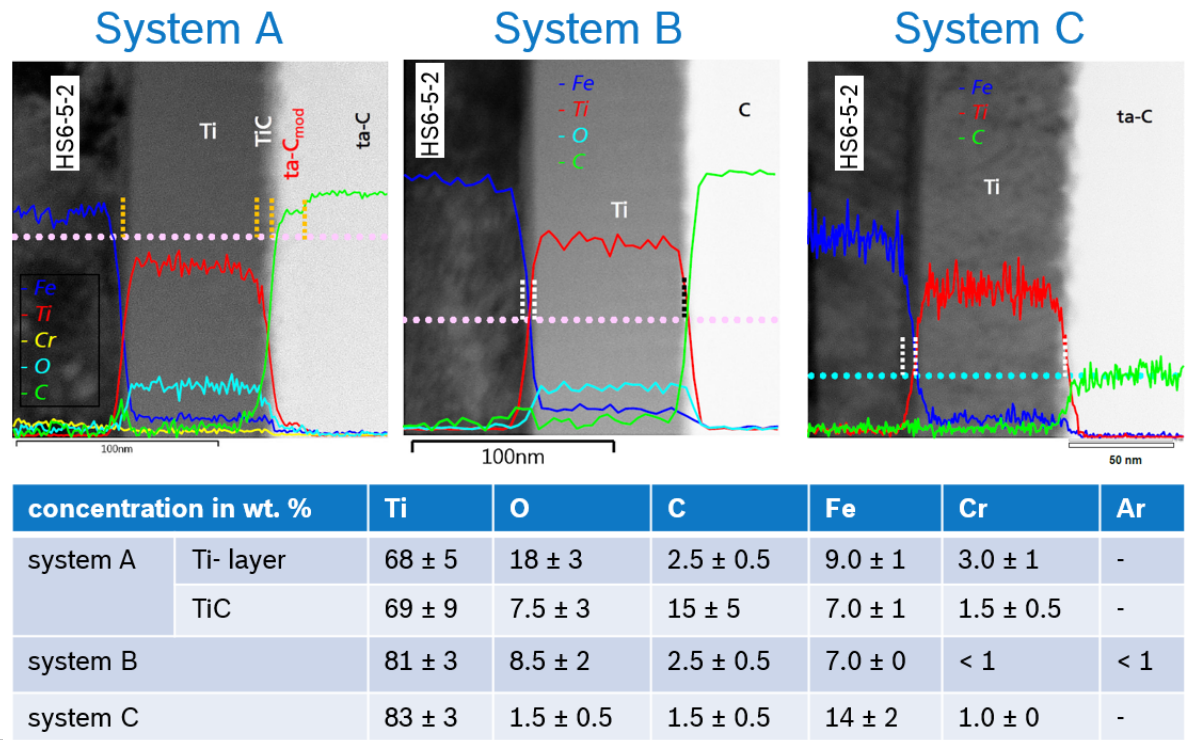


Figure 4.3: Summarized results for systems A, B and C from the EDX-report of *IWS Dresden*: EDX-line scans on TEM-lamellas of the interface regions. Single measuring spots are indicated by the dotted line. Extended quantitative data, extracted from the report, is summarized in the table below in wt. %.

Figure 4.4 a) shows the TED-results of the Ti layers, which are used in this work. For coating systems A, B (and J), the Ti-layers are quasi-amorphous (qu.-a.) with sharp diffraction rings and nano-crystalline (nc) for system C with *body centered cubic* (bcc) structure.

In figure 4.4 b), the binary phase diagrams for Fe-Ti [125] and C-Ti [126] are depicted, from which potential phases, which might have formed during deposition, can be identified. The thermodynamic stable hexagonal close-packed (hcp) Ti has a negligible solubility for Fe and C. With Fe, Ti forms a stable bcc (B2) phase with 50 at. % Ti. Furthermore, a metastable bcc phase with Fe concentrations of 0 to 22 at. % exists with the eutectoidal point at around 13 at. % of Fe.

In the C-Ti phase diagram, an extended stable *face centered cubic* (fcc) phase exists with maximum carbon concentration of 49 at. %. In its metastable state, this fcc phases allows a maximum Ti-concentration of 68 at. %.

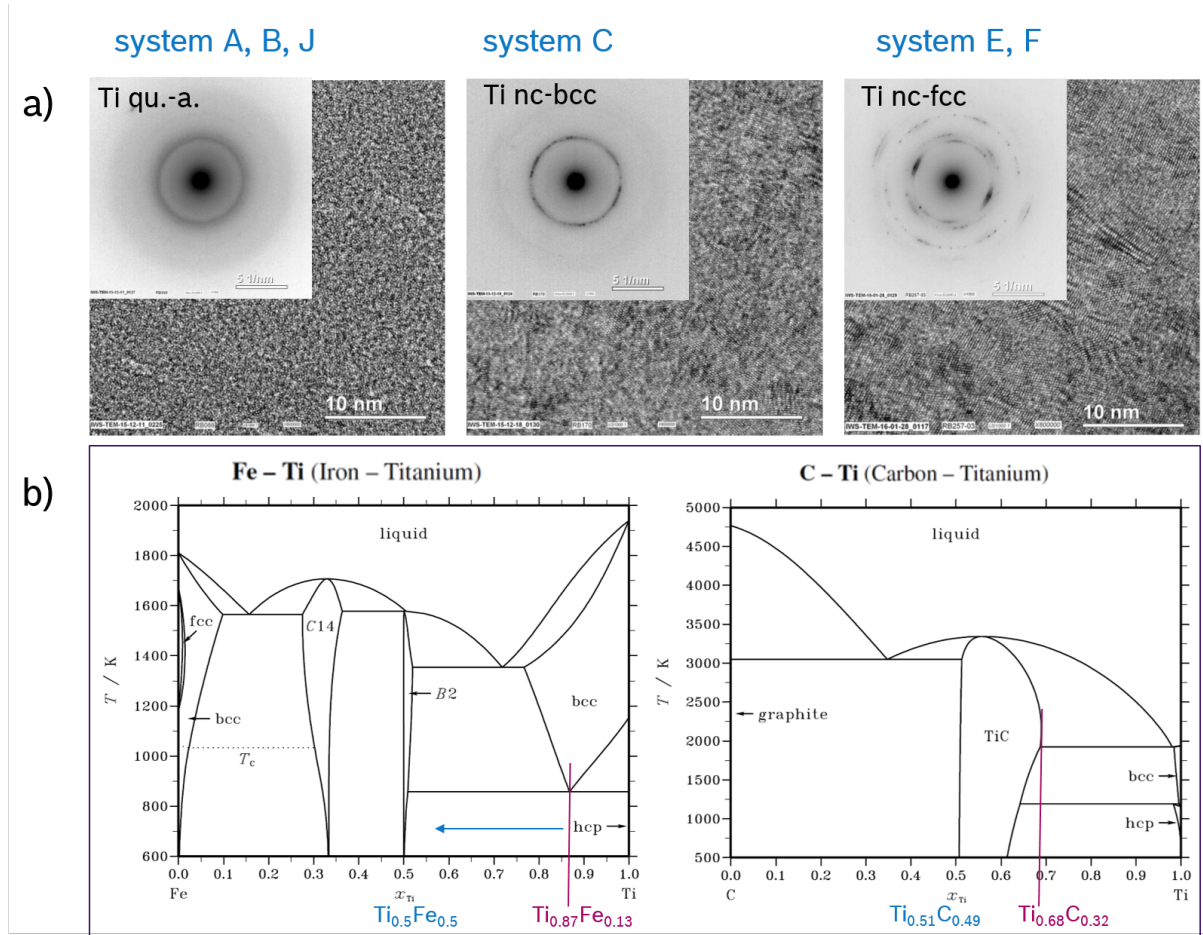


Figure 4.4: a) Electron diffractograms of the Ti layers, derived on the TEM-lamellas and b) binary phase diagrams of Fe-Ti [125] and C-Ti [126]. Some relevant compositions are highlighted.

From the data in the table in figure 4.3, the atomic composition is calculated. Complemented by structural aspects from TED-analysis and the binary phase diagrams, a rough estimation of the phase compositions is made and shown in figure 4.5.

Due to the fact, that a hexagonal structure of stable Ti was not detected in the TED measurement, the contaminants are supposed to prevent this structure. For systems A and B, the high amounts of oxygen in the adhesion layer are supposed to result in a monolithic phase consisting of Ti and TiO₂. The also significant amounts of C, Fe and Cr are preventing extended crystal phases, explaining the quasi-amorphous structure.

The maximum solubility of Fe in bcc Ti is 22 % at 1300 K [125]. Therefore it is likely that

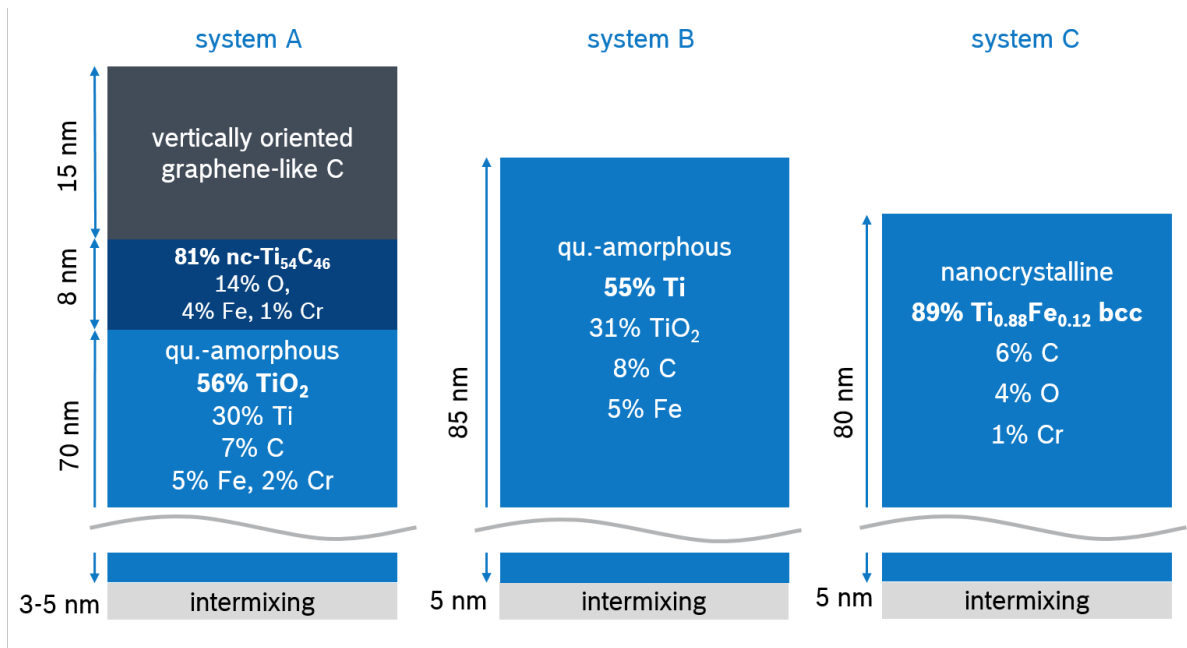


Figure 4.5: Estimated structure and phase compositions for systems with Ti adhesion layer and ta-C based functional layer, based on bright-field TEM, EDX, TED and binary phase diagrams [125, 126, 127, 128]. Substrate below the mixed zone and functional layer on top of the adhesion layer system are omitted for more clarity.

also Fe and Cr are at least partly present in oxide forms as otherwise they could not be solved in the residual Ti phase. The C is assumed to form a carbide phase, allocated close to the adjacent steel substrate, indicated by a local maximum in carbon signal in the EDX line scan (refer to fig.4.3). The upper intermixing zone of system A is mainly consisting of TiC, as intended by the additional biasing, but contaminated by a significant amount of impurities.

With 11 at. %, system C possess the highest Fe-content and furthermore some C, O and Cr. The high Fe content is supposed to stabilize the bcc structure in form of a TiFe solid solution close to the eutectoidal composition.

4.1.2 ta-C with Carbide Interlayers

Figure 4.6 a) shows the TEM bright-field images of the interface regions of the coating systems D, E and F with extended carbide interlayers as adhesive support for a ta-C2 functional layer. The 85 nm thick Cr base layer of system D exhibits a pronounced columnar structure, which is continued by the adjacent SiC interlayer with a thickness of 65 nm. Coating systems E and F possess a roughly 50 nm thick monolithic Ti adhesion layer with

textured carbide interlayers on top. The TiC layer of system E has a similar structure as the SiC layer of system D with a columnar carbide phase and channels with lighter material between the carbide grains. With 25 nm, the carbide phase of system E is much thinner compared to the one of system D.

The gradient phase of system F has a thickness of around 90 nm and exhibits some vertical channels as well, but additionally extensive channels of lighter material in horizontal alignment. Figure 4.6 b) shows a close-up of those horizontal channels.

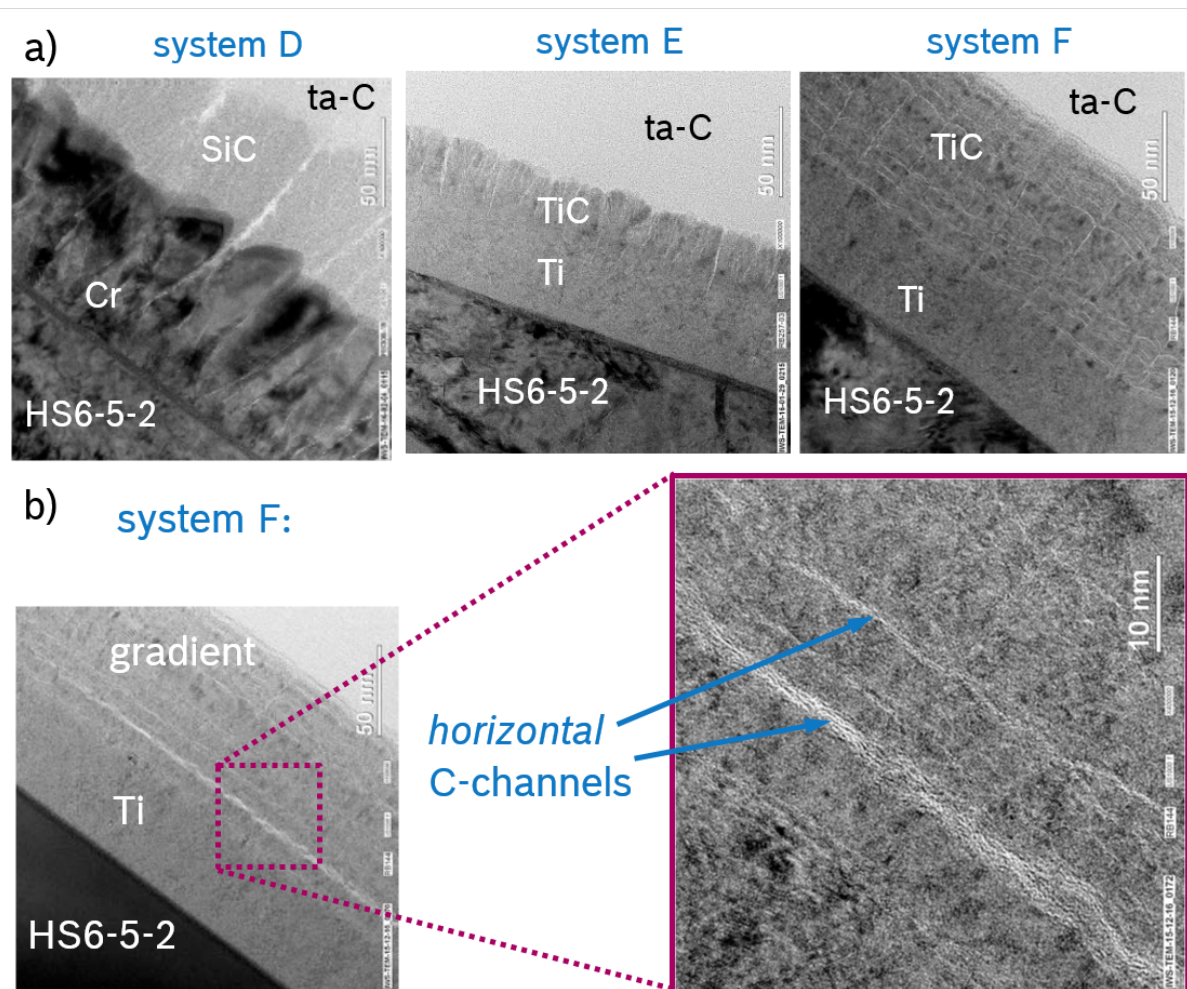


Figure 4.6: TEM bright-field images: a) interface regions of systems D, E and F with extended carbide phases and b) close-up of the horizontal C-channels, observed in high quantity for system F.

Figure 4.7 shows the EDX line scans across the interface regions of systems D, E and F and some additional data within the table below. Again significant amounts of contamination are found. Fe from the steel lugs is present in each phase, oxygen was detected in each of the phases of coating systems D and E.

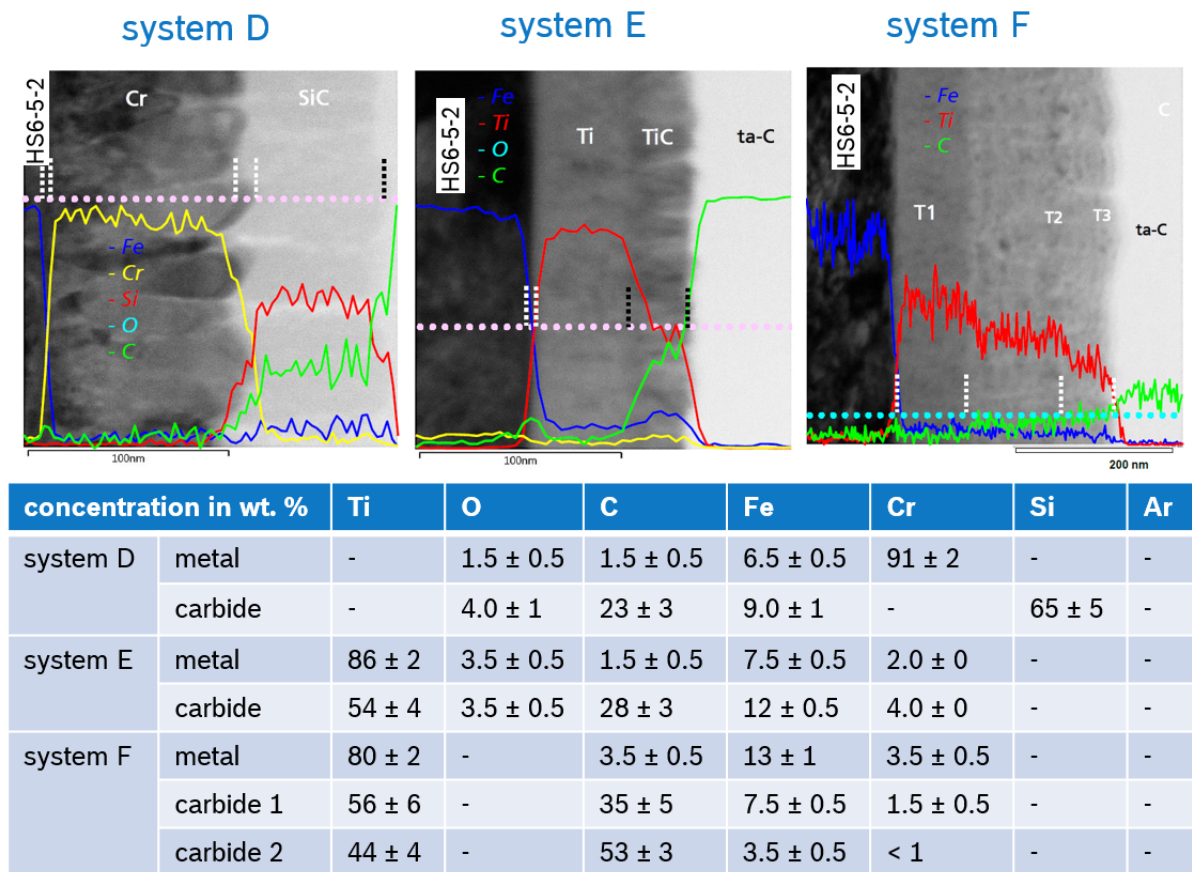


Figure 4.7: Summarized results for systems D, E and F from the EDX-report of *IWS Dresden*: EDX-line scans on TEM-lamellas of the interface regions. Single measuring spots are indicated by the dotted line. Extended quantitative data, extracted from the report, is summarized in the table below in wt. %.

In figure 4.8 a) a representative diffractogram of the Cr base layer is presented. The Cr base layers of coating systems D, G and H all exhibit a pronounced bcc structure. For pure Cr, bcc is the only crystal structure. In the binary phase diagram of Cr and Fe, which is depicted in figure 4.8 b), it can be seen that they form intermetallic phases also with bcc structure with complete mutual solubility [129], however at elevated temperatures. Towards room temperature the solubility vanishes successively, expressed by the miscibility gap in the phase diagram. Figure 4.8 c) shows the binary phase diagram of C-Si. The only compound in this system is a stoichiometric SiC phase. In contrast to systems A, B and C, the Ti base layer of coating systems E and F exhibit a nano-crystalline fcc-structure (refer to figure 4.4 a)). An fcc structure for Ti can be found in the C-Ti binary phase diagram (figure 4.4 b)). Furthermore, Ti does not form intermetallic fcc phases with Fe [125] or Cr [130], except of an Fe phase with very small

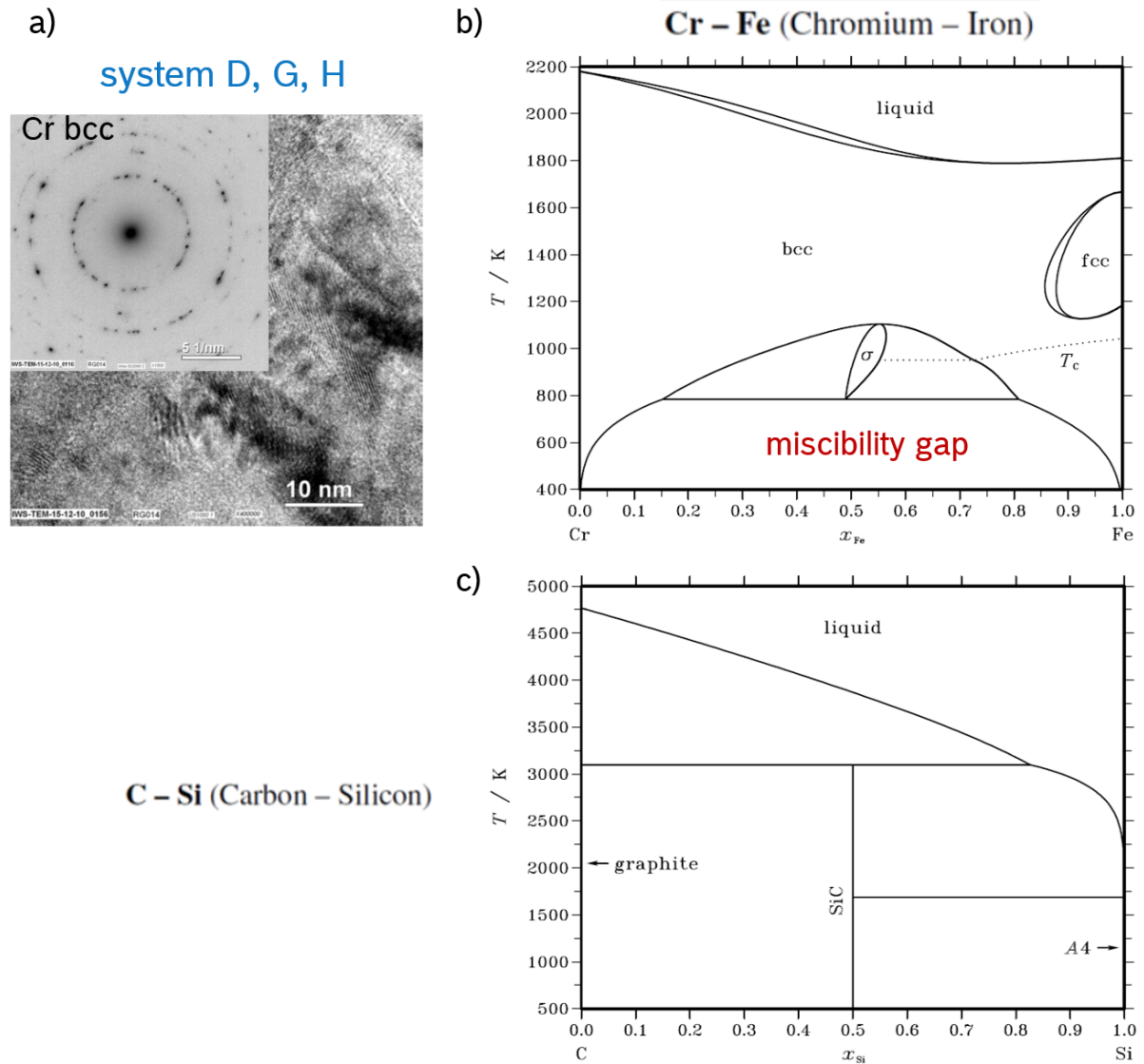


Figure 4.8: a) Electron diffractogram of the Cr base layer indicating a nano-crystalline bcc structure. b) binary phase diagram of Cr- Fe [129], the relevant miscibility gap is highlighted and c) binary phase diagram of C-Si [131]. The only compound is the stoichiometric SiC.

amount of Ti. Therefore, the signal must be related to a significant amount of crystalline TiC.

From the data in the table in figure 4.7, the atomic composition is calculated. Complemented by structural aspects from TED-analysis and the binary phase diagrams, a rough estimation of the phase compositions is made and shown in figure 4.9.

For the Cr base layer of system D, the detected amounts of Fe could be dissolved in a metastable intermetallic CrFe phase with bcc crystal structure. The contaminants of C and O are supposed to react immediately with the Cr. A likely source for the C contamination is the carbide deposition process, subsequent to the metal deposition. Hence it

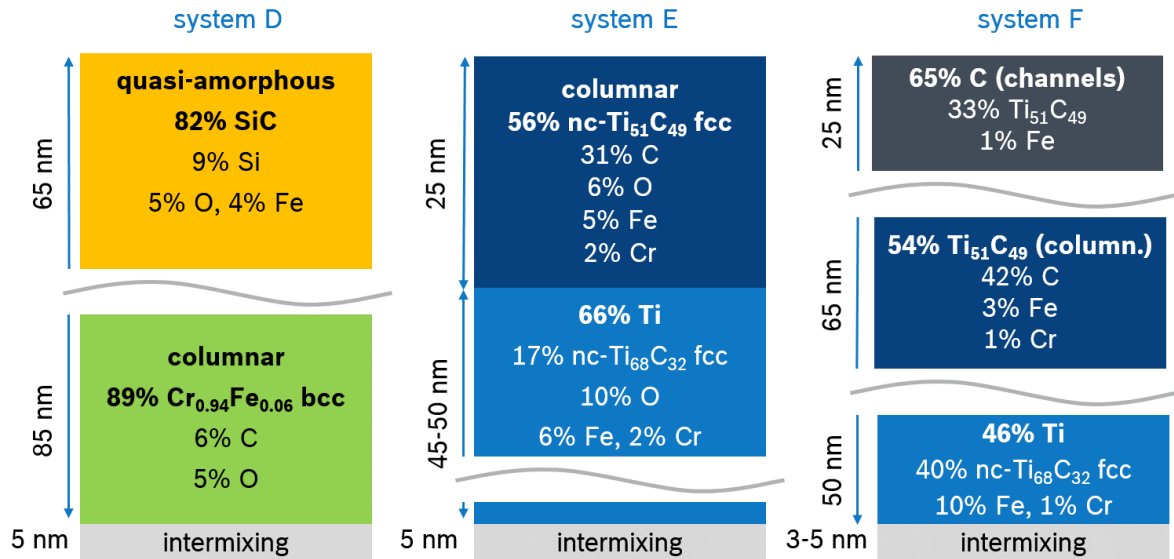


Figure 4.9: Estimated structure and phase compositions of the transition regions for the coating systems with carbide interlayers and ta-C based functional layer, based on bright-field TEM, EDX, TED and binary phase diagrams [125, 126, 128, 129, 131, 132, 133].

is possible that it is introduced in spaces between the columns. So the grain boundaries might form a Cr-rich Cr₂₃C₆-phase. The actual Fe concentration in the columns would then be higher than the indicated 6%. The adjacent SiC interlayer is quasi-amorphous with an expected stoichiometric composition. The crystallinity might be prevented by the contaminants O and Fe.

For systems E and F the fcc signal is a clear indicator for a significant amount of TiC phases. Due to the high amount of available Ti, Ti-rich carbides are expected. The indicated composition is the one with highest amount of Ti. Fe, Cr and O might be dissolved in a quasi-amorphous Ti phase in system E.

The columns of the carbide phases of systems E and F consist of nano-crystalline TiC with fcc structure, also with a significant amount of impurities. For system F the strongly pronounced C-channels, which are aligned in horizontal direction, correlate with a high C-content. The extensive channel formation can be attributed to the gradually increasing C-content, which is intentionally provided by the deposition process. Thereby an increase of the horizontally textured structure (parallel to the surface) is observed, accompanied by a gradual decrease of the impurity-content. The elemental composition of the upper part of the carbide phase indicates that it consists to almost two thirds of pure C located in the horizontal channels opposed by one third of metal carbide.

4.1.3 a-C:H-based Systems

Figure 4.10 a) shows the TEM images of the interface regions of coating systems with a-C:H functional layer, systems G, H and J. Systems G and H possess a strongly columnar Cr base-layer similar to the Cr base layer of system D, with roughly twice the thickness (160 to 170 nm). For system H more pronounced vertical channels between the columnar grains are observed.

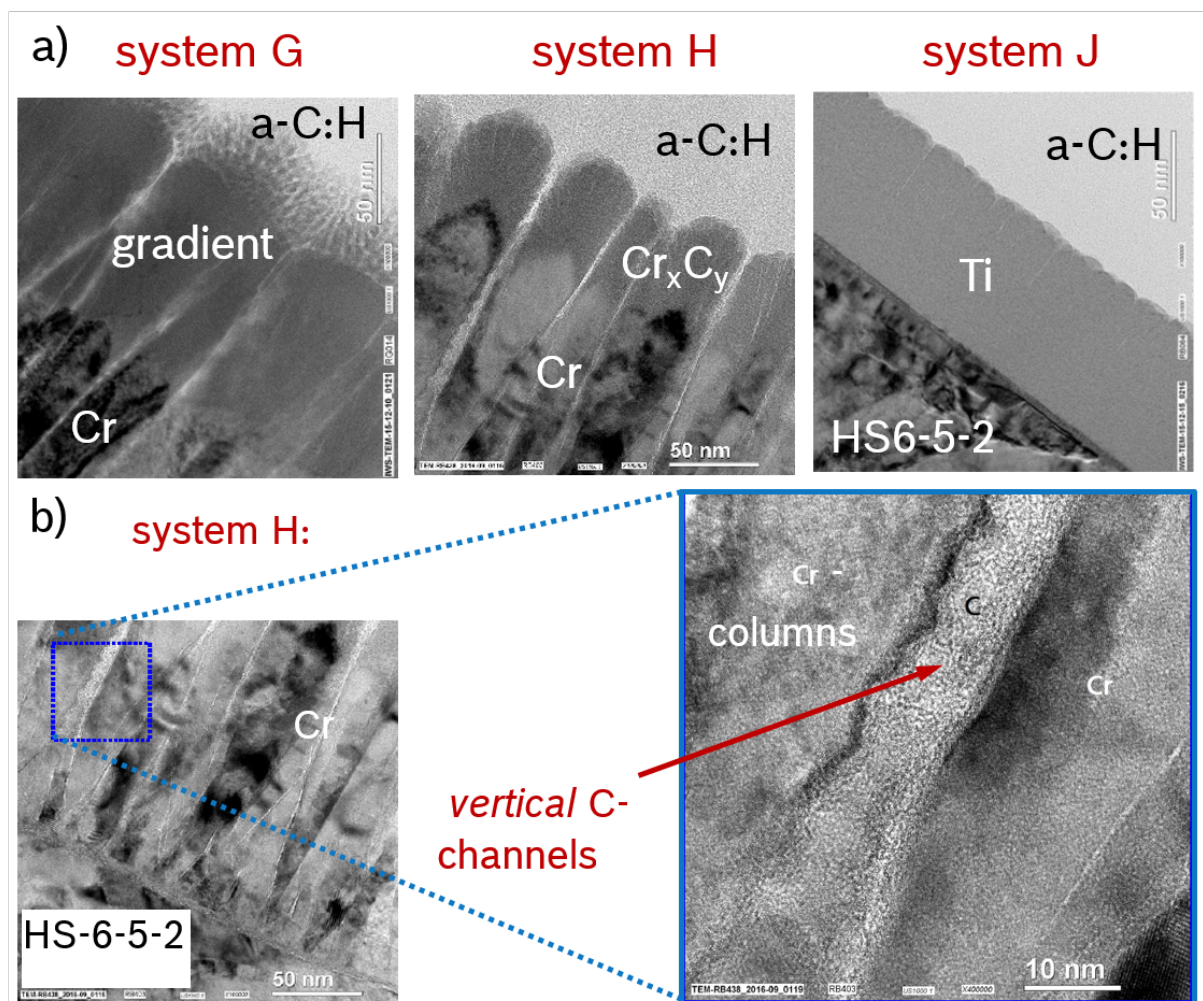


Figure 4.10: TEM-images of the interface regions of the coating systems with a-C:H functional layer G, H and J. System G with an extended transition from the metallic into the amorphous carbon phase, consisting of a step-wise and a gradual part with coral-like structure. For system H, only a step-wise transition prevails with distinct vertical channels. System J has a Ti adhesion layer and rather sharp transition, similar to coating system C. b) Close-up of the vertical channels of system H.

For system G, the gradual transition from the Cr- towards the carbon based phase has a thickness of 150-160 nm. A twofold step-wise transition is observed via the contrast, as well as a coral-like structure at the top similar to other reports [121], with 35-40 nm thickness. The transition region of system H only consists of one phase, similar to the upper monolithic phase of system G and with distinct vertical channels, which are highlighted in the close-up in figure 4.10 b).

System J possesses an 80 nm thick, monolithic Ti phase very similar to system C, just with an altered functional layer. At the upper end a columnar structure is visible with fine channels of less density.

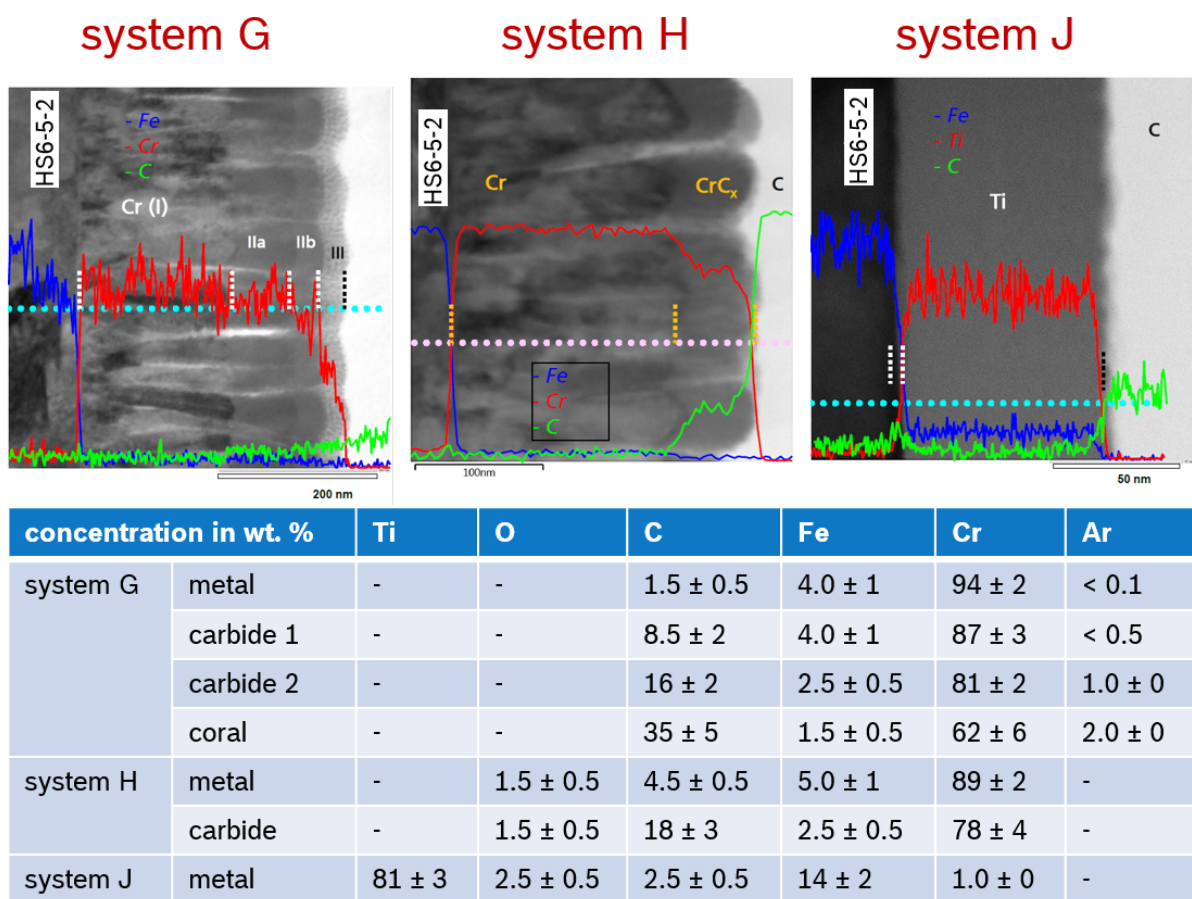


Figure 4.11: Summarized results for systems G, H and J from the EDX-report of *IWS Dresden*: EDX-line scans on TEM-lamellas of the interface regions. Single measuring spots are indicated by the dotted line. Extended quantitative data, extracted from the report, is summarized in the table below in wt. %.

Figure 4.11 shows the EDX line scans performed on TEM-lamellas of the interface regions of coating systems G, H and J. Extended quantitative data is summarized in the

table below.

Fe-contamination is found for each phase. The metal layer of system G is O-free, the one of system H has an increased amount of C, which might correlate with the more pronounced vertical channels between the columnar grains.

Figure 4.12 shows the binary phase diagram of C and Cr. Several carbide phases with distinct compositions are stable. The carbide phase with highest C-content even consists of more Cr than C, with a concentration of 60 at.% Cr.

C – Cr (Carbon – Chromium)

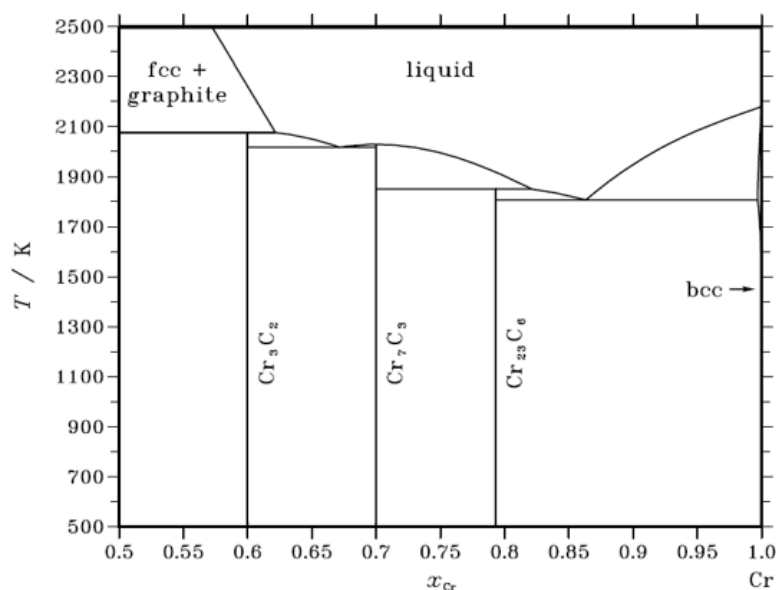


Figure 4.12: Binary phase diagram for C and Cr [133], which exhibits three stoichiometric stable carbides: $Cr_{23}C_6$, Cr_7C_3 and Cr_3C_2 .

From the data in the table in figure 4.11, the atomic composition is calculated. Complemented by structural aspects from TED-analysis and the binary phase diagrams, a rough estimation of the phase compositions is made and shown in figure 4.13.

The Fe-impurities of the Cr base layer of systems G and H are supposed to be solved in the metallic Cr bcc phase. For system G, the twofold step-wise transition is attributed to the stoichiometric carbides Cr_7C_3 and Cr_3C_2 as quasi-amorphous phases. The coral-like structure at the top consists of Cr_3C_2 nano-particles in an amorphous carbon matrix. The formation of this coral structure can be attributed to the missing of a carbide with less fraction of Cr. This is compensated by an increased share of the C-matrix and a decrease in Cr_3C_2 content. The transition region of system H only consists of one phase, similar to

the upper monolithic phase of system G with carbon rich Cr_3C_2 , however with a higher amount of carbon, resulting in distinct vertical channels, not in a coral-like structure.

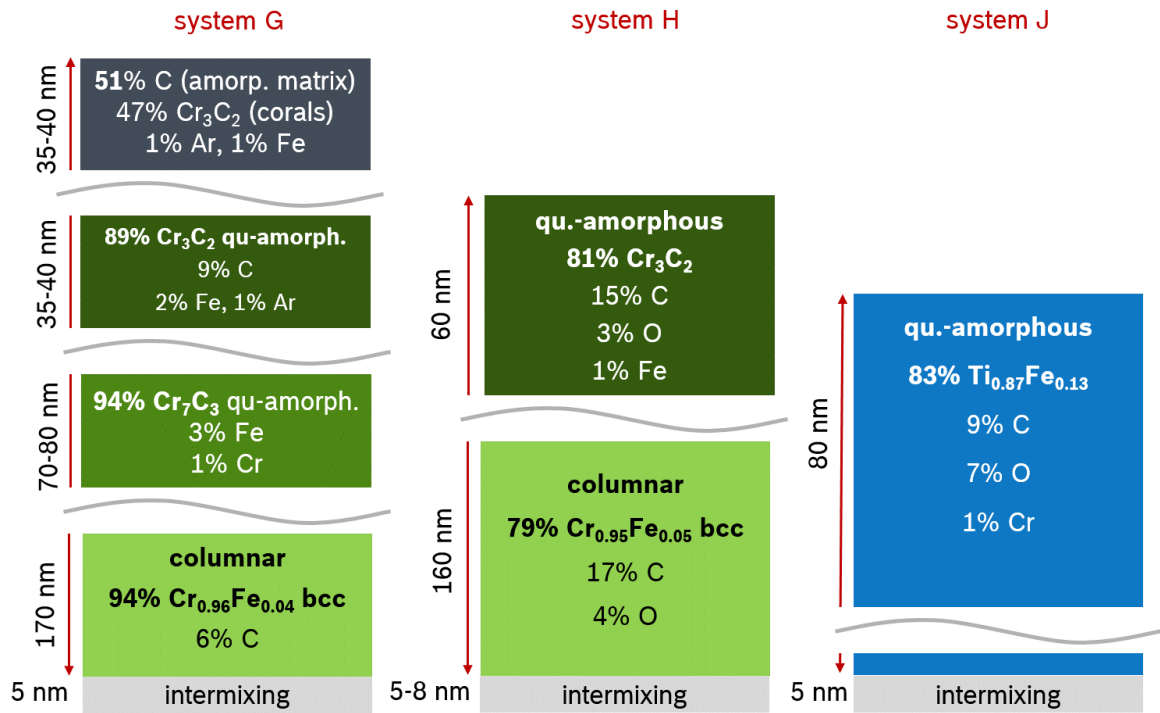


Figure 4.13: Estimated structure and phase compositions for systems with a-C:H functional layer, based on bright-field TEM, EDX and TED and binary phase diagrams [125, 126, 128, 129, 133].

According to the previous statements, most of the Cr of the transition regions of coating systems G and H is bound to carbon. So the Fe-impurities cannot be solved within a Cr-rich phase. Locally, some stoichiometric CrFe σ -phases might occur in the more Cr-rich carbide layers or cementite in the C-rich carbide layers. Pure Fe-phases are not expected due to the abundance of reaction partners. The adhesion layer of system J is very similar to system C with slightly more impurities.

4.1.4 Mechanical Characterization

The indentation measurements on the SACS only yield explicit results for those phases, which exhibits constant properties over a sufficiently large thickness. The corresponding results are summarized in table 4.1, supplemented by the intrinsic residual stress, determined by the curvature tests, H-content from resonant nuclear reaction analysis (NRA)

and an estimated value for ν_f .

For all coating systems, the same HS6-5-2 substrates were used with a measured hardness of $H_{IT,sub} = (10 \pm 1) \text{ GPa}$ and modulus $E_{IT,sub} = (260 \pm 10) \text{ GPa}$. The Cr-base layer of system G is around 4 GPa harder than the steel substrate, also the modulus is slightly higher. The hardness of the a-C:H functional layer is significantly higher with almost 25 GPa, the modulus however is slightly less compared to the HS6-5-2.

Table 4.1: Mechanical properties of substrate and functional layers, derived via nanoindentation on a SACS with the CSM-method and a maximum indentation depth of 40 nm. Thickness was determined from the TEM-images, intrinsic stress from curvature tests, ν_f estimated and H-content via NRA.

	thickness / μm		H_{IT} / GPa	E_{IT} / GPa	σ_0 / GPa	ν	H-content / %
	monolithic	gradient					
ta-C 1	1.3	0.4	42	420 ± 10	-2.65	0.2	
ta-C 2	0.7	1.2	57	540 ± 10	-2.73	0.2	
a-C:H	1.9		23 ± 2	220 ± 10	-1.7	0.2	30 ± 3
Cr			14	260 ± 10			
HS6-5-2			10 ± 1	260 ± 10			

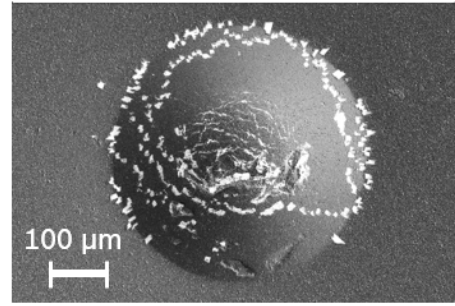
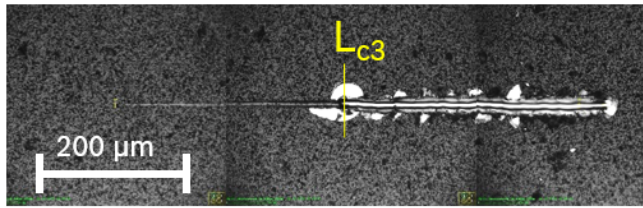
ta-C 1 is thicker and less hard compared to ta-C 2, but both are much harder compared to the other materials used in this work. On top of each ta-C variant, an a-C:H running-in layer is applied with gradually decreasing hardness towards the top surface. The running-in layers are differently thick, such that the total thickness of the functional layers are comparable. All functional layers exhibit high intrinsic residual stresses with -1.7 GPa for the a-C:H and around -2.7 GPa for the ta-C coatings.

4.2 Adhesion Performance Assessment

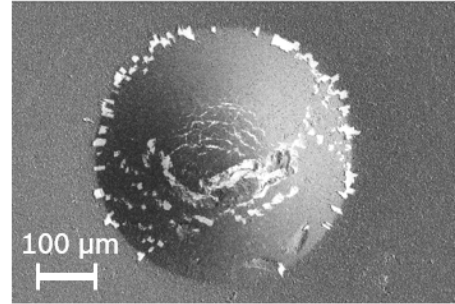
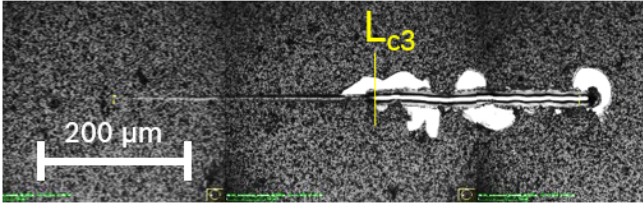
In the following, representative microscopic images of the nano-scratch tests and representative SEM-images of the HRC-tests are provided for all coating systems. Quantitative results in terms of L_{c3} -values according to EN ISO 20502:2016 [99], the measured area of delaminated coating around the scratch track, as well as HF-values from the HRC-measurement according to VDI 3198 [2] are summarized in table 5.1.

Figure 4.14 shows the results for ta-C coating systems with Ti adhesion layer. Delami-

system A



system B



system C

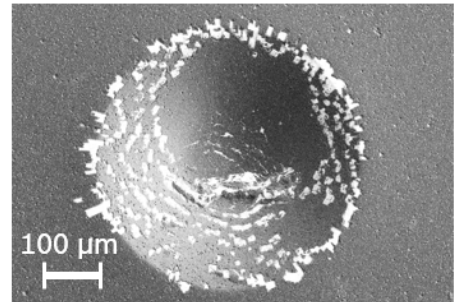
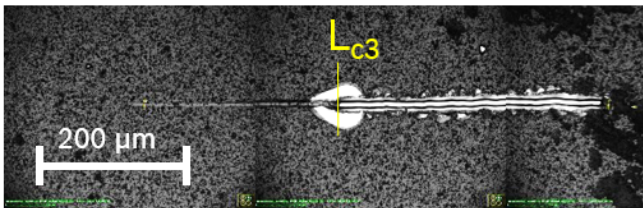


Figure 4.14: Representative images of scratch-tracks (microscopic) and HRC-imprints (SEM-images) for ta-C based coatings with Ti adhesion layer in the as-deposited state.

nation of very small fragments is observed with no significant difference between systems A to C. Microscopic assessment yields an HF2 for all three systems. The L_{c3} values from nanoscratch testing show slight differences, but the delamination behavior around the scratch tracks is noticeable. All three systems show a certain areal delamination, originating at the L_{c3} point, indicating a local buckling event. System B exhibits additional spots with local buckling induced delamination at the end of the track and also in the middle. Thereby, the measured delamination area is significantly higher compared to systems A and C. Interestingly, system B showed the highest L_{c3} .

In figure 4.15 the results for systems with carbide interlayers are presented. Systems D and E are rated HF2 with not much differences in the SEM-images and also similar to the previous systems. System F however shows areal delamination around the complete imprint yielding HF6. The delaminated area exhibits two clearly different contrasts in the

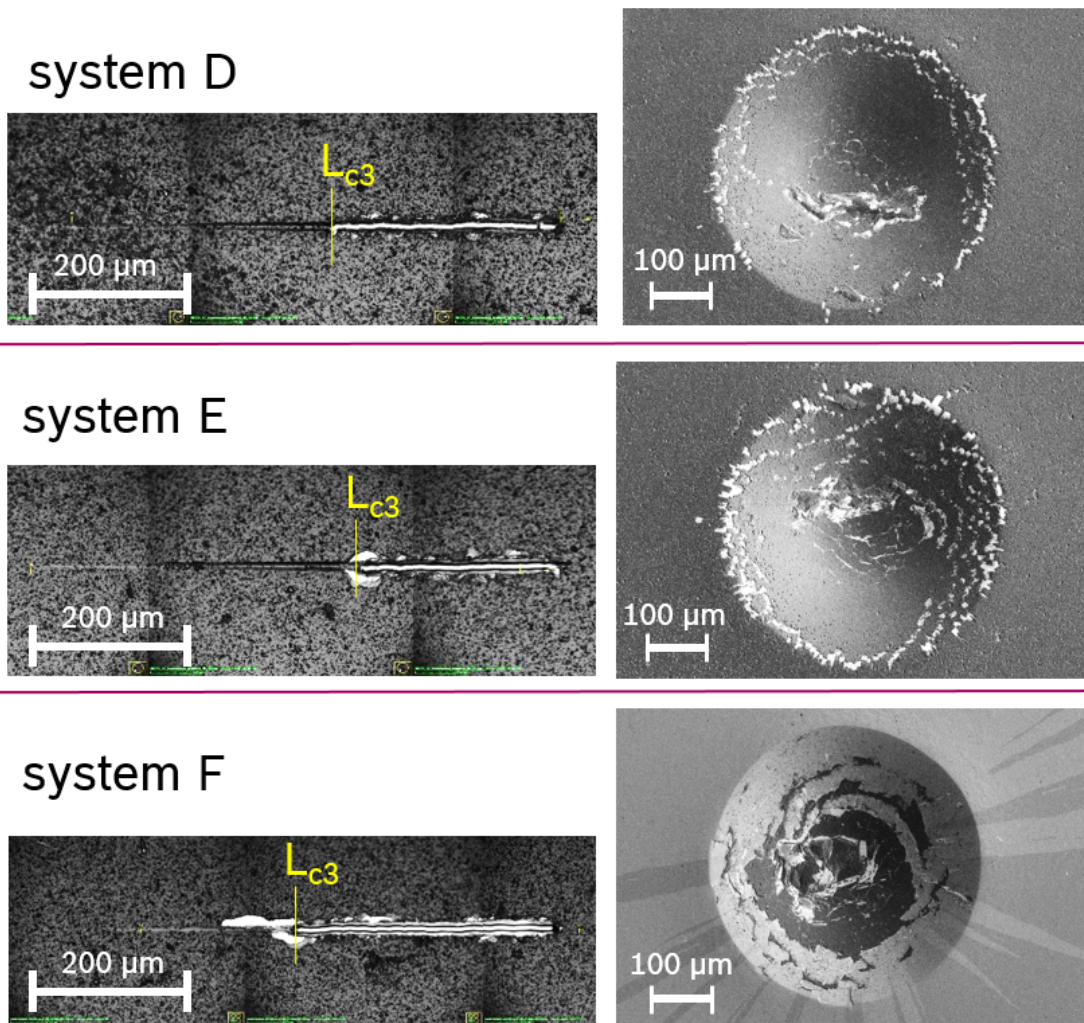


Figure 4.15: Microscopic images of representative scratch-tracks and SEM-images of representative HRC-imprints for ta-C based coatings with extended carbide interlayers in the as-deposited state.

SEM image, which lead to the conclusion, that in the delamination process, two different interfaces are involved.

Nanoscratch testing yield the highest L_{c3} -values in this work for systems D and E. Furthermore, virtually no delamination event can be detected around the scratch track for system D, not even at the L_{c3} -point.

The L_{c3} value for system F is comparable to the ones of the Ti-based systems. Interestingly, the area of delaminated coating is significantly less compared to system A, B and C, despite the result of the HRC-test. Peculiar however is the path of the buckling driven delamination, starting at the L_{c3} and propagating back towards smaller normal loads (refer to figure 4.15, L_{c3} is highlighted).

Results for systems G, H and J with a-C:H functional coating are depicted in figure 4.16.

Nanoscratch-testing yield no significant coating delamination for all three systems. The light spots, where substrate or interlayer gets visible are surrounded by conchoidal fractures within the a-C:H coating, implying that for these instances, crack advance within the functional layer is energetically preferred over crack advance at one of the present interfaces. L_{c3} values are comparable to that of the ta-C based coating systems despite the higher hardness of the latter.

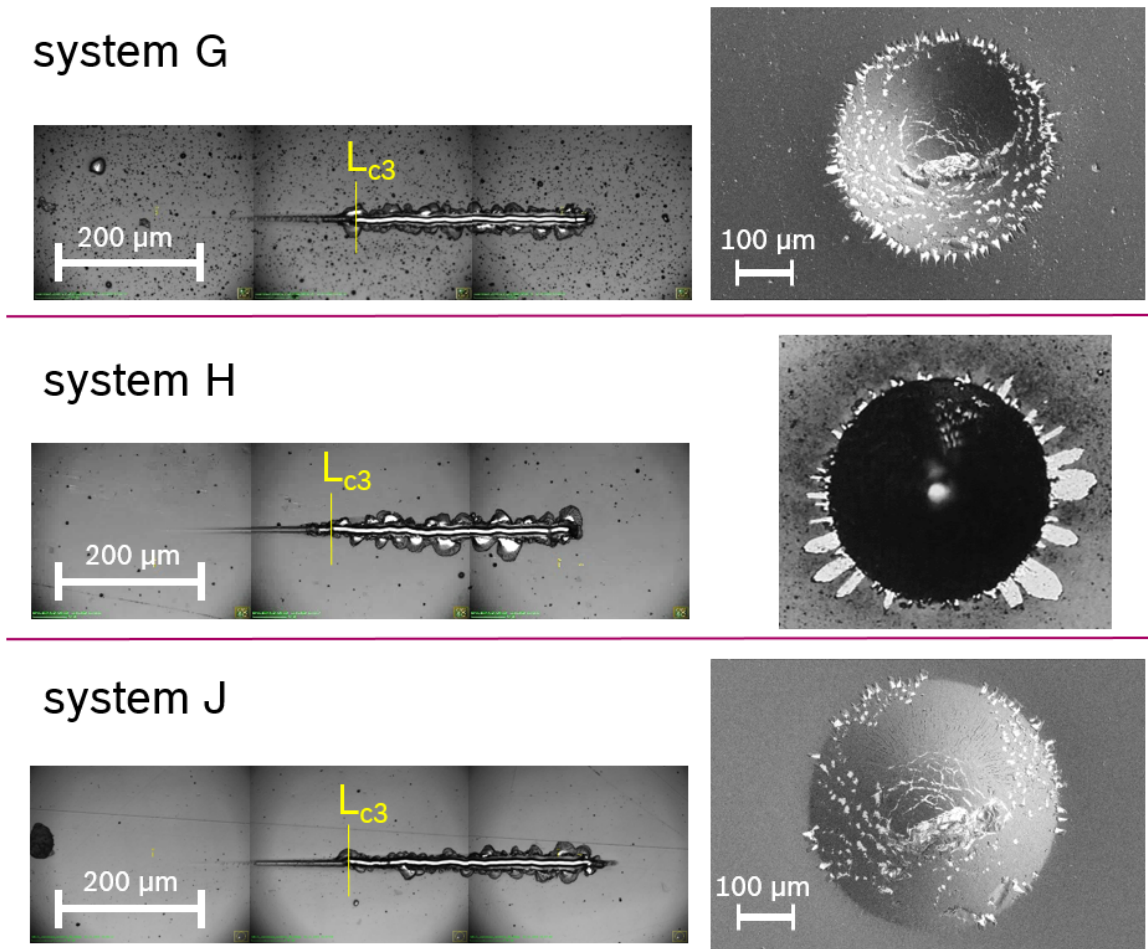


Figure 4.16: Microscopic images of representative scratch-tracks and SEM-images of representative HRC-imprints for a-C:H-based coating systems G, H and J in the as-deposited state (microscopic image for system H, HRC).

In the HRC testing, system J was rated best with HF2, followed by system G with HF2 to HF3. System H was significantly worse with an HF4 rating.

The findings highlight the general issue regarding comparison of qualitative adhesion tests. Especially when major properties vary, different tests respond differently. The HRC test shows a weak response behavior for the coating systems with ta-C functional coating.

Systems A to E were all rated HF2, although the delamination affinity seems to differ, indicated by the delaminated area around the scratch tracks in the nanoscratch test. Coating system F on the other hand is already rated several classes worse with HF6. In this case, the nanoscratch result is not explicit.

Table 4.2: Mechanical testing of the adhesion performance of coating systems A to J with HRC and nanoscratch test. For the latter, also the area of delaminated coating is evaluated via digital means.

sample	HRC	nanoscratch	
	HF	L_{c3} / N	$A_D / \mu\text{m}^2$
A	2	1000	2600
B	2	1150	8300
C	2	900	2200
D	2	1200	65
E	2	1250	570
F	6	1050	1300
G	3	1100	300
H	4	950	1300
J	2	1150	110

In contrast to the ta-C systems, for the systems with a-C:H functional layer, the HRC-tests seems to be more sensitive for differentiating the adhesion performance, whereas the nano-scratch tests shows no good response behavior.

To summarize the findings, it can be concluded that the HRC shows a sudden response for the ta-C coating systems in the case of system F and an increasing response for the a-C:H systems, showing a maximum for system H. Those extremes are the coating systems, for which a significant amount of graphite-like channels were found in the TEM studies (refer to figures 4.6 b) and 4.10 b)).

For system F extensive graphite-like phases in horizontal alignment are observed, which can explain the fracture behavior. High shear loads caused by the indentation can initiate cracks within these graphite channels and crack propagation is supposed to be enabled within these channels as well, resulting in large area delamination.

For system H also extended graphite-like phases are observed, however in vertical orientation. Cracks can be equally easy initiated, but they are not guided parallel to the substrate surface. So in this case crack propagation is not enabled in the direction parallel to the substrate surface, explaining why the extend of delamination is less severe

compared to system F.

Determination of the L_{c3} values (table 5.1) did not yield a clear trend for the coating systems. A measuring of the delaminated area around the scratch track is supposed to be a better assessment criteria for the adhesion performance, because it relates to a triggering of local, buckling driven delamination. The influence of the weak spots of systems F and H, presumably the graphite channels, is less pronounced in the scratch-test, but it also seems to influence the delamination behavior. E.g. system H exhibits significantly more spots, where delamination is initiated, compared to systems G and J (all with a-C:H functional layer). System F shows significantly more area of delaminated coating compared to systems D and E (all with carbide interlayer and ta-C based functional layer).

Furthermore, a correlation is found for the area of delaminated coating for the ta-C based coatings. The delaminated area is significantly lower for the coating systems with carbide interlayers.

4.3 Long Time Thermal Annealing

After long time annealing at 350 °C in the N₂-furnace with residual lab air, the coating systems are again assessed in terms of standard adhesion testing, as well as structure analysis via TEM-imaging, EDX and electron diffraction. Mechanical testing via nanoindentation on a SACS after long time annealing yield no significant change in hardness or modulus. Merely the thickness of the a-C:H running in layer was reduced for systems A to F. The monolithic a-C:H functional layer of systems G and H, significantly harder compared to the running in layers, were not remarkably reduced in thickness.

All annealed samples of coating systems B and J were completely delaminated after the thermal treatment. While for system B, the samples were completely silver in color, for system J the Ti adhesion layer was completely oxidized with green color. This is an evidence that samples of system B got delaminated subsequent to the annealing, presumably during cooling down, when the intrinsic residual stress level of room temperature gets reestablished, whereas samples of system J must be delaminated during annealing in order to generate the thick oxide layer. Exact mechanisms, which lead to the large area

delamination are analyzed in chapter 7.

4.3.1 Change in Adhesion Performance

In the following, the results of the adhesion performance assessment are presented for the annealed state. Figure 4.17 shows the adhesion test results after annealing for systems A and C.

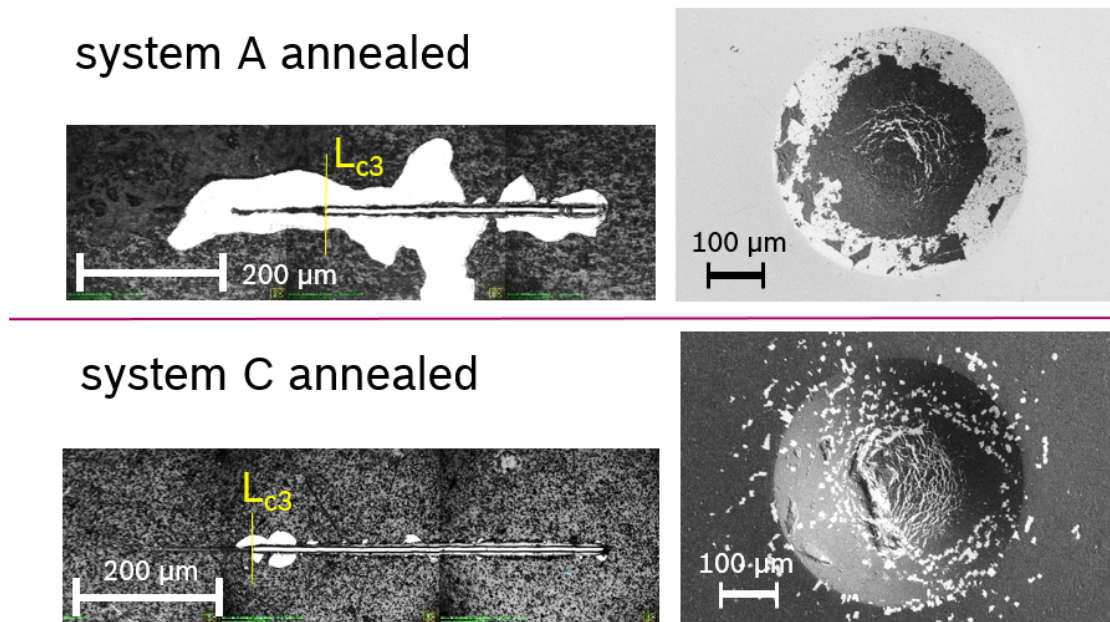


Figure 4.17: Microscopic images of representative scratch-tracks and SEM-images of representative HRC-imprints for ta-C based coatings with Ti adhesion layer in the annealed state. System B is missing due to complete delamination after annealing.

For system A, severe coating delamination is observed around the scratch track with a more than 20 times larger delaminated area, compared to the as-deposited state, while the L_{c3} -value is only slightly reduced. This behavior cannot be attributed to the introduced stress field of the nanoscratch, since the delamination is propagating away from its initiation point. It can rather be attributed to a buckling driven delamination, for which the intrinsic compressive stress is sufficient. This tendency for a self-contained delamination progression is from now on called *delamination affinity* in order to differentiate this behavior from the delamination, which is forced by an external stress field, as it was the case for system F in the as-deposited state.

The HRC-test yields an HF6 for system A. It cannot be trivially differentiated between a self-contained delamination progression, which was initiated during the test or a delamination which was forced by the stress field. Taken the result of system B into account, where the coating was completely delaminated after annealing, it can be stated that the ta-C 1 system with single Ti adhesion layer is prone to a thermal driven decrease in adhesion performance. During the annealing, the intrinsic stress is partly relaxed and reestablished after cooling, which can initiate some cracks in the interface region. Since no external force was applied when system B delaminated, it can be concluded that also for system B, the delamination affinity is increased.

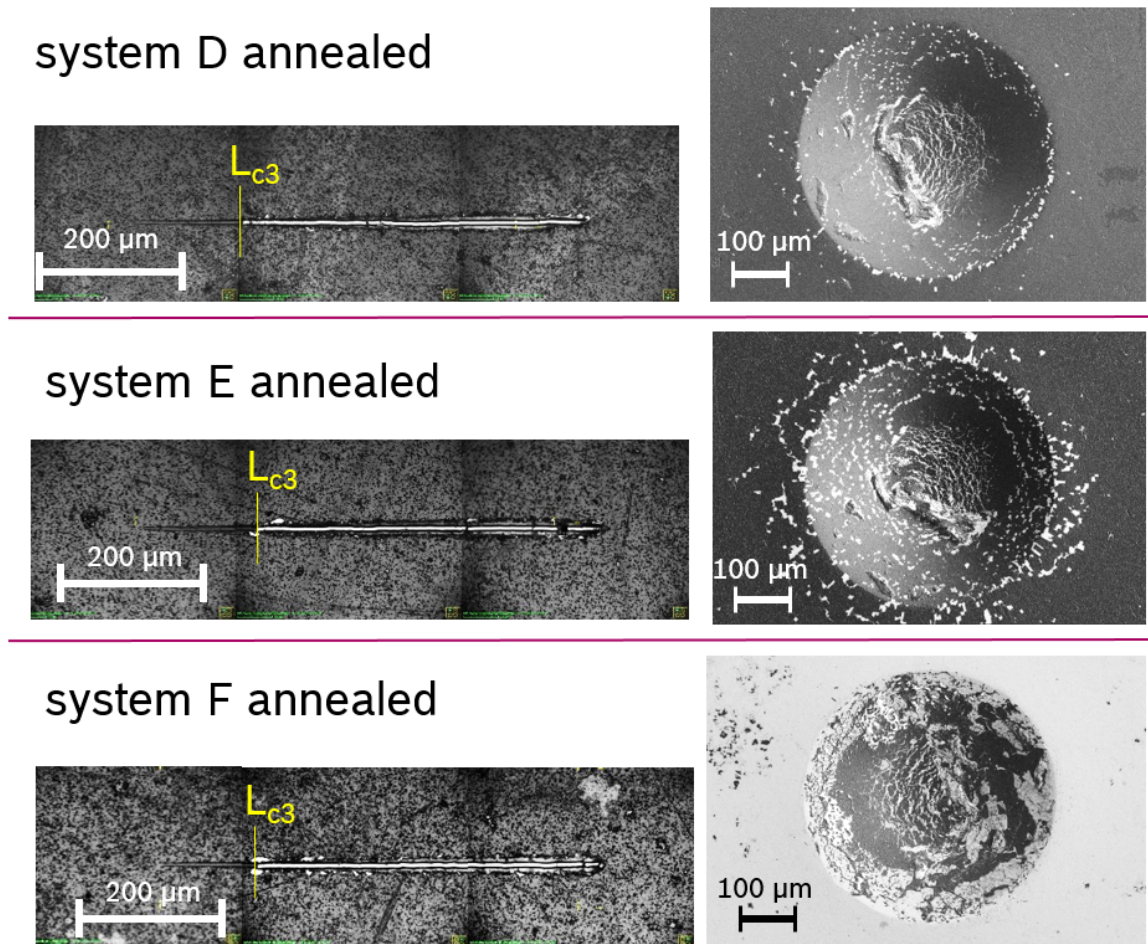
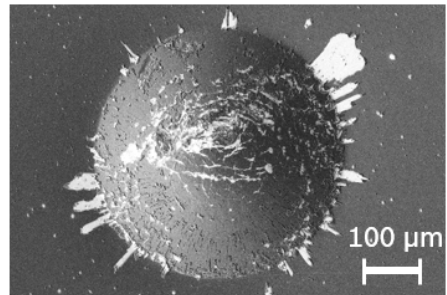
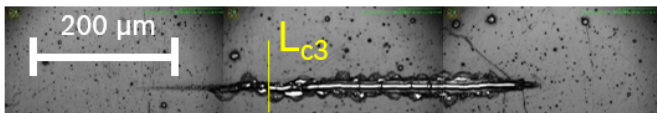


Figure 4.18: Microscopic images of representative scratch-tracks and SEM-images of representative HRC-imprints for ta-C based coatings with extended carbide interlayers in the annealed state.

For system C, the nanoscratch tests shows no increased delamination affinity. A single delamination event at the L_{c3} spot is observed with same amount and shape of delaminated area as in the as-deposited state. However this is observed at a shifted L_{c3} point with roughly half the value as before. Some scattered, local delamination events around the HRC-imprint can be found in the annealed state for system C.

The adhesion assessment after annealing for systems with carbide interlayers is depicted in figure 4.18. In the nanoscratch tests, almost no delamination around the scratch tracks is observed for all three systems, which corresponds to a decreased delamination affinity for systems E and F. Again, the HRC-imprints show scattered, local delaminations, slightly for system D and more severe for system E. System F instead shows large area delamination around the HRC-imprint (rated HF6), as already in the as-deposited state. Figure 4.19 shows the results for systems with a-C:H functional layer. The HRC-test yields an even slightly better result for system G compared to the as deposited state. However after several days, additional, delaminations were observed via SEM-imaging (refer to figure 4.19).

system G annealed



system H annealed

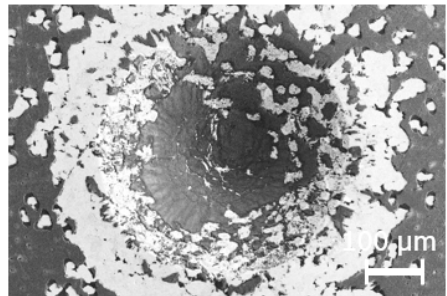
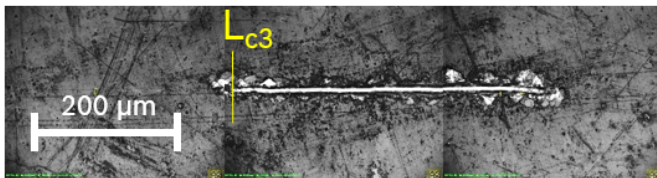


Figure 4.19: Microscopic images of representative scratch-tracks and SEM-images of representative HRC-imprints for a-C:H-based coating systems G and H in the annealed state. System J is missing due to complete delamination during annealing.

System H shows a very peculiar delamination behavior in the HRC-test with a large area of delaminated coating, however not as a result of a progressing delamination front, as observed for system F for instance. Instead, there is some evidence for local failures, initiating several independent delamination events in the area of influence of the indentation. In the nanoscratch test, uneven scratch tracks are observed with some minor delaminations but no distinct evidence for buckling driven delamination.

System J, for which complete delamination occurred, is analyzed in chapter 7. The homogeneous coloring of the samples suggests that the delamination affinity must be increased very fast via annealing, so that buckling driven delamination was initiated already during the annealing process with partly relaxed intrinsic stress and without external mechanical load.

In table 4.3, the quantitative results are listed in terms of HF-value from HRC, the L_{c3} -values from the nanoscratch test and the corresponding delaminated area around the L_{c3} -spot. The L_{c3} -values are lowered for all systems compared to the as-deposited state and do not correlated to the observed increased delamination affinity, which was observed for systems A, B and J, all with a single Ti adhesion layer. System C is the only system with single Ti adhesion layer, for which this was not observed. Systems F on the other hand, which already showed large area delamination in the as-deposited state, does not show an increased delamination affinity.

Table 4.3: Evaluation of adhesion performance of the coating systems in the annealed state via HRC and nanoscratch. In addition to the HF-values of the HRC test and the L_{c3} -values of the nanoscratch test, the area of delaminated coating around the scratch track is determined.

sample	HRC	nanoscratch	
	HF	L_{c3} / N	$A_D / \mu\text{m}^2$
A	6	850	56000
B	delaminated after annealing		
C	3	500	2100
D	2	650	83
E	3	550	110
F	6	450	370
G	2	800	410
H	5	700	640
J	delaminated during annealing		

4.3.2 Change in Structure

TEM-lamellas were also prepared for samples in the annealed state. Coating systems A and H are however missing due to a practical upper limit for the number of TEM-studies in this work. For coating systems B and J no TEM-lamellas were prepared, as they delaminated completely after or during the annealing respectively.

ta-C with Ti Adhesion Layer

During lamella preparation for coating system C in the annealed state, partial delamination of the functional layer just above the Ti-phase occurred (refer to figure 4.20 a)). This was not the case in the as-deposited condition, indicating that for all adhesion layer systems of this work with a single Ti adhesion layer are thermally not stable, resulting systematically in an increased delamination affinity.

Nevertheless it was possible to prepare a lamella for system C after annealing. Figure 4.21 shows the analysis results in terms of a TEM-bright-field image (a)) and an EDX line-scan (b)). The quantitative data is summarized in the table in c).

The 80-85 nm thick Ti phase appears monolithic, but with inhomogeneous chemical composition and several dark spots in the bright-field image. Furthermore, a significant increase in C-content compared to the as-deposited state is observed. The carbon content is especially increased for two small regions with 10 nm thickness. One is located close to the functional layer and one near the substrate surface. Furthermore, a nano crystalline fcc structure is observed via TED.

From the data in figure 4.21 c), the atomic composition is calculated. Complemented by structural aspects from TED-analysis and the binary phase diagrams, a rough estimation of the phase compositions is made and shown in figure 4.21 d).

The composition of the carbon-rich regions, the strong affinity of Ti to form carbides and the fcc signal in the TED are strong indications for narrow TiC phases. The contaminations of O, Fe and Cr likely form inclusions. The EDX data and the fcc signal from TED, indicate also a significant amount of TiC in the central part of the adhesion layer. The estimated metastable intermetallic phase of Ti and Fe (and maybe also Cr) in the

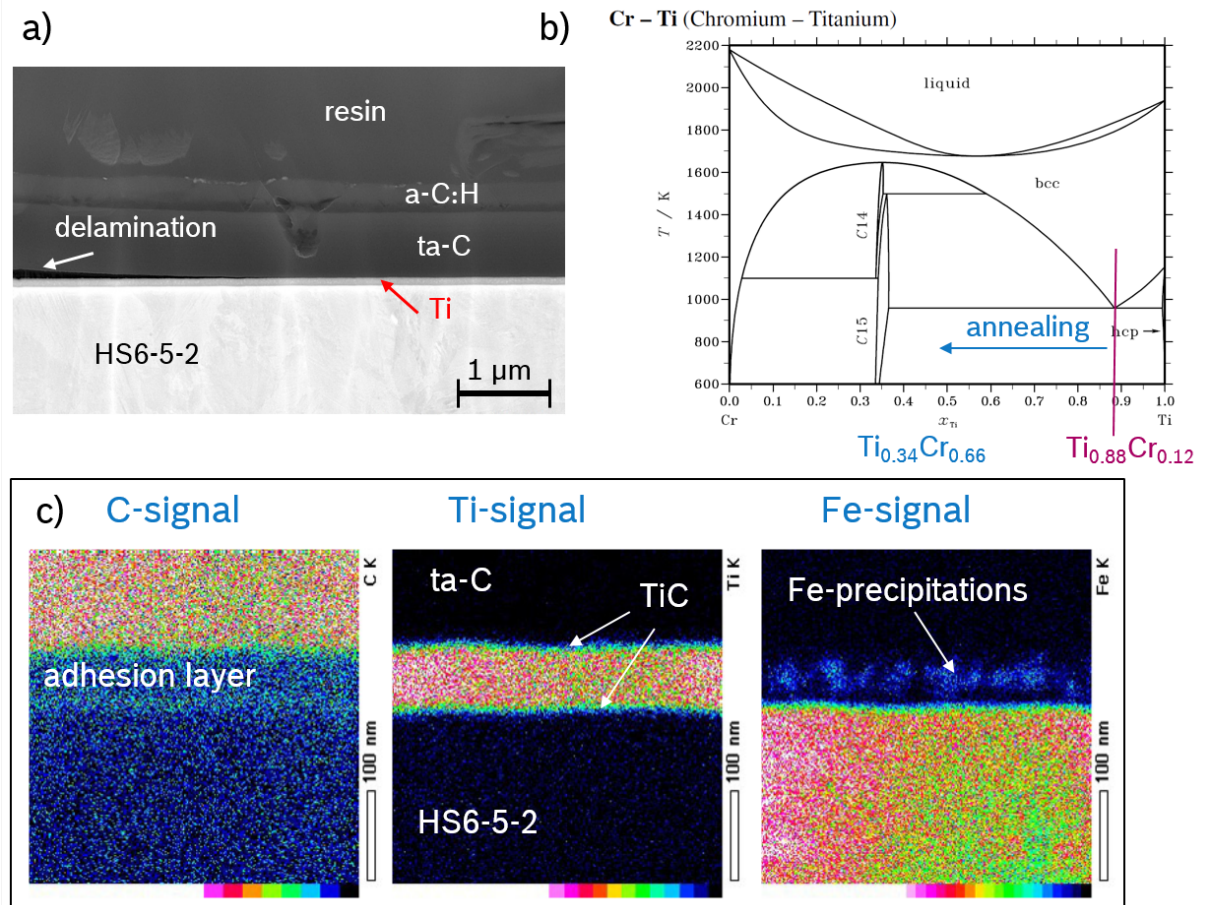


Figure 4.20: a) partial delamination during lamella preparation on coating system C, b) binary phase diagram Cr-Ti, relevant composition are indicated and c) EDX-mapping of the interface region of system A* after thermal treatment. The lateral inhomogeneous distribution of Fe, caused by segregation is clearly visible.

as-deposited state (refer to figure 4.5), is supposed to segregate into stable precipitation phases, as hardly any Fe is soluble in Ti at temperatures below 857.5 K [125] and practically no Cr below 959.3 K [130].

From the binary phase diagram of Fe-Ti in figure 4.4 b), it can be derived that a precipitation would result in the stoichiometric FeTi. Furthermore, the iron signal is significantly increased in the central part compared to the as-deposited state from 14 to 20 wt. % (see also the line-scan in fig. 4.21 b)), indicating local segregation which occurs simultaneously to the TiC formation in the narrow regions. Furthermore, the measuring spots of the EDX line scan, where the Fe signal is significantly increased coincide with the dark spots, which were observed in the bright-field image. This evidences that the dark spots correspond to the FeTi precipitation. The dark color can either result from a concentration of higher mass, related to the higher Fe-concentration or it can be an interference pattern caused

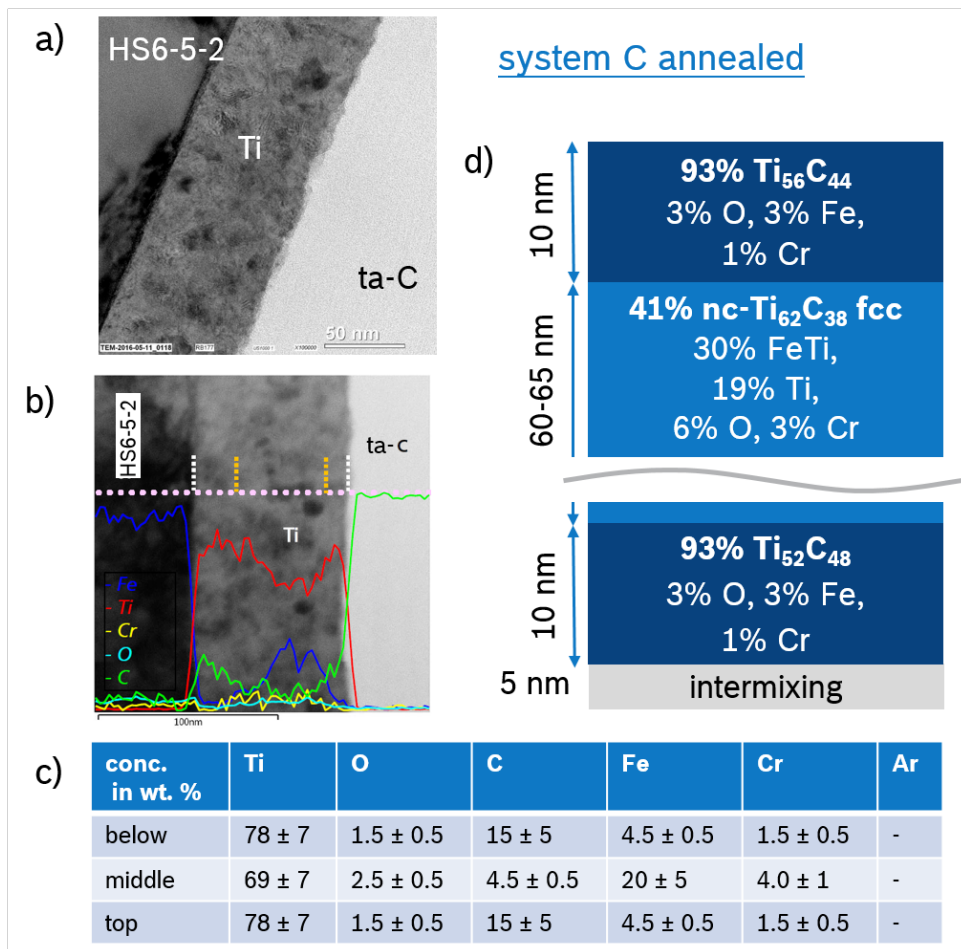


Figure 4.21: TEM-analysis of the interface region of coating system C in the annealed state: a) Bright-field image, b) EDX-line scan, c) table with EDX data and d) derived phase composition in at. %, based on bright-field TEM, EDX, TED and binary phase diagrams [125, 126, 130].

by diffraction at the crystalline precipitations.

Figure 4.20 c) shows an EDX-analysis in terms of a compositional distribution mapping of coating system A* after a heat treatment, comparable to the one in this work. System A* is very similar to system A and most importantly, the Ti adhesion layer is practically the same as for the coating systems dealt with in this work. So the findings are transferable. A lateral segregation is clearly visible. The distribution of the Fe-rich precipitation phases indicates a relation to the columnar structure of the layer, i.e. the precipitation might occur at the grain boundaries, where density is lower, compared to the columns. Alternatively, TiC forms at the grain boundaries and Fe-rich phases are left in the columnar grains.

Fe does not form stable carbides [128]. Following the model of Outka [114], it is concluded, that the Fe-rich precipitation phases destabilize the adhesion, when in direct contact with

the functional layer. Similar to a direct deposition of the functional layer onto steel with poor adhesion [32, 33, 116]. At the prepared spot of figure 4.21, the grown TiC-interlayer might serve as a thin barrier for the precipitation process, ensuring the adhesion performance at locations, where the formed carbide layer is sufficiently thick. Regarding the partly delamination during lamella preparation, this was apparently not the case at each spot.

Figure 4.20 b) shows the binary phase diagram for Cr and Ti. With respect to the previous discussion, the system Cr-Ti is very similar to Fe-Ti. Segregation is supposed to lead to a $\text{Cr}_{0.66}\text{Ti}_{0.34}$ -phase. In contrast to iron, chromium forms stable carbides. This has two effects. First, carbide formation is possible during the annealing and second, if Cr-precipitation occurs at the interface towards the C-coating, it is not expected to destabilize the adhesion.

ta-C with Carbide Interlayers

Figure 4.22 shows the TEM analysis of the coating systems D, E and F with carbide interlayers in the annealed state. From the appearance in the TEM images, no major structural change is observed.

For system D, also from compositional aspects, no significant change is detected. The metallic part of the adhesion layer of coating system E exhibits an increased amount of C, analogous to the Ti-layer of system C and also a local maximum of the C-signal in the vicinity of the interface towards the steel substrate is found. The Fe-content of the metallic base layer of systems E and F has a maximum in the center, similar to system C. A second local maximum for Fe is found in the EDX-analysis within the carbide phase for system E.

For system F, also some Fe is found in the carbide phase with a distinct local minimum at the upper end of the base layer. The C-content is not increased, compared to the as-deposited state. However the thickness of the carbide phase with lower C-content is decrease in favor of the thickness of the carbide phase with higher C-content. Thereby also the thickness of the graphite-like channels is decreased, which now appear more graphene-

like in the TEM-analysis.

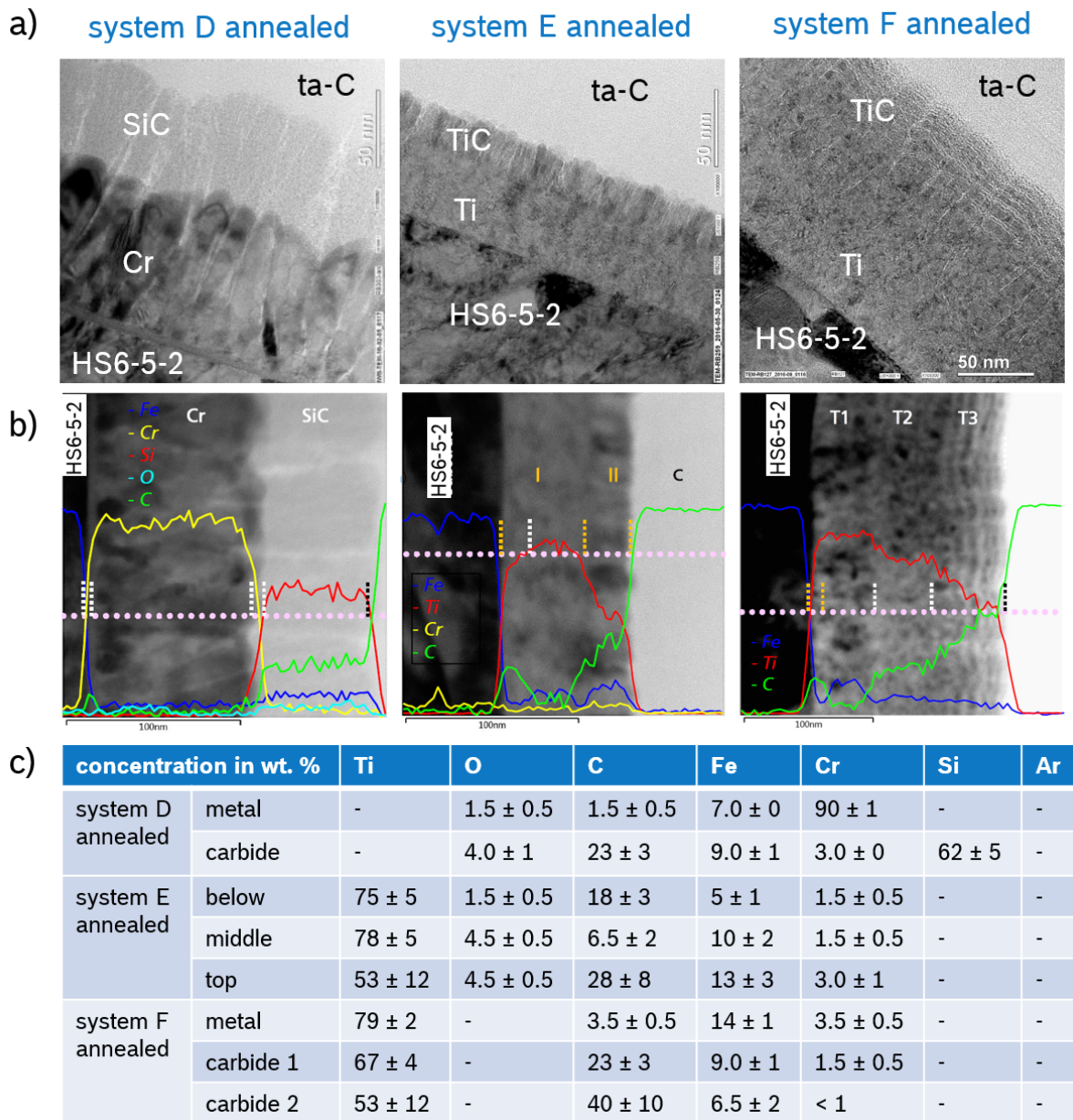


Figure 4.22: TEM-analysis of the interface region of coating systems with extended carbide interlayers D, E and F in the annealed state: a) Bright-field image, b) EDX-line scan and c) table with quantitative EDX data for each phase.

Analogous to the as-deposited state, EDX and TED-data are used to estimate a possible set-up of the adhesion layer systems, which is schematically shown in figure 4.23.

In the as deposited state, for system D in the metal base layer, a solid solution with 10% Fe in the bcc Cr phase was presumed. At the annealing temperature of 350 °C, roughly 3% Fe are soluble into Cr [129]. So a segregation is expected, resulting in precipitation of Fe-rich phases with a very small amount of Cr solved. With respect to a slow cooling after

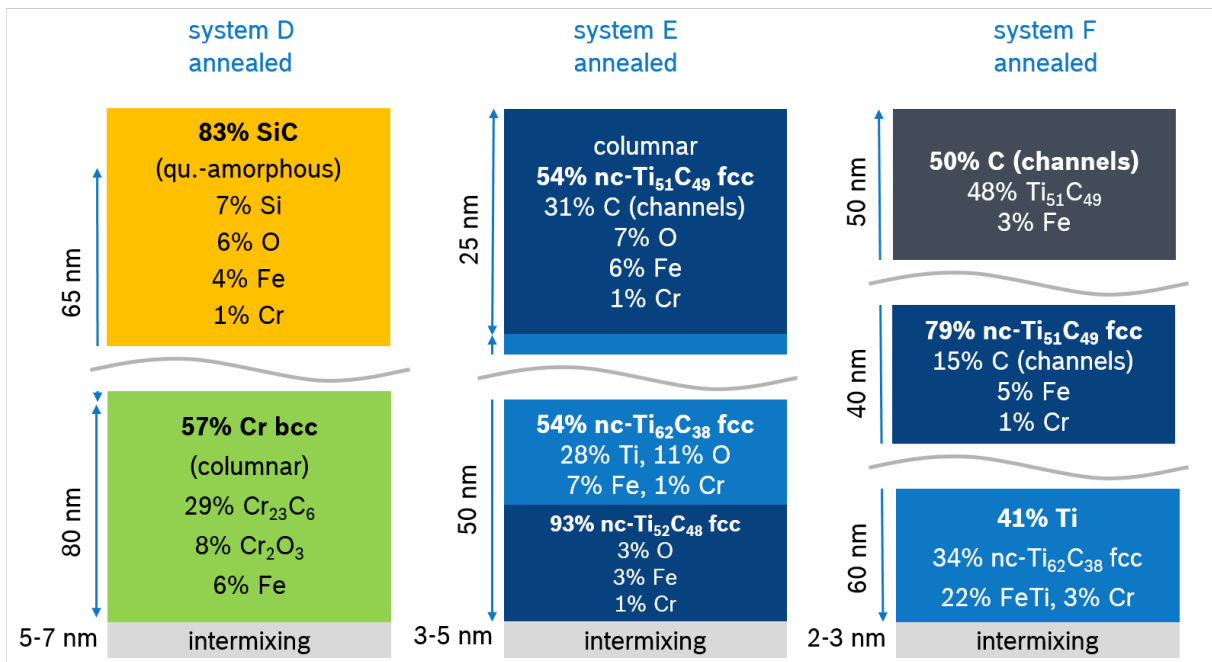


Figure 4.23: Estimated structure and phase compositions of the transition regions for the coating systems with carbide interlayer and ta-C based functional layer in the annealed state, based on bright-field TEM, EDX, TED and binary phase diagrams [125, 126, 127, 128, 129, 131, 132, 133].

the annealing to room temperature, where almost no Fe is soluble into Cr, a complete segregation is expected. The C- and O-contaminants are expected to form carbides and oxides with Cr, which is more abundant than Fe and has the stronger affinity to react with these species. These carbides and oxides might form inclusions or form at the grain boundaries of the columnar grains.

Regarding the adhesion tests after annealing, it can be stated, that the segregation has no influence on the adhesion performance, presumably because the SiC interlayer, which is sufficiently thick, hinders a precipitation of Fe at the interface towards the functional layer, which would destabilize the adhesion performance.

For system E, a significant carbide formation in the vicinity of the interface towards the steel substrate must be occurred. The upper end of the adhesion layer system was already formed in the carbide state by the deposition process. For systems E and F, Fe-precipitation is again most pronounced in the center of the former Ti phase, similar to system C.

For system E, Fe-precipitation is also allocated in the carbide phase. For system F, the diffusion of C in the carbide phases, followed by a thinning of the graphitic phases, can

serve as explanation for the increased adhesion performance observed in the scratch tests. A higher stress field, as it is introduced by the HRC tests, is necessary to force crack propagation parallel to the substrate surface, leading to areal delamination.

a-C:H-based Systems

Figure 4.24 a) shows a TEM-bright-field image of the interface region of system G after long time thermal annealing. An EDX line scan and quantitative results are presented in figure 4.24 b) and c). Compared to the as-deposited state, a recrystallization in the Cr_7C_3 phase is observed in form of dark structures, which can be attributed to an interference pattern. The Cr_3C_2 phase on top, as well as the coral-like structure do not show obvious differences in their appearance in the TEM-image, compared to the as-deposited state.

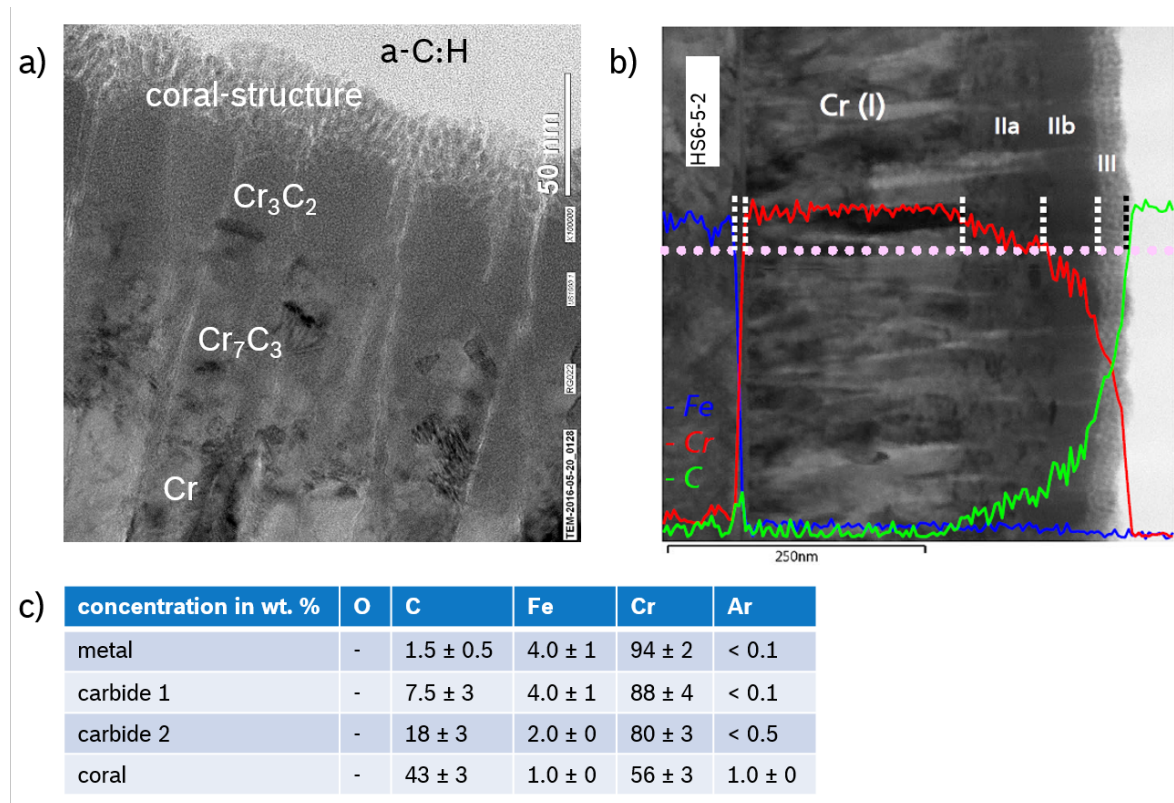


Figure 4.24: a) TEM bright-field image of the interface region of system G in the annealed state, b) EDX line scan and c) table with EDX data for each phase.

Figure 4.25 a) and b) show TED-results for the Cr_7C_3 region and for the Cr base layer respectively. Both indicate a Cr bcc structure. The former signal is attributed to

nanocrystals, the latter to larger crystals. Bright-field image, EDX and TED-data are used to estimate a possible set-up of the adhesion layer system, which is schematically shown in figure 4.25 c).

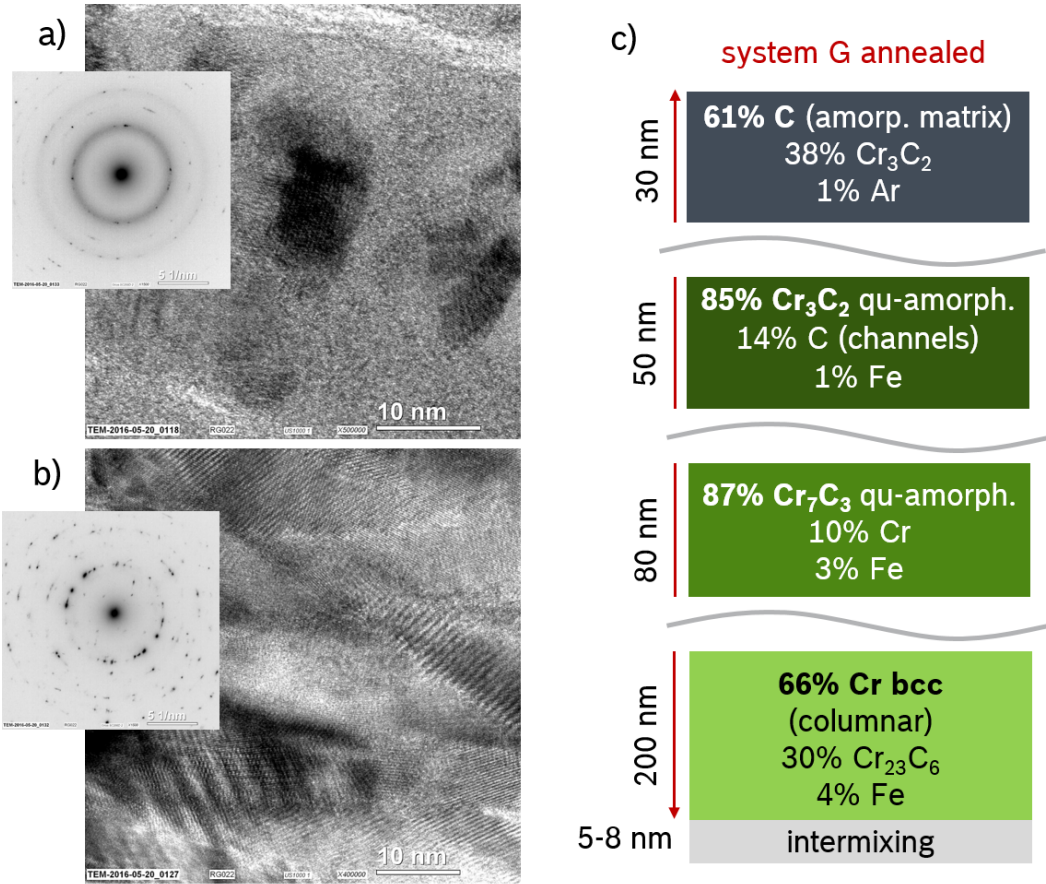


Figure 4.25: TED images of a) the Cr_7C_3 phase and b) the Cr base layer. c) the estimated structure and phase compositions, based on bright-field TEM, EDX, TED and binary phase diagrams [128, 129, 133].

The Cr base layer of system G is very similar to the one of system D, also with an expected complete segregation of the Fe-containing Cr bcc phase and also with the formation of Cr-rich carbides. In the adjacent quasi amorphous Cr_7C_3 phase above, the formation of Cr nano-crystals indicate that a metastable phase had been present. This might be a not stoichiometric Cr_7C_3 with excess of Cr, which is reordered during annealing. Alternatively this might be a reordering initiated by the segregation of the Fe-containing carbide layer or of the underlying Fe-containing metal layer.

In the coral structure, the phase composition gives no reason for a segregation within this phase. By this, the thermally stable adhesion performance might be explained. Further-

more, the retarded delamination found around the HRC-imprints can be explained by Fe-precipitation phases with a barrier layer on top: The coral structure provides the mechanical strength during the HRC-testing. Afterwards however, Fe-rich phases might be uncovered in the vicinity of the residual imprint, where additionally a stress field residues from the indentation. The low stability in conjunction with the stress field and a possible medium access enable a corrosion driven delamination, which is addressed in chapter 7.

Chapter 5

In-Plane Stress Field Analysis

In this chapter, buckling driven delamination around a large scale indentation, initiated by a nanoscratch is discussed as an advanced method for evaluating the adhesion performance of compressively stressed thin films. In the following, the method is called the *stress field nanoscratch*. The ta-C based systems A to F are used as benchmark samples in the as-deposited as well as in the annealed state, providing variations in atomic composition and structure of the interface regions and also variations of the functional layers (ta-C1 and ta-C2). Rockwell C test, as well as single nanoscratch test with increasing load, discussed in the previous chapter, serve as reference tests.

After comparison of the test results, the simulated stress fields derived by FEM simulation are discussed, supplemented with further investigations of the region around the indentation imprints, in order to assess the results of the HRC and the SFNS even further and to derive a generic model for a reliable assessment of the adhesion performance (section 5.2, f). Furthermore, a model based on Hutchinson stress analysis of the provoked buckling driven delamination is derived to quantify the critical strain energy release rate G_c (section 5.4) as a physical measure related to the adhesion performance.

5.1 Adhesion Performance Evaluation

The SFNS is a two stepped process. After the sole Vickers indentation, no delamination or buckling was observed for samples A to F and only very short radial cracks at the

corners of the imprint were observed with no radial cracks at the edges. Delamination is initiated by the nanoscratch in the second step.

5.1.1 Definition of Terminology

In order to facilitate the description of the results, some definitions will be made in advance, based on following facts: 1. Intrinsic in-plane compressive stress prevails within the coatings. 2. Additionally, a residual compressive stress field prevails within the coating around the residual imprint of the indentation[87]. 3. Delamination in compressively stressed thin films always occurs via buckling [4].

Therefore, delamination observed in the SFNS must always occur via buckling. The buckles, which correspond to delaminations, located directly at the scratch track, i.e. delaminations, initiated by the additional high local compressive stress of the nanoscratch, will be called *primary buckles* in the following. Those were already observed at the L_{c3} -points in figure 4.14 of chapter 4.2.

Delaminations remote from the scratch tracks are independent from the stress field of the scratch track. So delaminations, which progress away from the initiation spots are buckling driven and this process will be called *secondary buckling* in the following.

5.1.2 As-Deposited State

Figure 5.1 shows microscopic images of the SFNS-results for the coating systems A to F in the as-deposited state. After the nanoscratch through the residual stress field of the Vickers imprint, buckling driven delamination occurs with different characteristics for the different coating systems. Thereby, the secondary buckling starts at primary buckles along the scratch tracks and tends to progress on concentric annular paths around the residual indentation imprint.

Except for system D, all coating systems show secondary buckling, which is increasingly pronounced from coating system A to E, C and B, whereby for coating system B, the extensive secondary buckling was already initiated by a single nanoscratch. For coating

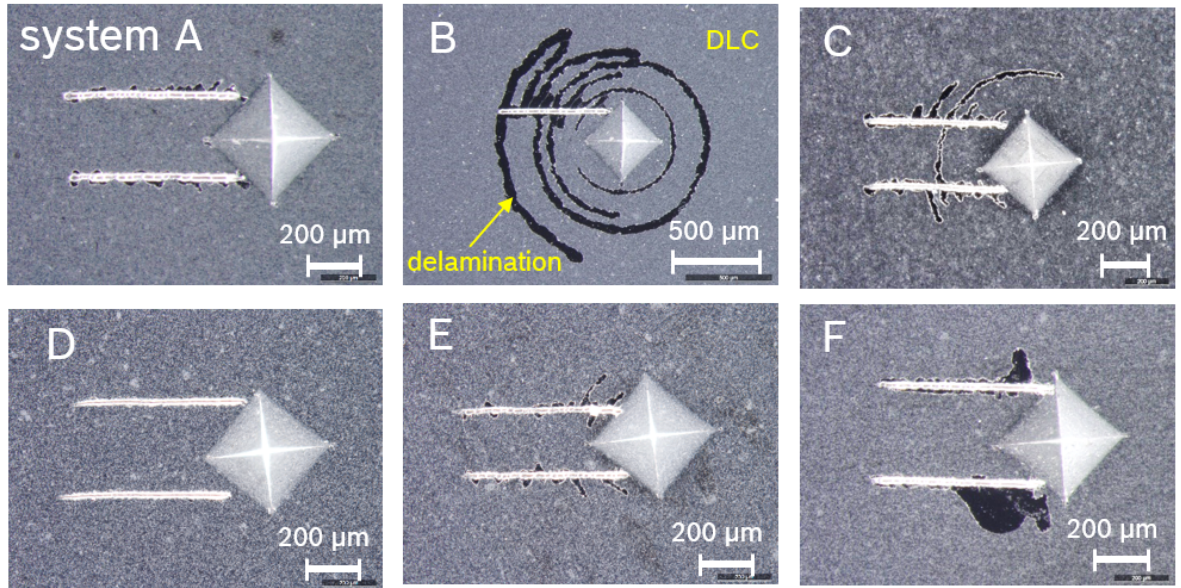


Figure 5.1: SFNS-results for coating systems A to F in the as-deposited state. No buckling was observed right after the Vickers indentations. Only during the subsequent scratch tests through the stress field, buckling is generated with increasing amount of secondary buckling for coating systems A to E, C and B. System D shows not even primary buckling, while system F exhibits larger buckle radii.

system D, not even primary buckling was observed, confirming the good results from the previous adhesion assessments via HRC and nanoscratch tests. System F on the other hand shows an altered behavior with less defined secondary buckling, but primary buckling with much larger radius.

In table 5.1, quantitative results of the SFNS are summarized, including the total area of delaminated coating, the maximum radial distance of the secondary buckling from the center of the imprint and the maximum annular path length of the secondary buckling. Corresponding results from the Rockwell C and nanoscratch tests are included for comparison.

Secondary buckling is exclusively driven by residual stress in the coating and is hence an indicator for the delamination affinity. By the introduction of the compressive stress field, the delamination affinity is locally increased, gradually increasing with decreasing distance to the residual imprint. In the SFNS, this increase is used to detect differences in the initial delamination affinity of different coating systems. Increasing delamination affinity was found for the coating systems in the order D, A, E, C and B, consistently by all three evaluated measures (r_{max} , l_{max} and A_D).

Coating system F is listed separately in table 5.1 because of its significantly different

Table 5.1: Mechanical testing of the adhesion performance of coating systems A to F with HRC, nanoscratch and SFNS test, sorted by the results from the SFNS with an extra category for system F, which shows a different delamination behavior.

coating system	HRC	nanoscratch		SFNS		
	HF	L_{c3}/N	$A_D/\mu\text{m}^2$	$r_{max}/\mu\text{m}$	$l_{max}/\mu\text{m}$	$A_D/\mu\text{m}^2$
D	2	1200	65	0	0	0
A	2	1000	2600	460	64	4600
E	2	1250	570	520	160	6400
C	2	900	2200	550	570	21000
B	2	1150	8300	710	3100	310000
F	6	1050	1300	420	210	37000

behavior. The primary buckles, initiated at the scratch track in the vicinity to the indentation imprint, grow much larger. Secondary buckling is initiated, but with a very low path distance. So the ability to grow larger buckles is not related to an increased delamination affinity. The altered behavior of system F can be attributed to the graphite sheets within the interlayer system, found in the TEM images, which already have been identified as possible origin of the concentric delamination resulting in the HF6 rating in the HRC test. Primary buckling is initiated via shear stress. It is likely that the graphite sheets are able to slip under the shear load, which enables primary buckling. In the other coating systems, buckle growth is stopped via spallation of the coating at the critical radius. Maybe this is prevented by the graphite sheets as well. In order to describe this altered behavior quantitatively in terms of SFNS test results, the ratio A_D/l_{max} can be used as an indicator.

With the findings of the SFNS for system F, the HF6 in the HRC test can be interpreted as primary buckling, where spallation is less likely to occur. The delamination around the imprint can grow via (primary) buckle growth within the residual stress field. Introduction and progression of delamination around an HRC indentation however embraces a complex interaction of different mechanisms. So this will be discussed in more detail in section 5.2. Furthermore, the delaminated area is not an independent measure for the delamination affinity and is disregarded here to avoid confusion. From the HRC results it can be concluded, that the test is not able to detect the apparently different delamination affinities of coating systems A to E, which are all rated HF2.

Also the results of the nanoscratch test are much less explicit for systems A to F compared

to the SFNS. The A_D yields significantly lower values for systems D and E compared to A and C, and a significantly higher value for system B. The value for system F is in between D/E and A/C. It can be concluded that A_D in the nanoscratch also correlates to the delamination affinity.

All the results, even though superficially contradicting, evidence that for system F, a high shear stress is necessary for primary buckling. Some property of the coating system ensures that spallation occurs with larger radius. In contrast, for systems A to C (Ti-adhesion layer) and E (TiC interlayer) the high shear stress of the HRC test is not able to form larger buckles. However at the L_{c3} -point in the scratch test, delamination via primary buckling is observed, where high stress concentrations at the interface prevail. When additional stress is provided by the residual stress field of the Vickers imprint, this leads to secondary buckling for these systems instead of growth of the primary buckles, as observed for system F.

It can be concluded, that the adhesion performance of systems A to F cannot be evaluated by a single scale. Systems B and F exhibit weak adhesion performances, which are only observable under different boundary conditions. This confirms the underlying hypothesis of the whole work, i.e. the generally accepted *adhesion* must not be used for the evaluation if a coating might delaminate in a certain application or not.

5.1.3 Annealed State

Figure 5.2 shows the SFNS-test results after long time thermal annealing for coating systems A, C, D, E and F, while the samples of system B were already completely delaminated after the heat treatment. Quantitative results corresponding to the adhesion performance are summarized in table 5.2.

For systems D and E, not even primary buckling is observed, which means no change in adhesion performance for system D and an increased performance for system E after thermal treatment. This was also observed in the nanoscratch test after annealing and indicates an increased resistance against primary buckling, which could be related to the carbide formation close to the substrate surface.

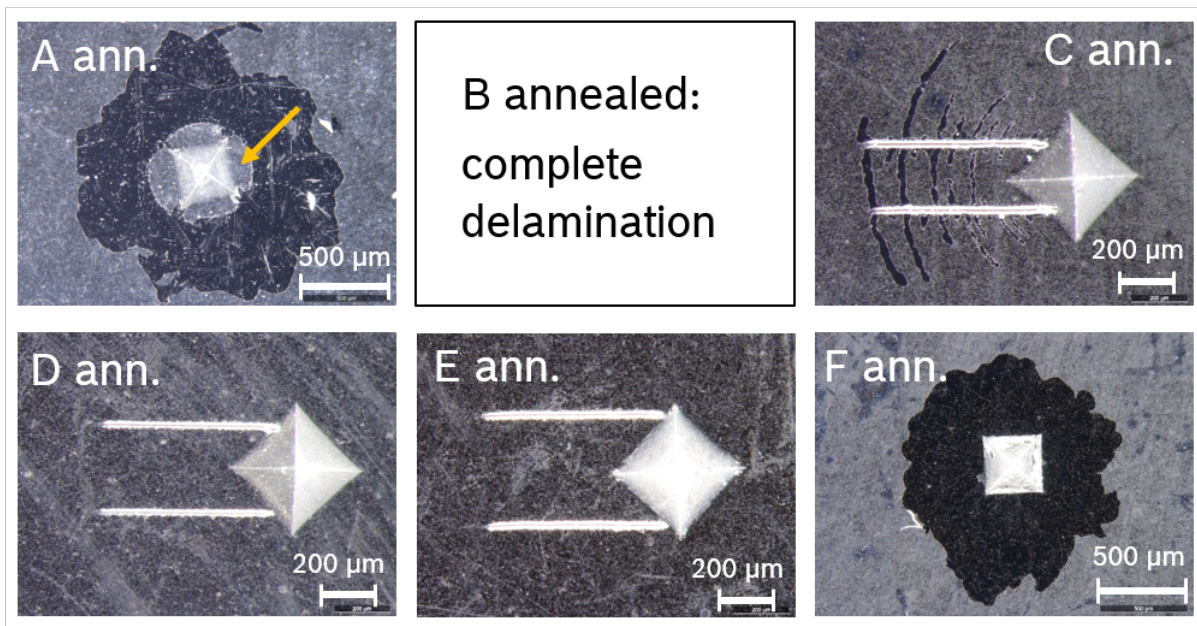


Figure 5.2: SFNS-results after thermal annealing. Systems A and F show large area delamination caused by the sole Vickers indentation. Thereby, for system A, the coating adheres in a circular area close to the imprint (yellow arrow), while it fully delaminates for system F. No buckling was observed right after the Vickers indentation for coating systems C to E. For coating system C, primary and secondary buckling was generated during the subsequent scratch tests through the residual stress field. Coating systems D and E show no buckling in the SFNS.

Contrary for coating systems A and F, the Vickers indentation leads to concentric large area delamination around the residual imprint similar to the observations of the HRC tests for both systems. This was not the case in the as-deposited state, so the thermal aging causes a reduction in adhesion performance for both systems. This might be via Fe-precipitation from a metastable solid solution of Fe in Ti, which was discussed in chapter 4 as a possible mechanism for the reduction of the adhesion performance by thermal aging.

An important subtlety is found in the concentric area close to the indentation imprint. For system A, the coating stays in this zone. For system F however, the coating is fully delaminated. A reproduction of the experiment yield reproducible results. So the occurrences are systematically.

The delamination for system F is again attributed to the horizontal graphite channels, where the shear stress of the indentation initiates crack formation and promotes crack propagation. Together with the results from the nanoscratch test, it can be stated, that the effect of the thermal aging is less pronounced for system F compared to the systems

with Ti adhesion layer, without carbide layer. For system F however, the as-deposited adhesion performance is already weak.

For system C, slightly more buckling is observed for the annealed state with an increased r_{max} (refer to table 5.2), which is now comparable to system B in the as deposited state. Also A_D is increased, but the l_{max} is decreased. With regard to the delamination events during TEM-sample preparation (refer to figure 4.20), it is likely that the thermal aging also occurred for system C, but the corresponding effect on the adhesion performance is less pronounced, compared to systems A and B. A possible reason for the different pronouncement might be slight differences in thickness or density of the thin carbide layer at the upper end of the Ti-layer. Slight local differences within a sample are also possible.

Table 5.2: Qualitative evaluation of the adhesion performance of coating systems A to F in the annealed state with HRC, nanoscratch and SFNS test, analogous to the as-deposited state. Sorted according the SFNS test result after annealing.

coating system	HRC	nanoscratch		SFNS		
	HF	L_{c3} / N	$A_D / \mu\text{m}^2$	$r_{max} / \mu\text{m}$	$l_{max} / \mu\text{m}$	$A_D / \mu\text{m}^2$
D annealed	2	650	83	0	0	0
E annealed	3	550	110	0	0	0
C annealed	3	500	2100	820	430	35000
F annealed	6	450	650	delamination after Vickers		
A annealed	6	850	56000	delamination after Vickers		
B annealed		delamination after thermal annealing				

5.2 Induced Anisotropic Stress Fields

Motivated by the different occurrences of delamination events, the introduced residual stress fields of the Vickers and Rockwell high load indentation are analyzed.

5.2.1 Stress Field Evaluation

A schematic set-up of an indentation experiment in a coating-substrate-system with a conical indenter is shown in figure 5.3 a), the coordinate system is indicated. After high load indentation with the diamond tip, a residual imprint is formed in the elastic-plastic

steel substrate, whereas the thin film follows the substrate surface and does not strongly influence the deformation process and the shape of the residual imprint [87].

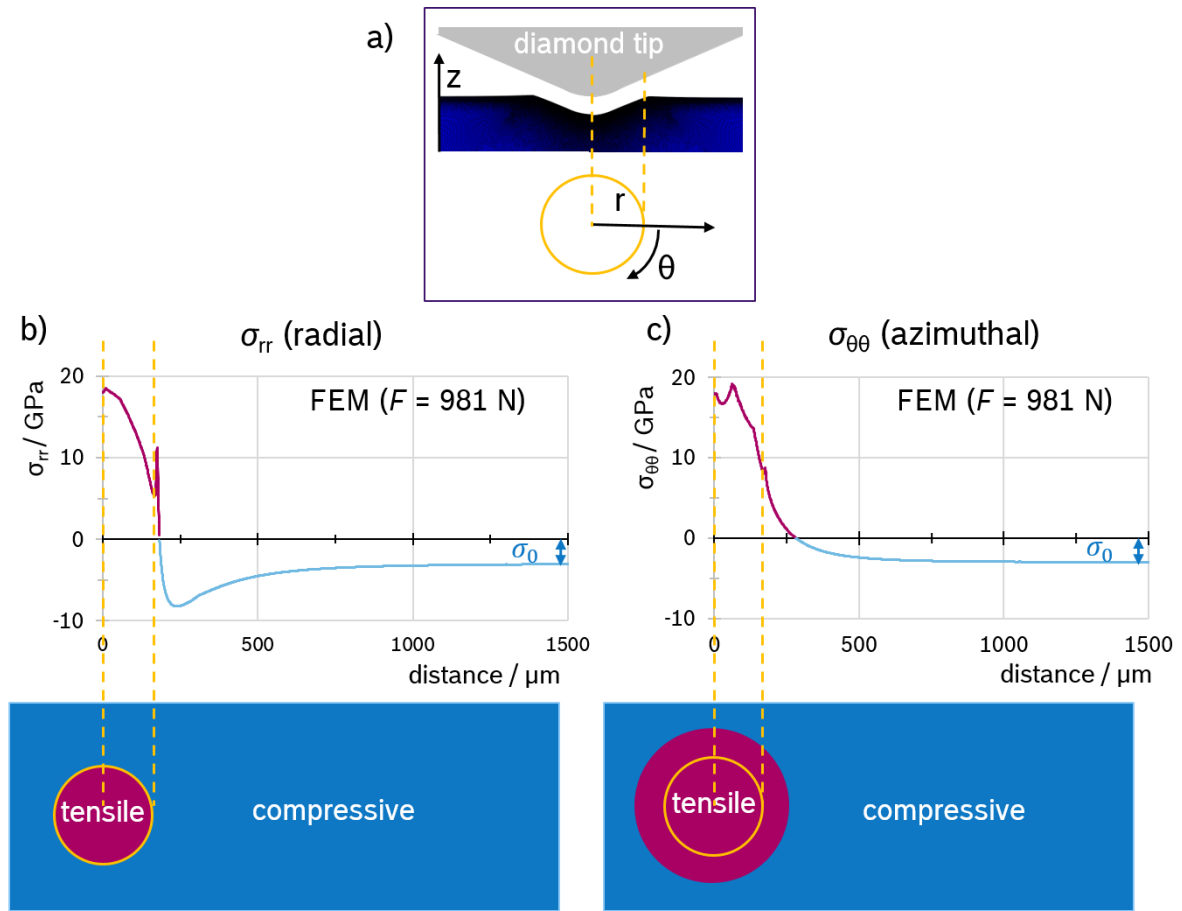


Figure 5.3: FEM simulation results of an indentation with a Vickers equivalent cone: a) Definition of coordinates, b) and c) in-plane residual stress components along the radial direction. The resulting planar distributions are schematically represented below the graphs. σ_{rr} : Tensile inside the residual imprint, compressive outside with a maximum close to the annular edge (yellow circle). $\sigma_{\theta\theta}$: Tensile region extends beyond the edge, compressive region remote from the indentation is caused by residual stress σ_0 .

Figure 5.3 b) and c) show the radial evolution of the radial σ_{rr} and azimuthal $\sigma_{\theta\theta}$ components of the in-plane residual stress within the thin film after the indentation, estimated with the FEM simulation. Inside the residual imprint, which is indicated by the yellow circle in the schematic drawing, both components are tensile. With respect to the large difference in scale between indentation depth and film thickness, inside the residual imprint, the thin film does not behave like a bending beam with tensile and compressive regions, but rather like a planar surface, which gets stretched into a hyper-surface in three dimensions. So the result is completely reasonable.

Outside the residual imprint, σ_{rr} is compressive with a maximum close to the annular edge of the imprint and slowly decreasing with increasing radial distance, approaching the initial stress level remote to the indentation, which is determined by the intrinsic residual stress σ_0 .

In azimuthal direction, the introduced stress is tensile only. $\sigma_{\theta\theta}$ exhibits a pronounced maximum at the indentation center, fast decreasing with increasing distance. Only due to σ_0 , a compressive azimuthal region exists. However, this region starts more remote from the imprint compared to the compressive region of the radial component, which has decisive consequences for potential damage progressions, as will be discussed in the following.

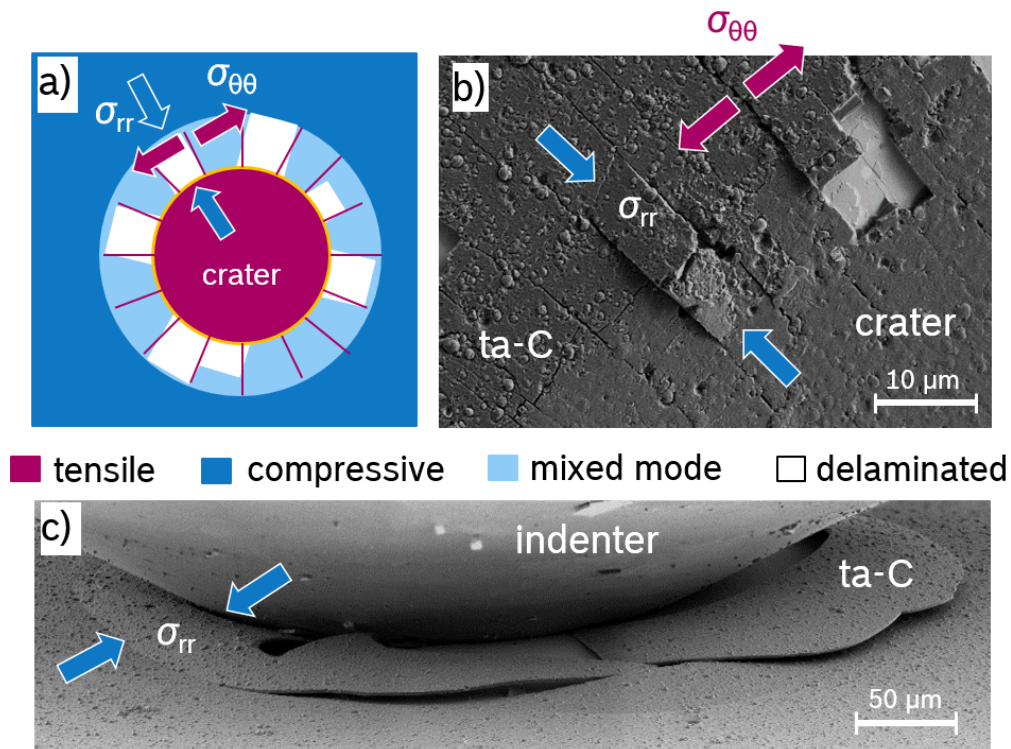


Figure 5.4: Stress states after conical indentation and corresponding coating failure modes: a) Schematic stress distribution in the thin film, with three characteristic zones. *Imprint crater*: Tensile stress only, *mixed zone*: Azimuthal tensile stress and radial compressive stress, *outer zone*: Compressive stress only. b) SEM-image of the mixed zone (system E) with annular coating segmentation by radial cracks and radial, beam-like buckling of some segments. c) In-situ HRC (system F, load step 400 N) with large radial, annular buckling in the mixed zone and no radial cracks.

The anisotropic, biaxial stress around the residual imprint can be derived by superposition of radial and azimuthal stresses. Figure 5.4 a) shows a schematic representation of the arising stress distribution in the coating. Three different zones can be defined in

order to identify potential failure modes.

In the first zone, inside the residual *imprint crater*, only tensile stresses prevail. Thus, buckling driven delamination is not possible, instead annular segmentation of the coating by radial cracks and radial segmentation by annular cracks are enabled. Outside the imprint crater, the residual stress field has a mixed stress state with a largely tensile $\sigma_{\theta\theta}$ and a compressive σ_{rr} , enabling annular segmentation and radial buckling. This zone will be called *mixed zone* in the following. The remote stress field is compressive only, enabling buckling in both directions. However, buckling in radial direction is preferred caused by the larger compressive stress. This will be referred to as the *outer zone*.

5.2.2 Damage Evolution

In section 5.1 it was concluded, that different properties can predominantly account for the adhesion performance. In system F, the low adhesion performance was attributed to the low shear resistance of the graphite layers, whereas for system B, the low adhesion performance was attributed to a high affinity for delamination via secondary buckling. It is hence indispensable to know for each adhesion performance test, which property is actually tested and which is possibly ignored.

Mixed Zone

In figure 5.4 b) and c), SEM images of indentation tests for coating systems E and F are presented, for which different paths of failure progression were observed. In b) (coating system E, ex-situ HRC), radial cracks in the mixed zone lead to annular segmentation followed by radial buckling of the formed coating segments, while in c) (system F, in-situ HRC) buckling in radial direction occurs in the mixed zone, forming an annular ring of delaminated coating.

For a testing of the delamination affinity of compressively stressed thin films, buckling must be provoked. So it is important to know exactly how the buckling is introduced in the scenario of system F. Buckle formation requires compressive stress and a sufficiently

large pre-crack [4]. In the mixed and in the outer zone, sufficient compressive stress is available to form a radial buckle. Inside the imprint crater this is not possible, thus buckling is initiated outside the crater.

A pre-crack however can form only via tensile or shear stress. The model of the three stress zones yields, that as long as the coating is attached to the substrate, tensile cracking outside the imprint crater is possible only via radial cracks. However, there is no driving force to deflect by 90° , which would be necessary for a crack advance along the substrate surface.

Therefore, shear stresses in the mixed zone must introduce the buckling for system F. By the indentation, the strain is introduced into the substrate and the coating equally. So shear stress results from a gradient within the stress field. This is exclusively given in radial direction for an indentation with radial symmetry. Hence, cracks parallel to the substrate surface can only be initiated in radial direction.

Once large scale buckling occurs, strain energy is relaxed and the annular segmentation, as found for system E, is prevented. Contrary, once the segmentation occurs, energy is dissipated and the radial cracks would interrupt a potential large scale buckling event. So there is a threshold for the shear strength of the adhesion layer system, which defines if annular buckling occurs in the mixed zone or radial cracking. The annular buckling, as observed for system F is therefore a clear indicator for a susceptibility to shear stress. This confirms the hypothesis, that the graphite planes aligned parallel to the surface are causing the HF6 result in the HRC, because they have a very low shear strength.

Outer Zone

In the outer zone, the azimuthal tensile stress vanishes and the situation changes. Figure 5.5 a) and b) show sections of the HRC imprints of coating systems F in the as-deposited and system A in the annealed state, both with concentric delamination (HF6). For system F, also inside the imprint crater, the coating is at least partly delaminated and in the mixed zone, no radial cracks were observed. In contrast, for system A-annealed, the coating remains attached to the substrate inside of the imprint, crater and radial cracks

in the mixed zone are observed. The coating in the mixed zone is however delaminated and also the coating in the outer zone. At the transition of these zones, also the Ti layer is delaminated, indicating an altered stress state.

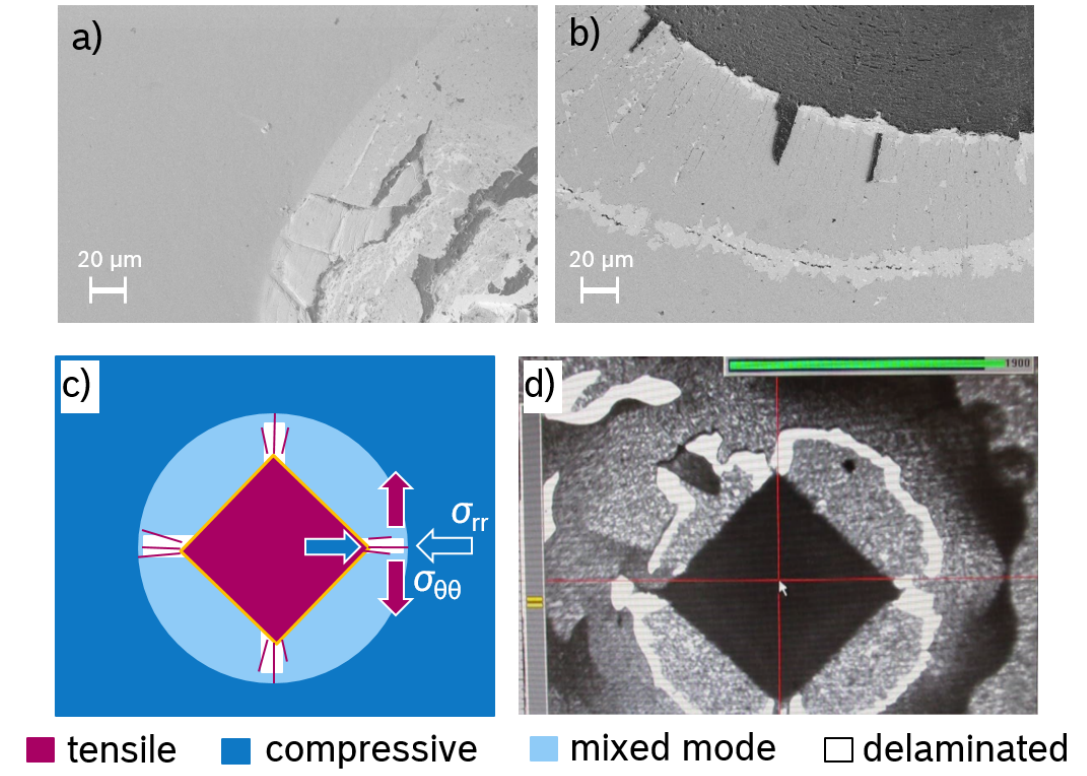


Figure 5.5: Large concentric buckling: a) HRC without radial cracks (system F), b) HRC with radial cracks (system A-annealed), c) schematic representation of the three stress zones for the Vickers geometry, radial cracks and buckling of annular segments are indicated and d) buckling evolution around a Vickers imprint (System A-annealed): A first concentric narrow buckle track has formed and spalled. Additionally secondary wave-like buckling occurs all around the narrow buckle and spreads. The coating remains adherent in the mixed zone.

The radial cracks must be formed in the DLC coating and were extended into the substrate surface, otherwise they would be observed in system F as well. After corresponding annular segmentation of the coating, the shear stress in the mixed zone might be able to buckle some of the narrow segments, e.g. enabled via local defects, and the delamination reaches the outer zone. Caused by the high delamination affinity and an increased compressive stress in radial and a compressive stress in azimuthal direction, the delamination spreads via secondary buckling. The process becomes more clear by looking at the Vickers indentation.

Figure 5.5 c) shows a schematic drawing of the stress field regions for the Vickers geometry and in d) the corresponding large scale buckling failure mode on hand on system A in the annealed state. Latter image is taken from a video, where the buckling evolution is captured.

Within the mixed zone, the annular segmentation by radial cracking is this time confined to the corners of the pyramidal imprint. Consequently, radial buckling of annular segments is localized at the corners too. A narrow concentric delaminated track is formed by secondary buckling, which is followed by further buckling driven delamination around this track resembling secondary waves. The wave-like buckling merges into an annular coating ring. The coating in the mixed zone at the edges is not affected and remains attached to the substrate.

It can be summarized, that two failure modes were found for the high load indentation with Rockwell or Vickers indenters. If the coating system exhibits a plane with low shear strength, the shear stress of the indentation initiates concentric buckling driven delamination around the indentation. If this is not the case, radial cracking occurs, initiated by the annular tensile stress. The resulting annular segments might be delaminated via the shear stress of the indentation. This depends however on the exact properties of the segments. If the coating system has a high delamination affinity, secondary buckling can be initiated by delaminated segments, leading to concentric delamination as well.

Because delamination is initiated by shear stress and delamination progresses in a mixed mode of tensile and shear stress, resulting from the buckling geometry, these processes might occur at different planes within the coating system. Some indications were found that the plane is switched during damage progression. E.g for system A in the annealed state, uncovered substrate is found with SEM- and EDX-analysis at the transition between the mixed and the outer zone, where the failure mode is changed. In the outer zone delamination is observed above of the Ti again. In system E, below the local buckling of some annular segments, adhesion layer is partly missing (compare to fig. 5.4b)).

5.3 Stress Fields in the SFNS

As demonstrated, the path of failure progression around an indentation is decided in the mixed-zone and is thereby determined by several coating properties. Annular segmentation occurs when the azimuthal stress first exceeds the mode I fracture strength of the coating with a defined crack density analogous to tensile tests of thin films [134], while for the activation of radial buckling, the introduced shear stress must exceed the mode II fracture strength of the interface region first. This leaves only a small window of potential fracture strength of the interface region where this failure mode is enabled, with a second chance when the azimuthal tensile stress drops below the fracture strength of the coating, as observed for system A in the annealed state. Due to the self-similarity, a further increase of the normal load changes little, as also the tensile stress increases.

The SFNS bypasses this issue by provoking buckling in a second step within the stress field of the indentation, preferably at the crack free edges of the Vickers imprint. In figure 5.6, SEM images of the SFNS results of coating systems C and B are presented for further discussion. Within the tracks of the secondary buckling the Ti adhesion layers are uncovered by spallation of the buckles. The concentric paths around single indentations exhibit an increasing width with increasing radial distance from the indentation center. If the nanoscratching is performed through the residual stress field of a pattern of residual imprints, the secondary buckling paths correspond to equipotential stress lines (compare to fig. 5.6 a)).

Figure 5.6 b) shows a detailed SEM image of the secondary buckling on system C. The contour of the secondary buckling fit to a succession of circles with similar radius. This evidences that the suggested mechanism is true, i.e. that the buckling driven delamination occurs by a succession of single circular buckles, which grow, spall and initiate the next buckle. Furthermore, this supports the model that the secondary buckling can be initiated via primary buckling at the nanoscratch.

Figure 5.6 c) shows a scratch track of the SFNS performed on system B. Plastic deformation of the substrate is confined to the scratch track. Close to this, the Ti-layer is delaminated at tiny spots, which is evidence for the high local shear stress, which initiated the primary buckling.

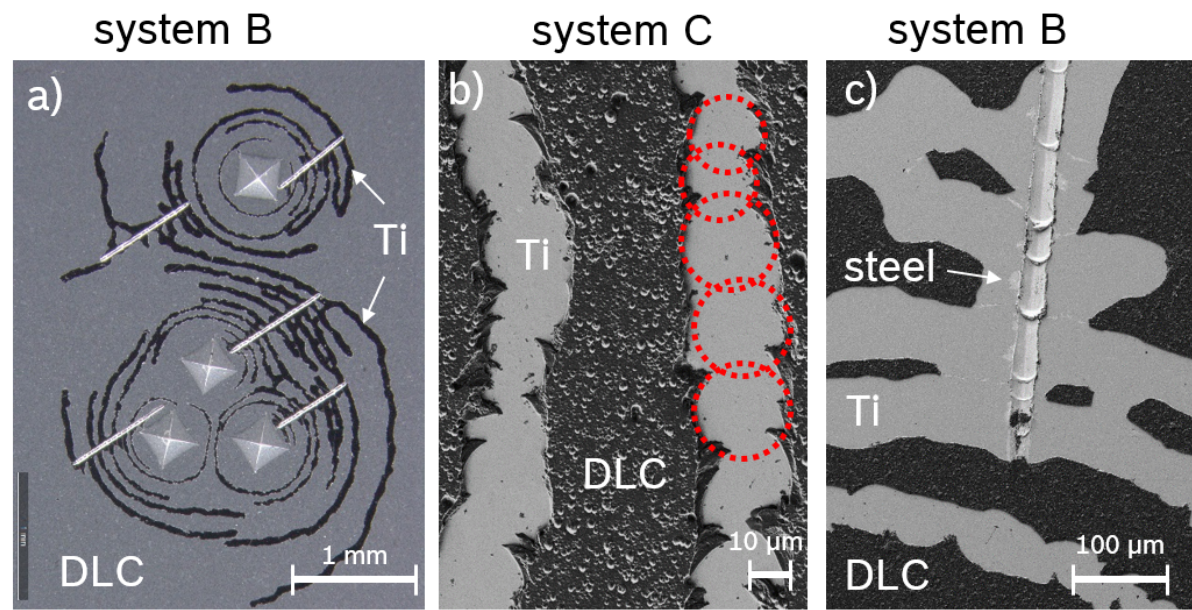


Figure 5.6: Buckling in the remote field of Vickers indentations activated by nanoscratch tests: a) With pattern of Vickers indentations, the equipotential stress lines become visible via buckling. b) The paths of buckling driven delamination exhibit circular contours, indicating secondary buckling. c) Plastic deformation concentrated at the scratch track only.

In contrast to a single scratch test with no long range stress field, the stress field of the high load indentation promotes secondary buckling on annular paths arising from the primary buckles along the scratch track. The high radial compressive stress of the indentation leads to spallation of the coating with a defined radius b_{spall} , which determines the width of the secondary buckling track. The azimuthal component of the residual stress field is significantly smaller, so that the succeeding buckle is initiated by the radial component. This is only possible next to the previous buckle on an annular line.

The contour of the secondary buckling path in system B is more straight compared to system C. This indicates, that the critical strain energy release rate for driving the buckle growth is smaller in system B and spallation occurs simultaneously or even after crack advance. The secondary buckling can therefore be treated as a straight-sided blister for the quantification of G_c .

5.4 Quantification of Strain Energy Release Rate

Buckle growth is stopped via spallation in radial direction, so the adhesion energy in terms of G_c has to be derived in annular direction where the secondary buckling progresses. This corresponds to $G_{c,\parallel}$ of a straight-sided blister.

For a quantification of $G_{c,\parallel}$, the stress state at the locations where delamination occurs is to derive, i.e. the anisotropic biaxial in-plane stress. Furthermore, the buckle geometry which defines the relaxed stress σ_c and the stress mode at the interface is to derive. Quantification is done for coating system B, which exhibits a high amount of secondary buckling. For each secondary buckling path, the radial distance to the indentation center is measured, as well as the path widths of the buckles (compare to fig. 5.7). The radial distance is a measure for the residual in-plane stress, the path width yields the buckle geometry.

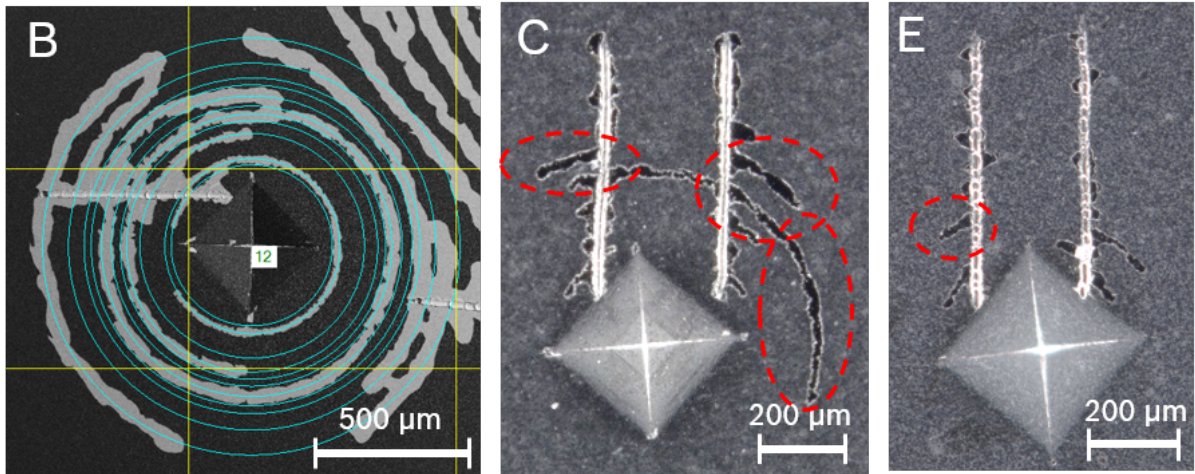


Figure 5.7: System B exhibits plenty of blister paths with a wide range of radial distances. For systems E and C blister paths for quantification are found (red marks). Too close to the indentation, azimuthal tensile stresses would complicate the calculations. Buckles close to the scratch track are influenced by its short range stress field.

Via equation 2.10, σ_{rr} is derived with the path width used as b_{spall} . Figure 5.8 a) shows the resulting graph together with σ_{rr} based on the FEM simulation. Both are in good agreement above 500 μm distance to the indentation center. Below, the data differ significantly, where the σ_{rr} derived from the spallation exhibits much higher values as for the simulation.

Furthermore, $\sigma_{c,\perp}$ perpendicular to the propagation is derived analytically from the straight-

sided blister model (equ. 2.7) with the estimated path width as $2a$. $\sigma_{c,\perp}$ is the stress which is relaxed during buckling and shows an almost constant shift to the simulated σ_{rr} in the graph in figure 5.8.

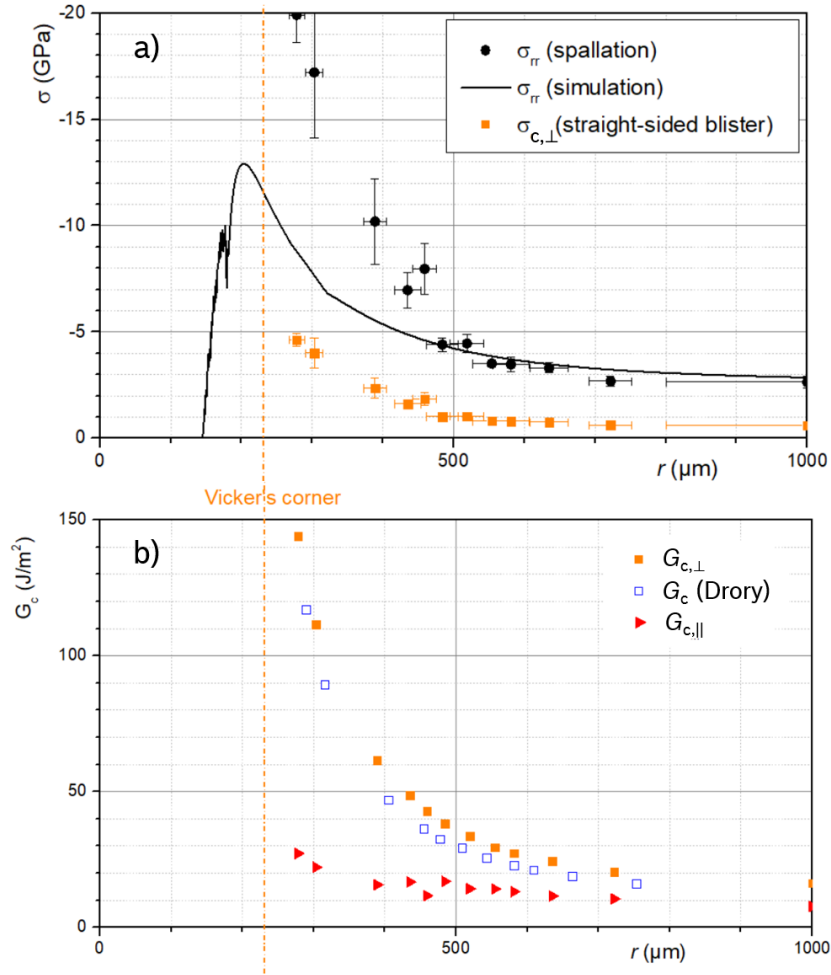


Figure 5.8: Quantification for system B: a) σ_{rr} derived via critical spallation radius and via FEM simulation. Close to the indentation σ_{rr} from spallation is overestimated due to anisotropy. $\sigma_{c,\perp}$ perpendicular to propagation direction of the straight-sided blisters (via equ. 2.7) shows an almost constant shift to the simulated σ_{rr} . b) Estimated $G_{c,\perp}$ perpendicular to blister propagation and via Drory model for comparison, yield a wide range of values, decreasing with increasing r . $G_{c,\parallel}$ however shows a fast saturation.

The large difference in the analytically derived and simulated σ_{rr} close to the indentation center can be due to several reasons. In the simulation the pyramidal indenter is substituted by a conical indenter. Close to the indentation center, the real geometry might be more relevant.

On the other hand, the assumptions for the analytical estimation become less valid close to the indentation center. The rather complex delamination propagation is supposed to

proceed as follows: A growing circular buckle spalls in radial direction and simultaneously initiate a secondary buckle in azimuthal direction. This represents a superposition of the two inherent stopping mechanisms of buckling and is provoked by the anisotropy of the Vickers stress field. With decreasing distance to the indentation center, the anisotropy increases in favor of the straight-sided blister shape. The critical spallation stress derived via equation 2.10 with the path width used as b_{spall} of a circular buckle is therefore overestimated. Farther away, the stress field is increasingly isotropic and the circular model becomes more accurate. Remote from the indentation, a saturation value of -2.65 GPa was derived from the spallation radius, which is in good agreement with the σ_0 from the curvature test of -2.73 GPa.

For further calculations, the simulated values for σ_{rr} are used. The energy release rates in radial direction $G_{c,\perp}$ and in azimuthal direction $G_{c,\parallel}$ are derived via equations 2.8 and 2.9 with the aforementioned $\sigma_{c,\perp}$. For a comparison, also the G_c from the Drory model is calculated (via equation 2.12), which accounts for σ_{rr} only, disregarding buckling and corresponding stress relaxation. Figure 5.8 b) shows all three results.

$G_{c,\perp}$ and G_c from the Drory model are much higher as they correspond to the strain energy, which is released in radial direction. The curves in the graph of both are very similar and strongly decreasing with increasing distance from the indentation center. This clearly shows, that both do not correspond to the adhesion energy, which is reasonable because the delamination progression in radial direction is stopped by spallation and not by a high fracture toughness.

In propagation direction, the steady state $G_{c,\parallel}$ is fast reaching a saturation with increasing radial distance to the indentation center. This saturation value is presumed to correspond to the state, where the adhesion energy is just exceeded. This means, that small inhomogeneities can stop the delamination progression. Closer to the indentation this is unlikely as $G_{c,\parallel}$ is higher, which agrees with the observations of 2π annular blisters. For the remote blisters which are stopped at some point, a $G_{c,\parallel}$ of 7.7 J/m^2 is derived. It can be presumed that this value corresponds to the adhesion energy of coating system B.

For the other coating systems, less buckling events are observed. $G_{c,\parallel}$ can be estimated however analogous at some positions (refer to figure 5.7). Their values are higher in ac-

cordance with the qualitative evaluations. In table 5.3, the results are summarized. For systems D and A no blisters are observed (only primary buckling for system A) and the quantification is not possible. Especially for system D, the shear stress provided by the nanoscratch in addition with the stress field of the large scale indentation was not sufficient for initiation of interfacial cracks which are large enough to enable buckling. In other words the mode II fracture strength of the interface region is too high. In an application, initiation of interfacial cracks would be likewise tough.

Table 5.3: Quantification of adhesion energy in terms of the critical strain energy release rate in propagation direction of the blisters, where the crack front just stabilizes

coating system	$G_{c, } / J/m^2$
B	7.7
C	11
E	15

By altering the coating thickness, the stress load can be further adjusted. With lower thickness and corresponding lower accumulated intrinsic stress, spallation might be prevented and stable buckling observed with the SFNS, giving the opportunity to estimate additionally the $G_{c,\perp}$ perpendicular to the propagation direction. With higher thickness and corresponding higher accumulated stress otherwise, buckling might be provoked for even higher adhesion strength.

5.5 Conclusions of the Stress Field Analysis

In this and the previous chapter it was shown that different phenomena can lead to a decreased adhesion performance in indentation based tests. The experimental findings can be summarized into two important initiation steps: Primary buckling initiation and secondary buckling initiation. If the shear strength of the interface system is weak in horizontal direction, as it was observed for system F, primary buckling initiation is very easy and can lead to areal delamination in a residual stress field.

If the shear strength in horizontal direction is higher, primary buckling requires higher shear stress and areal delamination is usually prevented by through thickness crack for-

mation. If the delamination affinity is high, secondary buckling can be initiated in some cases, leading to areal delamination as well. For the coating systems with Ti adhesion layer it was shown that a thermal treatment lead to precipitation of Fe-rich phases, which resulted in a successively increasing delamination affinity.

However, for an estimation of the delamination affinity secondary buckling must be sufficiently provoked. It was demonstrated, that for an assessment of the delamination affinity it is advantageous to separate the introduction of a residual stress field and buckling initiation. The novel introduced SFNS was able to differentiate between the different qualities of coating systems A to F.

For system B with sufficiently high shear strength of the interface region and a sufficiently high delamination affinity, it was possible to derive the corresponding adhesion energy in terms of the critical energy release rate via the SFNS in combination with FEM simulation.

5.6 Skewed Cylinder Test

The skewed cylinder tests of Djoufack et al. [103] were reproduced with the same experimental set-up and the same materials. The results are shown in figure 5.9.

The effect of spontaneous coating failure during skewed cylinder tests was confirmed. The experiments yield some additional coordinates, which had been missing in the parameter room of Djoufack et al (yellow circles in figure 5.9 a)). Furthermore, by means of SEM-imaging it could be shown that the spontaneous delamination occurred via buckling, as shown in figure 5.9 b) and c). The propagation directions of the extended buckles coincide either to the direction of the grinding grooves or to the direction of motion of the counter-body.

The results are evidence for an interface fatigue introduced at stress exaggerations, resulting from grinding grooves subjacent to the coating and from asperities of the counter-body. Fatigue as failure type of the interface region will be taken into consideration in chapter 8, when it comes to a holistic description. The importance is shown and has to be addressed more detailed in future works.

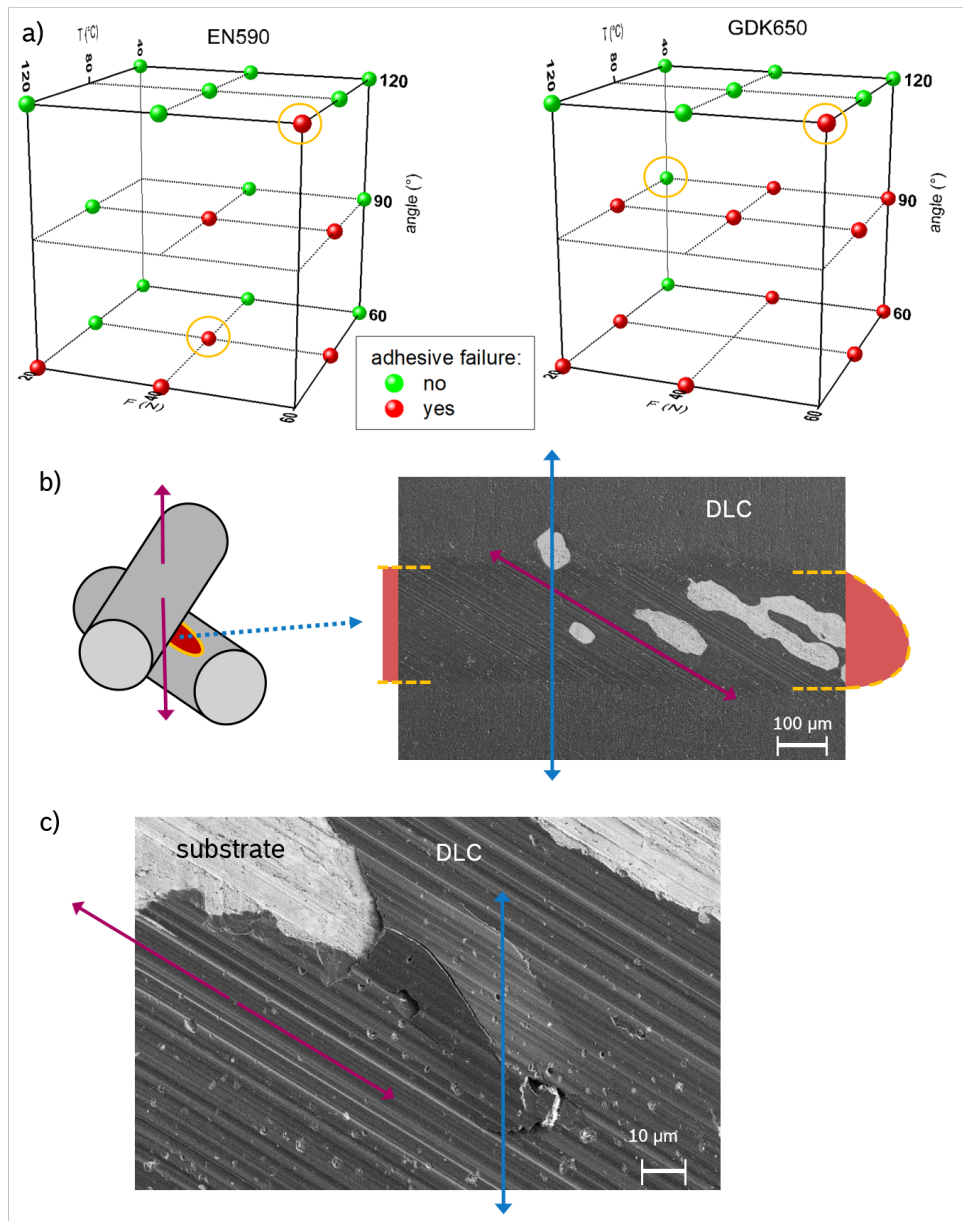


Figure 5.9: a) Three dimensional maps of the spontaneous failure mode (red dots) versus continuous abrasive wear mode (green) in a skewed cylinder model test according to Djoufack et al. [104]. Additional points originate from the reproduction of the experiment in the present work (yellow circles). The delamination behavior is influenced by temperature, mechanical load, tilt angle and Diesel type as lubricant. b) SEM-image of spontaneous coating failure in a wear track of a skewed cylinder test, where parts of the coating are delaminated. Those delaminations are aligned either to the abrasive wear grooves or to the initial preparation grooves of the cylindrical substrate. c) Delamination progression via buckling, where direction changes from alignment to the abrasive grooves into alignment to the preparation grooves.

Chapter 6

Local Thermo-Chemical Aging

In the previous chapters it was shown that delamination events can be traced back to different failure mechanisms, which rely on different loading conditions and different structural weaknesses of the adhesion layer system. E.g. for coating systems F and H, a significantly lower adhesion performance was found compared to the other systems. These could be attribute to the graphite layers found exclusively in systems F and H and the corresponding low shear strength.

In this chapter, the influence of structural weaknesses on the thermo-chemical degradation is analyzed on hand of system H, for which a decrease in adhesion performance via thermal annealing was already found. For comparison, system G with a similar but apparently thermally more stable interface set-up is analyzed likewise. The significant role of growth defects as a potential access route for chemical species is highlighted. Part of this chapter is published in [135] with explicit permission to reuse in a dissertation. Here the findings are further discussed within the concept of the adhesion performance and with regard to the findings of the TEM-analysis of chapter 4.

The coating systems with Ti adhesion layer, for which a significant decrease in adhesion performance has been observed via the same annealing conditions are discussed in the following chapter. The mechanisms are different and further experiments were performed in this case.

6.1 As-Deposited State

A first assessment of the mechanical adhesion performance in the as-deposited state via the Rockwell C test yield HF 2 to HF 3 for system G and HF 4 for system H. Both qualities are rated as acceptable adhesion according to DIN 4856 [97].

The main difference observed in the structural analysis via TEM-imaging (refer to chapter 4) was the larger extension of the transition region with a coral-like structure on top in system G and the vertical graphite channels in system H. A low shear stress can be attributed to the graphite channels, which evidences that these channels are causing the lower adhesion performance, which is less severe compared to system F most likely caused by the different orientations of the channels.

Figure 6.1 shows the cavitation erosion of the sonotrode test of samples of coating systems G and H in the as-deposited state. In both cases, the erosion shows a circular maximum and a halo-like second maximum extended over an annular ring.

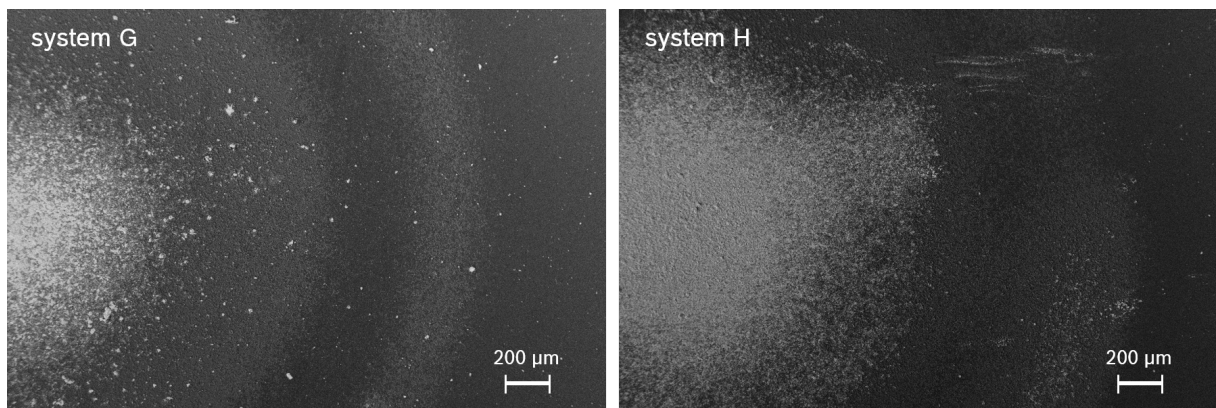


Figure 6.1: Cavitation erosion in the sonotrode test of a) system G and b) system H, both in the as-deposited state. Circular main maximum and annular second maximum are observed for both systems. For system H, the main maximum exhibits a larger area.

The circular maximum in system H is extended over a larger area indicating an accelerated cavitation erosion, compared to system G. Delamination with sharp edges, as it would be the case for buckling driven delamination is not observed. So the cavitation erosion is definitely not accelerated via an increased delamination affinity.

6.2 Long Time Thermal Annealing

Figure 6.2 shows representative samples of systems G and H in the annealed state. No defects were optically detected in system G, whereas system H exhibits areas of macroscopic delamination. Both systems are investigated separately in the following.

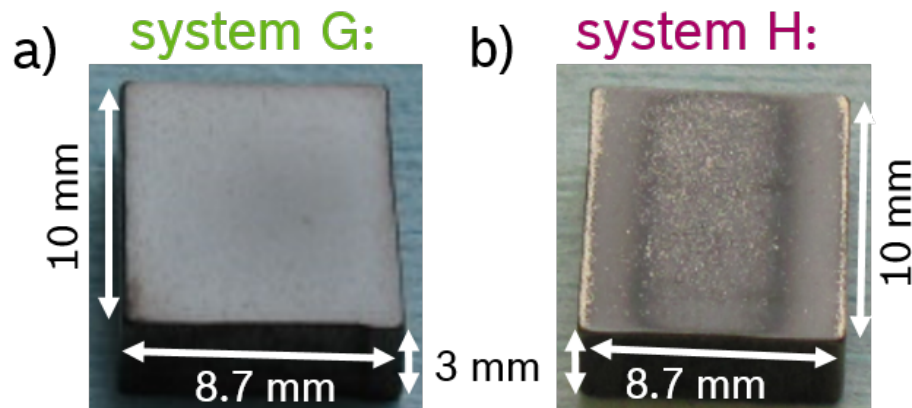


Figure 6.2: Photographs of representative samples for systems G and H in the annealed state (after longtime furnace annealing in N_2 -atmosphere with residual lab air at $350\text{ }^\circ\text{C}$ for 120 h): a) No visible defects for system G. b) Substrate locally visible for system H.

6.2.1 a-C:H System with Gradient Interlayer

SEM analysis of the coating surface of system G for different annealing states, yield a degradation of growth defects within the coating. Figure 6.3 shows how the degradation process evolves. In a) a representative SEM image of the surface of the a-C:H functional layer of coating system G in the as-deposited state is depicted, with some characteristic growth defects. The interfacial growth defects are supposed to be initiated by particles resting on the substrate prior to the coating process. This is hardly preventable as even in a clean room production the surface may become contaminated: During the coating process, inner movable parts of the coating machine also get covered by the coating material and flakes of it can fall down onto the substrate surface. Alternatively, non-metallic inclusions in the steel substrate, located at the surface region might act as a center of growth perturbation.

Particles, which rest on the substrate surface and did not get completely removed by

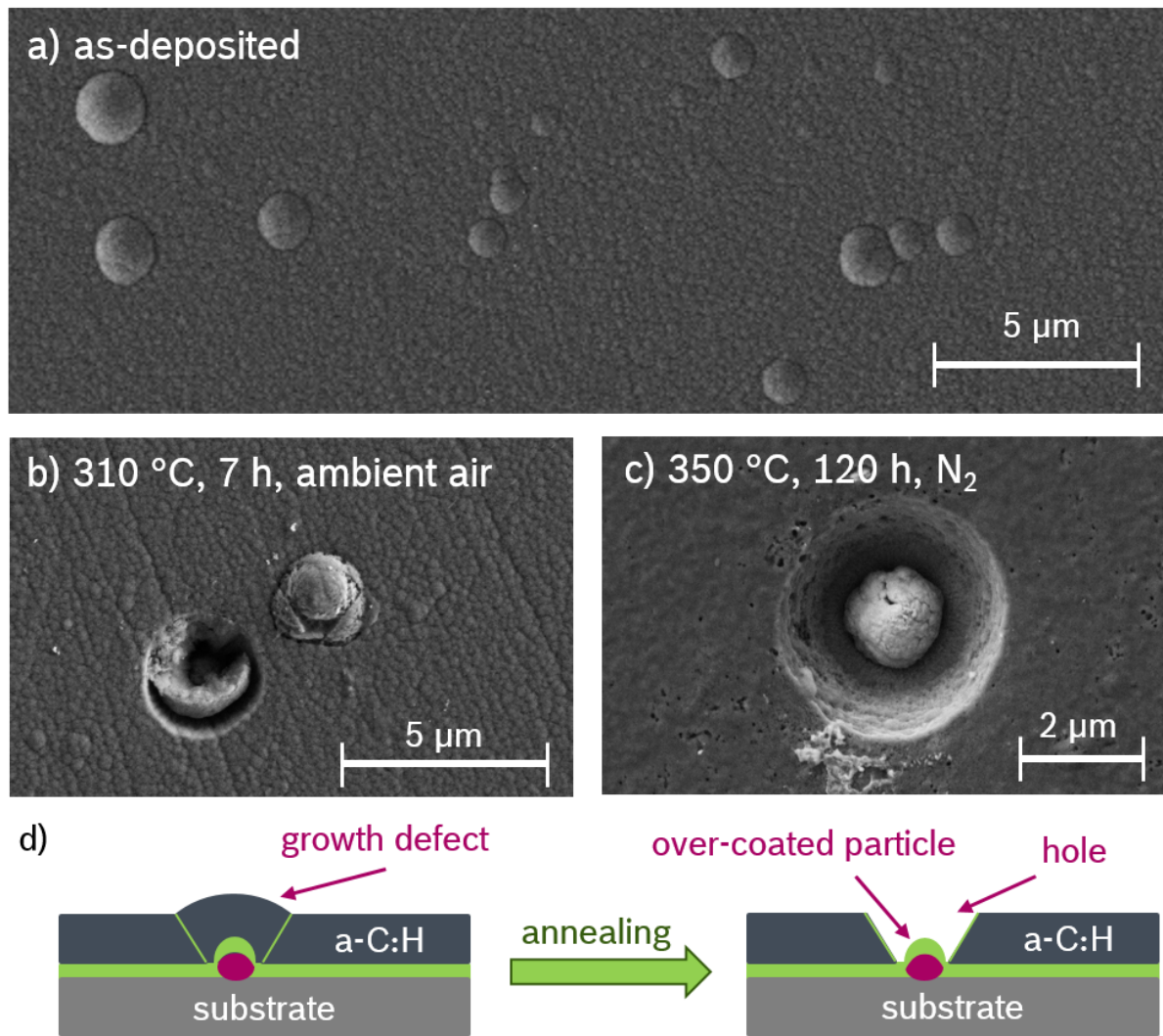


Figure 6.3: Evolution of growth defects into thermal defects, observed in system G after different annealing conditions: a) as-deposited state, b) ambient air, 310 °C, 7 h. Part of the growth defect lies upside down beneath its former place. c) N₂-furnace, 350 °C, 120 h. Pinhole has formed, over-coated particle remains in the middle. d) Scheme of the growth defect before and after annealing.

plasma etching, get over-coated by the adhesion layer. For the subsequent PECVD-process, those over-coated particles act as additional nucleation centers. By tilting the growth direction, they locally disturb the film growth of the a-C:H layer and nodules are formed. The nodules grow simultaneously with the film, so it is likely that they have comparable mechanical properties.

In some physical vapour deposition (PVD)-processes, droplets originating from solid targets [58] may deposit onto the growing film. Such an event can occur at any time during the growth process and initiate nodules in any depth of the coating. As the precursor in PECVD-processes is provided by the gas phase, droplet formation and incorporation

can be excluded. So for the coating systems G and H, for which the a-C:H is deposited via PECVD, the majority of initiation points for the growth defects are located at the later interface between adhesion and functional layer, which is schematically depicted in figure 6.3 d).

In figure 6.3 b) and c) characteristic annealing defects are shown. Size, appearance and distribution indicate that the annealing defects are degrading growth defects. Figure 6.3 b) shows an SEM-image of a spontaneously pushed out growth defect resting on the surface next to its former site after heating the sample at 310 °C for 7 h at ambient air. In figure 6.3 c) an SEM-image of a hole in the coating after 120 h at 350 °C is depicted. A spherical particle rests at the ground of the hole.

In Wöckel et al. [115] it was concluded that the degradation of the coating starts at the interface between the growth defect and the surrounding coating. We assume that their joint is loosened and the intrinsic stress of the coating acts on the conical growth defect and pushes it out of its site. The result is the observed hole in the coating with the over-coated particle at the ground (compare c) and d) in figure 6.3).

The pin-holes formed via degradation of the growth defects during thermal annealing are local weak spots, when mechanical loads are introduced. Therefore these pin-holes are utilized in this chapter to estimate the adhesion performance of the coating system after thermal treatment with external loads provided by Rockwell indentation, cavitation and nanoscratch testing. Furthermore the chemical stability of the coating systems can be assessed via exposure with the surrounding environment through the pin-holes. These conditions are provided by the long time annealing, where the pin-holes form at some stage and the thermal treatment endures. Similar coating defects are hardly introduced via mechanical means. In chapter 5, it was demonstrated, that indentation based methods introduces stress fields which hamper buckling driven delamination, which is not the case for the intrinsic defects.

Figures 6.4 a) and b) show the sample surface of system G after cavitation erosion subsequent to the furnace annealing: Buckling is not observed, indicating that the observed damage of the cavitation erosion is cohesive only and the delamination affinity is not increased. Furthermore, the damage looks nearly the same as the corresponding cavitation

erosion damage for the as-deposited state (refer to figure 6.1). The essential difference are circular features distributed all over the influenced zone.

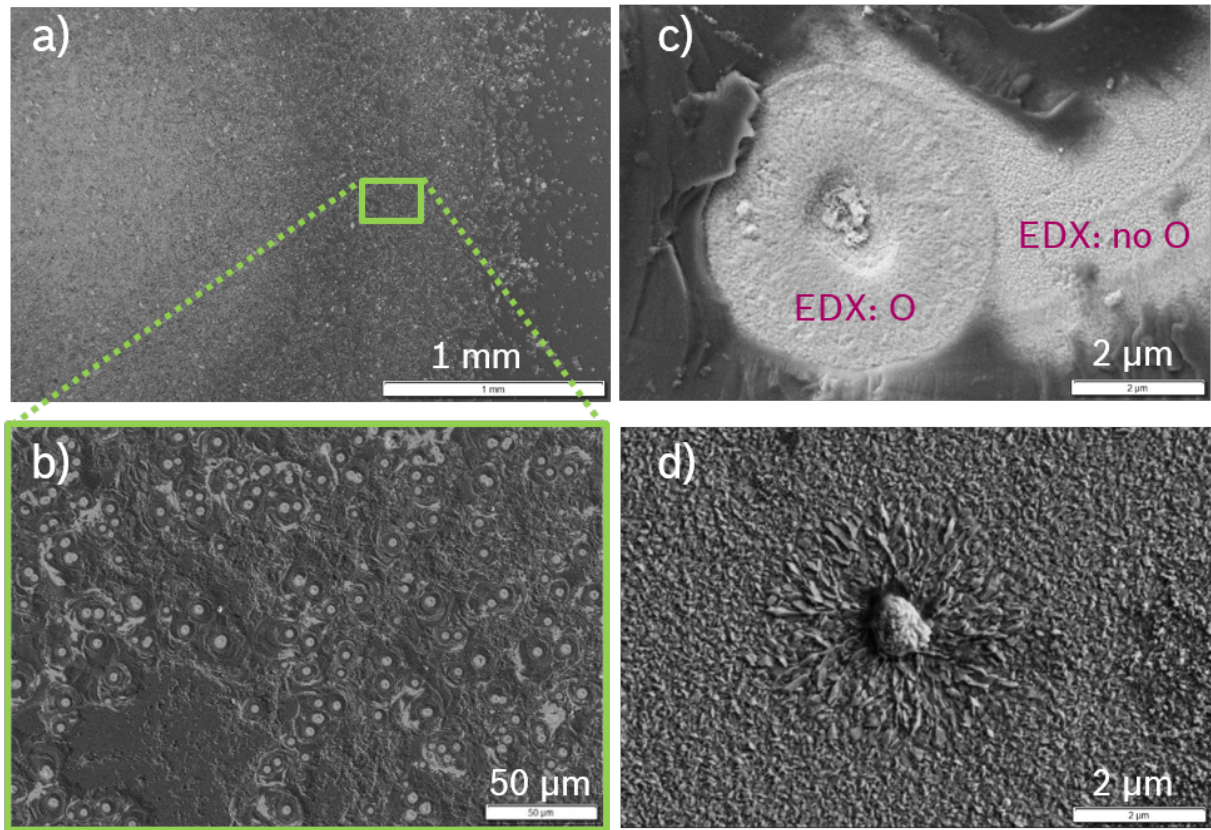


Figure 6.4: SEM-images of the local defects in system G after annealing (350 °C, 120 h) and postponed disruptive tests: a),b) Homogeneously distributed circular features on the eroded surface after cavitation, c) close-up of a circular area of oxidized adhesion layer near a scratch track, oxidation is confirmed via EDX-measurement and d) concentric texture around an over-coated particle after annealing at 500 °C, 120 h. a-C:H is completely removed by the 500 °C thermal treatment.

Same circular structures with a characteristic diameter of around $4.6 \mu\text{m}$ are also found via scratch and indentation tests performed on the annealed samples. A close-up of such an annealing defect near a scratch track is depicted in figure 6.4 c): A small area of uncovered adhesion layer is found with a distinct circular contour and a defect in its center. Via EDX, oxygen was detected in this area. In contrast, no oxygen or much less was detected at the neighboring uncovered adhesion layer. Figure 6.4 d) shows an SEM-image of a sample surface after a 500 °C longtime annealing: An over-coated particle surrounded by a concentric texture can be seen.

The concentric texture as well as the circular area of oxidized adhesion layer cannot be

found without preliminary annealing. It can be concluded that they are not growth defects. They must be formed during the annealing at spots of former growth defects. The holes created by the removal of the growth defects (refer to figure 6.3) can be seen as pinholes for further oxidation processes similar to pitting corrosion. As a consequence, the circular area, where the adhesion layer system got locally uncovered under the pin-holes can react with the surrounding medium.

When in contact with oxygen, Cr forms a protective oxide layer, which thickness depends on the growth conditions. At the elevated temperature, the oxide layer will grow thicker compared to room temperature. Therefore, the surrounding adhesion layer which got uncovered by the disruptive tests after the annealing, has a significantly thinner oxide layer compared to the area under the pin-hole, which explains the circular contour.

In the adhesion layer also Cr-carbide phases and Fe are present. The Cr-carbide act as a stable barrier layer against some corrosive species, but it is not able to form a passive layer at fresh defects, which could protect an Fe-rich phase. Furthermore, underneath the growth defects there could be some volume with favorable conditions for Fe-precipitation. Therefore an alternative hypothesis must be regarded. The light colored material in the center of the pin-hole in figure 6.3 c) might as well result from a precipitation into voids underneath the nodule during the thermal annealing. Corrosion reactions of the formed Fe-rich phases would cause a volume expansion. This process would as well be able to push out the nodule and form the pin-hole. A precondition would be, that O was already able to penetrate via the interface between nodule and the surrounding coating.

Nevertheless, the thermal defects are mechanical weak spots for the high loads of the disruptive tests, which are uncovering the defects in the observed manner. At 500 °C the degradation velocity is strongly increased. The degradation process of the growth defects takes place analogous to the 350 °C annealing, but at some stage, the coating disappears, whereby it is unclear if this is due to degradation of the DLC or via delamination. Postponed however, the complete adhesion layer surface gets oxidized. The oxidation is most pronounced in the areas with longest exposure time to the hot environment, which are again the circular shaped areas on the bottom of the pinholes.

The SEM-images in figure 6.5 show the influence of the cavitation erosion on a pinhole:

In a) a top-view is presented. The circular uncovered area has again a diameter of around $4.6\ \mu\text{m}$, the transition to the residual a-C:H coating is very smooth. In figures 6.5 b) and c), an ion milling cut through such a position is depicted: The smooth surface transition from the adhesion layer to the functional layer is confirmed. Furthermore no adhesive failure mode, i.e. interfacial cracks or buckling can be observed. The wear of the coating is cohesive only.

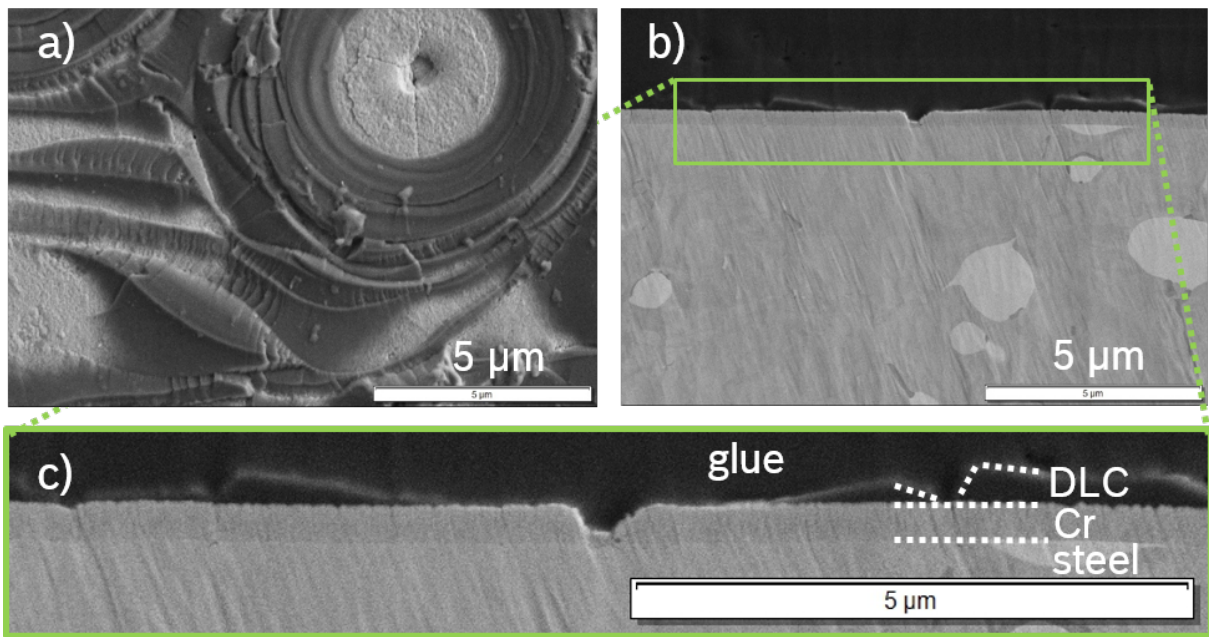


Figure 6.5: SEM-images of system G after cavitation subsequent to annealing ($350\ ^\circ\text{C}$, 120 h): a) Top-view of a circular uncovered area and b),c) ion milling cross section through such a position. The intact interface with the smooth transition from the DLC to the adhesion layer is confirmed.

The stable size of the uncovered area shows that even the cavitation forces do not extend the hole radially at the interface. In combination with the absence of delamination despite the heavy loading of thermal treatment and postponed cavitation erosion, it can be concluded that the adhesion performance of the system is very good. This is in contrast to systems A, B, C and J, where a thermal aging during the same annealing conditions lead to an increased delamination affinity, presumably via precipitation of Fe-rich phases. Depending on the exact conditions of an application, i.e. a combination of thermal and external mechanical load, the pinholes might be initial points for a cohesive damage, which has to be considered for the construction of a potential application. Vice versa, the resistance against an erosion is much dependent on the defect density of the coating

and has enormous potential, by decreasing this density, albeit this is a very challenging task. If Fe-precipitation is involved in the process of pinhole formation, it might suffice to avoid Fe contaminations in the adhesion layer.

6.2.2 a-C:H System with Step-wise Interlayer

In heating plate experiments with shorter duration, the pinholes formed via ejection of growth-defects are also observed for system H. In the long time furnace experiment however, more severe damage results from those defects: Figures 6.6 a) and b) show buckles around circular holes, resembling volcanoes. In figure 6.6 c) partially delaminated areas are depicted. The contours of these areas are of circular shape and over-coated particles (figure 6.6 d)) are found in their centers. Same kind of particles are located in the centers of the volcano-like structures. Around the particles no concentric structure has formed as it was the case for system G after 500 °C thermal treatment.

It can be concluded that the pinholes left by the removed growth defects gives the environmental species access towards the adhesion layer system. A pitting-like process must be prevented by a detachment of the coating. Thereby the path of failure progression is redirected into the direction parallel towards the substrate surface. At the annular edges at the ground of the hole, the residual stress of the coating is converted into shear stress, concentrated at the interface. In combination with the environmental access, a thermochemically driven advance of the strained crack tip might be enabled.

Figure 6.7 shows a high magnification SEM-image of an ion milling cross section through a spot of a former growth defect. The over-coated particle sits on the adhesion layer, centered in the pinhole and a large cavity has formed around the particle. The surfaces of the functional coating and the adhesion layer are still parallel to each other, a buckling as observed for the volcano-like structure does not occur in this case. Any significant volume expansions of the adhesion layer during annealing could not be detected, so this can be ruled out as a source of further stress on the coating.

The underside of the functional coating is hence the only part which significantly degrades. Lateral growth of the cavity along the interface might be explained by a process

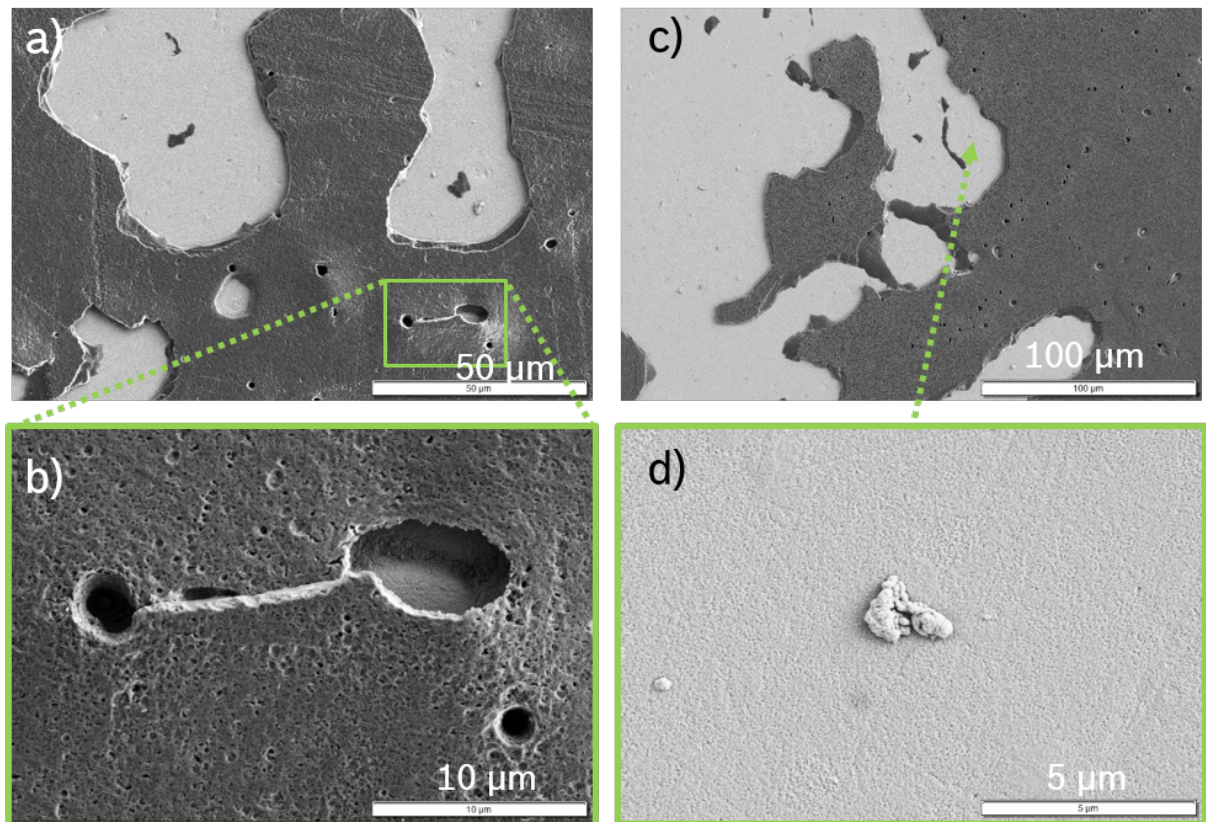


Figure 6.6: SEM-images of system H after annealing (350 °C, 120 h): a), b) Volcano-like structures are observed arising from the former pinholes. c) As they merge cracks are formed leading to partially delaminated areas with rounded contours. d) In their center over-coated particles remain. Circular areas of oxidized adhesion layer as in system G are not observed.

based on the shear stress and chemical access towards the interface, but not the additional degradation of the a-C:H-coating, radially around the particle. Apparently, the degradation is somehow strongly accelerated compared to the top surface of the coating, where no severe degradation is observed. It can be concluded that the activation energy of the relevant process must be lowered locally.

Possible causes can be the following. 1. A stress gradient in the functional layer might prevail with a higher stress level at the bottom side. This would alter locally the surface energy. 2. Alternatively, the adhesion layer might act as a catalyst, possibly in addition with Fe-precipitation. 3. The observed vertical graphite channels in system H have a lower density and thus are favorable for precipitation formation. Fe-rich precipitation phases are susceptible to corrosion. A potential severe, local corrosion might affect the surrounding C-coating as well. It has to be taken into consideration that some indications (e.g. corrosion products) got lost during sample preparation via the water cooled

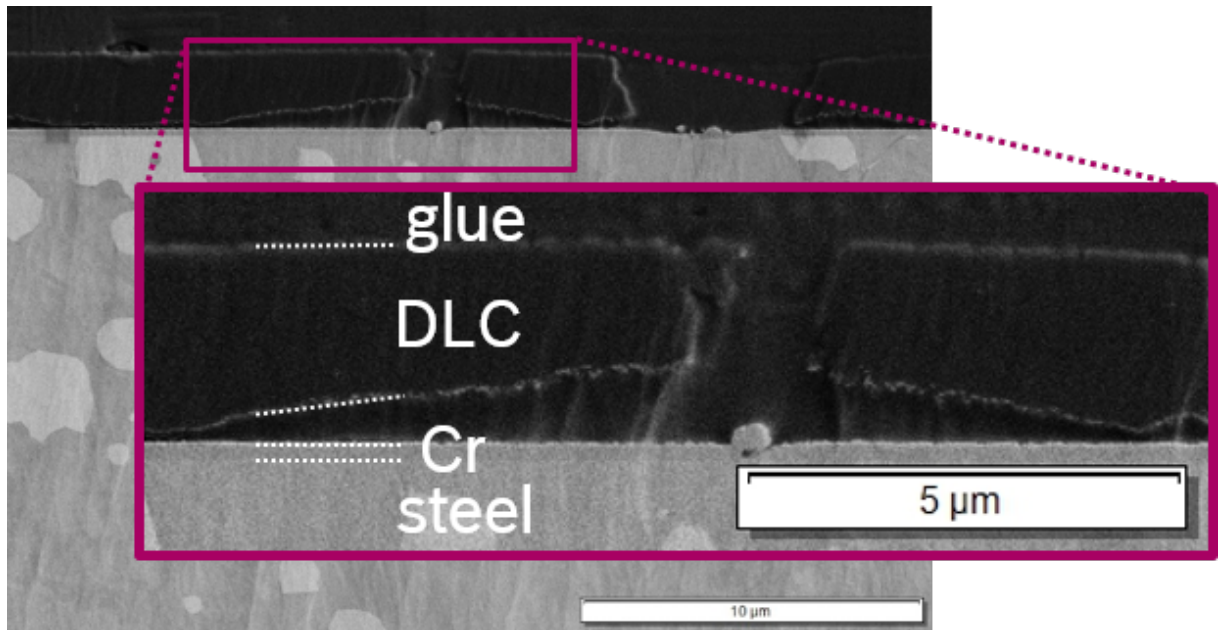


Figure 6.7: SEM-image of an ion-milling cut through an annealing defect (System H after annealing, 350 °C, 120 h): A huge cavity has formed around the over-coated particle of the former growth defect. The lateral extension of the cavity exceeds the size of the circular areas of system G by far. The volcano-like structure has not yet formed, as the coating is yet too thick for buckling.

mechanical cutting and Ar-ion milling.

With regard to the volcano-like structure, the model of a clamped circular plate [88] can be used to estimate the critical compressive stress, which is necessary for the formation of the observed circular buckles (refer to figure 6.6), as introduced by Evans and Hutchinson [4] (compare to equation 2.5). For E_{IT} , h_f and ν_f , the values of table 4.1 are used and the geometry-factor is set to $k = 14.68$ [4] accounting for the circular shape.

The observed buckles have been measured and for a representative average radius of $a = 8.8 \mu\text{m}$, the calculated compressive stress of more than -15 GPa is unrealistically high and exceeds the intrinsic stress of around -1.7 GPa (from the curvature test) by far. It can be concluded that the thinning of the coating via degradation and cavity formation is a precondition for buckling in the given system: According to equation 2.5, the critical buckle radius decreases with decreasing film thickness and constant stress level. With a buckle radius of $a = 8.8 \mu\text{m}$ and intrinsic stress of around -1.7 GPa, this gives a critical film thickness of $0.67 \mu\text{m}$ for the volcano-like structures. Accordingly, the cavity has to grow sufficiently large (increasing radius plus decreasing coating thickness) in order to enable buckling. This also explains why for the observed cavity depicted in figure 6.7, the

coating is not (yet) buckling as the thickness is still too high for doing so.

The mechanism of thinning the film as a requirement for buckling makes the buckles very stable, as the circumferential film is much thicker and thereby not able to buckle. Therefore neither buckle growth nor buckling driven delamination in form of secondary buckling occur, which would be the usual failure progressions of a buckled compressively stressed film [4]. Instead, neighboring cavities merge and cracks in the coating form. These are caused by tensile stresses due to the bending of the thinned coating and tend to start at the rim of the hole. Cracking leads to spallation of the bend coating in those regions, eventually resulting in the observed, characteristic circular contours of the partial delaminated areas.

Origin of the whole process are the over-coated particles, which remain in their centers (refer to figure 6.6). In their role they actually fit into the definition of a catalyst, for the degradation process in this case. The still adhering coating and the stable buckles suggest that also for system H, the delamination affinity was not significantly increased.

6.2.3 Comparison of both Systems

The decreased adhesion performance via annealing, observed for coating systems A, B, C and J with Ti adhesion layer, have been attributed to Fe-precipitation and a decreased linkage to the C-based coating caused by a positive Gibbs energy for Fe_3C .

For systems G and H on the other hand, the chromium carbides, detected via TEM analysis in the interface regions are energetically favorable: Cr_3C_2 with a calculated Gibbs energy of -0.89 eV [136] and Cr_7C_3 with -1.72 eV [136]. Accordingly, for both investigated Cr-based adhesion layer systems thermally stable interfaces were found at $350\text{ }^\circ\text{C}$ in the undisturbed regions of the coating system apart from coating defects.

The conditions for Fe-precipitation are also given for systems G and H, but the experimental results evidence, that a precipitation at large scales along the interface towards the C-coating is prevented, presumably by the stable Cr-carbide phases.

However, thermal defects are found in form of pinholes at former growth defects, which provide access to the interface for environmental species. In both investigated systems

they are detected, but significantly different thermo-chemical stabilities of the adhesion layer systems are observed. For system G, lateral spread of the degradation along the interface was prevented by an apparently thermo-chemically stable adhesion layer system. Furthermore a mechanical stability of the adhesion layer system could be confirmed in several tests: With indentation based tests at local thermal defects, it was not possible to introduce delaminations. Furthermore, on hand on the ion milling cut of the eroded surface of the cavitation test, subsequently to the annealing, the erosion test yield cohesive wear of the (annealed) functional layer only.

In system H, a severe damage progresses from the pinholes. Large cavities at the bottom of the pinholes are formed. The speed of cavity growth is quite slow (annealing went over several days at 350 °C) but much faster than degradation at the top-surface which is marginal at the most.

The lateral and radial cavity growth lead to a loss in contact between coating and substrate and a thinning of the coating. Only this combination enabled buckling of the film. Thereby, the buckles become untypically stable as the circumferential coating is too thick for buckling with the given radius of the circular defect. The resulting volcano-like structures merge and spall, forming partially delaminated areas. It should be noted that this is not triggered by an increased delamination affinity, but by a locally progressing process. Degradation of the interface region is opposed to a good adhesion performance resulting in a very slow damage progression in contrast to the much faster delamination progressions for the systems A, B, C and J with a significantly increased delamination affinity.

The observed degradations of systems G and H rely on the presence of growth defects. With increased temperature (500 °C), the process velocity is increased and the radial symmetric textures are even more pronounced. Main cause for the observed structures are either an oxidation of the adhesion layer, which is focused by the the small pin-holes formed via ejection of the nodules or via Fe-preipitation into voids around the growth defects.

The different thermo-chemical stabilities of systems G and H can be attributed to the structural differences in the coating systems, which are the graphite channels between

the columns of the adhesion layers of system H, the coral structure of system G and the Cr_7C_3 phase, which was only observed for system G (refer to chapter 4.1.3) and which has the higher Gibbs energy.

It can be concluded that the thermal stability of the whole coating system can rely on a sequence of failure modes. There is much evidence that the stability can be significantly increased by avoiding one of the elements of the sequence, e.g. the growth defects or contamination of some unfavorable species like Fe.

Chapter 7

Thermal Aging and Corrosion assisted Delamination

In this chapter, the influence of temperature and surrounding medium on the adhesion performance is investigated, which was found to manifest in two distinct ways: The first is a thermally driven increased delamination affinity of an intact coating system, i.e. an increased tendency for a delamination progression via secondary buckling, once primary buckling is introduced.

The second manifestation is a retarded secondary buckling, which can be accelerated by thermo-chemical means. In this case the coating system exhibits a local defect or primary buckle in advance to a thermal or chemical treatment. The lifetime of the coating therefore depends on exact application conditions and the probability of occurrence of defects, which provide access to the interface region for corrosive media.

For the purpose of identifying underlying mechanisms, system J is well suited as both phenomena occur very systematically. Progression of the coating delamination was identified as a cyclic sequence of three distinct steps: Time dependent corrosion at residual defects, buckling of the coating and spallation. After spallation, a pre-crack is always left enabling chemical attack, re-starting the cyclic sequence. Small defects in the coating as starting points can thereby lead to a complete delamination of the coated parts, even though Rockwell C tests indicated a good adhesion quality. The speed of the retarded delamination is demonstrated to be a function of the annealing time of the preceding thermal treatment.

7.1 Aging of the Interface Region

Contrary to other reports [116], a good adhesion in the as-deposited state was achieved for the a-C:H coating by introducing a Ti layer, as demonstrated for system J. Rockwell C imprints showed marginal delaminations, the adhesion can be rated between HF1 and HF2 according to VDI 3198 [2]. Also with further methods, no weaknesses of the interface region were detected (refer to chapter 4). In addition, the imprints of Rockwell C and the scratch tracks did not alter with time, at least for two years at room temperature in lab air. This observation has importance for the later discussion about retarded delamination progression.

In the annealed state however, the coating was completely delaminated (refer to section 4.3.2). From the preliminary studies in chapter 4 and 6, it can be concluded that the a-C:H functional layer is thermally stable in the investigated temperature-time regime and the coating was demonstrated to be impenetrable for corrosive media, which requires additional paths, such as pin-holes in order to access the interface region locally (see chapter 6). Therefore, it is presumed that the thermal aging relies on internal processes and the annealing experiments were performed at ambient air, simplifying observation. Post mortem, it will be verified that a homogeneous aging within the whole sample is given, justifying the annealing at ambient air.

Figure 7.1 shows samples of coating system J, which were deposited with different orientations within the coating machine and which are afterwards annealed until first delaminated areas were observed.

The reproducible delamination patterns are exclusively observed at two characteristic sample edges, which follow the tilt angle of the sample with respect to the orientation in the deposition chamber. It can be concluded that the delamination affinity is increased at these edges, caused by the sample holder rotation during the deposition process and not by substrate preparation.

Locally increased delamination affinity can be caused by either a local increase in intrinsic stress or a decrease in strength of the interface region. Residual stresses might be increased, caused by an exaggeration of the electrical field at sample edges and thereby locally increased kinetic energy of the incident ions. The mounted samples have a certain

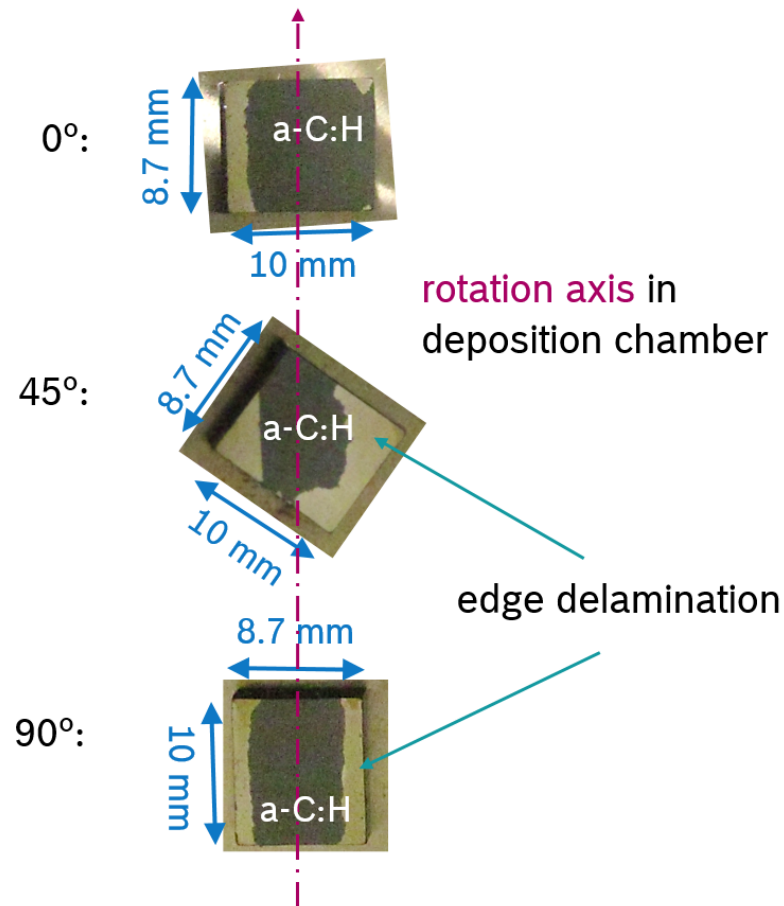


Figure 7.1: Influence of the sample orientation on the delamination edges. The characteristic edges stay fixed with respect to the rotation axes. This is evidence for a dependency of the time dependent incident angle of the deposition species. Substrate preparation on the other hand can be ruled out as root cause.

shielding effect on each other. By the vertical arrangement of the samples, the shielding might be located at the horizontal edges, so that only at the vertical edges, the fields are exaggerated.

A further possible cause can be the angle of incidence of the deposition species, which exhibits a timely periodical alternation and which differs significantly in vertical and horizontal direction with the given rotation system. Local growth parameters of the adhesion layer have certainly the potential to alter the adhesion performance locally in the observed way, by structural deviations (density/porosity) or by deviations in mechanical properties. With the assumption, that the thermal degradation, driven by internal processes, occurs on the whole sample equally, the appearance of the characteristic delamination pattern is used to define an *incubation state*, i.e. the state where the degradation is sufficient, that delamination at locations with the highest delamination affinity is enabled. This method

allows for an estimation of the *incubation time* for different temperatures in experiments with convenient observation times.

Incubation times are determined for several annealing temperatures in the range of 300 to 500 °C. Figure 7.2 shows the findings for the aging experiment in an Arrhenius plot ($1/t_{crit}$ vs. $1/T$), in which each point corresponds to the incubation time t_{crit} at a given temperature T . The data points form a straight line indicating that a thermal activation is required for the aging process.

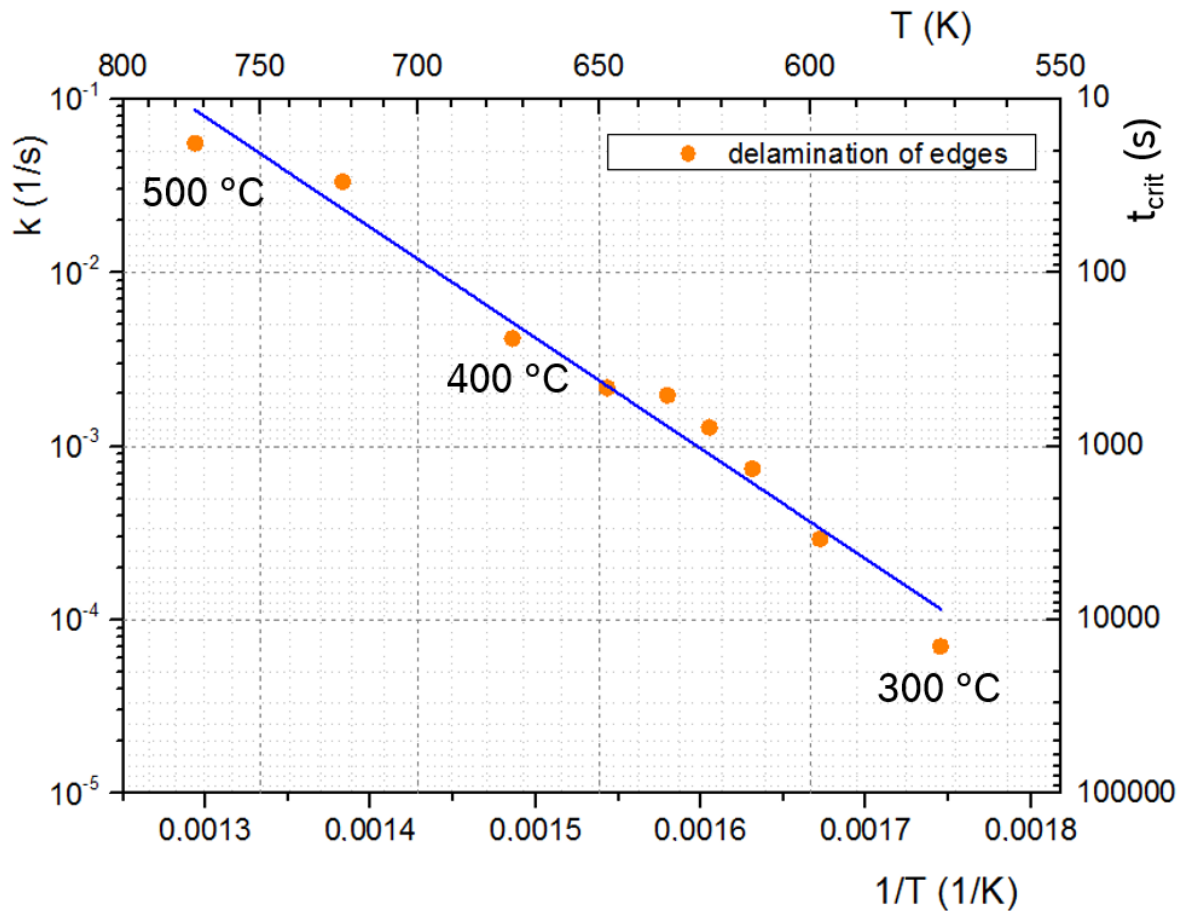


Figure 7.2: Arrhenius plot of the aging process (continuous decrease of the adhesion performance): Normalized rate constant k (equal to $1/t_{crit}$) versus $1/T$. The annealing temperatures are indicated. From the slope which is $-\frac{E_A}{R}$, the activation energy of $E_A = 53 \text{ kJ/mol} \hat{=} 0.55 \text{ eV}$ was derived.

As the data fit to the Arrhenius law, the reciprocal of t_{crit} can be regarded as a rate constant k for a reaction at the interface which decreases the adhesion performance continuously, eventually enabling buckling driven delamination in the edge region. The activation energy E_A for this process can be derived from the slope which is $-\frac{E_A}{R}$, with

the universal gas constant $R = 8.314 \text{ Jmol}^{-1}\text{K}^{-1}$. A value of $E_A = 53 \text{ kJ/mol} \hat{=} 0.55 \text{ eV}$ was determined which lies in a plausible order of magnitude, when diffusion processes are expected.

For a better assessment of the underlying mechanisms, it must be taken into account that coating delamination of the aged samples did not occur instantaneously. The decreased adhesion performance is rather expressed by an acceleration of the delamination propagation, which is somehow retarded. This behavior is analyzed in the following.

7.2 Retarded Delamination Progression

A delamination front serves as an ideal initial damage for the delamination progression experiments. Alternative initial damages, induced by external loads are always inferior as they bring additional, anisotropic stress fields, usually with tensile components hampering a damage progression via buckling, as discussed in the following.

The Arrhenius law indicates that with the different combinations of annealing temperature and time, the same level of adhesion performance is achieved, which is sufficiently low for the intrinsic stress at the edges to drive the delamination. In this and the following sections, the central part of the samples is examined where the coating is still adherent after cooling down to room temperature. In the whole central region, the intrinsic stress is distributed homogeneously as will be shown later on by the observed constant spallation radius. First, a model for damage propagation is built. Therefore, the progression of the delamination subsequent to the annealing at room temperature in laboratory air is monitored.

7.2.1 Buckling Driven Delamination

Figure 7.3 a) shows microscopic images of the starting of a spontaneous delamination which was found at a substrate defect on an aged sample ($340 \text{ }^\circ\text{C}$, 23.5 min). The growth of the delaminated area was monitored over several weeks in laboratory air at room temperature. Delamination proceeds along the interface between DLC and Ti (verified via

SEM/EDX-analysis) in form of half-circle areas with a characteristic size. Thereby, only one half-circle area at a time delaminates, a periodical pattern arises successively on the subjacent adhesion layer.

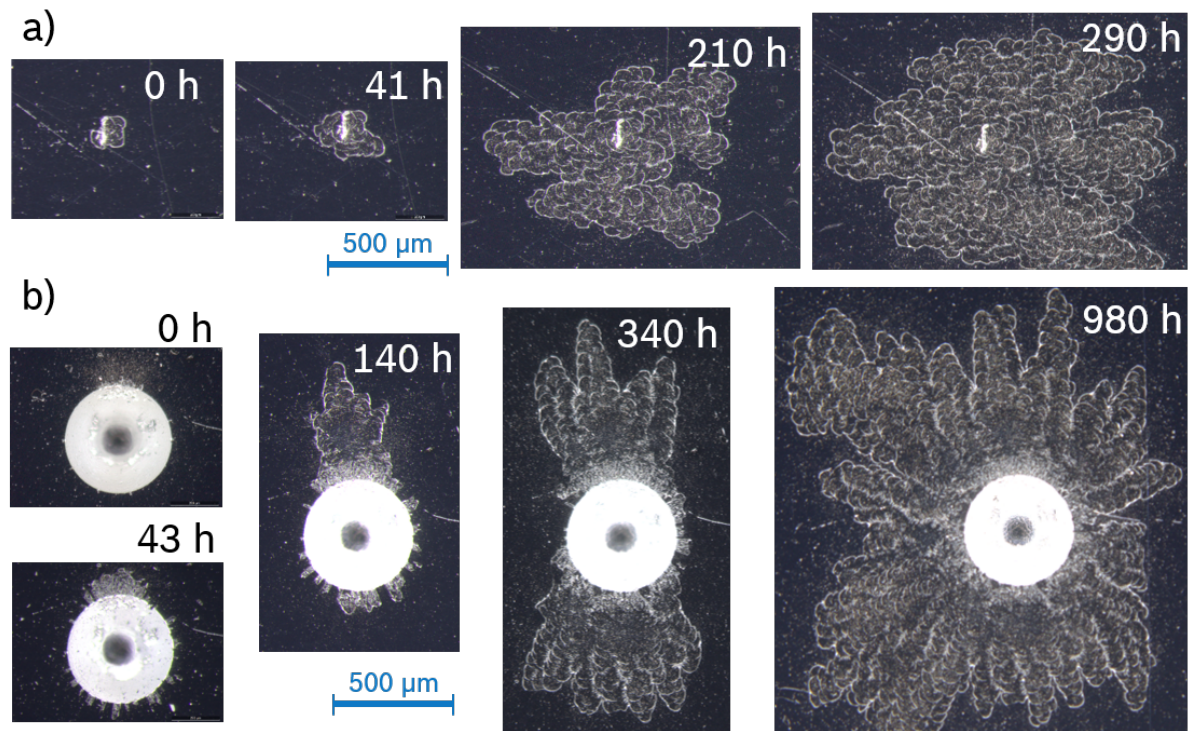


Figure 7.3: Initiation and growth of delamination at room temperature in air: a) At an intrinsic defect, presumably a small scratch in the substrate (aging: 340 °C, 23.5 min). b) Around a Rockwell C imprint. The half-circle-pattern from buckling and spallation is clearly visible in the undisturbed area. The characteristic spallation radius indicates a homogeneous stress distribution. This is not the case within the mixed zone of the indentation resulting in a different buckle shape (aging: 350 °C, 14 min).

In figure 7.3 b), the monitoring of a Rockwell C imprint is depicted (aged sample, 350 °C, 14 min): After the indentation, almost no delamination occurs. With time, i.e. several days, delaminations along radial cracks around the indent arise. Delamination proceeds with the half-circle pattern, growing out of the previous delaminated areas. A characteristic size of the half-circles is observed again. The stress field of the indentation alters the pattern in a quite undefined manner. In the same sample a second indentation took much longer time to initiate the delamination, whereas later on, remote to the residual imprint, the delamination progression velocity was the same as for the first imprint. SEM in combination with EDX revealed that the periodic pattern is formed by sharp annular delaminations of the Ti-layer uncovering the steel substrate. These sharp annular

delaminations are visible as the light contours of the half-circle areas in the microscope images. This is shown in figure 7.4 with a survey on repeating units of the periodical pattern in a) and a close-up of a spot with missing adhesion layer in b). The annular shape of these patterns correspond to the annular shape formed in the a-C:H layer via spallation. This indicates, that both mechanisms are related.

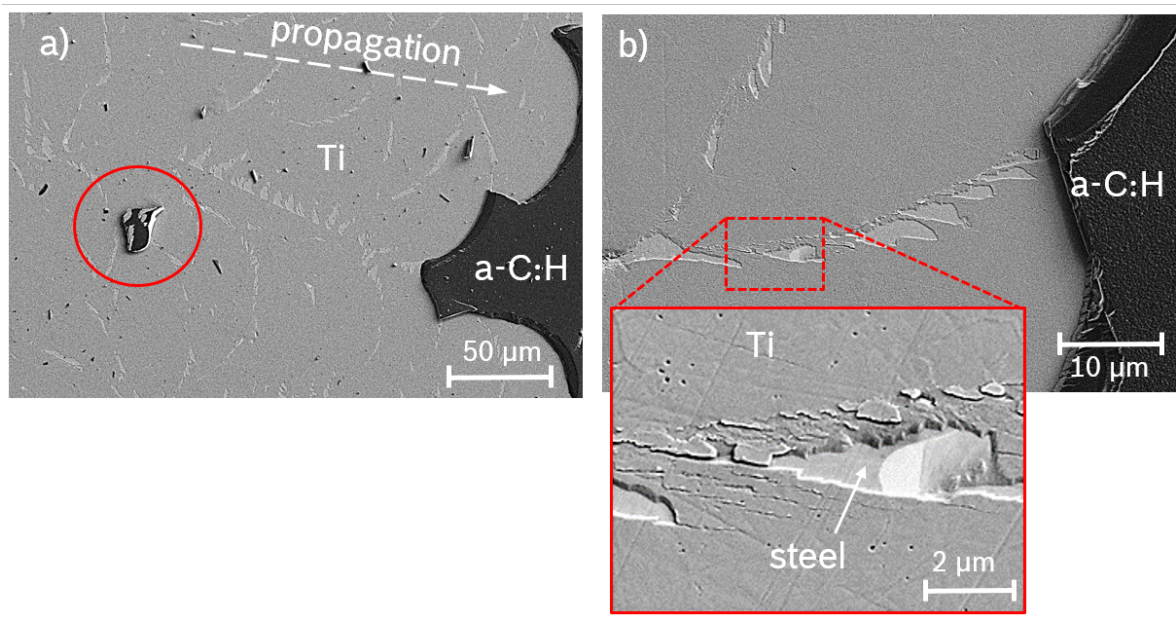


Figure 7.4: SEM images of the periodical pattern of half circles within the adhesion layer: Survey a) and close-up b). Propagation direction of the delamination is indicated with the arrow in a) and a part laying up-side down is highlighted with the red circle.

Spallation produces a characteristic “through thickness” fracture within the functional layer. This is at the point of highest bending, so that an additional interfacial pre-crack is left. From the geometrical set-up, it is rather unlikely that the spallation process additionally produces the annular delamination in the Ti layer.

It is concluded, that as soon as the buckle vanishes via spallation, the interfacial crack growth is hampered by the disappearance of the tensile stress at the crack tip. Secondary buckling is not introduced, as observed for annealed systems B and C for instance. This means the delamination affinity of system J is lower, i.e. the residual crack after spallation is below the critical value for buckling under the load of the intrinsic stress of the a-C:H coating.

For a delamination progression, the crack must grow before the next buckle can form. The conditions for the crack growth are shear stress resulting from the residual intrinsic stress

and the broken symmetry, access for environmental species and an uncovered Ti-layer, which might exhibit Fe-precipitation phases (refer to section 4.3.2).

These conditions are decisively different from the conditions during the previous delamination progression via growth of a buckle, which was driven by tensile stress, accompanied with a crack growth between DLC and adhesion layer. Under the new conditions, a crack must grow under shear stress, which might also occur in a different plane, as e.g. between Ti and the steel substrate.

By extrapolating the annular delamination within the Ti layer towards the remaining DLC segment (compare to figure 7.4 b)), it is observed that it does not coincide with the through thickness fracture from spallation, but rather the spot, where the crack tip of the residual crack after spallation is expected to be located. In figure 7.4 a), a spalled coating piece is found up-side down (red circle) with metallic residues, resembling the pattern. The residues are not exclusively at the edges of the piece. Both findings are evidence for a delamination of the Ti under the shear stress at the edge of the DLC coating.

The retarded character of this crack growth under shear stress can be attributed to a creep of the amorphous a-C:H towards the edge of the coating, where the residual stress is not opposed. The surrounding medium might also lead to an embrittlement of the Fe-containing Ti phase close to the crack tip, which would also explain the retarded character of the process.

The periodic pattern is thus formed by an alternating buckling and spallation of the coating. The observation that only spallation occurred and no altered buckle shape like the straight-sided or sinusoidal blister, can be attributed to the rather high thickness of the DLC compared to observations on thinner coatings in literature. According to equation 2.10, the critical radius for spallation decreases with increasing thickness. A spallation radius of $b_{spall} = (45 \pm 0.9) \mu\text{m}$ is measured, corresponding to an intrinsic stress of $\sigma_0 = (-1.5 \pm 0.06) \text{ GPa}$ (equation 2.10), which is in good accordance with the intrinsic stress derived from the curvature test (-1.7 GPa, chapter 4).

For the very first buckling on a sample, the conditions are similar to the situation after spallation, but without the residual crack, which is left after spallation. Initiation of the whole delamination process therefore relies on local defects, which is confirmed by the

observation in figure 7.3, that the first buckles occurred at defects (intrinsic or induced) while the rest of the coating does not buckle at all.

Figure 7.5 shows a TEM image with a partially delaminated DLC coating and a crack through the Ti adhesion layer (system D), which suggests that also surface-near inhomogeneities in the substrate might be initiation points for cracking. Crack initiation can be caused by locally discontinuous properties, which result in concentrations of the residual intrinsic stress.

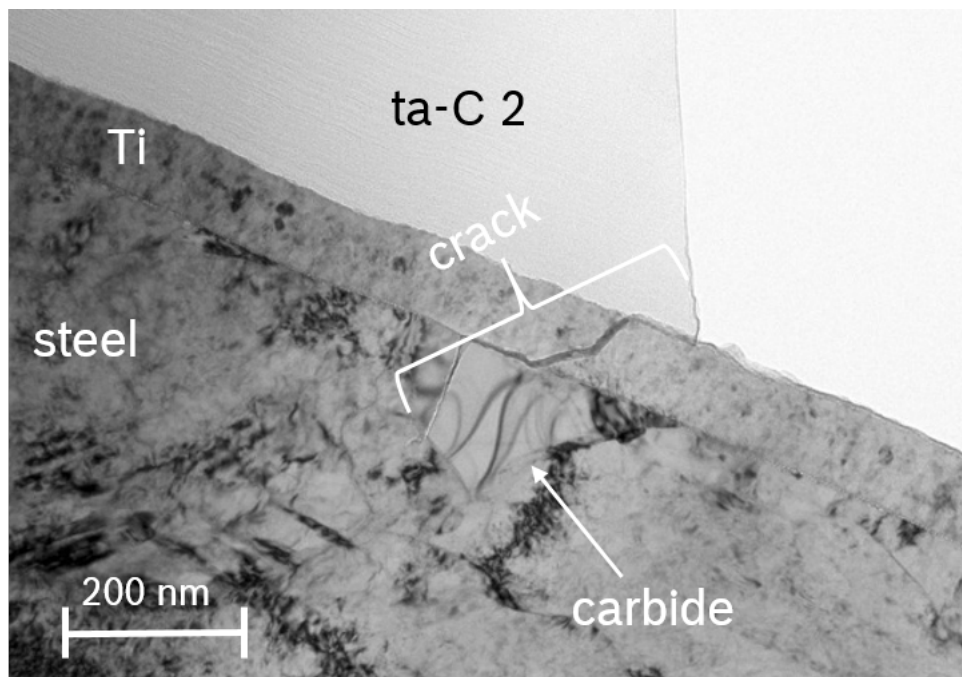


Figure 7.5: TEM-image of system C at a surface-near, hard carbide. A crack is widely extended and goes through the whole carbide, the thickness of the Ti layer and commences along the interface towards the ta-C coating. Crack initiation due to local stress concentrations at discontinuous properties is likely. Furthermore, a change in crack plane is observed in the direct vicinity of the discontinuity.

The estimated incubation times, which followed the Arrhenius law evidences a sufficient defect density at the sample edges. The residual cracks after spallation are assumed to have a characteristic dimension, caused by a characteristic spallation radius. With this precondition, the kinetics of the retarded delamination are further analyzed. The time scale and the preconditions indicate a medium driven mechanism: After spallation the environmental medium has access to the crack front, where shear stress is localized.

7.2.2 Medium Driven Progression

The retarded initiation of secondary buckling was attributed to a (mechanical) creep or to chemical processes in combination with the shear stress at a residual crack tip. In this section, the influence of environmental media is analyzed. Figure 7.6 shows the characteristic pattern in an SEM close-up.

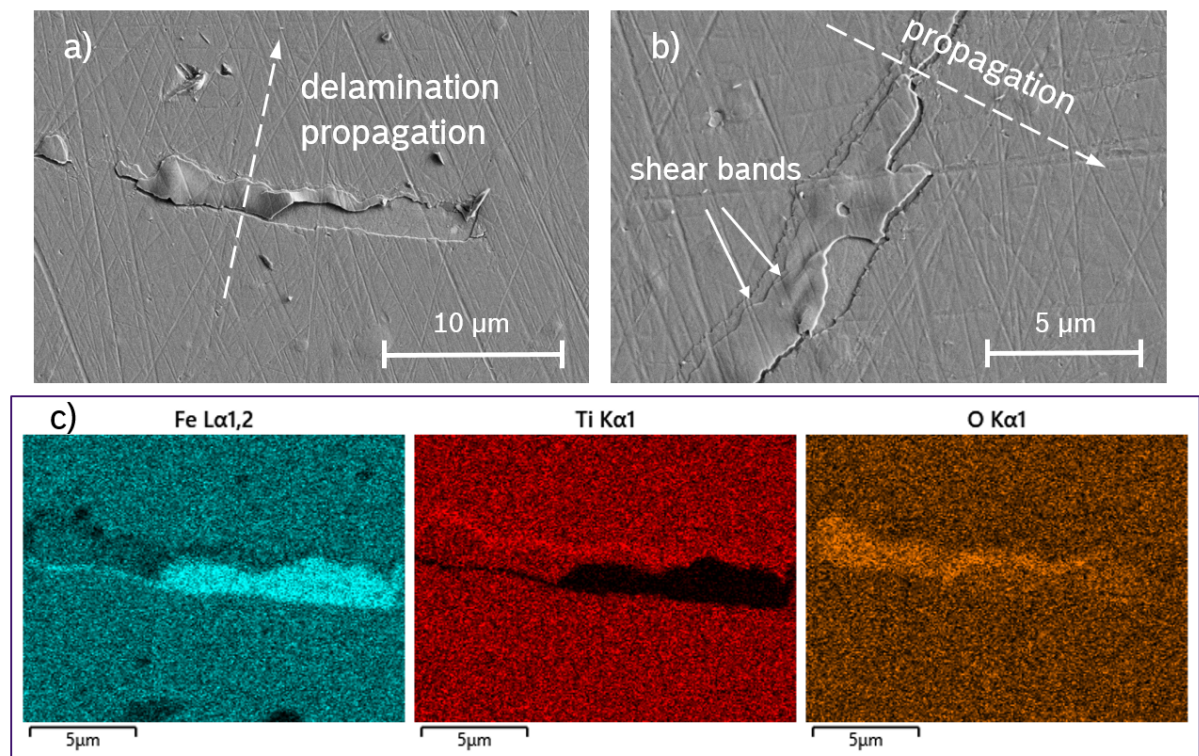


Figure 7.6: SEM-images of spots of the characteristic, periodical pattern after delamination progression in air, where adhesion layer is partly remaining in the half circles. The loosened adhesion layer is assumed to act as buckle nuclei. In b) shear bands introduced by the edge of the a-C:H layer are visible. c) EDX elemental mapping of position a) reveals oxidation of the altered adhesion layer in the half-circle.

In this case the delaminated Ti-layer is partly still attached to the substrate. From its wave-like appearance, it can be assumed that the detached parts act as nuclei for buckling of the a-C:H coating. In b) the segments shape evidences a shearing in the direction towards the already delaminated region with some stopping points. EDX analysis yields an increased O-signal (figure 7.6 c)) at the adhesion layer segment. It can be concluded that the retarded delamination at room temperature of the aged coating system J is caused by a slow delamination of the Ti from the substrate under the shear load of the non-opposed DLC-coating edge. It is likely, that this process requires an oxidation of the stressed Ti

layer.

Retarded delamination progression was exclusively observed for the aged coating system. In chapter 4, some evidence was found, that Fe-precipitation occurs during thermal treatment within the adhesion layer. Fe-rich phases do not form passivation layers in contrast to Ti. Therefore, Fe-precipitation is probably the main cause for enabling the retarded delamination progression.

Influence of Aging Duration

In the following experiments, the delamination progression subsequent to the thermal aging is monitored on a longer time scale. Amongst others, it will be shown that the aging of the interface region and corresponding decreased adhesion performance has occurred homogeneously on the whole sample for coating system J.

Figure 7.7 shows the monitoring of three samples with different annealing durations at 400 °C. Hereby, the annealing duration of 5 min corresponds to the incubation time of the previous section, whereas the other two samples are annealed successively longer.

After acclimatization in laboratory air at room temperature, constant delamination velocities are observed for all samples. The velocities are in the order of microns per hour so that they could be monitored over long periods. As can be seen from the measured length l vs. time in figure 7.7, the velocity remained constant up to full delamination. However the delamination velocity increases with increasing annealing time. The experiment has been repeated with an annealing temperature of 300 °C and annealing times of 277 min and 300 min. Again, constant delamination velocities were observed: 0.55 $\mu\text{m}/\text{h}$ and 66 $\mu\text{m}/\text{h}$ respectively. So depending on the annealing temperature, small deviations in the duration from the incubation time can alter tremendously the delamination progression velocity.

The observations confirm that the aging relies on an internal process. An alternative aging via chemical reactions with the surrounding media can be ruled out, as in this case a gradient in the propagation velocity would be expected. In the central part of the sample, the medium exposure time would be much smaller, as access is only given after

delamination occurred. Hence the delamination velocity must be much lower. Contrary, the constant velocity of the delamination progression for each aging temperature over the whole distance up to complete delamination clearly indicates that the adhesion performance is homogeneously decreased over the whole sample, presumably via inner diffusion processes and Fe-precipitation.

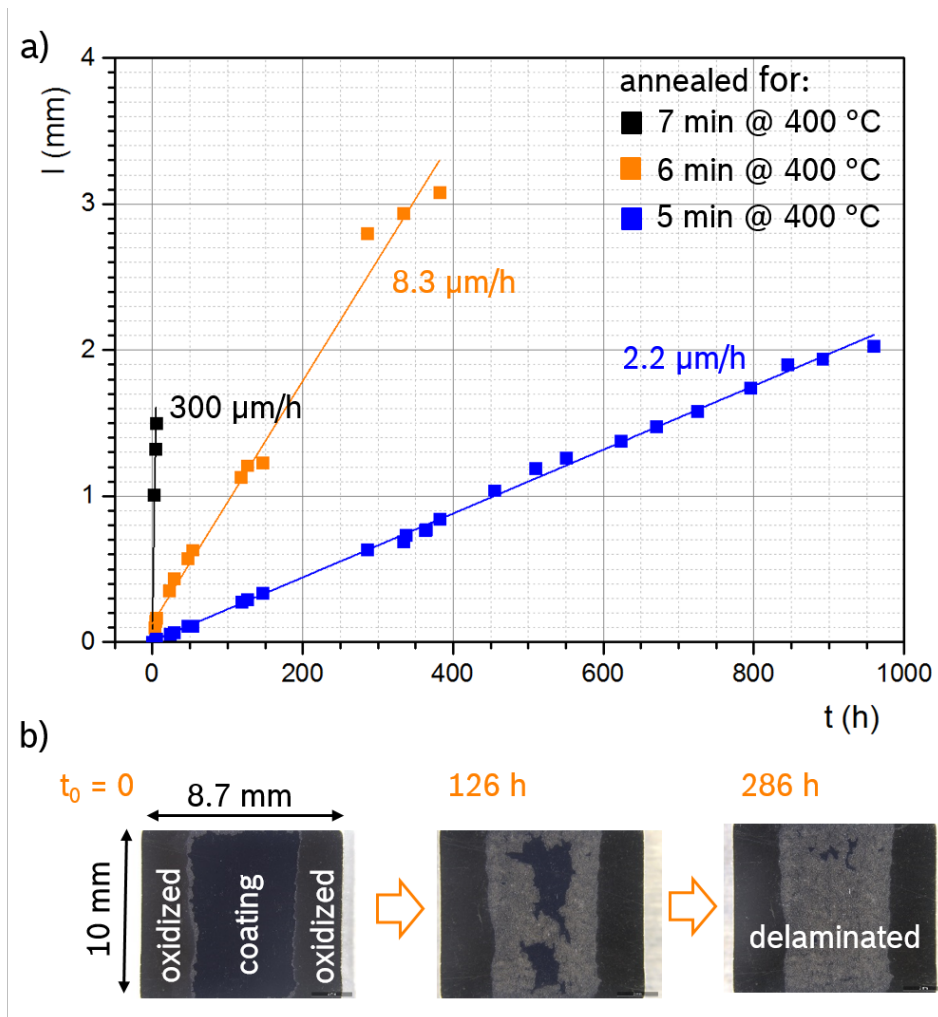


Figure 7.7: a) Delamination length vs. time at RT for the coating after different annealing times at 400 °C: A constant delamination velocity is observed, which increases with increasing aging time. b) Example part (6 min at 400 °C) at different stages: The dark-colored stripes are the two edges, delaminated and oxidized during annealing. The central part is of interest now: The substrate gets successively uncovered (light-colored) at room temperature. The same characteristic spallation pattern arises as observed in figure 7.3.

A continuous increase in delamination velocity with increasing annealing time, indicates furthermore, that the time-dependent step of the cyclic delamination progression is continuously accelerated. The time-dependent step is the retarded crack advance after

spallation, which can either be accelerated by an increased delamination affinity, i.e. a smaller crack is able to initiate the much faster buckling. Or it can be accelerated by a successively increased susceptibility for medium driven crack advance with successively longer annealing time. A successively increased susceptibility for medium driven crack advance can be caused by successively increased amounts of Fe-precipitations in the interface region with increasing annealing time.

In the Rockwell C test, the coatings exhibited the same adhesion performance as compared to the initial as-deposited state, thus the shear strength of the interface region was not significantly decreased. And also in the nano-scratch test, a significant increase in delamination affinity was not observed. However, delamination takes place again via medium driven crack advance in air around the imprint (refer to figure 7.3), as well as starting from the scratch track.

The retarded delamination did not occur without annealing for both tests. A significant decrease in mechanical strength of the interface region via annealing is therefore unlikely, which evidences, that it is the susceptibility for corrosion which is increased via annealing. Due to its self-healing oxide film formation, Ti is very resistant against environmental corrosion. Fe does not form passivation layers, thus the increasing susceptibility for corrosion is a further evidence for the Fe-precipitation.

Influence of Temperature and Medium

In the following the influence of temperature and medium on the progression of delamination is discussed. The samples were annealed at different temperatures until the incubation time, when delamination at the edges was detected. Thereby it is assumed, that regardless of the (T, t_{crit}) -pair, the samples exhibit the same level of lowered adhesion performance as all the pairs lie on the same line in the Arrhenius plot (refer to fig. 7.2). After the annealing, the samples were treated again at different T and under water exposure. Figure 7.8 shows the influence of temperature as well as the exposure to water on the delamination velocity. The room temperature value (RT) is the average velocity of all samples in the incubated state (different T with corresponding t_{crit}). The velocities of

the samples in the incubated state are in the same range for all $T-t_{\text{crit}}$ pairs. This confirms the assumption that the samples are in the same condition regarding the adhesion performance and presumably the amounts of Fe-precipitation.

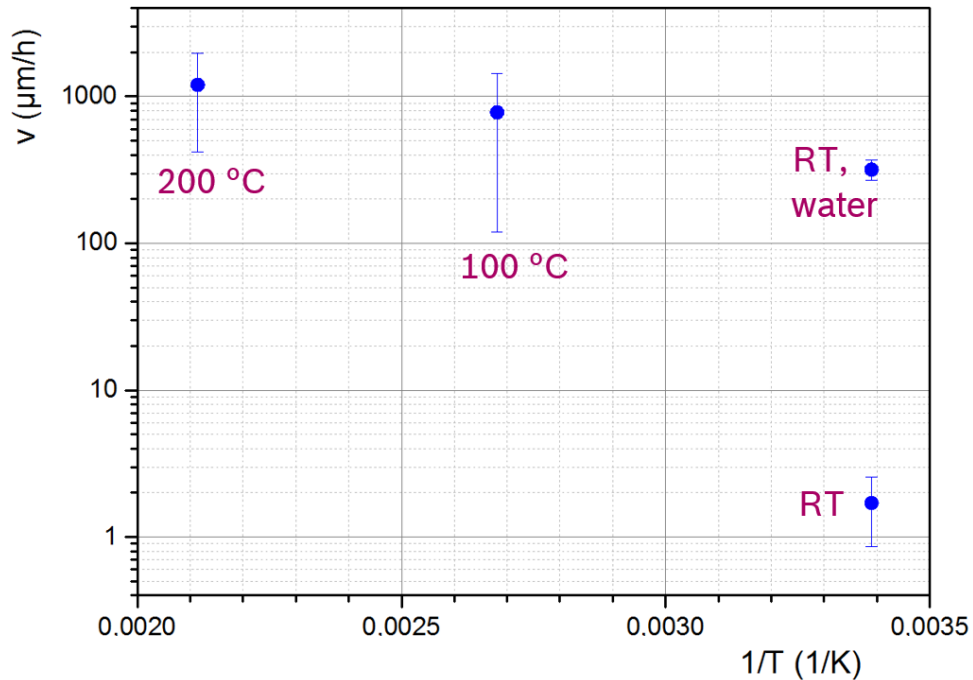


Figure 7.8: Influence of temperature and medium on the delamination velocity: At 100 and 200 °C as well as exposed to water, the velocity is increased by at least two orders of magnitude compared to the (dry) room temperature state RT. Error bars correspond to standard deviations arising from test repetitions.

Additional to room temperature, the progression velocity was measured at 100 °C (annealing conditions: 400 °C, 5 min) as well as 200 °C (ann.: 325 °C, 58 min) by putting the samples again on the heating plate for some minutes. The velocity is increased by more than two orders of magnitude. During this second heat treatment, a part of the intrinsic stress is released temporarily caused by the different thermal expansion coefficients of substrate and a-C:H. The effect of accelerating the retarded crack propagation is observed to be dominant however.

After cooling to room temperature, the initial delamination velocity is observed again. The second thermal treatments at 200 and 100 °C thereby did not significantly change the adhesion performance, as expected from the Arrhenius plot: At the low T , the time scale is large, whereas the duration of the second annealing step was a few minutes only. A similar acceleration of the delamination progression is observed for samples during

exposure to water at room temperature (ann.: 330 °C, 46 min; 340 °C 23.5 min): The velocities are again two orders of magnitude higher. The effect was verified for tap water as well as deionized water with no obvious difference. After the exposure, the dried samples exhibit the RT velocity again as shown in figure 7.9. This is consistent with the presumed mechanism: The medium acts on the crack tip only. Furthermore it can be concluded that a significant penetration of gas and water through the coating or along the interface was not possible. Otherwise the velocity after exposure should stay increased, as molecules or atoms of the corrosive species would already be acquired after the exposure to the medium.

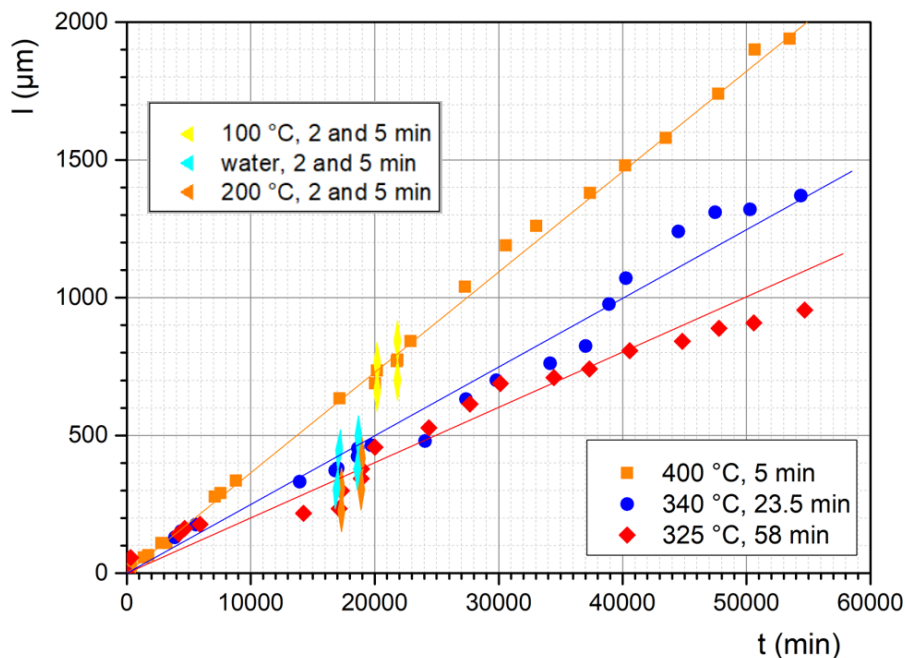


Figure 7.9: Reversible acceleration of the delamination velocities via exposure to 100 and 200 °C, as well as exposure to deionized water. Exposure durations are 2 min and 5 min each, arrows indicate the slope in the accelerated state. Initial velocity (dry, RT) reconstitutes after the exposure with more or less scattering, which however lies in a lower order of magnitude compared to the acceleration via exposure experiments.

In figure 7.10, SEM-images of a sample in the incubated state are presented after water exposure and corresponding advanced delamination. Two different characteristic patterns are observed.

The first pattern was formed at laboratory air at room temperature with the characteristic annular segments missing in the Ti adhesion layer. A second, similar pattern arises

from the exposure to water as a continuation of the previous pattern, however this time the annular structures are raised on top of the surface level of the adhesion layer. The annular shape is slightly less well defined, but the width of the annular half rings is nearly the same for both patterns.

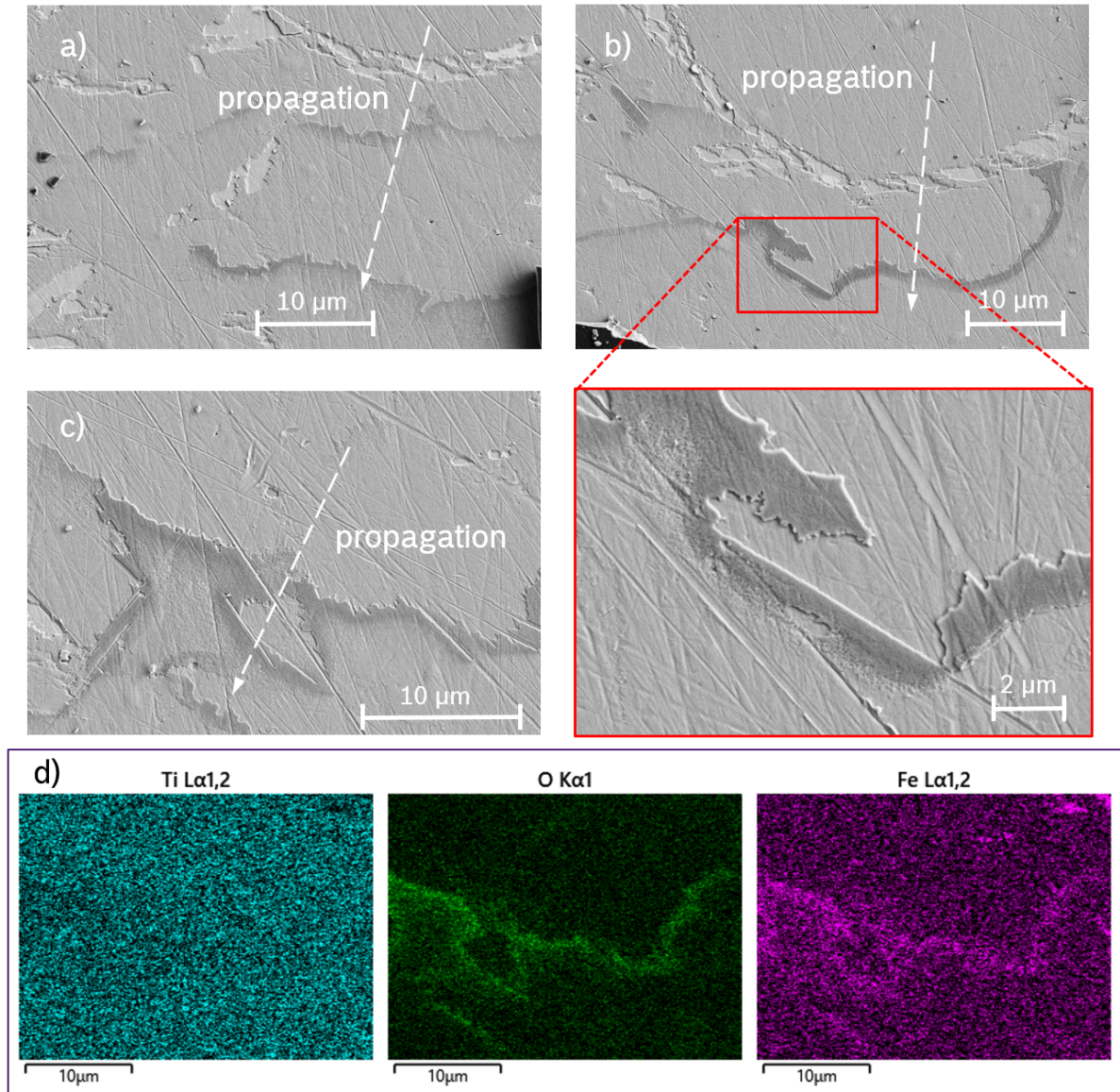


Figure 7.10: Characteristic pattern via exposure to deionized water. a), b) Former progression at air during incubation time can be well discriminated from the progression via water exposure: Former is characterized by missing adhesion layer in the annular areas, whereas raised structures with darker appearance prevail at the latter. c) Further close-up with EDX-analysis in d), uncovering oxidation of Fe.

Figure 7.10 d) shows the EDX analysis of position c), which indicates that the raised structures consists of some sort of Fe-oxide or hydroxide. Other parts of the adhesion layer surfaces are unaffected as well as the already uncovered steel surface.

The locality of the grown Fe corrosion compound evidences a crevice or filiform corrosion, which progresses underneath the DLC and lets the residual crack from spallation grow. The corrosion products will not support the adhesion of the coating. Once the critical radius is reached, the coating buckles and the locally enhanced corrosion is stopped by the vanishing of the crevice during rapid buckle growth. The buckle grows until the spallation radius is reached again.

The results confirm that there is a high influence of the surrounding medium on the time limiting process between spallation and buckling. The velocity of this process is accelerated significantly with temperature and by changing the medium from laboratory air to water. In air, an embrittlement of the uncovered adhesion layer via oxidation can be associated with the retarded crack growth, which relies on a creep under shear stress. Temperature influence is supposed to rely on an acceleration of the underlying diffusion and chemical reactions. Exposure to water alters the type of progression to an electrochemical crack advance.

The findings confirm that the Fe-precipitation associated with the thermal aging is a precondition for the medium driven delamination.

7.3 Post Mortem Oxidation of Titanium

In the experiments on the heating plate for system J, freshly uncovered adhesion layer was found to be always silver in color. Only subsequent to delamination and further thermal treatment, a fast, continuous shift in color occurs. The color change was monitored at a temperature of 330 °C, some representative pictures are shown in figure 7.11. The titanium colors can be correlated to the thickness of the oxide layers. This is done with the data from [137] and plotted versus time in the graph in figure 7.11. A linear growth rate of 0.40 nm/min is derived.

The linear curve has its origin at the incubation time and not at zero, emphasizing that the oxidation is only subsequent to the delamination, once more confirming, that the a-C:H coating acts as an oxygen barrier. At the residual crack tip after spallation however, the oxygen has access and is supposed to drive the crack propagation within the

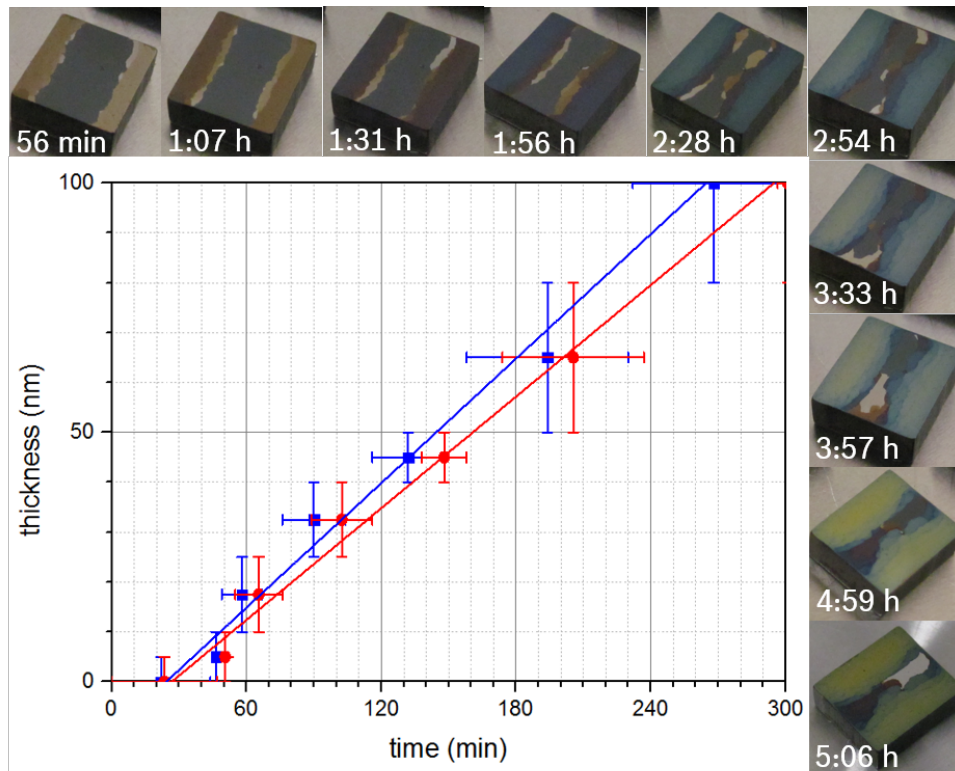


Figure 7.11: Post mortem oxidation of the Ti-layer: Representative time steps are shown. The color is correlated with the thickness of the oxide and plotted versus annealing time. A linear growth of thickness of the oxide layer is determined for both edges (blue and red in the graph).

adhesion layer system via embrittlement of the material at the crack tip, resulting in the cleavage of the annular parts of aged adhesion layer.

7.4 Passivation of Pre-Damages

Thermal annealing of all the coating systems with a single Fe-containing Ti adhesion layer lead to a decreased adhesion performance with much evidence, that this is caused by Fe-precipitation. A decrease in shear strength of the interface regions, which would enhance primary buckling, was not detected for any of the systems.

For the ta-C based coatings (systems A, B and C), the decreased adhesion performance manifests in an increased delamination affinity expressed by secondary buckling in residual stress fields within the coating. For system J with an a-C:H functional layer, the reduced adhesion performance is expressed by a retarded progression of a buckling driven delamination. The instantaneous secondary buckling is not found for system J. This

might be due to the lower intrinsic residual stress in the a-C:H coating, which lowers the delamination affinity.

In this section, it is analyzed, if the retarded delamination occurs also for a ta-C based system. A first indication for a delamination progression via delamination of the Ti layer was found in figure 5.5 of chapter 5, when the progressing delamination surpasses the border of the mixed zone into the outer zone of the residual imprint. At this spot, the driving stress state alters and a significant distance is covered accompanied with Ti delamination, which is comparable to the Ti delamination for system J, when the stress state is altered via spallation.

Analysis is done at coating systems A* and C*. The former is very similar to system A with a small increase in duration of the additionally applied bias voltage for intermixing at the interface between Ti and ta-C. The latter is very similar to system C, but the a-C:H top layer was not applied. All other process steps of sample preparation are equivalent to systems A and C respectively. For the following tests regarding the proof of the environmentally driven damage progression, the mentioned differences are assumed to have no significance.

Figure 7.12 shows results from cavitation erosion tests of coating system A* in the as-deposited and the annealed state. While in the as-deposited state, only a small part of the coating is missing without evidence for delamination or buckling, in the annealed state the coating is completely delaminated along the whole sample surface. The visual extension of the cavitation erosion is however nearly the same. Furthermore, during preparation of another annealed sample of system A* via water cooled mechanical cutting (for further intended experiments), the coating was completely delaminated.

In figure 7.12 c), an area far remote to the water cooled cutting event is shown, where some coating remained adherent. In this particular case two spalled buckles are still attached to the residual coatings at some points, making them observable.

Both experiments show, that the medium driven delamination is very pronounced in the case of the exposure to water. The external mechanical loads of the cavitation and from the cutting tool are thereby only initiating the primary buckling. The water on the other hand is driving the delamination progression via corrosion, combined with the intrinsic

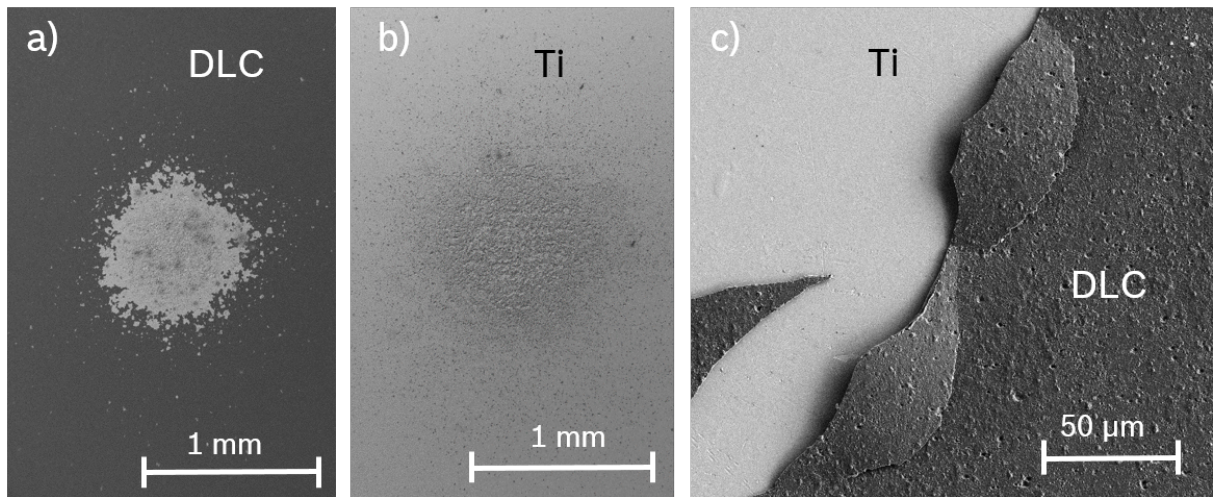


Figure 7.12: Results of cavitation erosion tests of coating system A* a) in the as deposited state and b) in the annealed state. Both show concentric erosion damage, but the annealed sample additional large area delamination. c) Residual coating remote to the damage initiation after large area delamination during water cooled cutting of a sample of system A*. Single spalled buckles are still partially attached to the residual coating, making them observable.

compressive stress, which enables the buckling driven delamination.

Retarded delamination progression at air, as observed for system J, was not observed for system A*. Figure 7.13 a) shows the residual damages from Vickers indentation and scratch tests, which were done months ago for system A*.

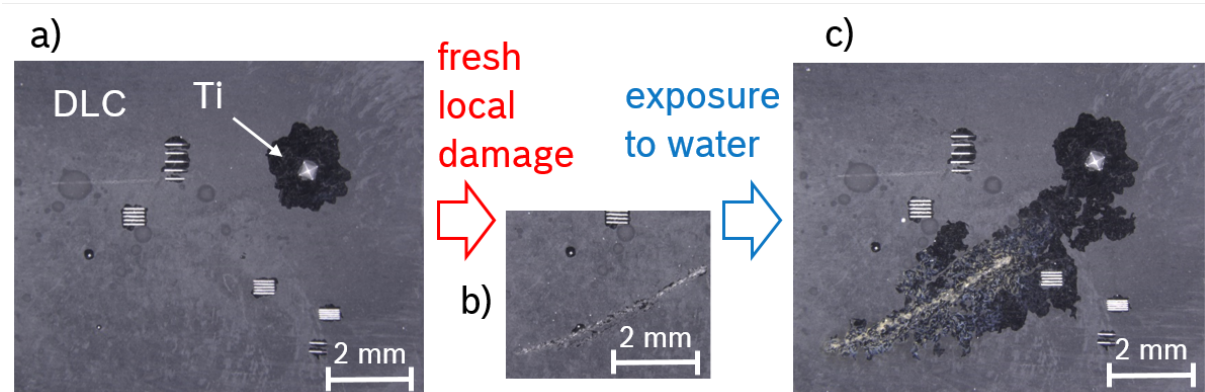


Figure 7.13: Water exposure tests on coating system A*: a) Passivated pre-damages (Vickers imprints and arrays of scratch tracks with some delaminations) do not show delamination progression after exposure to deionized water for 20 min. b) fresh engraving and c) subsequent exposure for 10 min deionized water. Areal delamination progression is observed starting at the engraving.

The delaminated area around the residual imprints of the tests had not been grown, although the residual cracks after spallation are supposed to be initiation points for buckling.

Furthermore, an exposure to deionized water for 20 min did not increase the delaminated area, which contradicts the previously found observations in the sonotrode tests and for the water cooled cutting.

Figure 7.13 b) shows an engraving track, which was additionally introduced. A few primary buckles are observed along the track. The result after subsequent exposure to water of the fresh pre-damage is presented in figure 7.13 c). The exposure to water lead to an immediate, areal delamination progression, starting around the graving track and beyond its region of influence.

The contours of the older pre-damages still exhibit no delamination progression. It can be concluded, that a passivation of the pre-damages occur for the ta-C based coating systems, which does not drive delamination progression, as it was observed for system J. It even hinders the mechanism of water driven delamination. The passivation layer is expected to consist of TiO_2 , which is known for its protective effect.

For system A* medium driven crack propagation thus relies on a corrosion based process. For system J however, accelerated delamination progression was additionally achieved observed during heating. Furthermore, the long time annealing lead to a delamination in the case of system J during the thermal treatment, for system B (ta-C based functional layer) delamination occurred after the thermal treatment.

Two possible hypotheses are reasonable. 1. Aging occurs with the same time scale for systems B and J, but the coating delaminates spontaneously only for system J, since only for system J, oxidation driven delamination progression is possible. Via the much longer aging, which is therefore possible for the ta-C based systems (days in the furnace vs. hours on the heating plate), the high delamination affinity with the observed secondary buckling can be explained.

2. The process of aging can have different time scales for the both systems. E.g. the presumed Fe-precipitation towards the interface between Ti and DLC can be more complicated for the ta-C based coating systems, compared to the a-C:H based systems. This could be due to the lower density of the a-C:H coating or the a-C:H might possess a certain micro-porosity, so that Fe-precipitation towards the interface between metal layer and DLC is eased. Alternatively, the H-content of the a-C:H coating might be relevant

and despite the lack of liquid medium during the thermal treatment, corrosion occurs, e.g. via H-embrittlement of the adhesion layer with H supplied by the a-C:H film.

Figure 7.14 shows the results of the exposure to different media on passivated pre-damages on a sample surface of coating system A*. After exposure to neutral water (from a) to b)), delamination is not observed, confirming sufficient passivation. After a second exposure, this time to diluted HCl solution (figure 7.14 c)), areal delamination has spread over the major part of the sample. The experiment shows that the acid is able to reactivate the passivated surface at the coating edge.

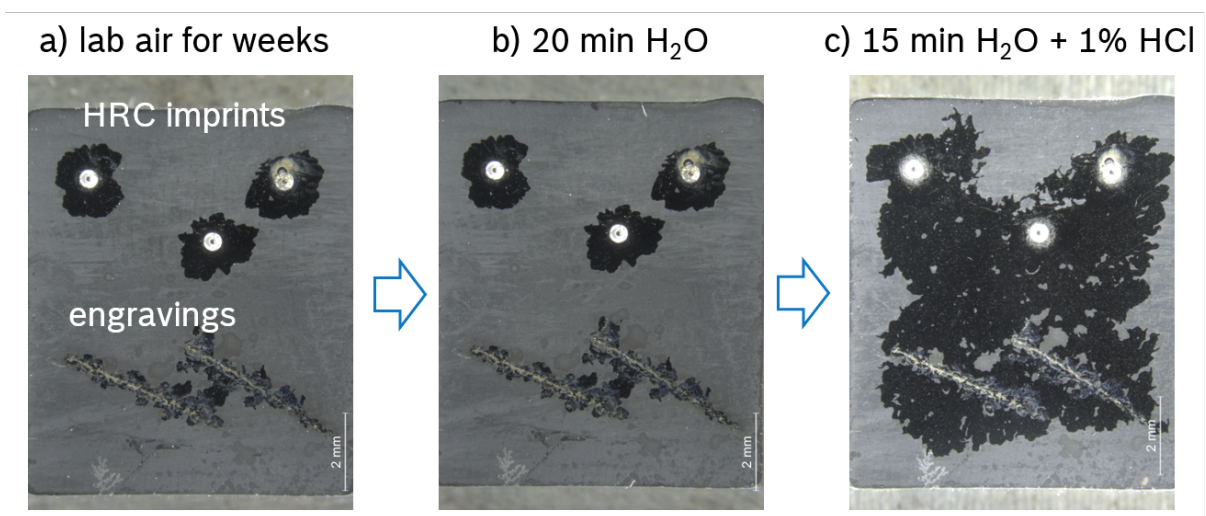


Figure 7.14: HCl exposure tests on coating system A*: a) Passivated pre-damages (HRC-imprints and engravings) with already large delaminated area. b) No delamination progression after exposure to deionized water for 20 min. c) After additional 15 min of exposure to deionized water add with 1 % HCl lead to large area delamination.

After exposure to air with high humidity, the corrosion driven delamination was also triggered. Figure 7.15 shows findings in the SEM investigation on a sample of coating system C* after the humidity test.

The SEM investigations revealed spots, where delamination was stopped via spallation and was re-initiated and progressed. At these spots, where corrosion driven crack advance is presumed, raised structures are observed surrounded by visually intact surface of the Ti layer. At all other locations of uncovered adhesion layer, apart from the spallation edges, corrosion did not occur. Here the delamination is presumed to be buckling driven. The findings evidence, that the high humidity enables a corrosion driven crack advance by the formation of a local electro-chemical cell, analogous to filiform corrosion. Crack

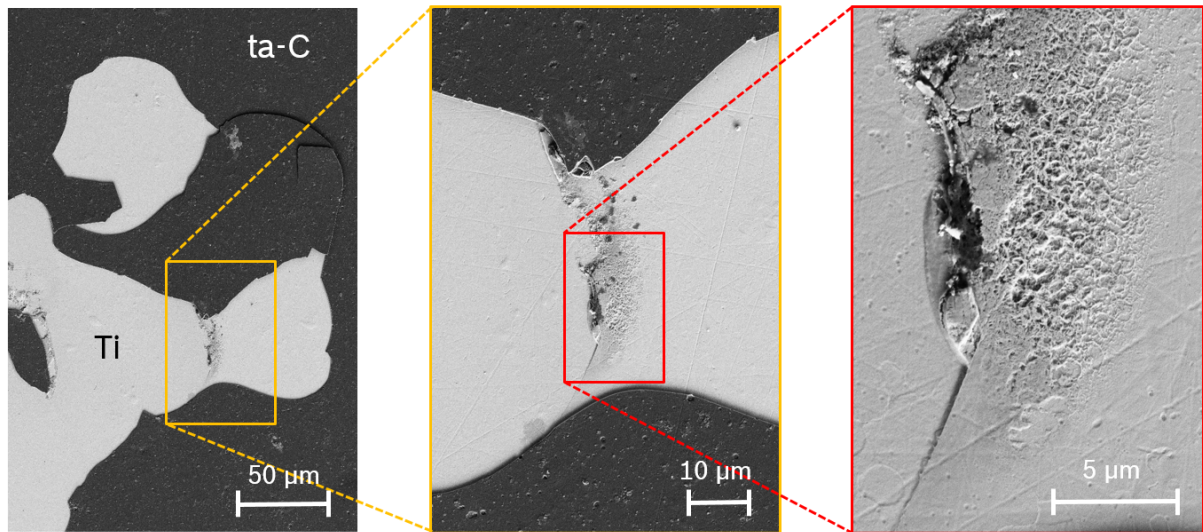


Figure 7.15: Corrosion driven delamination progression for ta-C in coating system C*.

advance is supposed to be driven via the volume expansion close to the crack front by the deposition of the corrosion products of the cathodic reaction or via the anodic metal dissolution directly at the crack front. Furthermore, a strong Fe-signal in the EDX measurement in the raised structure evidences that the corrosion process requires the preceding Fe-precipitation.

In figure 7.16, a similar spot of crevice or filiform corrosion is depicted. In this case, its circular contour resembles the structures found in the investigations of the aged growth defects (refer to chapter 6). A relation of these findings is likely.

EDX-measurements (figure 7.16 b)) confirm that the structure mainly consists of Fe and O. The exact corrosion product cannot be derived from EDX. FeOOH is the usual corrosion product of Fe, which can further react into Fe_3O_4 or Fe_2O_3 . In figure 7.16 c), it can be seen, that the underlying Ti is intact and seems quite unaffected.

The circular structure suggests a growth of corrosion products around a small intrinsic defect at the substrate surface. The shape furthermore suggest that no lateral entrance for environmental media is available and a small void at the most, where the corrosion products can be deposited. So there must have been some access from above through a pinhole for oxygen and water molecules. The filigree texture is supposed to result from the growing of the corrosion products against the subsurface of the DLC, which is presumed to have a similar sub-micro surface roughness.

From the dimensions, the observed structure resembles exactly the cavity, which was

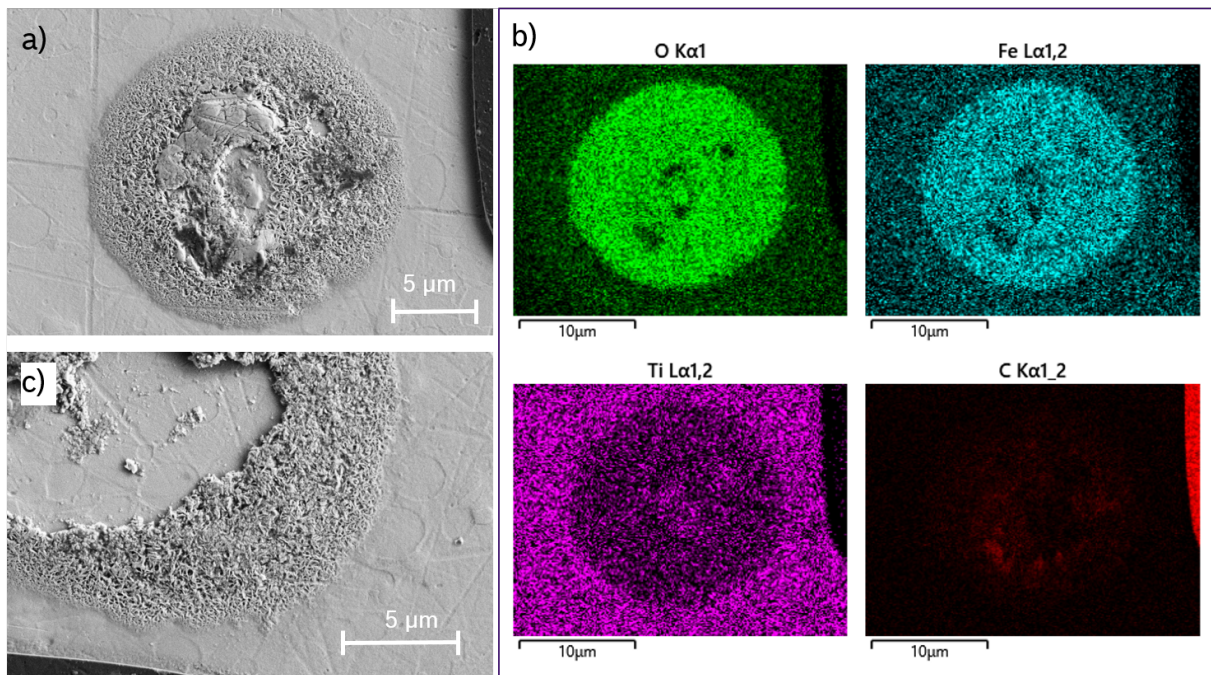


Figure 7.16: Circular grown structure of Fe-corrosion products, observed in the atmospheric corrosion test for the ta-C-system (coating system C^{*}). The circular structure appears to be similar to the ones found in chapter 6 for the a-C:H based systems.

found in the ion milling cut through the annealed sample of system H, at the bottom of the pinhole of a former growth defect (refer to chapter 6). Thus it is possible, that both structures have similar causes. As can be seen in figure 7.16 c), the grown structure does not adhere strongly at the substrate, thus it is likely, that it gets removed during a preparation of an ion milling cut, for which a mechanical cut under water cooling was made. The annealing of the sample of coating system H was performed at a dry atmosphere, thus the exact growth process of an Fe-oxide structure must be different however.

7.5 Conclusions on Thermo-Chemical Stability

In this chapter, a continuous decrease of the adhesion performance for coating system J was demonstrated. As-deposited, the adhesion performance is excellent but the interface region is metastable. With experiments in the temperature range between 300 and 500 °C, an activation energy of 0.55 eV was derived for a continuous reduction of the adhesion performance, attributed to a successive phase transition of a metastable Ti phase into a stable one, accompanied with Fe-precipitation. This internal process occurs homoge-

neously over the whole sample, enabling a medium driven delamination progression.

It was further demonstrated that once a critical aging state is achieved, a progression of delamination fronts occurs systematically even in ambient air at room temperature. Delamination progression was thereby identified to occur as a threefold alternating process of buckling driven delamination, interruption via spallation and medium driven crack advance under shear stress.

The latter is the time dependent step which determines the delamination velocity, buckling on the other hand occurs almost instantaneously. The findings evidenced, that medium driven crack advance relies on a corrosion of the precipitation phases of the adhesion layer. Crack advance is thus accelerated with increasing temperature and via exposure to a corrosive medium. Thereby the cyclic sequence of delamination progression is accelerated as well. Furthermore, the velocity of medium driven crack advance is dependent on the annealing duration, most likely related to the amount of Fe-precipitation and is enabled at a certain threshold (incubation time) and accelerated via successively longer annealing. A similar mechanism was found for ta-C based coatings with the same Ti based adhesion layer concept. A passivation of the uncovered adhesion layer however prevents the oxidation driven crack advance. Exposure to deionized water in the active state or exposure to a dilute HCl in the passivated state however lead also to a fast delamination progression. For ensuring the adhesion performance of a coating system for an application at elevated temperature, both aspects has to be taken into account: Interface regions must be intrinsically stable within the application $T-t$ regions and must be thermo-chemically stable at possible defects in the coating, where environmental media can attack. In the presented analysis it was demonstrated that metastable phases which are able to morph into stable phases might be problematic, especially if this is accompanied with precipitation phases. Fe incorporation is seen as very critical, as it is not soluble in most used metal interlayers and Fe-precipitation phases are prone to chemical attack. Furthermore Fe does not form stable carbides, which could maintain a stable interface.

7.5.1 Consequences for Analysis

The found alternating process of buckling driven delamination, interruption via spallation and medium driven crack growth has also tremendous influence on analyzing and testing. For the delamination velocities at varied temperatures (figure 7.8), the curve flattens towards higher temperatures agreeing with the findings of Falub et al. [105]. This is because, in both cases the velocity of the medium driven crack advance is convoluted with the much faster buckling velocity. For an investigation of the kinetics of the corrosion processes, the much smaller length of the medium driven crack advance has to be considered, leading to much smaller velocities.

For an adhesion performance testing, based on indentation, such as HRC or scratch tests, the surrounding medium has also a tremendous influence on the test results. Humidity must be controlled for standard tests. Furthermore, to cover the whole scope of adhesion performance, the tests have to be extended by exposure to relevant media and a prolonged observation of a possible retarded delamination progression.

For system J, HRC and nanoscratch test evaluated excellent adhesion performance for the as-deposited state, but also an excellent adhesion after annealing treatment. The decisive difference observed however, is the time dependent behavior after the tests, as medium driven crack advance is enabled in the annealed and disabled in the as-deposited state.

A reasonable method for lifetime estimation [70] includes a post treatment within a corrosive medium similar to the later application environment and measuring of the delamination velocity. For an application at elevated temperatures, it must further be tested if critical phase transitions with relevance for the adhesion performance, can occur. These are two distinct aspects.

With the spallation radius, the intrinsic stress of the coating was estimated with a good agreement to the curvature test. Thus the behavior of system J can be utilized as a measurement technique of the intrinsic stress, directly on complex parts coated with an a-C:H coating. For an application, the adhesion layer system must be replaced by the Fe-containing Ti layer for the test part. Thermal annealing enables the delamination and a measurement of the spallation radius, from which the intrinsic stress can be evaluated.

Chapter 8

Summary and Conclusions

In this work, nine different adhesion layer systems for DLC coatings were investigated concerning their suitability for tribological applications at elevated temperatures. The adhesion layer systems have been successfully assessed by introducing the *adhesion performance* as a novel concept for assessing the risk of an adhesive failure of DLC coatings in a given application.

With the coating system design, different concepts have been tested with respect to their adhesion performances. The assessment was done by a combination of detailed SEM-analysis of damages produced via common adhesion tests (HRC and nanoscratch tests) and analysis of the introduced stress fields, derived via simulation. The interrelation to structural aspects of the adhesion layer systems was drawn via cross-sectional TEM analysis. Furthermore, the stress field nanoscratch test was introduced as a reliable test of the delamination affinity of a coating system, i.e. its tendency for a delamination progression via secondary buckling. In order to analyze the cyclic fatigue behavior of the adhesion layer system, skewed cylinder tests and cavitation erosion tests were performed at exemplary coating systems.

With thermal annealing tests in the range of 300 to 500 °C, the thermal stability of the adhesion layer systems was tested. Furthermore, the complex mechanism of delamination progression was analyzed via tracking of the delamination velocity under different conditions and via microscopic and SEM-analyses of the coatings after different thermal and chemical treatments.

In the following, the results of this work are summarized and conclusions are drawn, divided up into three parts. In part one, the model for the adhesion performance of DLC coatings is presented (section 8.1). Part two covers the results and conclusions for a holistic and reliable evaluation and quality control with respect to the adhesion performance (section 8.2). In this context, also the assessment of the tested adhesion layer systems is shown. Part three covers the conclusions for a general layout design for an enhanced adhesion performance (section 8.3).

8.1 New Concept: Adhesion Performance

Based on the perceptions of this work, it can be stated that the common concept of *adhesion* as a mechanical design parameter for DLC coatings is premature. In this work, therefore the term *adhesion performance* of coatings under compressive stress is introduced, which comprises the resistance against primary buckle initiation, against buckle growth and against initiation of secondary buckling. Figure 8.1 schematically shows the corresponding holistic model, derived in this work.

For compressively stressed thin films such as DLCs, the elastically stored strain energy enables buckling driven delamination, which is the most important mechanism for this coating type related to the adhesion performance. It was found to be convenient to distinguish between the susceptibility to the introduction of a primary buckle and the *delamination affinity*, which describes the tendency for secondary buckling.

Under typical application and testing conditions, primary buckling is introduced by brute force in mode II, acting against the mode II fracture strength and toughness of the whole adhesion layer system. Secondary buckling is a re-initiation of buckling after spallation and leads to a spread of the delamination. It typically occurs remote from an initial brute force event and is instead driven by the intrinsic residual stress. During the re-initiation the intrinsic stress acts in shear mode at the crack tip of the remaining residual cracks of preceding buckling events and is opposed by the mode II fracture toughness. Surrounding media which now have access towards the crack tip can influence the crack growth decisively. Both mechanisms, primary and secondary buckling, will be explained in more

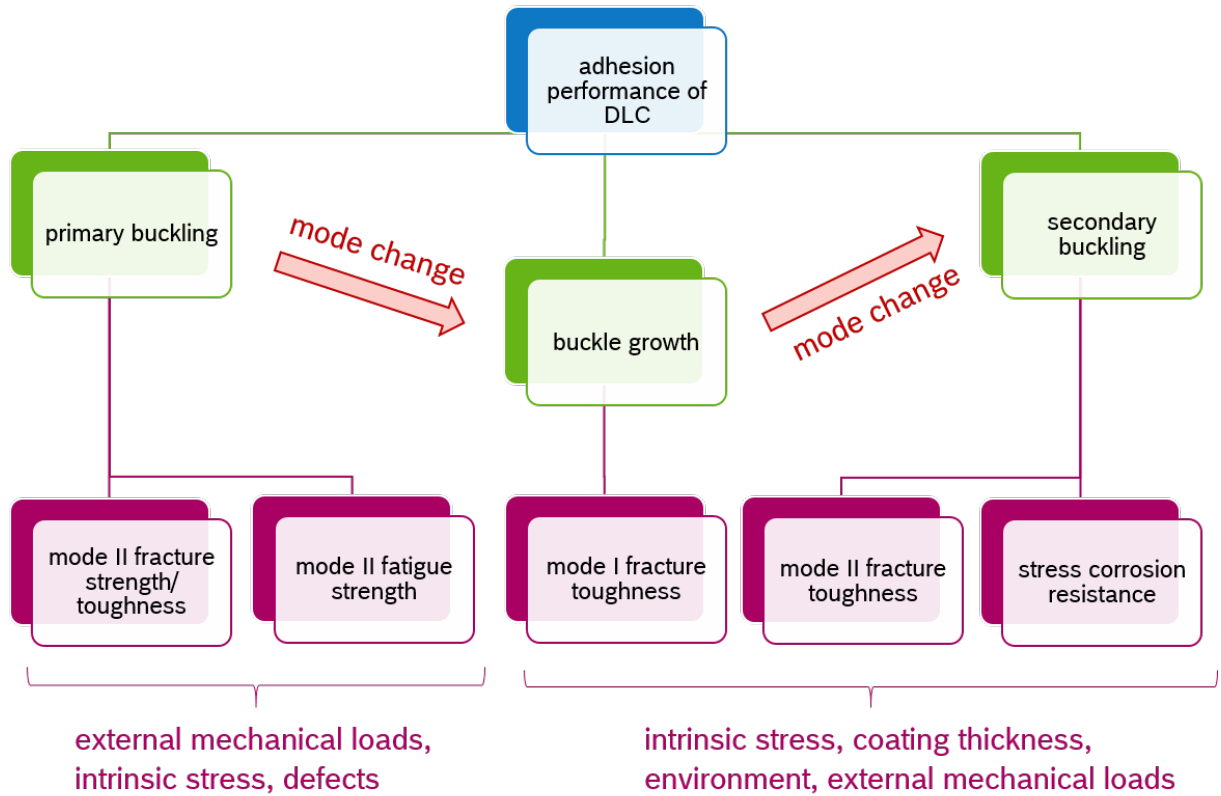


Figure 8.1: Holistic model for the adhesion performance of compressively stressed thin films: Adhesion performance comprises the resistance against primary buckle initiation, against buckle growth and against initiation of secondary buckling. The necessity of this distinction is based on the mode-changing character of the buckling. All three failure modes can be attributed to distinct properties of the adhesion layer system. The mode II fracture strength and toughness are the decisive parameters for the initiation of an adhesive failure. Regarding buckle growth, the mode I fracture toughness is most important and the resistance against secondary buckling manifests in the mode II fracture toughness, environmental effects can influence the crack growth, if corrosion is possible.

details in the following.

The erection of a buckle is a purely elastic relaxation of a part of the coating. Therefore, the susceptibility to primary buckling depends on the likelihood for the formation of a crack with critical size a_c , where buckling sets in. However, this susceptibility is not exclusively determined by the strength and toughness of the interface region, but also by the size of a_c . The key point is, that the sum of residual and external load is not only acting against the interfacial strength, but also decreases a_c and thereby the critical distance the crack must grow. This is especially important, if crack growth relies on the additional external load and if the range of the introduced shear stress is in the same order of magnitude as a_c .

For an initial crack with penny-shape form, a_c can be estimated with the reordered equa-

tion for the critical stress according to Evans and Hutchinson [4]:

$$a_c = h_f \cdot \sqrt{\frac{k \cdot E_f}{12 \cdot (1 - \nu_f^2) \cdot (\sigma_0 + \sigma_{ext})}} \quad (8.1)$$

As can be seen, a_c increases linearly with the film thickness because the film becomes stiffer and a_c decreases with increasing residual and external compressive stress ($\sigma_0 + \sigma_{ext}$). Tensile stresses however would act in the opposite direction and hamper primary buckling. It was shown that under typical testing and application conditions, primary buckling must be initiated via shear load, for which crack propagation is quite inefficient since the mode II fracture toughness is typically very high for brittle materials [138]. However crack initiation is facilitated at defects and for the crack growth under shear loading, the plasticity of crystalline phases within the adhesion layer system can play a major role, which relies on the movement of dislocations, which can be generated at the interfaces [139, 140]. It was shown, that planes with a low shear stress, such as the planes between stacked graphene sheets are therefore weak spots and are able to initiate primary buckling. Furthermore, shear stress is generally increased where the symmetry is broken, i.e. at defects or coating edges.

On the other hand, without a plane with low mode II fracture toughness, the analyses in chapters 4 and 5 indicated that primary buckling is prevented by a too large a_c or is restricted to the location where a higher compressive stress reduces a_c sufficiently, e.g. directly at the track of a nanoscratch.

For reciprocating contact conditions, it was shown, that a cyclic loading can weaken the strength of the interface region in terms of fatigue. The high modulus of the coating transfers a high share of the stress towards the adhesion layer system below the coating or even to the substrate surface. If the fatigue strength is exceeded, an accumulation of micro cracks is presumed to enable buckling of the coating after the corresponding cycle time. Additionally, the cyclic loading decreases the critical crack size cyclically according to equation 8.1.

Once a primary buckle is initiated, tensile stress occurs at the adhesion layer system (refer to section 2.5.2). If the initiation occurred within a crystalline phase, crack growth can be decelerated via plastic zone formation at the crack tip. However, crack growth can also

progress at an alternative, brittle interface. Then, the buckle grows until spallation.

It was found, that after spallation a crack with a very defined size remains, which is a potential pre-crack for further delamination via secondary buckling. At the breaking edge of the coating, the intrinsic residual stress is not opposed, which leads to a shear stress. Secondary buckling is initiated, if the crack grows up to the critical buckle radius, which is again determined by the coating thickness and the residual stress, however it can be slightly different from a_c , as the considered coating segment is not spherical anymore, but resembles a half moon (refer to chapter 7). The delamination affinity is now determined by the difference in size of the residual and the critical crack size, by the load at the crack tip and by the mode II fracture toughness of the adhesion layer system.

Crack advance under the mode II loading can again occur at a different plane compared to the crack advance during buckle growth. In this case the secondary buckle forms, if the total size of the deflected crack reaches the critical value.

From the findings in chapter 7, it can be stated that the difference in residual and critical crack length for buckling re-initiation can be very small. The observed patterns indicated a value of below $2\mu\text{m}$ for the given cases. There are several possibilities to overcome this distance. E.g. the compressive stress can be increased, which decreases a_c . This is exploited in the stress field nanoscratch via mechanical pre-loading. Furthermore, crack advance can be driven by cyclic loading, e.g. with a reciprocating counter body or via cavitation erosion. Since a pre-crack is already present after spallation and the surrounding media have access towards the adhesion layer system, stress corrosion can drive the initiation of secondary buckling, if a part of the adhesion layer system is susceptible. In contrast, it was found that a passivation of the adhesion layer can prevent this mechanism (refer to chapter 7).

The concepts so far are related to the as-deposited state. If thermal stability is not given, the adhesion performance can change during applications at elevated temperatures. E.g. in this work, it was shown that the susceptibility for chemical attack can change during thermal annealing. This was attributed to the formation of Fe-precipitation, resulting from the segregation of metastable intermetallic phases, which resulted from the plasma deposition at low deposition temperatures with limited surface diffusion. The adhesion

performance thereby becomes a function of preceding annealing time and temperature. Much evidence has been found, that the Fe-rich precipitation phases are negatively influencing the adhesion performance by increasing the delamination affinity. I.e. secondary buckling was eased, which can be attributed to the fact, that Fe, when precipitated towards the interface is not able to form stable carbides (positive Gibbs energy) and furthermore the corrosion resistance is decreased by the presence of Fe. This is presumed to accelerate a crack advance via stress corrosion cracking. It was shown, that the aging process followed the Arrhenius law with a certain threshold, where this mechanism was observable, presumably via successive increase in amount of Fe-precipitation.

The holistic model explains very well the frequent observation, that an acceptable result in common adhesion tests does not guarantee that extensive delamination of a coated part will not occur, even without heavy loading. This is because initiation of primary buckling is the by far toughest part of the delamination process and thereby for the testing. Under common application conditions, as well as for common adhesion tests, when a pull test is not applicable, a quite large crack must be initiated under shear load only. However, if this is somehow achieved, crack growth under buckling conditions is rapid and also secondary buckling can be fast because a preexisting crack must be advanced only a small distance. Hence the potential for large area delamination might be high, but it is not easy to detect.

Furthermore, a misinterpretation of the analysis of a damage progression is likely, since the greater share of the delaminated area was formed by buckle growth under tensile loading. Preventing buckle growth however would require to improve the mode I fracture toughness of the adhesion layer system, which is a very tough task. On the other hand, large area delamination is completely prevented by preventing primary or secondary buckle initiation, for which only the mode II fracture strength or fracture toughness has to be large enough. It was demonstrated, that the focus of the analysis must therefore be on the spots where buckling is initiated once and re-initiated several times. This is aside from the large area where buckle growth occurred. The fracture origin is supposed to be located at defects or at a spot of a load exaggeration. The re-initiation spots can be visible, e.g. when for the crack advance, the plane is changed (chapter 7).

8.2 Holistic Measurement of Adhesion Performance

For a reliable assessment of the adhesion performance, either the relevant, often anisotropic, properties of the adhesion layer system (i.e. mode II fracture strength, mode II fatigue strength, mode I and II fracture toughness, as well as intrinsic residual stress, coating thickness and susceptibility for corrosion) have to be evaluated or alternatively, model tests have to be performed considering primary and secondary buckling.

In figure 8.2, a flow chart is presented in which a holistic procedure for the determination of the adhesion performance of the considered system of DLC coatings for automotive applications and beyond is suggested. The test procedure forces primary buckling initiation in step 1 and secondary buckling in step 2, while other aspects like thermal and chemical stability of the adhesion layer system are determined by changes in the buckling behavior depending on the pre- and post-treatments.

The as-deposited resistance against primary buckle initiation is tested via the introduction of high shear stress below the functional coating into the adhesion layer system. Plastic deformations and introduction of in-plane tensile stress must be kept as low as possible, in order not to obstruct possible delamination progression via buckle growth or secondary buckling. Therefore a nanoscratch is suitable, based on its lateral force component and small normal load. A fatigue test, e.g. the skewed cylinder test, yields an analysis of the cycling fatigue behavior, which is not accessible with static tests. Hence, if fatigue is application relevant this has to be tested in parallel. Since crack initiation is achieved within a larger extended area in a fatigue test, this can also be used as a pre-damage for the measurement of secondary buckling.

An increase of the compressive stress (step 0.2) is recommended. With the stress field nanoscratch in chapter 5, an adequate set-up was achieved by the introduction of additional compressive residual stress into the coating system in a separate pre-loading step. With a pre-loading (in advance of step 1 or during), primary and secondary buckling are provoked likewise by decreasing a_c . If the additional loading is performed subsequently to step 1 (post-loading), secondary buckling is enhanced only. A high load indentation

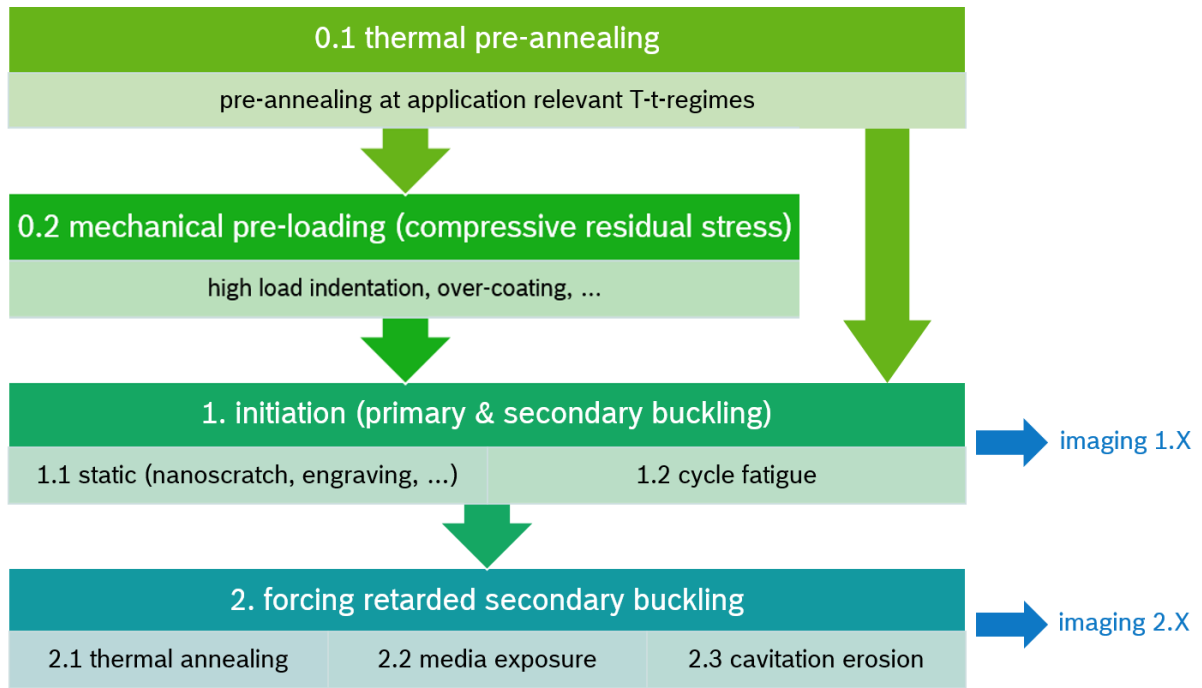


Figure 8.2: Flow chart of the suggested adhesion performance test: 0. optional pre-loading (0.1 thermal, 0.2 mechanical), 1. main step, i.e. interfacial damage initiation (static or cyclic), 2. acceleration of the retarded delamination. The blue arrows indicate the necessity for imaging. Comparison of image 1 with image 2 yield an estimation of the delamination affinity. Thermal stability is tested by comparing the results w/ and w/o thermal pre-treatment.

for instance can provide a local increase of the compressive residual stress with a good range, as performed in the SFNS. This step can be difficult for tiny parts, however the indentation load can often be adjusted to the part geometry. Alternatively, with a set-up of several nanoscratches with small distances between each other, the nanoscratches can provide both, pre-loading and primary buckle initiation. Depending on the part properties and geometry it is also possible to introduce compressive stress via mechanical loading, bending or via substrate compression at low temperatures, presuming the thermal expansion coefficient of the substrate at the cooling temperature being larger than the one of the coating. Load of the coating can be further increased by increasing the coating thickness or by applying an additional top-layer [89] with increased compressive stress. However it has to be considered, that the increasing thickness also increases a_c .

In chapter 7, it was shown that an aging of the interface can occur and decrease the adhesion performance successively. This is independent of the initial adhesion performance and is not accessible for a measurement in the as deposited state. The thermal stability of the adhesion performance can be assessed via thermal pre-annealing (step 0.1) and

comparison of the results of the subsequent measurement (step 0.2 if possible plus step 1) with the results without this thermal pre-treatment.

As the delamination progression can be retarded (refer to chapter 7) and only occurs via medium driven crack advance, this aspect must as well be tested, which is done in step 2, performed in both, the as-deposited and the annealed state with the pre-damages of step 1 as origins.

Retarded delamination progression can be accelerated with adequate critical media or again via temperature. However, chemical treatment has the advantage that the results can be distinguished from a possible thermal aging of the interface region, an impenetrability of the coating for the medium presumed. A more elaborated method for accelerating potential delamination progression is the sonotrode test. Besides cavitation erosion of the coating itself, also the interface region is cyclically loaded. Possibly, a fatigue corrosion cracking is activated as well. The sonotrode test can also be used for introduction of the initial damage, but this can be time-consuming. With a pre-damage introduced by other means the testing duration is possibly decreased.

Table 8.1 shows a suggested scale for the adhesion performance assessment with the above stated holistic test. The scale is divided into three categories related to mechanical stability, retarded delamination progression and thermal stability of the adhesion performance. If temperature and environmental influence are application relevant, it is required that all three categories are considered and the assessment of a coating system can be indicated by a triple of M-, R- and T- grades.

Grade M1 stands for pristine mechanical adhesion performance, i.e. neither secondary nor primary buckling occurs, even with the pre-loading of step 0.2 analogous to the SFNS. This was the case for coating systems D, G and J in the as-deposited state. PVD and PECVD are obviously able to provide strong interfaces, that are able to resist primary buckle provocation tests. Coating systems D and E in the annealed state were also rated M1, which indicates excellent thermal stability for system D and an increase in adhesion performance via thermal annealing for system E, which is not rated M1 in the as-deposited state.

Table 8.1: Threefold scale of the adhesion performance. The M-scale represents mechanical stability, the R-scale the retarded buckling behavior and the T-scale the thermal stability. Depending on which steps are performed (indicated by the “x”) and on the corresponding results, the analyzed adhesion system can be evaluated. The signs in the result columns have the following meaning: “x”: occurred; “-”: did not occur; “=”: same result as without step 2 (R-scale) or step 0.1 (T-scale) respectively; “>”: more pronounced; “≥”: same result or more pronounced; “opt.”: optional step enabling evaluation of the annealed state (step 0.1) or refinement of the scale (steps 0.2).

category	steps				result		coating systems
	0.1	0.2	1	2	primary buckling	secondary buckling	
M1	opt.	x	x	-	-	-	D, G, J, D _{an} , E _{an}
M2	opt.	x	x	-	x	-	H, G _{an}
M3	opt.	-	x	-	x	-	A, H _{an}
M4	opt.	x	x	-	x	x	B, C, E, F, C _{an} , F _{an}
M5	opt.	-	x	-	x	x	A _{an} , B _{an} , J _{an}
R1	opt.	opt.	x	x	=	=	A to J, D _{an} , E _{an} , F _{an}
R2	opt.	opt.	x	x	>	=	G _{an} , H _{an}
R3	opt.	opt.	x	x	≥	>	A _{an} , B _{an} , C _{an} , J _{an}
T1	x	opt.	x	opt.	=	=	D, E, F
T2	x	opt.	x	opt.	>	=	G, H
T3	x	opt.	x	opt.	≥	>	A, B, C, J

For grades M2 and M3, secondary buckling does also not occur, but primary buckling can be initiated in step 1, however the pre-loading of step 0.2 is necessary for primary buckle initiation in category M2. In this case, it is useful to estimate the amount of total compressive stress, which was present at the initiation point. This requires some simulation effort. Examples for grade M2 are systems H in the as-deposited and system G in the annealed state, where primary buckles were generated in the HRC-test, but not clearly in the single nanoscratch test. This behavior was attributed to weak spots in the adhesion layer system – carbon channels in system H (refer to figure 4.10) and thermal defects in system G_{an}. Note that there is much evidence, that only in the presence of such pronounced weak spots, a single indentation test can provide an extended stress field and the primary buckling initiation at the same time. Examples for M3 are system A for which primary buckling is initiated by a single nanoscratch test and system H in the annealed state with primary buckling around thermal defects.

Grades M4 and M5 are characterized by the formation of secondary buckling with mechanical pre-loading (M4) or without (M5), respectively. If secondary buckling is sufficient, the adhesion energy may be determined according to the procedure of chapter 5. This was

possible for systems B, C and E (all rated M4) with different intensity of the secondary buckling and values for critical strain energy release rate of 7.7, 11 and 15 J/cm². The combination of high Fe contents in the Ti adhesion layers and the high intrinsic stress is supposed to be the reason for the increased delamination affinity. System F is also categorized M4 in the as-deposited as well as in the annealed state. This behavior is attributed to the horizontal carbon layers as weak planes (refer to figure 4.6) and the TiC barrier layers against disadvantageous diffusion processes during thermal annealing.

The annealed coating systems A, B and J are rated M5. Single nanoscratch testing initiated secondary buckling in system A, whereas buckling driven delamination was initiated via thermal annealing in systems B and J. In all three systems, this was attributed to the Fe-precipitation from the Fe-containing Ti phase.

It was shown that for some coating systems, a retarded delamination progression can occur and furthermore, that this progression can be accelerated by certain critical media or via temperature, if the adhesion layer system is prone to corrosion. It should be noted that air with a high humidity can already be a critical medium. This process of medium driven delamination progression can be decisive for the life-time of a coated part and is indicated by the R-scale.

For grade R1, chemical stability against the tested medium is given, which is determined by the absence of secondary buckling along the pre-damage of step 1 under exposure to the corresponding medium and also no additional primary buckling occurs. Chemical stability against water and laboratory air was given for all samples in this work in the as-deposited state. Additionally, coating system D to F showed no susceptibility to medium driven delamination in the annealed state, which is attributed to the carbide interlayers which represent a barrier layer for the precipitated Fe, so that it does not influence the adhesion performance.

For grade R2, retarded primary buckling can occur. Indications for this behavior are found for the annealed coating systems G and H. For system G, an additional primary buckle was observed after re-inspection of the residual imprint of the HRC test several days after the first analysis and for system H, thermally induced primary buckles are observed around former growth defects. The Fe content in the Cr-based layers is less than

compared to the Ti adhesion layers of the other systems and the binary phase diagram of Cr and Fe shows a spinoidal decomposition which might explain the less severeness of the thermal degradation compared to the Ti-system, where no Fe is soluble in Ti up to 857.5 K [125].

Grade R3 means a strong susceptibility for medium driven delamination progression, characterized by the activation of secondary buckling in step 2. The coating can delaminate rapidly under the exposure to the corresponding medium, driven by buckling and corrosive re-initiation of the buckling after spallation (refer to chapter 7). This was found in the annealed state for all systems with Fe-contaminated Ti adhesion layer and without barrier layer. In this work it was concluded, that the Fe precipitated during the thermal annealing, which decreases the chemical adhesion performance tremendously. For a refinement of the R-scale, the delamination velocity and the corresponding treatment of step 2 can be indicated for samples with R3 rating.

Thermal stability can be rated by a comparison of mechanical and chemical stability in the as-deposited and the annealed state. For a grade T1, the pre-annealing has no influence on the M- and R-ratings. The analyzed coatings with carbide interlayers as barrier layers belong to this category. T2 corresponds to a decreased resistance against primary buckling initiation. Systems G and H with Cr-based adhesion layer and seemingly insufficient barrier layer showed this medium thermal stability. Grade T3 indicates a severe decrease in adhesion performance via thermal treatment in terms of an increased occurrence of secondary buckling and/or an increased susceptibility for medium driven delamination progression. For a refined scale within the T3-grade, the corresponding temperature, dwell time and resulting M-/R-scale can be indicated. Systems A, B, C and J, the systems with single Ti adhesion layer are all rated T3, since the thermal annealing eased both, secondary buckling and medium driven delamination.

Note that for a coating system which is not of quality T1, the M- and R-ratings are T - and t - dependent. This means that the presented scales M and R are valid only for the current state of the coating system and the assessment can change when thermal aging occurs. E.g. for coating systems A to C and J, a sequence of thermal annealing, local damaging and exposure to water can lead to a complete delamination of a coated part,

while this would not happen without thermal aging. System J for instance is assessed as (M1, R1, T3) in the as-deposited state. The T3 indicates that thermal stability is not given and with rather short durations at temperatures above 300 °C, the rating changes to M1, R3, T3. For an application which operates far from this temperature regime, the coating system can be adequate, however.

Note that the fatigue behavior of the interface region requires a more sophisticated testing. For this purpose, a cyclic loading has to be chosen for the primary buckle initiation (step 1). In this case the assessment of the adhesion performance within the area of contact can alter from the surrounding assessment. So in this case the adhesion performance is locally load and cycle number dependent. A reasonable assessment can be done by a Wöhler-curve analogous to classical fatigue experiments. More analysis of the fatigue behavior of adhesion layer systems is necessary in future works.

8.3 Holistic Layout Design

From the holistic picture drawn in figure 8.1, a concept for an application specific layout design for a stable adhesion performance can be derived. Figure 8.3 schematically shows a set-up, where measures are included against all aspects, covered in this work. They will be discussed in the following.

8.3.1 Mechanical Strength

Intrinsic adhesion can be described by the enthalpy density along the interface, i.e. the product of number and strength of the participating bonds per unit area [86]. For the substrate surface, a well performed, preliminary cleaning and surface activation is mandatory to increase the number of bonds at the interface to the first deposited layer. In order to provide a good matching [117] to the substrate material on the atomic scale, an adhesion supporting layer can be introduced, tuning the strength of the interfacial bonds (avoiding weak bonds, such as van-der-Waals bonds) and intrinsic stresses which are related to the scale of the lattice mismatch.

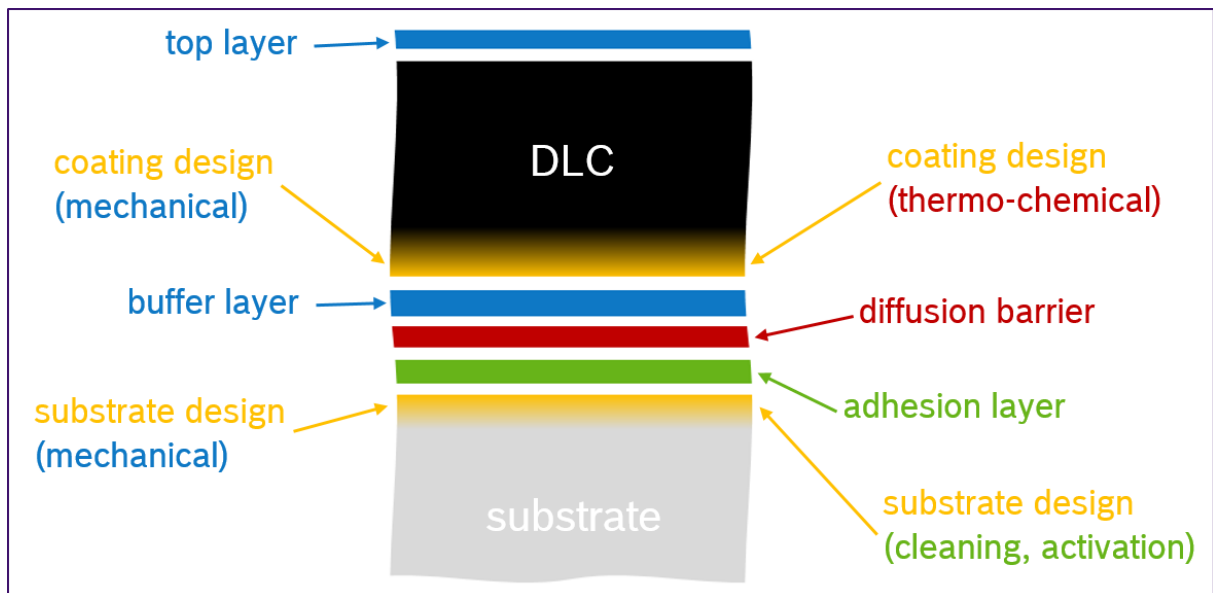


Figure 8.3: Holistic view of a design optimization with diverse measures for the several, possible requirements. The relevance of each measure depends on the concrete application conditions. Diffusion processes, stress flow and atomic matching are considered.

In order to increase the intrinsic adhesion, the deposition process has to be well understood, including the characteristics of the deposition chamber (gas fluxes, electrical contacts and inner resistances, the loading of the chamber, externally applied and self-bias, rotation of the part holders, characteristics of the part, etc.). These all influence the electromagnetic fields of the plasma, potential contaminations, angle of incidence of the ions and their mean free path, which determines their energy distribution. In turn, they all affect the properties of the adhesion layer system tremendously and thereby the adhesion performance of the coating system.

It was demonstrated that crack initiation at the interface is a crucial process regarding delamination. Defects can serve as stress raisers leading to crack initiation and also as sites for chemical attacks. The growth defect density is related to the amount of contaminations, part geometry and corresponding field exaggerations, as well as part rotation in the deposition chamber. A reduction of possible initiation sites for buckling can be beneficial, but the introduction of defects can usually not be avoided, so that the fracture toughness of the interface region must be sufficiently high, so that generated micro-cracks do not grow up to the critical value a_c .

8.3.2 Stress Management

Stress management is also important for controlling the adhesion performance. First of all, by decreasing the intrinsic stress, the internal load is decreased and thereby the delamination affinity. Drawback of a decreased compression, is a loss in tensile crack resistance. A thinner coating also decreases the load but simultaneously decreases the critical buckle radius, as the coating becomes more flexible.

Stress management can be furthermore optimized by the insertion of buffering layers which take some of the load by elastic deformation. This could be especially beneficial at locations with defects and corresponding stress exaggerations. Proven concepts for improved stress management are e.g. gradient- [117, 23] or multi-nano-layers [141, 142], which might be applied at the lower side of the functional layer. In general, thermodynamic and kinetic aspects define the morphology of each individual layer [37] with corresponding influence on the mechanical properties and residual stresses. Furthermore, the substrate surface can be pre-processed to modify the surface-near properties.

8.3.3 Thermal and Chemical Stability

Thermodynamic aspects are relevant for the thermal stability of the interlayer system and the adhesion performance. Low deposition temperatures and impacting ions decrease the surface diffusion tremendously, which is wanted for the functional layer but also leads to metastable phases in the interface region. Especially material compositions without stable room temperature solid solutions have to form a metastable phase, with intrinsic stresses. Higher deposition temperatures with increased surface diffusion however contradict the low temperature deposition concept for high hardness DLC coatings. Time consuming cooling-down steps in between however are uneconomically.

More convenient are barrier layers with superior thermal stability, which can be introduced in order to hinder diffusion processes and to protect underlying layers from corrosive species as well as precipitation in the interface region, as demonstrated with coating systems D to F with different kinds of carbide interlayers. Generally, it seems advisable to avoid segregation by avoiding critical compositions, such as Fe incorporation into Ti

or Cr.

On the other hand, with a sophisticated design, segregation reactions might be beneficially usable. E.g. if precipitation phases have advantageous mechanical properties, they could be used for in-service protection, e.g. if they form under a certain load at defects and fill up voids and thereby prevent micro-cracks. Another possibility would be the in-service formation of a passivation layer. This can be achieved via Si-doping [70] of the functional layer for instance. In the ta-C based systems it was observed that also a passivation of the Ti layer inhibits the medium driven delamination progression. A medium driven delamination progression occurred only via corrosion, which was attributed to the participation of Fe. So by avoiding Fe contamination completely, this system might show a good adhesion performance with thermal and chemical stability (M1, R1, T1).

Bibliography

- [1] J. Vetter, G. Barbezat, J. Crummenauer, and J. Avissar. Surface treatment selections for automotive applications. *Surface and Coatings Technology*, 200(5-6):1962–1968, 2005.
- [2] Verein Deutscher Normen. VDI 3198. 1991.
- [3] European Committee for Standardization. Fine ceramics (advanced ceramics, advanced technical ceramics) - Rockwell indentation test for evaluation of adhesion of ceramic coatings (ISO 26443:2008). 2016.
- [4] A. G. Evans and J. W. Hutchinson. On the mechanics of delamination and spalling in compressed films. *International Journal of Solids and Structures*, 20(5):455–466, 1984.
- [5] S. Aisenberg and R. Chabot. Ion beam deposition of insulating carbon thin films on room temperature substrates, considering transparency, index of refraction, insulating capacity, glass scratching ability, etc. *Journal of Applied Physics*, 42:2953–2958, 1971.
- [6] W. Jacob and W. Möller. On the structure of thin hydrocarbon films. *Applied Physics Letters*, 63(13):1771–1773, 1993.
- [7] D. R. McKenzie. Tetrahedral bonding in amorphous carbon. *Reports on Progress in Physics*, 59(12):1611–1664, 1996.
- [8] D. F. Shriver, P. W. Atkins, and C. H. Langford. *Inorganic Chemistry*. Oxford University Press, New York, 1989.

- [9] J. C. Angus and C. C. Hayman. Low-pressure, metastable growth of diamond and diamondlike phases. *Science (New York, N.Y.)*, 241(4868):913–921, 1988.
- [10] J. Robertson. Amorphous carbon. *Advances in Physics*, 35(4):317–374, 1986.
- [11] J. Robertson and E. P. O’Reilly. Electronic and atomic structure of amorphous carbon. *Phys. Rev. B*, 35(6):2946–2957, 1987.
- [12] J. Robertson. Mechanical properties and coordinations of amorphous carbons. *Phys. Rev. Lett.*, 68(2):220–223, 1992.
- [13] P. J. Fallon, V. S. Veerasamy, C. A. Davis, J. Robertson, Amaratunga, G. A. J., W. I. Milne, and J. Koskinen. Properties of filtered-ion-beam-deposited diamondlike carbon as a function of ion energy. *Phys. Rev. B*, 48(7):4777–4782, 1993.
- [14] N-H. Cho, K. M. Krishnan, D. K. Veirs, M. D. Rubin, C. B. Hopper, B. Bhushan, and D. B. Bogy. Chemical structure and physical properties of diamond-like amorphous carbon films prepared by magnetron sputtering. *Journal of Materials Research*, 5(11):2543–2554, 1990.
- [15] T. A. Friedmann, J. P. Sullivan, J. A. Knapp, D. R. Tallant, and D. M. Follstaedt. Thick stress-free amorphous-tetrahedral carbon films with hardness near that of diamond. *Applied Physics Letters*, 71:3820, 1998.
- [16] B. Schultrich, H.-J. Scheibe, D. Drescher, and H. Ziegele. Deposition of superhard amorphous carbon films by pulsed vacuum arc deposition. *Surface and Coatings Technology*, 98(1-3):1097–1101, 1998.
- [17] Shi Xu, D. Flynn, B. K. Tay, S. Praver, K. W. Nugent, S. R. P. Silva, Y. Lifshitz, and W. I. Milne. Mechanical properties and Raman spectra of tetrahedral amorphous carbon films with high sp^3 fraction deposited using a filtered cathodic arc. *Philosophical Magazine B*, 76(3):351–361, 1997.
- [18] A. C. Ferrari, B. Kleinsorge, N. A. Morrison, A. Hart, V. Stolojan, and J. Robertson. Stress reduction and bond stability during thermal annealing of tetrahedral amorphous carbon. *Journal of Applied Physics*, 85(10):7191–7197, 1999.

- [19] Y. Pauleau. Residual stresses in DLC films and adhesion to various substrates. In Christophe Donnet and A. Erdemir, editors, *Tribology of Diamond-like Carbon Films*, pages 102–136. Springer, New York, ©2008.
- [20] V. Zavaleyev, J. Walkowicz, G. Greczynski, and L. Hultman. Effect of substrate temperature on properties of diamond-like films deposited by combined DC impulse vacuum-arc method. *Surface and Coatings Technology*, 236:444–449, 2013.
- [21] A. K. Gangopadhyay, P. A. Willermet, M. A. Tamor, and W. C. Vassell. Amorphous hydrogenated carbon films for tribological applications I. Development of moisture insensitive films having reduced compressive stress. *Tribology International*, 30(1):9–18, 1997.
- [22] Kyoung Hoon Er and Myoung Gi So. The mechanical and structural properties of Si doped diamond-like carbon prepared by reactive sputtering. *Journal of Ceramic Processing Research*, (12 (2)):187–190, 2011.
- [23] D. Hofmann, S. Kunkel, K. Bewilogua, and R. Wittorf. From DLC to Si-DLC based layer systems with optimized properties for tribological applications. *Surface and Coatings Technology*, 215:357–363, 2013.
- [24] U. Depner-Miller, J. Ellermeier, H. Scheerer, M. Oechsner, K. Bobzin, N. Bagcivan, T. Brögelmann, R. Weiss, K. Durst, and C. Schmid. Influence of application technology on the erosion resistance of DLC coatings. *Surface and Coatings Technology*, 237:284–291, 2013.
- [25] Stéphane Neuville. Quantum electronic mechanisms of atomic rearrangements during growth of hard carbon films. *Surface and Coatings Technology*, 206(4):703–726, 2011.
- [26] Marko Petrik, Ralf Wittdorf, Helge Thomsen, Peter Kaestner, and Jan Peter Kropp. Beschichtungen für Zahnräder. *Vakuum in Forschung und Praxis*, 20(4):6–12, 2008.
- [27] Jianliang Lin, William D. Sproul, Ronghua Wei, and Roman Chistyakov. Diamond like carbon films deposited by HiPIMS using oscillatory voltage pulses. *Surface and Coatings Technology*, 258:1212–1222, 2014.

- [28] A. A. Voevodin, J. G. Jones, T. C. Back, J. S. Zabinski, V. E. Strel'nitzki, and I. I. Aksenov. Comparative study of wear-resistant DLC and fullerene-like CN_x coatings produced by pulsed laser and filtered cathodic arc depositions. *Surface and Coatings Technology*, 197(1):116–125, 2005.
- [29] F. Jansen. The effects of hydrogenation on the properties of ion beam sputter deposited amorphous carbon. *Journal of Vacuum Science & Technology A: Vacuum, Surfaces, and Films*, 3(3):605, 1985.
- [30] Thomas Wintrich and Daniel Köhler. Clean diesel approach for future requirements. *SIA Powertrain - Rouen*, 2016.
- [31] Konrad Reif. *Diesel engine management: Systems and components*. Bosch professional automotive information. Springer Fachmedien, Wiesbaden, 2014.
- [32] X. L. Peng and T. W. Clyne. Residual stress and debonding of DLC films on metallic substrates. *Diamond and Related Materials*, 7(7):944–950, 1998.
- [33] X. L. Peng and T. W. Clyne. Mechanical stability of DLC films on metallic substrates Part II — Interfacial toughness, debonding and blistering. *Thin Solid Films*, 312(1):219–227, 1998.
- [34] T. Michler, M. Grischke, K. Bewilogua, and A. Hieke. Continuously deposited duplex coatings consisting of plasma nitriding and a-C:H:Si deposition. *Surface and Coatings Technology*, 111(1):41–45, 1999.
- [35] K. Taube, M. Grischke, and K. Bewilogua. Improvement of carbon-based coatings for use in the cold forming of non-ferrous metals. *Surface and Coatings Technology*, 68–69(0):662–668, 1994.
- [36] J. S. Wang, Y. Sugimura, A. G. Evans, and W. K. Tredway. The mechanical performance of DLC films on steel substrates. *Thin Solid Films*, 325(1–2):163–174, 1998.

- [37] John A. Thornton. Influence of apparatus geometry and deposition conditions on the structure and topography of thick sputtered coatings. *Journal of Vacuum Science and Technology*, 11(4):666–670, 1974.
- [38] Y. Lifshitz, S. Kasi, and J. Rabalais. Subplantation model for film growth from hyperthermal species: Application to diamond. *Physical Review Letters*, 62(11):1290–1293, 1989.
- [39] Y. Lifshitz, G. D. Lempert, and E. Grossman. Substantiation of subplantation model for diamondlike film growth by atomic force microscopy. *Phys. Rev. Lett.*, 72(17):2753–2756, 1994.
- [40] C. A. Davis. A simple model for the formation of compressive stress in thin films by ion bombardment. *Thin Solid Films*, 226(1):30–34, 1993.
- [41] J. Robertson. Deposition mechanisms for promoting sp^3 bonding in diamond-like carbon. *Diamond and Related Materials*, (2):984–989, 1992.
- [42] M. A. Tamor and W. C. Vassell. Raman "fingerprinting" of amorphous carbon films. *Journal of Applied Physics*, 76:3823, 1994.
- [43] Xiaowei Li, Peiling Ke, He Zheng, and Aiyang Wang. Structural properties and growth evolution of diamond-like carbon films with different incident energies: A molecular dynamics study. *Applied Surface Science*, 273:670–675, 2013.
- [44] E. S. Machlin. *Materials Science in Microelectronics*. Elsevier, Amsterdam and London, 2nd ed. edition, 2005-2006.
- [45] J. Robertson. Classification of diamond-like carbons. In Christophe Donnet and A. Erdemir, editors, *Tribology of Diamond-like Carbon Films*, pages 13–24. Springer, New York, ©2008.
- [46] B. Window and K.-H. Müller. Strain, ion bombardment and energetic neutrals in magnetron sputtering. *Thin Solid Films*, 171(1):183–196, 1989.
- [47] J. Robertson. Diamond-like amorphous carbon. *Materials Science and Engineering: R: Reports*, 37(4-6):129–281, 2002.

- [48] M. Weiler, S. Sattel, K. Jung, H. Ehrhardt, V. S. Veerasamy, and J. Robertson. Highly tetrahedral, diamond-like amorphous hydrogenated carbon prepared from a plasma beam source. *Applied Physics Letters*, 64(21):2797, 1994.
- [49] John Robertson. The deposition mechanism of diamond-like a-C and a-C:H. *Proceedings of the 4th European Conference on Diamond, Diamond-like and Related Materials*, 3(4-6):361-368, 1994.
- [50] P. Koidl, Ch. Wild, B. Dischler, J. Wagner, and M. Ramsteiner. Plasma Deposition, Properties and Structure of Amorphous Hydrogenated Carbon Films. In *Materials Science Forum*, volume 52, pages 41-70.
- [51] Klaus Bewilogua, Jochen Brand, Helge Thomsen, Martin Weber, and Ralf Wittorf. Structure, properties and applications of diamond-like carbon coatings prepared by reactive magnetron sputtering. *Zeitschrift für Metallkunde*, 96(9):998-1004, 2005.
- [52] Kirsten I. Schiffmann, Matthias Fryda, Günther Goerigk, Rolf Lauer, Peter Hinze, and Andreas Bulack. Sizes and distances of metal clusters in Au-, Pt-, W- and Fe-containing diamond-like carbon hard coatings: A comparative study by small angle X-ray scattering, wide angle X-ray diffraction, transmission electron microscopy and scanning tunnelling microscopy. *Thin Solid Films*, 347(1-2):60-71, 1999.
- [53] K. Bewilogua, R. Wittorf, H. Thomsen, and M. Weber. DLC based coatings prepared by reactive d.c. magnetron sputtering. *Thin Solid Films*, 447-448:142-147, 2004.
- [54] M. Weiler, K. Lang, E. Li, and J. Robertson. Deposition of tetrahedral hydrogenated amorphous carbon using a novel electron cyclotron wave resonance reactor. *Applied Physics Letters*, 72(11):1314, 1998.
- [55] M. Chhowalla, C. A. Davis, M. Weiler, B. Kleinsorge, and Amaratunga, G. A. J. Stationary carbon cathodic arc: Plasma and film characterization. *Journal of Applied Physics*, 79(5):2237, 1996.
- [56] P. Martin and M. G. Haines. Poloidal magnetic field around a tokamak magnetic surface. *Physics of Plasmas*, 5(2):410, 1998.

- [57] J. Vetter. 60 years of DLC coatings: Historical highlights and technical review of cathodic arc processes to synthesize various DLC types, and their evolution for industrial applications. *Surface and Coatings Technology*, 257:213–240, 2014.
- [58] M. Hakovirta, V.-M. Tiainen, and P. Pekko. Techniques for filtering graphite macroparticles in the cathodic vacuum arc deposition of tetrahedral amorphous carbon films. *Diamond and Related Materials*, 8(7):1183–1192, 1999.
- [59] H.-J. Scheibe and B. Schultrich. DLC film deposition by Laser-Arc and study of properties. *Special Issue: Frontiers in Thin Film Research*, 246(1–2):92–102, 1994.
- [60] K. Sridharan and V. Sundaram. Diamond-like carbon coatings for tribological applications. *Plasma Surface Engineering Research and its Practical Applications*, page 247, 2008.
- [61] V. Zavaleyev and J. Walkowicz. Application of the Taguchi approach of the design of experiments for determination constructional and working parameters of the linear Venetian blind microdroplet filter. *5th International Symposium on Vacuum-based Science and Technology SVST5 held at Kaiserslautern, Germany, 28th to 30th September 2010*, 86(9):1248–1254, 2012.
- [62] ISO 14577. Metallic materials - Instrumented indentation test for hardness and materials parameters. 2015.
- [63] W. C. Oliver and G. M. Pharr. An improved technique for determining hardness and elastic modulus using load and displacement sensing indentation experiments. *Journal of Materials Research*, 7(06):1564–1583, 1992.
- [64] Benoit Merle, Verena Maier, Mathias Göken, and Karsten Durst. Experimental determination of the effective indenter shape and ϵ -factor for nanoindentation by continuously measuring the unloading stiffness. *Journal of Materials Research*, 27(1):214–221, 2012.
- [65] C. Schmid, V. Maier, J. Schaufler, B. Butz, E. Spiecker, S. Meier, M. Göken, and K. Durst. Highly resolved analysis of the chemistry and mechanical properties of

- an a-C:H coating system by nanoindentation and auger electron spectroscopy. *Thin Solid Films*, 528:263–268, 2013.
- [66] G. G. Stoney. *Proceedings of the Royal Society A: Mathematical, Physical and Engineering Sciences*, 82:1729, 1909.
- [67] Z.B Zhao, J Hershberger, S.M Yalisove, and J.C Bilello. Determination of residual stress in thin films: A comparative study of X-ray topography versus laser curvature method. *Thin Solid Films*, 415(1):21–31, 2002.
- [68] F. J. von Preissig. Applicability of the classical curvature–stress relation for thin films on plate substrates. *Journal of Applied Physics*, 66(9):4262–4268, 1989.
- [69] T. W. Clyne. Residual stresses in surface coatings and their effects on interfacial debonding. In *Interfacial Effects in Particulate, Fibrous and Layered Composite Materials*, volume 116 of *Key Engineering Materials*, pages 307–330. Trans Tech Publications, 1995.
- [70] Claudiu Valentin Falub, Götz Thorwarth, Christian Affolter, Ulrich Müller, Cyril Voisard, and Roland Hauert. A quantitative in vitro method to predict the adhesion lifetime of diamond-like carbon thin films on biomedical implants. *Acta Biomaterialia*, 5(8):3086–3097, 2009.
- [71] Simone Anders, Joel W. Ager III, George M. Pharr, Ting Y. Tsui, and I. G. Brown. Heat treatment of cathodic arc deposited amorphous hard carbon films. *Thin Solid Films*, 308-309:186–190, 1997.
- [72] R. Kalish, Y. Lifshitz, K. Nugent, and S. Prawer. Thermal stability and relaxation in diamond-like-carbon. A Raman study of films with different sp^3 fractions (ta-C to a-C). *Applied Physics Letters*, 74(20):2936–2938, 1999.
- [73] Hsiao-chu Tsai and D. B. Bogy. Characterization of diamondlike carbon films and their application as overcoats on thin–film media for magnetic recording. *Journal of Vacuum Science & Technology A: Vacuum, Surfaces, and Films*, 5(6):3287–3312, 1987.

- [74] T. A. Friedmann, K. F. McCarty, J. C. Barbour, M. P. Siegal, and Dean C. Dibble. Thermal stability of amorphous carbon films grown by pulsed laser deposition. *Applied Physics Letters*, 68(12):1643–1645, 1996.
- [75] Sanjay Bhargava, H. D. Bist, A. V. Narlikar, S. B. Samanta, J. Narayan, and H. B. Tripathi. Effect of substrate temperature and heat treatment on the microstructure of diamondlike carbon films. *Journal of Applied Physics*, 79(4):1917–1925, 1996.
- [76] N.M.J. Conway, A. C. Ferrari, A. J. Flewitt, J. Robertson, W. I. Milne, A. Tagliaferro, and W. Beyer. Defect and disorder reduction by annealing in hydrogenated tetrahedral amorphous carbon. *Diamond and Related Materials*, 9(3-6):765–770, 2000.
- [77] J. Ristein, R. T. Stief, L. Ley, and W. Beyer. A comparative analysis of a-C:H by infrared spectroscopy and mass selected thermal effusion. *Journal of Applied Physics*, 84(7):3836–3847, 1998.
- [78] Ch. Wild and P. Koidl. Thermal gas effusion from hydrogenated amorphous carbon films. *Applied Physics Letters*, 51(19):1506–1508, 1987.
- [79] R. Stief, J. Schäfer, J. Ristein, L. Ley, and W. Beyer. Hydrogen bonding analysis in amorphous hydrogenated carbon by a combination of infrared absorption and thermal effusion experiments. *Amorphous Semiconductors-Science and Technology*, 198:636–640, 1996.
- [80] B. Dischler, A. Bubbenzer, and P. Koidl. Bonding in hydrogenated hard carbon studied by optical spectroscopy. *Solid State Communications*, 48(2):105–108, 1983.
- [81] Camargo, S. S. Jr., Baia Neto, A. L., R. A. Santos, Freire, F. L. Jr, R. Carius, and F. Finger. Improved high-temperature stability of Si incorporated a-C:H films. *Diamond and Related Materials*, 7(8):1155–1162, 1998.
- [82] Andrea Carlo Ferrari. Determination of bonding in diamond-like carbon by Raman spectroscopy. *Diamond and Related Materials*, 11(3-6):1053–1061, 2002.

- [83] S. E. Rodil and S. Muhl. Bonding in amorphous carbon nitride. *Diamond and Related Materials*, 13(4-8):1521–1531, 2004.
- [84] J.P Sullivan, T. A. Friedmann, and A. G. Baca. Stress relaxation and thermal evolution of film properties in amorphous carbon. *Journal of Electronic Materials*, 26(9):1021–1029, 1997.
- [85] Simone Anders, Javier Diaz, Joel W. Ager, Roger Yu Lo, and David B. Bogy. Thermal stability of amorphous hard carbon films produced by cathodic arc deposition. *Applied Physics Letters*, 71(23):3367–3369, 1997.
- [86] Stéphane Neuville. Transient transverse electrical field induced by selective adsorption on low gap semiconducting thin films. *Sensors and Actuators B: Chemical*, 121(2):436–444, 2007.
- [87] M. D. Drory and J. W. Hutchinson. Measurement of the adhesion of a brittle film on a ductile substrate by indentation. *Proceedings of the Royal Society A: Mathematical, Physical and Engineering Sciences*, 452(1953):2319–2341, 1996.
- [88] Stephen Timoshenko and James M. Gere. *Theory of elastic stability*. A McGraw-Hill classic textbook reissue. Dover Publications, Mineola, N.Y., 2nd ed., dover ed. edition, 2009.
- [89] P. Waters and A. A. Volinsky. Stress and moisture effects on thin film buckling delamination. *Experimental Mechanics*, 47(1):163–170, 2007.
- [90] M. W. Moon, H. M. Jensen, J. W. Hutchinson, K. H. Oh, and A. G. Evans. The characterization of telephone cord buckling of compressed thin films on substrates. *Journal of the Mechanics and Physics of Solids*, 50:2355–2377, 2002.
- [91] Ned Bowden, Scott Brittain, Anthony G. Evans, John W. Hutchinson, and George M. Whitesides. Spontaneous formation of ordered structures in thin films of metals supported on an elastomeric polymer. *Nature*, 393(6681):146–149, 1998.
- [92] J. W. Hutchinson and Z. Sou. Mixed mode cracking in layered materials. *Advances in Applied Mechanics*, 29, 1992.

- [93] S. Miyagawa, S. Nakao, M. Ikeyama, and Y. Miyagawa. Deposition of diamond-like carbon films using plasma based ion implantation with bipolar pulses. *Surface and Coatings Technology*, 156(1):322–327, 2002.
- [94] Stefan Flege, Ruriko Hatada, Wolfgang Ensinger, and Koumei Baba. Properties of hydrogenated DLC films as prepared by a combined method of plasma source ion implantation and unbalanced magnetron sputtering. *Journal of Materials Research*, 27(5):845–849, 2012.
- [95] American Society for Testing and Materials. Standard Test Methods for Rockwell Hardness and Rockwell Superficial Hardness of Metallic Materials. (ASTM E18), 2004.
- [96] DIN Deutsches Institut für Normung e.V. Metallic materials - Rockwell hardness test. 2016.
- [97] DIN Deutsches Institut für Normung e.V. Carbon-based films and other hard coatings – Rockwell penetration test to evaluate the adhesion. 2018.
- [98] N.B. Thomsen, A.C. Fischer-Cripps, and M.V. Swain. Crack formation mechanisms during micro and macro indentation of diamond-like carbon coatings on elastic-plastic substrates. *Thin Solid Films*, 332(1):180–184, 1998.
- [99] European Committee for Standardization. Fine ceramics (advanced ceramics, advanced technical ceramics) - determination of adhesion of ceramic coatings by scratch testing (ISO 20502:2005 including Cor 1:2009). 2016.
- [100] S. J. Bull and E. G. Berasetegui. An overview of the potential of quantitative coating adhesion measurement by scratch testing. *Tribology International*, 39(2):99–114, 2006.
- [101] J. A. Williams. Analytical models of scratch hardness. *Tribology International*, 29(8):675–694, 1996.

- [102] J. Schaufler, C. Schmid, K. Durst, and M. Göken. Determination of the interfacial strength and fracture toughness of a-C:H coatings by in-situ microcantilever bending. *Thin Solid Films*, 522:480–484, 2012.
- [103] M. H. Djoufack, U. May, N. Bagcivan, T. Broegemann, and K. Bobzin. Tribological evaluation of hydrogenated DLC in Diesel lubricated model test. *Surface and Coatings Technology*, 258:381–391, 2014.
- [104] M. H. Djoufack. *Tribological evaluation of hydrogenated (a-C:H) and hydrogen-free (ta-C) diamond-like carbon coatings in Diesel lubricated model tests*. PhD Thesis, 2015.
- [105] C. V. Falub, U. Müller, G. Thorwarth, M. Parlinska-Wojtan, C. Voisard, and R. Hauert. In vitro studies of the adhesion of diamond-like carbon thin films on CoCrMo biomedical implant alloy. *Acta Materialia*, 59(11):4678–4689, 2011.
- [106] R. H. Dauskardt, M. Lane, Q. Ma, and N. Krishna. Adhesion and debonding of multi-layer thin film structures. *Engineering Fracture Mechanics*, 61(1):141–162, 1998.
- [107] Robert F. Cook and Eric G. Liniger. Kinetics of indentation cracking in glass. *Journal of the American Ceramic Society*, 76(5):1096, 1993.
- [108] Robert F. Cook. Environmentally-controlled non-equilibrium crack propagation in ceramics. *Materials Science and Engineering: A*, 260(1-2):29–40, 1999.
- [109] Russell H. Jones and R. E. Ricker. Mechanisms of stress-corrosion cracking. In Russell H. Jones, editor, *Stress-corrosion cracking*, pages 1–40. ASM International, Materials Park, Ohio, 1999.
- [110] Stephen W. Freiman. Stress-corrosion cracking of glasses and ceramics. In Russell H. Jones, editor, *Stress-corrosion cracking*, pages 337–344. ASM International, Materials Park, Ohio, 1999.
- [111] L. Chandra, M. Allen, R. Butter, N. Rushton, A. H. Lettington, and T. W. Clyne. The effect of exposure to biological fluids on the spallation resistance of diamond-

- like carbon coatings on metallic substrates. *Journal of Materials Science: Materials in Medicine*, 6(10):581–589, 1995.
- [112] U. Müller, R. Hauert, B. Oral, and M. Tobler. Temperature stability of fluorinated amorphous hydrogenated carbon films. *Surface and Coatings Technology*, 76:367–371, 1995.
- [113] R. Hauert. An overview on the tribological behavior of diamond-like carbon in technical and medical applications. *Novel Carbons in Tribology*, 37(11):991–1003, 2004.
- [114] D. A. Outka, Wen L. Hsu, K. Phillips, D. R. Boehme, N.Y.C. Yang, D. K. Ottesen, H. A. Johnsen, W. M. Clift, and T. J. Headley. *Compilation of diamond-like carbon properties for barriers and hard coatings*. 1994.
- [115] J. Woeckel, A. Benkenstein, B. Dzur, M. Keunecke, M. Mueller, S. Rath, and D. Spreemann. Thermal Degradation of DLC Coatings: Poster at PSE, Garmisch-Partenkirchen, 2014.
- [116] Chi-Lung Chang and Da-Yung Wang. Microstructure and adhesion characteristics of diamond-like carbon films deposited on steel substrates. *Diamond and Related Materials*, 10(8):1528–1534, 2001.
- [117] A. A. Voevodin, M. A. Capano, S.J.P. Laube, M. S. Donley, and J. S. Zabinski. Design of a Ti/TiC/DLC functionally gradient coating based on studies of structural transitions in Ti-C thin films. *Thin Solid Films*, (298):107–115, 1997.
- [118] M. M. Morshed, D. C. Cameron, B. P. McNamara, and M. S. J. Hashmi. Pre-treatment of substrates for improved adhesion of diamond-like carbon films on surgically implantable metals deposited by saddle field neutral beam source. *Surface and Coatings Technology*, 174-175:579–583, 2003.
- [119] R. Hauert. DLC Films in Biomedical Applications. In Christophe Donnet and Ali Erdemir, editors, *Tribology of Diamond-Like Carbon Films: Fundamentals and Applications*, pages 494–509. Springer US, Boston, MA, 2008.

- [120] Christoph P.O. Treutler. Industrial use of plasma-deposited coatings for components of automotive fuel injection systems. *Surface and Coatings Technology*, 200(5-6):1969–1975, 2005.
- [121] Jens Schaufler, Guang Yang, Karsten Durst, Erdmann Spiecker, and Mathias Göken. Microscopic study on the interfacial strength of hydrogenated amorphous carbon coating systems. *Surface and Coatings Technology*, 205:3429–3433, 2011.
- [122] M. Dao, N. Chollacoop, K. J. van Vliet, T. A. Venkatesh, and S. Suresh. Computational modeling of the forward and reverse problems in instrumented sharp indentation. *Acta Materialia*, 49(19):3899, 2001.
- [123] Tobias Schmiedl. *Untersuchung des Bruchverhaltens diamantartiger Kohlenstoffschichten (DLC)*. Master Thesis, TU Darmstadt, Darmstadt, 2016.
- [124] American Society for Testing and Materials. Annual Book of ASTM Standards. 1994.
- [125] P. Franke and D. Neuschütz. Fe-Ti. In P. Franke and D. Neuschütz, editors, *Binary systems. Part 3: Binary Systems from Cs-K to Mg-Zr: Phase Diagrams, Phase Transition Data, Integral and Partial Quantities of Alloys*, pages 1–3. Springer Berlin Heidelberg, Berlin, Heidelberg, 2005.
- [126] P. Franke and D. Neuschütz. C-Ti. In P. Franke and D. Neuschütz, editors, *Binary systems. Part 2: Elements and Binary Systems from B – C to Cr – Zr: Phase Diagrams, Phase Transition Data, Integral and Partial Quantities of Alloys*, pages 1–3. Springer Berlin Heidelberg, Berlin, Heidelberg, 2004.
- [127] P. Franke and D. Neuschütz. Fe-O. In P. Franke and D. Neuschütz, editors, *Binary systems. Part 3: Binary Systems from Cs-K to Mg-Zr: Phase Diagrams, Phase Transition Data, Integral and Partial Quantities of Alloys*, pages 1–3. Springer Berlin Heidelberg, Berlin, Heidelberg, 2005.
- [128] P. Franke and D. Neuschütz. C-Fe. In P. Franke and D. Neuschütz, editors, *Binary systems. Part 2: Elements and Binary Systems from B – C to Cr – Zr: Phase*

- Diagrams, Phase Transition Data, Integral and Partial Quantities of Alloys*, pages 1–3. Springer Berlin Heidelberg, Berlin, Heidelberg, 2004.
- [129] P. Franke and D. Neuschütz. Cr-Fe. In P. Franke and D. Neuschütz, editors, *Binary systems. Part 2: Elements and Binary Systems from B – C to Cr – Zr: Phase Diagrams, Phase Transition Data, Integral and Partial Quantities of Alloys*, pages 1–5. Springer Berlin Heidelberg, Berlin, Heidelberg, 2004.
- [130] P. Franke and D. Neuschütz. Cr-Ti. In P. Franke and D. Neuschütz, editors, *Binary systems. Part 2: Elements and Binary Systems from B – C to Cr – Zr: Phase Diagrams, Phase Transition Data, Integral and Partial Quantities of Alloys*, pages 1–4. Springer Berlin Heidelberg, Berlin, Heidelberg, 2004.
- [131] P. Franke and D. Neuschütz. C-Si. In P. Franke and D. Neuschütz, editors, *Binary systems. Part 2: Elements and Binary Systems from B – C to Cr – Zr: Phase Diagrams, Phase Transition Data, Integral and Partial Quantities of Alloys*, pages 1–3. Springer Berlin Heidelberg, Berlin, Heidelberg, 2004.
- [132] P. Franke and D. Neuschütz. Fe-Si. In P. Franke and D. Neuschütz, editors, *Binary systems. Part 3: Binary Systems from Cs-K to Mg-Zr: Phase Diagrams, Phase Transition Data, Integral and Partial Quantities of Alloys*, pages 1–3. Springer Berlin Heidelberg, Berlin, Heidelberg, 2005.
- [133] P. Franke and D. Neuschütz. C-Cr. In P. Franke and D. Neuschütz, editors, *Binary systems. Part 2: Elements and Binary Systems from B – C to Cr – Zr: Phase Diagrams, Phase Transition Data, Integral and Partial Quantities of Alloys*, pages 1–3. Springer Berlin Heidelberg, Berlin, Heidelberg, 2004.
- [134] D. C. Agrawal and R. Raj. Measurement of the ultimate shear strength of a metal-ceramic interface. *Acta Metallurgica*, 37(4):1265–1270, 1989.
- [135] R. Braak, U. May, L. Onuseit, G. Repphun, M. Guenther, C. Schmid, and K. Durst. Accelerated thermal degradation of DLC-coatings via growth defects. *Surface and Coatings Technology*, 349:272–278, 2018.

- [136] Ihsan Barin. *Thermochemical data of pure substances*. VCH, Weinheim, Federal Republic of Germany, 1989.
- [137] Hoffmann. Implantatbeschichtung, <http://www.titan-anodisieren.eu/14.html>.
- [138] Qiuhua Rao, Zongqi Sun, O. Stephansson, Chunlin Li, and B. Stillborg. Shear fracture (Mode II) of brittle rock. *International Journal of Rock Mechanics and Mining Sciences*, 40(3):355–375, 2003.
- [139] Vito Volterra. Sur l'équilibre des corps élastiques multiplement connexes. *Annales scientifiques de l'É.N.S. 3^e série*, (24):401–517, 1907.
- [140] Geoffrey Ingram Taylor. The mechanism of plastic deformation of crystals. Part I.—Theoretical. *Proc. R. Soc. Lond. A (Proceedings of the Royal Society of London. Series A, Containing Papers of a Mathematical and Physical Character)*, 145(855):362–387, 1997.
- [141] Juergen M. Lackner, Wolfgang Waldhauser, Boguslaw Major, Lukasz Major, and Marcin Kot. Plastic deformation in nano-scale multilayer materials — A biomimetic approach based on nacre. *Thin Solid Films*, 534:417–425, 2013.
- [142] Xiaoyan Guan, Yongxin Wang, Qunji Xue, and Liping Wang. Toward high load bearing capacity and corrosion resistance Cr/Cr₂N nano-multilayer coatings against seawater attack. *Surface and Coatings Technology*, 282:78–85, 2015.

Danksagung

Zu guter Letzt möchte ich mich bei einigen Leuten bedanken, deren Unterstützung und Zutun dazu beigetragen haben, dass dieses Werk entstehen konnte. Allen voran danke ich Leni Onuseit für den Vertrauensvorschuss und die anfängliche Betreuung seitens Bosch und Ulrich May für die Fortführung der Betreuung. Ich hatte somit das Glück zwei hervorragende Betreuer in der richtigen Reihenfolge zu haben. Leni half mir besonders am Anfang "Zug" und Struktur in die Sache zu bringen, während Ulli mir den nötigen kreativen Freiraum bei der Fokussierung der relevanten Aspekte gab und mich bei der Modellbildung durch gemeinsames "Hirnen" unterstützte.

Prof Karsten Durst danke ich für die universitäre Betreuung der Arbeit. Vor allem bei der Strukturierung, Stimmigkeit und Kohärenz der schriftlichen Ausarbeitung fand ich viel Unterstützung.

Mein Dank gilt auch den Mitarbeitern des Fachgebiets physikalische Metallkunde, die mich gut aufgenommen haben, wenn ich auch, auf Grund der ausreichend großen Distanz, nur sporadisch vor Ort sein konnte. Das gemeinsame Seminar in Grass-Ellenbach habe ich sehr genossen. Besonders danke ich Christoph Schmid für die Bereitstellung seiner Expertise und Hilfsbereitschaft vor Ort in Darmstadt. Außerdem danke ich Tobias Schmidl für sein Engagement während seiner Masterarbeit, die ich betreuen durfte und den Input der sich daraus ergab.

Ich danke Siegfried Ruthardt und Gernot Rephun, die die Arbeit seitens Bosch erst möglich gemacht haben, ebenso wie die Teilnahmen an internationalen Konferenzen (insbesondere der ICMCTF in San Diego) und für den tollen und herzlichen Umgang mit ihren Mitarbeitern. Allen Mitarbeitern der DS/ETD bzw. PS/EAT danke ich für ein tolles Arbeitsklima mit steter Hilfsbereitschaft für den jeweils Anderen. Dies gilt ebenso für die Kollegen im Büro, wie auch für die Kollegen im Labor. Ich bin froh weiterhin ein

Teil des Teams zu sein.

Marcus Günther und Jens Emmerlich danke ich für wichtige, fruchtbare Gespräche und kompetenten Input bei der Auswahl bzw. Gestaltung der Schichtsysteme, mit jeweils unterschiedlichen Herangehensweisen. Außerdem danke ich für das Durchführen der Beschichtungschargen, die die Grundlage der praktische Arbeit waren.

Sarah Siepa danke ich für das ins Leben rufen und am Laufen halten des DAK (Doktoranden-Arbeits-Kreis) "Plasma" und außerdem den Teilnehmern in diesem spannenden Arbeitskreis. Die gemeinsamen Mittagessen vermisse ich.

Stefan Grosse und seiner Gruppe danke ich für erkenntnisreiche Gespräche, insbesondere in den ACC-Meetings von Michael Fraune.

Meinem Kollegen Günther Durst danke ich für das Bereitstellen seiner praktischen Erfahrung in Bezug auf Plasmabeschichtung, sowie Kavitationstests. Mein Dank geht auch an Harald Schulze and Daniel Franz für umfangreiche Diskussionen innerhalb des C3-Teams, aus denen ich viel gelernt habe.

Danke auch an die Kollegen aus dem "Boulder-Team", unter anderem unseren Praktikanten aus Übersee. Das war und ist eine wichtige Abwechslung vom Alltag für mich und hilft, den Kopf freizubekommen. Herzlichst danke ich auch meiner Familie und meinen Freunden für ihren Rückhalt, allen voran meiner Frau Kristina, die mich besonders in der schwierigen Zeit des Schreibens unterstützt bzw. ertragen hat.

Kurz gesagt, vielen Dank an Alle, auch an diejenigen, die ich nicht explizit erwähnt habe oder möglicherweise vergessen habe hervorzuheben! Danke!

List of Abbreviations

100Cr6	chrome steel
a	radius of initial crack
a_c	critical radius for buckling
A	contact area
A_D	total area of delaminated DLC
α	small angle
a-C	amorphous carbon
a-C:H	hydrogenated amorphous carbon
b_{spall}	critical spallation radius
B	number of bonds at the crack tip
bcc	body centered cubic
c	constant
CAE/CVAD	cathodic arc evaporation / cathodic vacuum arc deposition
CFST	constant force scratch test
CoF	coefficient of friction
CSM	continuous stiffness measurement
DC	direct current
DLC	diamond-like carbon
E	Youngs modulus of substrate (_{sub}) or thin film (_f)
E_A	activation energy
E_{IT}	indentation modulus of substrate (_{sub}) or thin film (_f)
ϵ_{ij}	biaxial strain components
η	energy per bond area
ECR	electron cyclotron resonance
ECWR	electron cyclotron wave resonance
EDX	energy dispersive X-ray spectroscopy
EN590	European standard Diesel
F	normal load
fcc	face centered cubic
FEM	finite element method
FIB	focused ion beam
G	strain energy release rate
G_c	critical strain energy release rate
$G_{c,\perp}$	critical strain energy release rate perpendicular for the straight blister
$G_{c,\parallel}$	critical strain energy release rate in propagation direction
G_{TH}	threshold strain energy release rate
GDK	Diesel fuel with less additives

h	indentation depth
h	thickness of substrate (_{sub}) or thin film (_f)
H	hardness
H_{IT}	indentation hardness of substrate (_{,sub}) or thin film (_{,f})
hcp	hexagonal close-packed
HF1 to HF6	adhesion classes acc. to VDI 3198
HiPIMS/HiPPMS	high power pulse magnetron sputtering
HRC	Rockwell C test
HS6-5-2	high speed steel
HV	Vickers hardness
ICP	inductively coupled plasma
IWS	Fraunhofer-Institut für Werkstoff- und Strahltechnik
k	geometry factor
k	rate constant
K	stress intensity factor
l	length
l_{max}	maximum annular path length
L_{c1} to L_{c3}	critical loads
LSM	laser scanning microscope
m	crack growth exponent
M_i	molar mass
MD	molecular dynamic simulation
Me-DLC	metal doped DLC
MPST	multi-pass scratch test
MS	magnetron sputtering
n_0	plasma density
ν	Poisson ratio of the substrate (_{sub}) and film (_f)
nc	nano-crystalline
NRA	resonant nuclear reaction analysis
Ω	strain energy per unit area, initially (₀)
P_{max}	maximum indentation load
PBS	phosphate buffered saline
PECVD / PACVD	plasma enhanced/assisted chemical vapor deposition
PFST	progressive force scratch test
PIPS	precision ion preparation system
PTFE	polytetrafluoroethylene
PVD	physical vapor deposition
qu.-a.	quasi-amorphous
r	radial distance
r_{exp}	radius of curvature
r_{max}	maximum radial distance
r_{round}	radius of corner rounding
R	universal gas constant
R_z	surface roughness parameter
RF	radio frequency
RT	room temperature

σ, π	binding states
σ_0	intrinsic residual stress
σ_c	critical buckle stress
$\sigma_{c,\perp}$	critical buckle stress perpendicular for the straight blister
σ_{ext}	external compressive stress
σ_{ij}	biaxial stress components
σ_{max}	maximum stress
σ_{tensile}	tensile stress
S	stiffness
SACS	small angle cross section
SCC	stress corrosion cracking
SE	secondary electron
SEM	scanning electron microscopy
SFNS	stress field nanoscratch
sp^1, sp^2, sp^3	hybridization states
t	time, initially ($_0$)
t_{crit}	incubation time
T	temperature
T_c	Curie temperature
T_{degr}	degradation temperature
T_{dep}	deposition temperature
T_e	electron temperature
θ	azimuthal polar coordinate
ta-C	tetrahedral amorphous carbon
ta-C:H	hydrogenated, tetrahedral amorphous carbon
TED	transmission electron diffraction
TEM	transmission electron microscopy
UBMS	unbalanced magnetron sputtering
UNAT	universal nanomechanical tester
v	propagation velocity, initially ($_0$)
VHF	very high frequency
w_i	mass fraction
w/wo	with/without
WP	work package
x_i	atomic fraction